Doctoral theses at NTNU, 2020:329

Cristian Torres Rodríguez

Examination of the Effect on Tungsten on the Corrosion Properties of 25% Cr Super Duplex Stainless Steel by Advanced Electrochemical Techniques

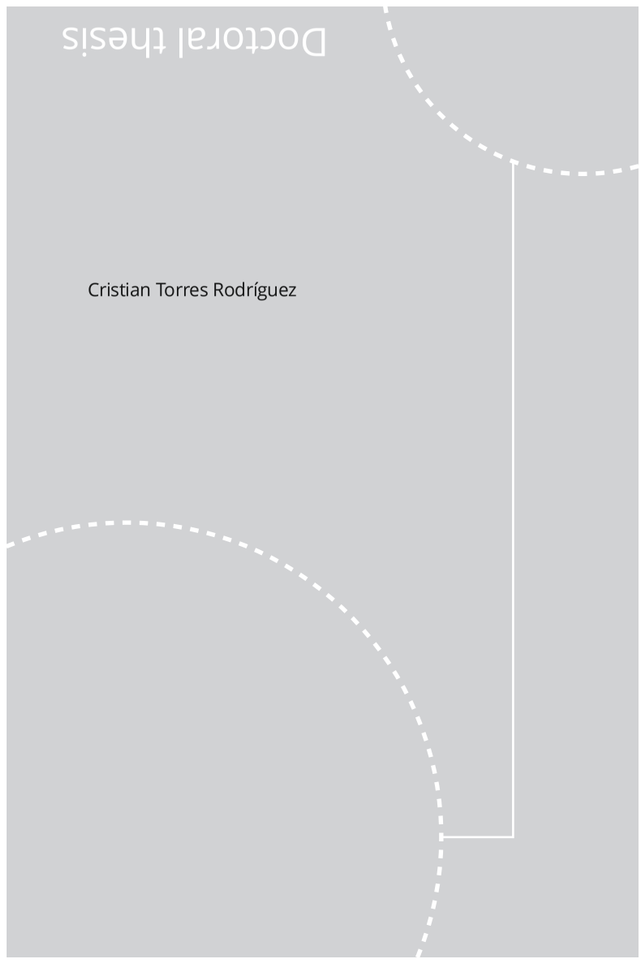

ISBN 978-82-326-5004-0 (printed ver.)
ISBN 978-82-326-5005-7 (electronic ver.)
ISSN 1503-8181

NTNU
Norwegian University of
Science and Technology

NTNU
Norwegian University of Science and Technology
Thesis for the Degree of
Philosophiae Doctor
Faculty of Engineering
Department of Mechanical and Industrial
Engineering

Doctoral theses at NTNU, 2020:329

NTNU
Norwegian University of
Science and Technology

Cristian Torres Rodríguez

Examination of the Effect on Tungsten on the Corrosion Properties of 25% Cr Super Duplex Stainless Steel by Advanced Electrochemical Techniques

Thesis for the Degree of Philosophiae Doctor

Trondheim, October 2020

Norwegian University of Science and Technology
Faculty of Engineering
Department of Mechanical and Industrial Engineering

NTNU
Norwegian University of
Science and Technology

NTNU
Norwegian University of Science and Technology

Thesis for the Degree of Philosophiae Doctor

Faculty of Engineering
Department of Mechanical and Industrial Engineering

ISBN 978-82-326-5004-0 (printed ver.)
ISBN 978-82-326-5005-7 (electronic ver.)
ISSN 1503-8181

Doctoral theses at NTNU, 2020:329

Printed by NTNU Grafisk senter

Education is the most powerful weapon which you can use to change the world

-Nelson Mandela

Preface

This doctoral thesis is submitted to the Norwegian University of Science and Technology (NTNU), in fulfilment of requirements for the degree of Philosophiae Doctor. The work included in this thesis has been carried out at the Department of Mechanical and Industrial Engineering from May 2016 to June 2020. Prof. Roy Johnsen has been the main supervisor, Prof. Mariano Iannuzzi from Curtin University and Dr. Mariano Kappes from Comisión Nacional de Energía Atómica (CNEA) have been the candidate's co-supervisors. The main experimental part of the work has been carried out at the Corrosion laboratory (Corrlab) belonging to SINTEF. Several laboratories from the Department of Mechanical and Industrial Engineering and the Department of Materials Science and Engineering at NTNU were employed as well for the specimen preparation and characterization.

This work was financed by NTNU's Department of Mechanical and Industrial Engineering and included collaboration with Curtin University, Perth, Western Australia.

The thesis consists of two parts. Part I (Chapters 1 to 9) includes introduction, literature review and a summary of the work. Part II (Chapter 10) contains three peer-reviewed journal papers published or summitted to scientific journals and two papers presented at international conferences.

Cristian Torres Rodriguez

July 2020

Acknowledgements

First and foremost, I would like to thank Professor Roy Johnsen for giving me the opportunity to do this PhD when I told him that I was interested in the topic of localized corrosion. You have been an amazing supervisor, always supporting and guiding me through all the research hardships I have encountered. You have taught me a lot and are an example of a dedicated researcher, taking care of my experiments while I was on holidays, working late in the lab or even in the weekends. You have my most sincere appreciation.

I am very grateful to Professor Mariano Iannuzzi, for all the guidance and knowledge you have provided to me during these 4 years. Even though you have supervised me from another continent, you have constantly followed my progress and often offered feedback. Thank you as well for keeping up with my draft manuscripts updates almost daily in these last months.

A special mention goes to Professor Nuria Espallargas. You are the responsible that I am today here in Norway, in NTNU, investigating in topics related to corrosion. Thank you very much for asking me to stay and for all your help inside and outside work.

Thank you very much to all my friends and colleagues at the Department of Mechanical and Industrial Engineering and the group of Materials and Nanotechnology at SINTEF. Even though my stay as PhD-student lasted 4 years, I have been almost 9 years working here. During all this time, many people (too many to mention here) have come and go who have contributed to my growth as researcher. My requests for help was always granted with a smile. Everybody was always willing to share their knowledge, creating an amazing working atmosphere.

To all my friends, in Trondheim and abroad, thanks for being part of my life. Special thanks to my flatmate for his encouragement and listening to my daily updates during the writing process.

My deepest gratitude goes to my friends in Valencia, especially to Vicen, Ale and Dani who welcome me back every time I take holidays in Spain like the distance does not exist. Thanks for prioritizing the time with me and, despite the distance, being the greatest support all the time. Our friendship is stronger than before I left so many years ago.

Last but not least, thanks to my family, especially to my father, Rafael Torres Ferrer. The only reason I have managed to achieve so much is thanks to the assistance provided continuously since I was a kid. Even though you said when I was 12: “I cannot help you in Math, Chemistry or Physics anymore”, you have helped me all these years in many ways, allowing me to focus on my studies and the goals I set for myself. Thank you very much.

Abstract

In this thesis, the effect of Tungsten (W) on localized corrosion resistance of 25Cr super duplex stainless steel (SDSS) was investigated.

Firstly, the effect of W on precipitation kinetics of intermetallic phases in SDSS was studied. Three SDSSs differing in their W content (0, 0.6 and 2.1 wt.%) were isothermally heat treated (IHT) at different combinations of temperature and time followed by microstructure analyses with different microscopy techniques. A critical pitting corrosion test was performed to correlate the actual microstructure with the corrosion resistance of the materials.

Secondly, the three SDSSs were tested in the solution annealed (SA) condition and their critical crevice corrosion repassivation potential ($E_{R,Crev}$) was measured using a potentiodynamic-galvanostatic-potentiodynamic (PD-GS-PD) technique at different temperatures. Critical crevice corrosion repassivation temperature ($T_{R,Crev}$) was determined from the $E_{R,Crev}$. Additionally, the two SDSSs with 0 and 2.1 wt.% W were further tested in natural seawater polarized to different fixed potentials. The temperature was increased stepwise to obtain the critical crevice temperature (CCT) and, after initiation of crevice corrosion, the temperature was decreased stepwise to measure $T_{R,Crev}$, which was compared with the output from the PD-GS-PD technique. In addition, some samples with selected IHT temperature-time combinations from the microstructure characterization were tested with the same procedure in natural seawater.

Lastly, the W-free and the 2.1 wt.% W SDSSs were tested in the SA condition in solutions simulating crevice corrosion environments at different temperatures. Two different solutions were used: 1M HCl as solution reference for 0 pH, and 7M LiCl adjusted to 0 pH to represent the solution in a stable propagating crevice corrosion attack. Galvele's acidification model was employed to estimate the critical potential (E_{crit}) values of these materials and compare them with the results from the other used techniques.

Results obtained with all the techniques demonstrated a beneficial effect of W on the localized corrosion resistance of SDSS. In SA specimens, the higher the W content, the larger the enhancement. On the other hand, results showed that there exists a W content range within which W retarded and decreased the amount of deleterious phase precipitation on IHT specimens. Outside this range, W became detrimental as the deleterious phases precipitated earlier and in larger amount than the reference W-free material.

Table of Contents

List of Figures

List of Tables

Abbreviations

AES: Auger electron spectroscopy

ANOVA: Analysis of the variance

BCC: Body-Centered Cubic

BCT: Body-Centered Tetragonal

BSE: Back scattered electron

C: Concordant

CCT: Critical Crevice Temperature

Cl^-: Chloride

CPP: Cyclic Potentiodynamic Polarization

CPT: Critical Pitting Temperature

CRA: Corrosion-resistant alloy

D: Discordant

d'_M: Dissolution ratio of element M

$d'_{M.congruent}$: Dissolution required to be congruent with respect to the dissolution of Fe

$d'_{M.experimental}$: Dissolution ratio measured by ICP-MS of element M

df: Degrees of freedom

DSS: Duplex Stainless Steel

E_B: Breakdown potential

E_{Crev}: Crevice corrosion potential

E_{corr}: Corrosion potential

E_{crit}: Critical potential

E_{Flade}: Flade potential

E_{inh}: polarization required in the presence of buffers or inhibitors

E_P: Pitting corrosion potential

E_{Prot}: Protection potential

E_R: Repassivation potential

$E_{R,Crev}$: Crevice corrosion repassivation potential

E_{Trans}: Transpassive potential

EBSD: Electron backscatter diffraction

EDS: Energy-Dispersive X-ray Spectroscopy

FCC: Face-Centered Cubic

FIB: Focused ion beam

GS: Galvanostatic polarization

H_0: Null hypothesis

H_1: Alternative hypothesis

HCP: Hexagonal closest packed

HR: High-resolution

i: Current density

i_{crit}: Critical current density

i_{Flade}: Flade current density

i_{GS}: Galvanostatic polarization current density

i_{pass}: Passive current density

ICP-MS: Inductively Coupled Plasma Mass Spectrometry

IFM: Infinite Focus Microscope

IHT: Isothermal heat treatment

LOM: Light optical microscopy

MANOVA: Multivariate analysis of the variance

MS: Mean squares

OCP: Open circuit potential

OPS: Oxide polishing suspension

PD: Potentiodynamic polarization

PD-GS-PD: Potentiodynamic-Galvanostatic-Potentiodynamic

PRE: Pitting Resistance Equivalent

PRE_N: Pitting Resistance Equivalent considering the N content

$PRE_{N,W}$: Pitting Resistance Equivalent considering the N and W content

PS: Potentiostatic polarization

PTFE: Polytetrafluoroethylene

Q: Electric charge

Q_{exp}: Experimental electrical charge calculated from the GS and reverse PD steps from the PD-GS-PD technique.

r: Pearson's correlation coefficient

SA: Solution annealed

SAD: Selected area electron diffraction

SCE: Standard calomel electrode

SEM: Scanning Electron Microscope

SDSS: Super Duplex Stainless Steel

SS: Sum of squares

STEM: Scanning transmission electron microscopy

T_{Prot}: Protection temperature

T_R: Repassivation temperature

$T_{R,Crev}$: Crevice corrosion repassivation temperature

Txty: IHT temperature-time combinations

TEM: Transmission electron microscopy

THE: Tsujikawa-Hisamatsu Electrochemical

TTT: Temperature-time-transformation

TTTC: Temperature-time-transformation-corrosion

x: Depth localized attack

$x_{Crit,Trans}$: Critical transpassive size attack

XPS: X-ray photoelectron spectroscopy

W: Tungsten

α: Ferrite (metallography) or Error type I (statistics)

β: Error type II

γ: Austenite

γ_2: Secondary austenite

η: Overpotential

ρ: Spearman's correlation coefficient

σ: Sigma

τ: Kendall's correlation coefficient

ϕ: ohmic potential drop

χ: Chi

CHAPTER 1: INTRODUCTION

This chapter includes an introduction to the research topic performed in this thesis, i.e., an explanation of the background and the scope of this study together with an overview of all the topics focused on in this thesis.

Chapter 1: Introduction

1.1. Motivation

Super Duplex Stainless Steels (SDSS) are widely used in aggressive environments such as in the Oil & Gas industry due to their exceptional mechanical and corrosion resistance properties. The good corrosion resistance is achieved thanks to the high content of elements like Cr and Mo, among others. A promising element that could enhance corrosion resistance is W. Investigations regarding alloying element additions need to consider two different roles: (i) the element added in solid solution in Solution Annealed (SA) material conditions, and (ii) influence on the precipitation kinetics of intermetallic phases of isothermal heat treated materials. However, in the scientific community there is still a strong disagreement on the role of W on the corrosion resistance properties of stainless steels. Published literature, as explained in detail in section 2.6, seems to report controversial results regarding both roles of W, especially on the effect of deleterious phase precipitation kinetics.

1.2. Objectives

The investigation in this thesis involved the study of three SDSS materials which differed mainly in the W content. One of them was W-free and was used as a reference material. The others contained 0.6 and 2.1 wt.% W. The techniques employed to study the effect of W focused on the influence on precipitation kinetics of deleterious phases and the effect on SA conditions. The main goals of this investigation were to:

- Determine the effect of W on precipitation kinetics of deleterious phases, quantify their volume fraction and correlate the quantification with the localized corrosion resistance of the materials.
- Quantify the crevice corrosion resistance of SA materials as a function of their W content.
- Verify the crevice corrosion resistance by exposing the materials long-term in natural seawater.
- Analyze the role of W in localized corrosion environment by means of Galvele's critical acidification model.

1.3. Thesis overview

The background and the outcome of the research in this thesis are presented in 9 chapters, in addition to a 10th chapter which includes the appendixes. The content of each chapter is summarized as follows:

- Chapter 1: Introduction to the background, scope and overview of the thesis.
- Chapter 2: Theoretical framework explaining different concepts and methodologies followed during this investigation.
- Chapter 3: Heat treatment procedure, characterization techniques to identify and quantify the intermetallic phases precipitating in the materials, and volume fraction results of the deleterious phases.
- Chapter 4: Corrosion tests and procedures employed to study the effect of W on the corrosion resistance of the materials.
- Chapter 5: Characterization techniques and procedures used to analyze the specimens and solutions after the corrosion tests.
- Chapter 6: Summary of the outcome of the three peer-reviewed journal papers produced during this investigation.
- Chapter 7: Methodology, results and main conclusions from the long-term natural seawater exposure used to verify the corrosion resistance results from the techniques used in the journal papers.
- Chapter 8: General conclusions drawn by the complete investigation performed during the PhD, in addition to suggested future experiments to complete this investigation.
- Chapter 9: Includes all references used in the thesis.
- Chapter 10: Appendix including the three peer-review journal papers and the two conference papers which are the main outcome of the thesis.

1.4. List of papers and conferences

During this PhD thesis, three peer-reviewed journal papers were produced, in addition to two international conference papers. The conference papers were published before the end of the investigation; thus, this PhD thesis focuses on the journal papers in addition to some experimental results which have not yet been published.

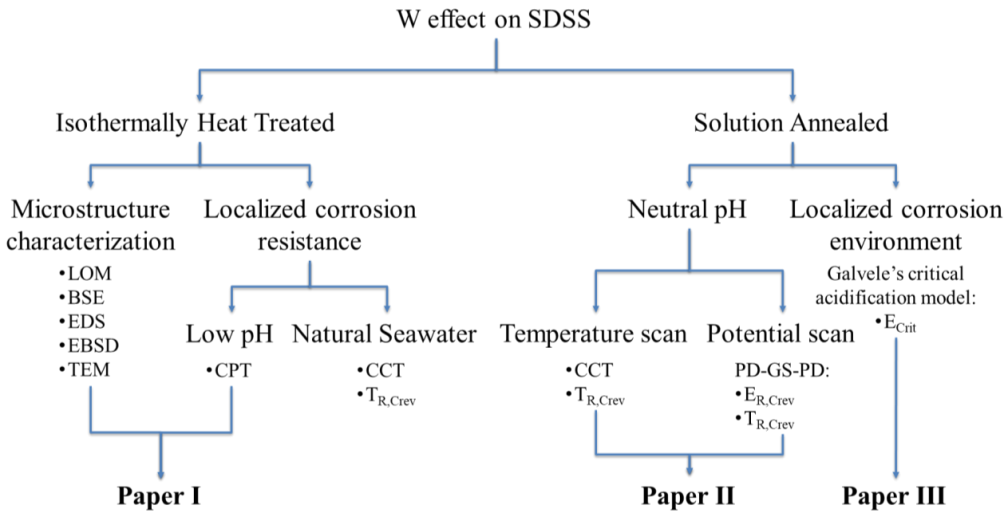

Figure 1-1. Overview of the performed experiments in connection to the journal papers included in this thesis.

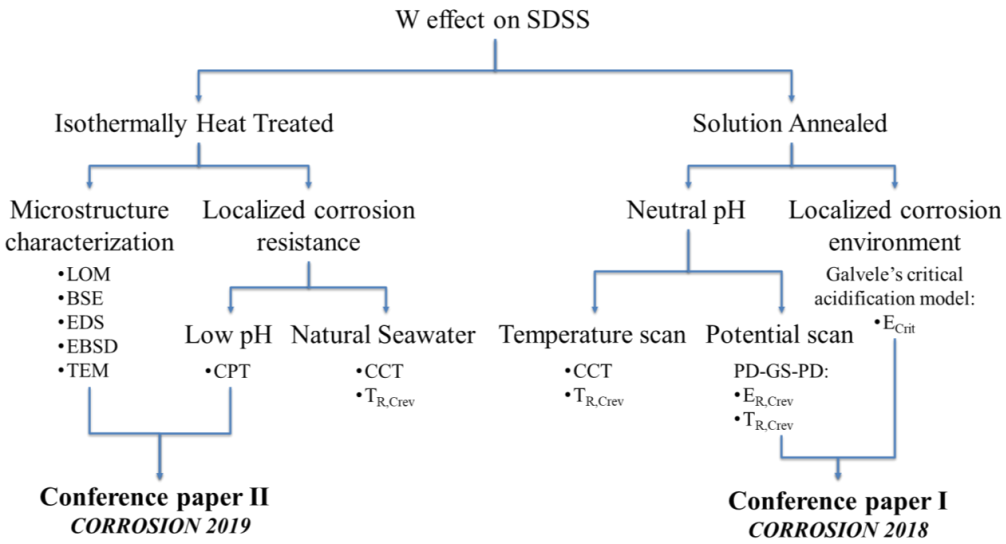

Figure 1-2. Overview of the performed experiments in connection to the conference papers in this thesis.

Figure 1-1 and Figure 1-2 illustrate the overview of the full investigation outcome, indicating which topics each journal and conference paper covered, respectively. The conference papers include information that were later included in the journal papers. As seen in Figure 1-1 and Figure 1-2, conference paper I contains information included in Paper II and Paper III, whereas conference paper II constitutes some results published in Paper I.

The three peer-reviewed journal papers (one published and two submitted) included in the appendixes of this thesis are:

I. **C. Torres**, M. S. Hazarabedian, Z. Quadir, R. Johnsen, M. Iannuzzi, The Role of Tungsten on the Phase Transformation Kinetics and its Correlation with the Localized Corrosion Resistance of 25Cr Super Duplex Stainless Steels, *Journal of The Electrochemical Society*, 167 (2020), 081510.

   Contributions: RJ and MI designed and coordinated the study. CT performed the heat treatments and the microscopy characterization apart from the TEM. MSH and ZQ performed some EBSD and all the TEM. CT, MSH, RJ and MI interpreted the results. All the authors helped to draft the manuscript and gave final approval of publication.

II. **C. Torres**, R. Johnsen, M. Iannuzzi, Crevice Corrosion of Solution Annealed 25Cr Duplex Stainless Steels: Effect of W on Critical Temperatures, *accepted for publication in Corrosion Science (date 29.09.2020).*

   Contributions: CT, RJ and MI designed and coordinated the study. CT performed all the experimental work. All the authors helped to interpret the results, drafted the manuscript and gave final approval of publication.

III. **C. Torres**, M. Iannuzzi, R. Johnsen, Use of the Critical Acidification Model to Estimate the Influence of W in the Localized Corrosion Resistance of 25Cr Super Duplex Stainless Steels, *accepted for publication in Metals, special issue "Localized Corrosion of Metals and Alloys".*

   Contributions: CT, RJ and MI designed and coordinated the study. CT performed all the experimental work. All the authors helped to interpret the results, drafted the manuscript and gave final approval of publication.

During the PhD project, the candidate participated in several international conferences. Participation and contribution in each international conference are indicated below:

- **CORROSION 2018**

  15-19 April 2018, Phoenix, Arizona, USA

  Poster presentation: Influence of Tungsten on Crevice Corrosion Resistance of 25Cr Duplex Stainless Steels in Natural Seawater.

  Oral presentation: Influence of Tungsten on Passivity Breakdown and Repassivation of 25Cr Super Duplex Stainless Steel.

  Published conference proceeding: Influence of Tungsten on Passivity Breakdown and Repassivation of 25Cr Super Duplex Stainless Steel (Paper no. C2018-11102).

- **17th Nordic Corrosion Congress**

  23-25 May 2018, Copenhagen, Denmark

  Oral presentation: Effect of Tungsten on the Critical Crevice Temperature of 25Cr Duplex Stainless Steel in Seawater.

- **CORROSION 2019**

  24-28 March 2019, Nashville, Tennessee, USA

  Oral presentation: Effect of W on Phase Transformation kinetics and its Correlation with Localized Corrosion Resistance for UNS S39274.

  Published conference proceeding: Effect of W on Phase Transformation kinetics and Its Correlation with Localized Corrosion Resistance for UNS S39274 (Paper no. C2019-13233).

CHAPTER 2: THEORETICAL FRAMEWORK

This chapter includes theoretical knowledge about materials, metallurgy, electrochemistry and methodologies used during the investigation in this thesis.

2.1. Localized corrosion

Stainless steels were discovered in the 19th century when at least 10.5-12 wt.% Cr was added as alloying element to carbon steels. It was observed that Cr forms an oxide layer on the surface of the steel acting as a chemical barrier and, thus, increasing the corrosion resistance of the material. This layer is called passive layer and it is able to self-heal itself spontaneously in case of a damage as illustrated in Figure 2-1. However, in some aggressive media, often containing chloride (Cl^-) ions, the passive layer might suffer from breakdown in specific localized points or areas. In the cases in which the aggressive environment does not let the self-healing process to occur, the result will be localized corrosion. Two of the most important types of localized corrosion are pitting and crevice corrosion [1].

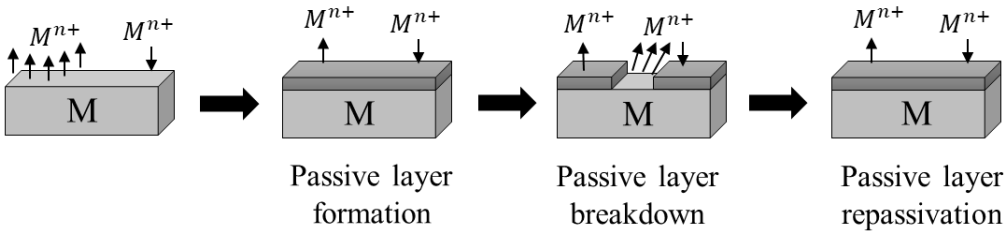

Figure 2-1. Illustrations of passive layer formation, breakdown and repassivation.

Pitting corrosion occurs in areas exposed to the bulk material, whereas crevice corrosion develops in occluded areas. Some researchers suggested that crevice corrosion is a type of pitting in occluded areas, while others stated that pitting is a type of crevice corrosion attack [2] because both corrosion processes have a lot of similarities. Both corrosion attacks involve localized breakdown of the passive layer. The local environment is acidic and with large concentration of chloride ions [3]. Materials susceptibility are ranked similarly for both corrosion processes in most cases [2], indicating a similar mechanism and alloy chemical composition influence [4]. The mechanism includes parameters such as critical temperatures (critical pitting temperature (CPT) and critical crevice temperature (CCT)) and critical potentials (critical pitting corrosion potential (E_P), critical crevice corrosion potential (E_{Crev}))) above which localized corrosion occurs [1, 4, 5]. Consequently, these two processes are often studied together [1, 6-8], since both are viewed as following the same electrochemical behavior [9]. Nevertheless, there are some differences between pitting and crevice corrosion; the geometry being the most important [1, 9]. In the occluded site where crevice corrosion occurs, diffusion to/from the bulk environment is limited causing, initially, a lower incubation time for

the crevice corrosion to initiate in comparison to pitting corrosion [5]; and at a later stage, a more aggressive environment harder to dilute. Consequently, CCT, crevice corrosion repassivation potential ($E_{R,Crev}$) and crevice corrosion repassivation temperature ($T_{R,Crev}$) are lower than CPT, pitting repassivation potential and pitting repassivation temperature, respectively [6]. Consequently, it is agreed that crevice corrosion is more detrimental than pitting corrosion in practice [4, 5].

As localized corrosion initiates by passive layer breakdown, many other different elements have been studied in order to further enhance this passive layer and, hence, improve the corrosion resistance of stainless steels. The most beneficial elements are N and, especially, Mo. However, these elements by themselves do not strengthen the material. Instead, Mo combined with Cr (Cr+Mo) and N combined with Mo plus Cr (Cr+Mo+N) increase clearly the corrosion resistance properties of stainless steels [10]. As a result, Lorenz and Medawar [11] and later Truman [12] proposed an empirically derived parameter referred to as Pitting Resistance Equivalent (PRE) to correlate the observed localized corrosion resistance of stainless steels with composition according to Equation 2.1. In this equation, the sub-index N indicates that the original PRE formula proposed by Lorenz and Medawar was modified to include N [13]. The *%M* represents the wt.% of element *M* present as alloying element in solid solution in the material. The higher the PRE number, the higher the resistance to localized corrosion (pitting and crevice) of the material.

$$PRE_N = \%Cr + 3.3\%Mo + 16\%N \quad (2.1)$$

2.2. Super Duplex Stainless Steel

As environments become more corrosive; high alloyed stainless steels have been adopted. Duplex stainless steels (DSS) are a family of stainless steels defined for having a dual phase microstructure, composed of austenite (γ) and ferrite (α). Both phases need to be stainless, i.e., contain more than 10.5 to 12 wt.% Cr, and be present in a ratio close to 50/50 to attain a good combination of chemical and mechanical properties [14, 15]. In this manner, DSS is stronger than austenitic stainless steels thanks to its fine grained microstructure [14, 16], as seen in Table 2-1. Additionally, DSS has better corrosion resistance performance than austenitic stainless steels, due to the higher Cr and Mo content, especially in the higher grades [14, 15].

Table 2-1. Typical values of mechanical properties comparing austenitic, ferritic, DSS and SDSS [14].

Stainless steel type	Tradename	UNS	Ultimate tensile strength (MPa)	0.2% proof stress (MPa)
Austenitic	AISI 304	S30400	515-690	210
Ferritic	AISI 430	S43000	450	205
DSS	Alloy 2205	S31803	680-880	450
SDSS	Alloy 2507	S32750	800-1000	550

DSS are classified in four different groups depending on their PRE_N value [16]: lean duplex ($PRE_N \leq 35$), standard duplex ($35 < PRE_N < 40$), super duplex ($40 \leq PRE_N < 45$) and hyper duplex ($PRE_N \geq 45$). SDSS contains approximately 25 wt.% Cr, resulting in a $PRE_N \geq 40$ [14, 17]. SDSS can be used in aggressive environments, such as natural and chlorinated seawater applications up to 20ºC according to ISO 21457 and NORSOK M-001 [18, 19]. However, DSS are only suggested in applications within the temperature range -50 to 250°C [14], due to the brittle behavior of α, and the possibility of deleterious phase precipitation at higher temperatures.

2.3. Intermetallic phase precipitation

High alloyed stainless steels, such as SDSS, can suffer phase transformation when the alloy is exposed to high temperatures, e.g., during welding or heat treatment. During the solidification process, α is formed first, being transformed afterwards into γ [15, 16]. However, the higher quantity of Cr and Mo, the more intermetallic phases precipitate within the microstructure of the material [14, 20-22]. These intermetallic phases are usually called secondary phases. However, in the case of DSS, the intermetallic phases receive the name of tertiary phases, since there are already two phases in the microstructure in the SA condition: γ and α. The most studied intermetallic phases in stainless steels, shown in Table 2-2, are: sigma phase (σ), chi-phase (χ) and chromium nitrides (usually as Cr_2N) [10, 14, 20, 21, 23-50].

Table 2-2. Summary of the most relevant deleterious phases in (S)DSS [10, 14, 20, 21, 23-50].

Deleterious phase	Nominal chemical formula	Crystal structure	Temperature range (°C)
Sigma (σ)	Fe-Cr-Mo (W, Mn, Si)	BCT	600-1000
Chi (χ)	Fe-Cr-Mo (W)	BCC	750-850
Nitrides	Cr_2N (CrN, less common)	HCP	700-900

- Sigma-phase (σ): σ-phase is a hard brittle intermetallic particle that is principally rich in Cr and Mo. In addition, it has a body-centered tetragonal (BCT) structure and it is not magnetic [29, 30, 51, 52]. It is the most studied intermetallic phase since σ is usually the most common precipitate found in stainless steels after being exposed at temperatures in the range between 600-1000ºC [10, 14, 20, 21, 27, 29-31, 34, 37-50, 53-58]. However, the precipitation of σ-phase depends on other factors such as time and type of microstructure present in the material. There are several arguments that explain why microstructure has a strong influence on the kinetics of the precipitation. The main reason is that Cr has faster diffusion through ferrite than through austenite since ferrite has a body-centered cubic (BCC) structure in contrast to the face-centered cubic (FCC) structure of austenite, i.e. ferrite is less compact than austenite. In fact, some studies have pointed out that the difference in kinetics between the two phases is about 100 times [51, 59].

In DSS, σ-phase precipitates at the interface between austenite and ferrite and grows towards the ferrite (Figure 2-2a). The mechanism follows a eutectoid reaction (Equation 2.2) where ferrite disappears producing σ-phase and a new austenite phase called secondary austenite (γ_2) creating a lamellar structure.

$$ferrite \rightarrow sigma + austenite \tag{2.2}$$

Kobayashi et al. [30] suggested that, at low temperatures (under 900ºC), the σ-phase grows in cooperation with γ_2 forming a lamellar structure. This cooperation is based on the fact that γ_2 pushes aside Cr and Mo for the σ-phase growth and, simultaneously, σ-phase rejects Ni to assist the evolution of γ_2. On the other hand, at higher temperatures (above 900ºC), the elements need

to diffuse a longer distance, increasing the difficulty of a lamellar formation. Instead, a "divorced eutectoid" is formed consisting of separated massive forms created by means of a non-cooperative growth. Figure 2-2 illustrates both cases: (a) lamellar structure, and (b) divorced eutectoid.

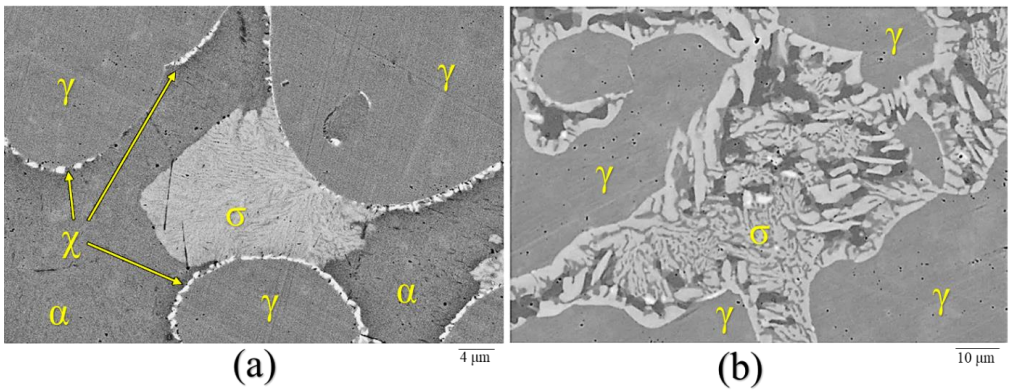

Figure 2-2. Scanning electron microscopy (SEM) pictures in back scattered electron (BSE) mode of intermetallic phases found in UNS S32760 isothermally aged for 1200 s at (a) 790ºC, and (b) 920ºC.

- Chi-phase (χ): χ-phase is a deleterious phase less known than σ-phase as it usually precipitates in smaller quantities. Additionally, χ-phase precipitates at lower isothermal heat treatment (IHT) times and at lower IHT temperatures compared to σ. Chi-phase is composed of the same main elements as σ-phase, although χ-phase is richer in Mo and poorer in Cr [32]. Precipitation of χ-phase occurs preferentially at α/γ interfaces and α/α grain boundaries. Several studies [21, 59, 60] found that χ-phase precipitation density decreased as the IHT time increased. As χ-phase precipitated earlier than σ-phase, it has been suggested that χ-phase acts as nucleation site for σ-phase precipitation.

- Chromium nitrides: Two different types of chromium nitride have been observed. The first and most common one is Cr_2N and the second one is CrN [33, 35, 36]. Even though they are identify as chromium nitrides, in reality they are composed of additional elements [36]. Austenite formation reduces nitride precipitation because nitrogen solubility in austenite is high. On the contrary, ferrite has low nitrogen solubility [36, 61, 62]. Consequently, all the excess of nitrogen in ferrite precipitates in the form of nitrides.

There is no agreement on where Cr_2N precipitates. Some authors [33, 63] state that Cr_2N appears inside the grain, whereas others [21, 61] claim the precipitation to occur at grain boundaries. On the other hand, Cr_2N precipitation starting at grain boundaries and, later, continuing inside the grains has also been observed [61]. Miranda et al. [52] reported that the precipitation location depended on the type of specimen treatment. In the case of a fast cooling process, the nitride will appear intragranularly; while it will develop at grain boundaries in case of isothermal heat treated specimens. Additionally, it has been suggested that the nitrides can act as nucleation points for intermetallic phases [21].

Most of these intermetallic phases are rich in Cr and Mo, especially σ-phase is rich in Cr and χ-phase is rich in Mo [32]. As result, a Cr- and Mo-depleted zones appear around these phases after precipitation. These depleted areas have a lower PRE number due to their reduced content of Cr and Mo, generating a weaker passive layer in those areas and facilitating the initiation of localized corrosion in the material [40, 41, 48, 54-56]. It has been reported that the toughness of stainless steels starts to decline when the volume of precipitated secondary phases is higher than 5% [25, 43, 47, 64]. However, corrosion resistance is reported to deteriorate with a lower density of tertiary phases, 1-2 vol.% [58, 65].

A simple and visual approach to study intermetallic phase precipitation kinetics in a specific material is to develop the Temperature-Time-Transformation (TTT) diagram. Figure 2-3 shows a TTT diagram develop by Nilsson et al. [14] for SDSS UNS S32750.

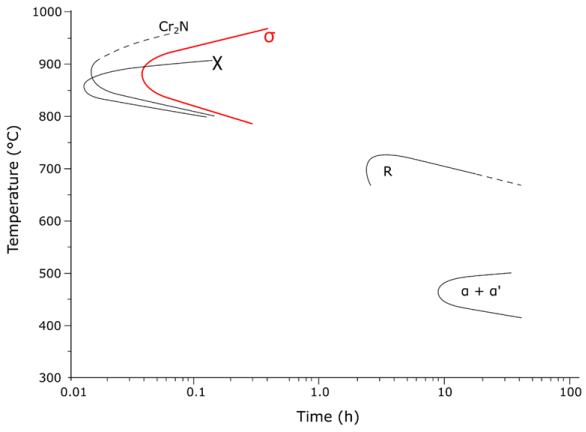

Figure 2-3. TTT diagram for UNS S32750 by Nilsson et al. [14].

2.4. Localized corrosion resistance quantification

Localized corrosion, i.e. pitting and crevice corrosion, is a type of corrosion that is difficult to discover during service due to the localized nature of the attack. By the time localized corrosion is identified, the corrosion attack has normally penetrated deep into the material often causing leakage or fracture. Consequently, scientists have been researching for many years different ways to arrest, control or delay this phenomenon.

Already in 1937, it was discovered that above a certain electrochemical potential value, the passive layer suffered from breakdown resulting in localized corrosion attacks. This critical potential value was called *rupture potential* [66, 67]. Later, rupture potential has been named as *breakdown potential* (E_B) in the literature [3, 4] or, depending on the type of localized corrosion, *pitting corrosion potential* (E_P) and *crevice corrosion potential* (E_{Crev}), respectively.

According to the definition of E_B, the determination of the critical potential value shall be obtained by means of potentiostatic tests, where the potential is fixed to investigate whether localized corrosion is initiated at the actual potential. By testing different fixed potentials, E_B will be obtained as the minimum potential at which localized corrosion initiates. However, if the exact E_B is needed, many different fixed potentials must be used, resulting in a lot of tests. Consequently, a much faster technique requiring a smaller number of tests is required. The most widely used technique to obtain the critical potential value is a potentiodynamic scan where the E_B is obtained at the potential where the current increases rapidly. This breakdown potential is noted as $E_B^{'}$ (apostrophe indicating that it is obtained from the potentiodynamic test, not from potentiostatic test). Nonetheless, it has been shown that for pitting corrosion, $E_P^{'}$ is approximately equal to E_P [68]; even though E_P data is usually scattered over a wide range of potentials due to their stochastic nature following a normal distribution. The standard deviation normally decreases as the aggressiveness of the solution increases [69, 70]. However, this approximation is not valid in the case of crevice corrosion [71]. Therefore, a better parameter is needed in order to define more accurately the potential limit for initiation of localized corrosion.

In 1961, Vanleugenhaghe et al. [72] defined for the first time the *protection potential* (E_{Prot}), a potential below which localized corrosion was completely prevented. The potential was decreased during the occurrence of localized corrosion to investigate when the corrosion stopped. Theoretically, there are two mechanisms by which localized corrosion is arrested [67]: (i) deactivation of the pits, i.e., the material becomes immune due to the low potential achieved,

and (ii) repassivation of the pits. For stainless steels, a Cr content lower than 16.5 wt.% results in the deactivation mechanism, since the E_{Prot} needs to be decreased to very low values; whereas a Cr content exceeding 16.5 wt.% leads to repassivation of the pits [67]. Tsujikawa and Hisamatsu [73] were the first to name this E_{Prot} as *repassivation potential* (E_R), according to the process by which localized corrosion was arrested in most of the stainless steels.

Consequently, three regions are identified depending on the corrosion potential (E_{corr}) [66, 67, 74, 75]:

- Potentials more positive than the breakdown potential ($E_{corr} > E_B$); localized corrosion initiates and propagates.
- Potentials between the breakdown potential and the protection potential ($E_{Prot} < E_{corr} < E_B$); only initiation of metastable attacks occur, but existing stable pits/crevices continue to propagate.
- Potentials more negative than the protection potential ($E_{corr} < E_{Prot}$); no initiation nor propagation. Localized corrosion is completely prevented.

Consequently, E_R is the most important parameter for characterization of localized corrosion resistance of a stainless steel to avoid any localized attack, since pits/crevices can continue to propagate below E_B [9, 76]. Hence, different techniques to determine E_R are described hereunder.

The most widely used technique is the cyclic potentiodynamic polarization (CPP) described in ASTM G61 [77]. In a CPP test, a cyclic voltammetry is performed to a potential more positive than the E_B, usually defined by a high current density used as threshold value. Then, the potential scan is reversed and the E_R is obtained at the potential cross-over with the forward scan [78]. Sometimes, E_R is defined when the current drops back to the passive current density values [79]. Nevertheless, this technique has some disadvantages. The main issue is that, in some cases - especially for corrosion-resistant alloys (CRA) like SDSS -, the E_R values vary a lot [69, 70]. Some authors [74, 75, 80, 81] have documented the dependence of E_R with the depth of the localized corrosion attack, i.e. the electric charge (Q) passed during the attack. For very deep attacks, E_R becomes independent of the depth, i.e., it is constant [70, 75, 82-84]. Consequently, the CPP technique does not allow enough propagation of the localized attack to occur since the potential scan reverts as soon as the threshold current density is reached.

To avoid the limitations of the CPP technique, Tsujikawa and Hisamatsu [73] developed a technique named the Tsujikawa-Hisamatsu Electrochemical (THE). This technique was

standardized in the ASTM G192 [85] and consists of three steps: (i) potentiodynamic polarization (PD) to a potential above the E_B, normally defined by a high current density corresponding to the galvanostatic polarization current density (i_{GS}), (ii) galvanostatic polarization (GS) at i_{GS} value for 2 hours, and (iii) iterative potentiostatic polarization (PS), lowering the potential 10 mV every 2 h until repassivation. Repassivation is defined as the most positive potential at which the current stops increasing. The GS step included in the middle of both PD scans allows localized attack to propagate, applying sufficient Q for the E_R to become constant [70, 75, 82, 83]. Nevertheless, this technique presents some drawbacks as well. For instance, the repassivation definition used has been reported to be inaccurate [86]; besides the long exposure period required to perform the third step of the technique.

Mishra and Frankel [86] modified the THE technique by changing the third step to a reverse potentiodynamic polarization. This new technique is called the PD-GS-PD due to the three steps that consists of: (i) forward PD scan until the chosen i_{GS} threshold, (ii) GS step at the i_{GS} chosen for a specific time, and (iii) reverse PD scan until repassivation is achieved. In this method, repassivation is defined in the same way as in the CPP technique. Figure 2-4 illustrates the E-log(i) behavior of the PD-GS-PD technique.

Several studies [78, 86, 87] have compared the E_R measured by these three techniques. The material, the environment conditions and the i_{GS} threshold used were the same in all cases. The E_R obtained with the PD-GS-PD resulted in the least noble values, i.e., PD-GS-PD resulted in the most conservative E_R values. The development of the localized attacks with the PD-GS-PD technique were independent of the scan rate used during the PD steps [86], torque in the case of crevice corrosion (if greater than 2 N·m) [78], and the Q passed during the GS step [87]. Consequently, the PD-GS-PD technique proved to give more reliable E_R values, while avoiding the disadvantages with the CPP and THE techniques.

Localized corrosion does not only depend on potential, but on temperature as well. Hence, equivalent to the E_B and the E_R, critical parameters exist for temperature driven testing as was discovered in 1973 by Brigham and Tozer [88]. In this type of test, the temperature is increased while keeping the tested specimen at a constant applied potential. This method can be found nowadays as standard ASTM G150 [89]. Some years later, Qvarfort [90, 91] proved that the critical temperatures parameters can be obtained by performing potentiodynamic techniques at different temperatures. Additionally, Qvarfort identified the relationship between the critical pitting potential and the critical pitting temperature as a reversed S-shaped curved. Actually,

the curve is more similar to a Z-shape due to the sharp transition from transpassive corrosion to localized corrosion. Thereby, CPT, CCT and protection temperature (T_{Prot}), sometimes named repassivation temperature (T_R) are becoming widely used due to their practical and more convenient threshold definitions [6, 92, 93].

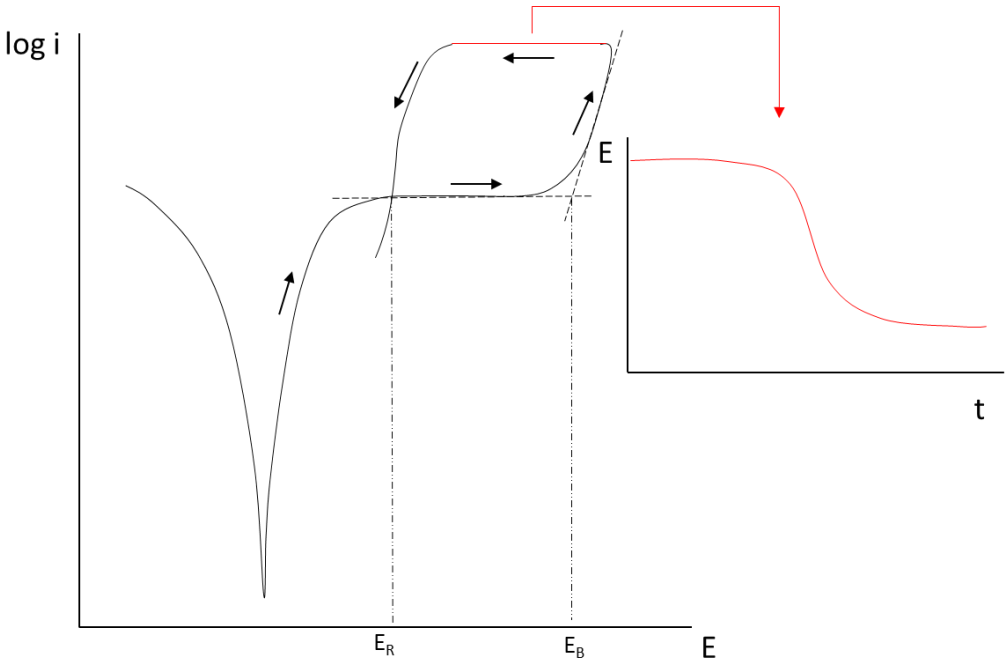

Figure 2-4. E-log(i) behavior of the PD-GS-PD technique. The GS step is represented in red, with the potential evolution with time in a small insert. Arrows point the direction of the scan.

2.5. Critical acidification model

Once localized corrosion has initiated, the environment inside the pit/crevice differs from the bulk solution. As the material corrodes following the reaction shown in Equation 2.3, the metallic cations dissolved are hydrolyzed as illustrated in Equation 2.4 [94, 95]. These reactions are written for a generic metallic element, M.

$$M \rightleftarrows M^{n+} + ne^- \tag{2.3}$$

$$M^{n+} + nH_2O \rightleftarrows M(OH)^{(n-1)+} + H^+ + (n-1)H_2O \rightleftarrows M(OH)_n + nH^+ \tag{2.4}$$

The hydrolyzation of the cations causes a drop in the pH, as seen by the H^+ product of the reaction in Equation 2.4. Additionally, these equilibrium reactions represented in Equations 2.3 and 2.4 imply an increase of cations inside the pit/crevice. To balance the charge created inside this local environment, chloride anions (Cl^-) migrate into the pit/crevice. As a result, an aggressive environment that can initiate and propagate localized corrosion due to a low pH and high Cl^- concentration is generated inside the pit/crevice.

The first model to consider the migration of chemical species in and out of the pit/crevice was the critical acidification model developed by Galvele [8]. This model consists of a one-dimensional approach where the transport of species is considered in order to determine the acidification generated inside the pit/crevice. Pitting and crevice corrosion are treated as the same phenomena from an electrochemical point of view; being the only difference between them the diffusion length. The model employs the parameter called "pitting or crevice stability product" to determine the acidification degree at which the pit/crevice would stabilize. This stability product, constant for a given material in a specific electrolyte, consists of the product between the critical current density (i_{crit}) at the bottom of the pit/crevice and the depth of the localized attack (x). Thereby, the stability product indicates the threshold above which localized corrosion stabilizes. Consequently, the critical potential (E_{crit}) is defined in this model by Equation 2.5:

$$E_{crit} = E_{corr}^{*} + \eta + \phi + E_{inh} \tag{2.5}$$

Where E_{corr}^{*} is the corrosion potential inside the pit/crevice, η is the anodic polarization required to reach i_{crit} at the bottom of the pit or crevice, ϕ is the ohmic potential drop along the pit or crevice, and E_{inh} is an additional polarization required in the presence of buffers or inhibitors.

This model has been validated by Newman [96] and has been used in many studies [3, 97-101]. Galvele et al. [101] employed the model to study the effect of Mo in ferritic stainless steels (18Cr), Hornus et al. [99] studied Mo content in austenitic stainless steels (UNS S30400 and UNS S31600), whereas Bocher et al. [97] studied the effect of Mo as alloying element in Ni-alloys. Significant differences due to Mo were obtained with the results from Galvele's critical acidification model in these studies.

Kappes et al. [3] performed a detailed review about simulating artificially the aggressive environment created inside a propagating pit or crevice by controlling the pH and Cl^-

concentration of the solution. Additionally, these authors studied the variation on Cl^- concentration in crevice-like-solutions at the same pH (in all cases a pH of 0) for one DSS and one SDSS (UNS S32750). The outcome of this work was a critical Cl^- concentration of approximately 7N for precipitation of a metallic salt film, which is a possible indication of the propagating pit/crevice stability [102, 103]. Additionally, the maximum limiting current density measured for the materials were obtained at 7N Cl^-.

2.6. Role of Tungsten

Nowadays, new materials are being developed to withstand increasingly aggressive conditions. In the corrosion field, the main goal is strengthening the passive layer by optimizing the alloying composition. One element considered to improve the passive layer is W. ISO 21457 [18] includes this element in the PRE formula. Thereby, the sub-index W is included in Equation 2.6 to indicate the addition of W to the calculation formula. Nevertheless, there is not a clear evidence of the beneficial effect of W on the localized corrosion resistance of stainless steels.

$$PRE_{N,W} = \%Cr + 3.3\ (\%Mo + 0.5\ \%W) + 16\ \%N \quad (2.6)$$

W does not form a passive layer by itself [104]. However, Bui et al. [104] reported the presence of W in the passive layer of austenitic stainless steels in absence of Mo in the form of WO_3 both in acid and neutral media containing Cl^-. This layer enhanced the corrosion resistance of the tested material. The mechanism by which this layer acted differed depending on the pH of the solution. WO_3 was insoluble at low pH, whereas the WO_3 bonded to the substrate in neutral pH. Additionally, Bui and co-workers tested tungstates dissolved in the solution. These cations attached to the passive layer by adsorption and inhibited corrosion. In contrast, Belfrouh et al. [105] tested as well Mo-free austenitic stainless, but the W addition to the material resulted in a detrimental effect on the corrosion resistance. Different W additions (from 0.18 to 2.67 wt.%) were studied by Tomashov et al. [106]. The results indicated a better corrosion resistance with increased W content. However, an addition of 0.18 wt.% W gave reduced corrosion resistance compared to the W-free base material.

In ferritic stainless steel, W had a clear beneficial impact on the corrosion resistance of the material in neutral- and acid-chloride environments [107-109]. However, Ahn et al. [107] reported that double addition of W in wt.% was needed to achieve the same beneficial effect

as Mo, i.e., both elements had the same enhancement on the corrosion properties when added in the same at.%. This is a similar correlation as reported by the $PRE_{N,W}$ formula in equation 2.6. The authors attributed this behavior to the similar chemical an electrical properties of these two elements, although no explanation was given to why the difference was exactly the difference of the atomic weight between the elements. This statement was corroborated by Cho et al. [108] who specified that the ratio was 1.6 (1.6 times more addition of W in wt.% to achieve the same result as Mo). In contrast, Goetz et al. [109] stated that Mo was more beneficial than W, even when added at equal at.%. Additionally, these authors attributed the beneficial effect of Mo and W not to the enrichment of these elements in the passive layer, but to a decrease in the Fe activity.

In amorphous Fe-Cr alloys, W had a greater beneficial effect than Mo [110]. Habazaki et al. [110] explained that these elements strengthened the passive layer by inhibiting Cr dissolution. However, when Mo or W were added above 10 at.%, the inhibition effect disappeared. These results, together with Tomashov et al. [106], indicate the existence of an optimal W concentration range within which W plays a beneficial role on the corrosion resistance. Outside this range, the effect seems to be lost or become detrimental.

Recently, two SDSSs with W content of 0.55 and 2.2 wt.%, respectively, were tested in a neutral Cl^--containing solution by Haugan et al. [6]. The alloy with 2.2. wt.% W showed a higher localized corrosion resistance by comparing different parameters like CPT, CCT and T_R. Nevertheless, no W-free material used as a reference was included to verify the beneficial effect of W on SDSS. In addition, both materials were from different product forms: an extruded bar and a rolled plate, adding the influence of an extra variable with an unknown effect on the corrosion resistance of the material.

Heretofore, the current state-of-the-art review included only studies where W was added to materials not isothermally aged, i.e., SA specimens. Nevertheless, the investigations found in literature are mostly focusing on the effect of W on intermetallic phase precipitation. W seems to promote precipitation of χ-phase, in contrast to σ-phase being the main precipitate in W-free materials [39-41, 44-46]. Additionally, the TTT curves for all secondary phases are shifted to higher temperatures [14, 53]. Nevertheless, as seen for SA materials, there is no agreement on the effect of W regarding the precipitation kinetics of the deleterious phases.

On one side, Nilsson et al. and Hertzman et al. [38, 45] concluded that precipitation of σ- and χ-phase increased by adding W. On the other hand, Kim et al. and other researchers [40, 44,

46-49, 57] reported that σ-phase precipitation is retarded when W is added by promoting, instead, χ-phase. Both sides were endorsed by computational simulations [20, 53]. However, the materials tested by both sides were different. Nilsson, Hertzman and co-workers used a W-free SDSS which was welded with a W-rich filler. Whereas Kim and others employed W-rich materials that were isothermally aged. Consequently, the properties of the welds are expected to differ. Additionally, Nilsson [14] explained that the DSS filler materials are richer in Ni, causing a more pronounced partitioning of Cr and Mo than in the corresponding base alloy, resulting in the TTT curves to be displayed to shorter times.

As explained in section 2.3, these intermetallic phases are rich in Cr and Mo, generating a depleted zone of these elements around them. These depleted zones are susceptible to localized corrosion, since Cr and Mo strengthen the passive layer. Thereby, it has been reported that the E_P drops to less noble values for DSS (UNS S31803) when the σ-phase concentration was above 15 vol.% [56]. In another study, a concentration of σ-phase in the range 2 to 6 vol.% decreased significantly the CPT for UNS S31803 and UNS S32750 [65]. Deng et al. [58] reported a reduction in CPT of 10ºC with 1 vol.% σ-phase precipitation, while the reduction increased by 20ºC when the vol.% was higher than 5.

2.7. Statistical analyses

2.7.1. Box and whisker plot

Box and whisker plots, sometimes abbreviated to box plots, are a type of diagram developed by John Tukey [111] to visualize distribution datasets. It receives its name due to its shape: a box where the majority of the dataset points are included, and the whiskers, represented by vertical lines, extended to the extreme values of the dataset.

There are five descriptive statistics employed in the representation of the data: maximum and minimum values, median value, first (lower) quartile, and third (upper) quartile. Figure 2-5 represents this diagram with detailed explanation of each feature and its representation.

This type of diagram gives the same information as a histogram, in addition to the median value and whether the extreme dataset values are considered statistically outliers. Additionally, due to its smaller size compare to the histogram, comparisons with other datasets are easier. Box and whisker plots are very useful to study whether the dataset follows normal distribution by comparing the lengths of the quartiles and whiskers and whether the median is at the center of

the box. The more symmetric the box and whiskers are, the closer the dataset approximation is to a normal distribution. Consequently, box and whiskers plots are part of the statistical test, known as normality test, performed to corroborate whether a dataset follows a normal distribution or not.

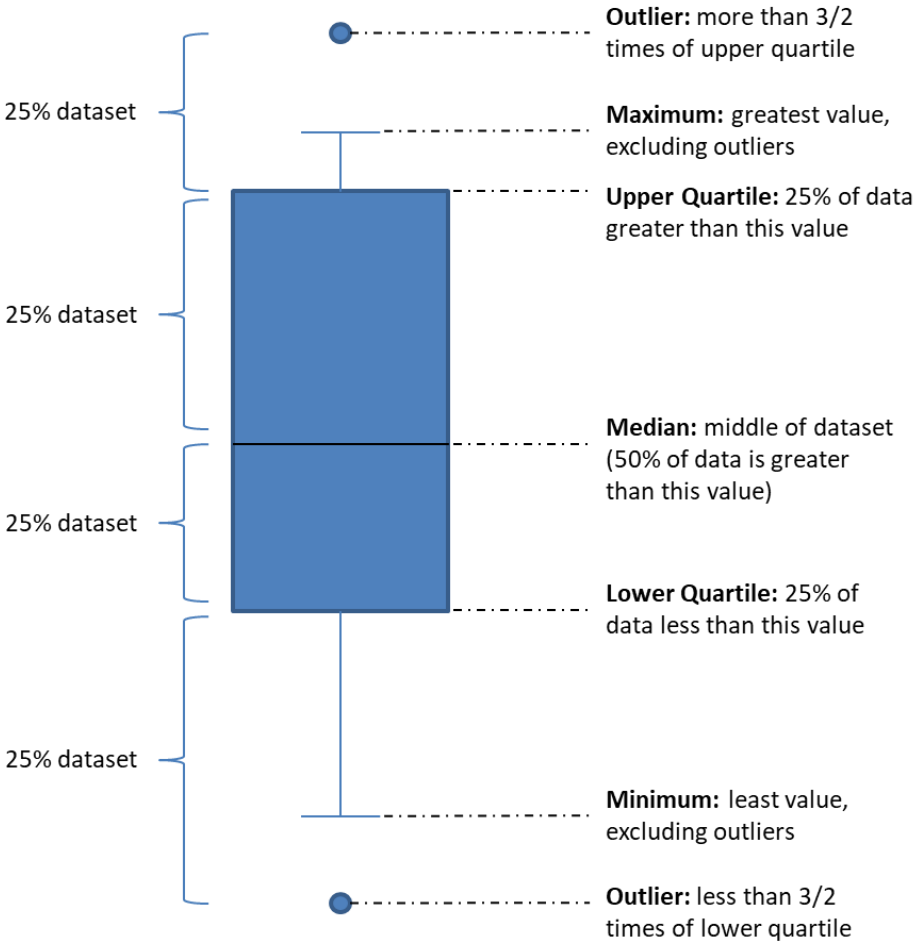

Figure 2-5. Detailed schematic of a box and whisker plot.

2.7.2. ANOVA

Analysis of the variance (ANOVA) was developed in the 1930s by Ronald A. Fisher [111]. This is a statistical technique where one or two independent variables is/are studied by analyzing its/their effect on a dependent variable. The independent variable is called factor or categorical variable because it is divided into groups. The dependent variable is a continuous

quantitative variable, used to compare the different groups of the independent variable and determine whether any group differs from the other. The ANOVA takes into consideration the variation of each group to conclude if the difference among the mean values is significant or not. Thereby, ANOVA is widely used in hypothesis testing [111]. The test starts assuming an initial hypothesis called the null hypothesis (H_0), stating that there is no difference between the different groups; whereas the alternative hypothesis (H_1) states that there is a difference between the groups. H_1 is only accepted once the H_0 is rejected by the outcome of the ANOVA test.

If only one factor is studied, the type of ANOVA employed is called "One-way ANOVA" [111]. If, instead, two independent variables are studied, it is called a "Two-way ANOVA" [111]. Additionally, the term "replication" is added to the "Two-way ANOVA" when the measurement is duplicated [112]. The studied factors can be divided in as many groups as needed. For example, if three materials (A, B and C) are being studied, the variable will be "Material" and will consist of three different groups: material A, material B and material C. Additionally, the dependent variable needs to be continuous and quantitative to be used as measurement to compare the factor/s being studied. In the previous example, materials A, B and C are exposed in a corrosion test, where the corrosion rate is measured. Consequently, the dependent variable is, in this case, the corrosion rate. The ANOVA would calculate the mean corrosion rate for each material and compare the three values to determine if the materials significantly differ based on this measurement. If the corrosion test is performed at two different temperatures, for instance at 30ºC and 60ºC, the ANOVA will be a "Two-way ANOVA" as it will consist of two independent variables: (i) "Material" being A, B and C; and (ii) "Temperature", divided into two groups, 30ºC and 60ºC; where the corrosion rate will be the quantitative variable used to measure the differences. If more than one dependent variable is used in the test, the test is called a multivariate analysis of the variance (MANOVA) [111].

There are two types of errors in hypothesis testing [111]: (i) error type I (α), indicating the probability of rejecting the H_0 and, thus, accepting H_1 when in reality there is no difference; and (ii) error type II (β) representing the probability of accepting the H_0 when there is a difference. It is usually acceptable to assume an α equal to 5%, which is equivalent to a p-value of 0.05 [111]. If the ANOVA results in a lower p-value than 0.05, the risk of committing a type I error is lower than 5% and, hence, H_0 can be rejected and H_1 instead accepted. The p-value is calculated at the end of the ANOVA using the F-statistic [113].

In this thesis, the two-way ANOVA with replication was chosen as two different independent variables (heat treatment and material) were analyzed based on a quantitative variable (CPT) and two measurements were performed for each condition. In this case, there are more than one H_0 because there is an H_0 for each independent variable, plus one more for the interaction between the factors.

The steps followed by the two-way ANOVA with replication are shown below [114], where *A* refers to one factor and *a* is the number of groups factor *A* is divided into, *B* refers to the second factor and *b* is the number of groups is divided into, *r* is the number of replications, *n* is the total number of measurements and *Y* refers to the dependent variable being measured. In addition, the steps are applied to the example given above for visual assistance.

1) Set up a matrix where the columns represent the groups of one factor and the rows are the groups of the other factor. Table 2-3 shows the matrix for the Two-way ANOVA with replication given above as example, where factor "Material" has three levels (i=1, 2, 3), factor "Temperature" has two levels (j=1, 2), there are two replications (k=1, 2), and Y_{ijk} represents the values of the dependent variable (corrosion rate) measured in each case.

Table 2-3. Example of a Two-way ANOVA with replication matrix.

		Material (A)		
		A (i=1)	**B (i=2)**	**C (i=3)**
Temperature (B)	**30ºC (j=1)**	Y_{111} Y_{112}	Y_{211} Y_{212}	Y_{311} Y_{312}
	60ºC (j=2)	Y_{121} Y_{122}	Y_{221} Y_{222}	Y_{321} Y_{322}

2) Calculate the mean value ($\overline{Y}_{ijk}$) of each cell of the matrix (in case of ANOVA with replication), the mean of each column ($\overline{Y}_{Ai}$) and row ($\overline{Y}_{Bj}$), and the total mean of the matrix ($\overline{Y}_{T}$) as illustrated in Table 2-4.

Table 2-4. Table 2-3 with all the mean values calculated required for the two-way ANOVA study.

		Material (A)			
		A (i=1)	**B (i=2)**	**C (i=3)**	**Average**
Temperature (B)	**30ºC (j=1)**	Y_{111} Y_{112}	Y_{211} Y_{212}	Y_{311} Y_{312}	
		$\bar{Y}_{11}$	$\bar{Y}_{21}$	$\bar{Y}_{31}$	$\bar{Y}_{B1}$
	60ºC (j=2)	Y_{121} Y_{122}	Y_{221} Y_{222}	Y_{321} Y_{322}	
	Average	$\bar{Y}_{12}$	$\bar{Y}_{22}$	$\bar{Y}_{32}$	$\bar{Y}_{B2}$
	Average	$\bar{Y}_{A1}$	$\bar{Y}_{A2}$	$\bar{Y}_{A3}$	$\bar{Y}_{T}$

3) Calculate the sum of squares (SS) for each factor, their interaction, the error (within) and the total following the Equations 2.7 to 2.11. SS is a parameter representing the degree of deviation of the measurement from the mean value, i.e., the variation that data has [113]. The larger the SS of the factors, the higher probability to reject H_0.

$$SS_A = r \cdot b \cdot \sum_i (\bar{Y}_{Ai} - \bar{Y}_T)^2 \quad (2.7)$$

$$SS_B = r \cdot a \cdot \sum_j \left(\bar{Y}_{Bj} - \bar{Y}_T\right)^2 \quad (2.8)$$

$$SS_{error} = \sum_i \sum_j \sum_k \left(Y_{ijk} - \bar{Y}_{ij}\right)^2 \quad (2.9)$$

$$SS_T = \sum_i \sum_j \sum_k \left(Y_{ijk} - \bar{Y}_T\right)^2 \quad (2.10)$$

$$SS_{AB} = SS_T - SS_A - SS_B - SS_{within} \quad (2.11)$$

4) Calculate the degrees of freedom (df) of each factor and their interaction following Equations 2.12 to 2.16:

$$df_A = a - 1 \quad (2.12)$$

$$df_B = b - 1 \quad (2.13)$$

$$df_{AB} = (a-1) \cdot (b-1) \quad (2.14)$$

$$df_{error} = (n-1) - (a-1) - (b-1) - (a-1) \cdot (b-1) \quad (2.15)$$

$$df_T = n - 1 \quad (2.16)$$

5) Calculate the mean squares (MS) of each factor and their interaction following the Equation 2.17. MS is a parameter indicating the variance of the data. In the ANOVA, MS indicates the variance between groups and the MS_{error} is the variance within the dataset [113].

$$MS = \frac{SS}{df} \tag{2.17}$$

6) Calculate F-ratio as indicated by Equation 2.18:

$$F_{ratio} = \frac{MS}{MS_{error}} \tag{2.18}$$

7) The p-value, defined as the probability of the F distribution to be above the F-ratio (obtained in the previous step), can be calculated as indicated by Equation 2.19. The p-value definition is represented visually in Figure 2-6 [113].

$$\text{p-value} = P(F \geq \text{F-ratio}) \tag{2.19}$$

8) Once the p-value is obtained, it is compared to the chosen α used as critical significant level. If the p-value is smaller than the α, H_0 can be rejected and H_1 accepted. Otherwise, H_0 cannot be rejected.

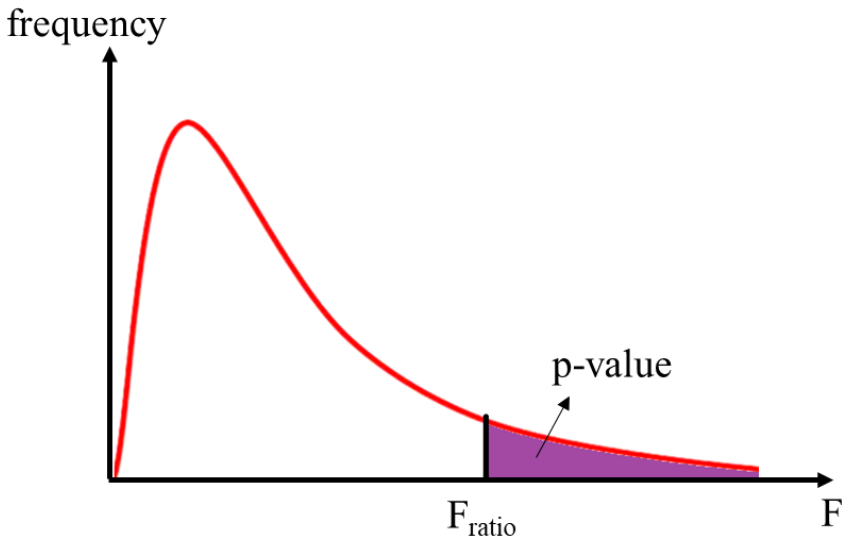

Figure 2-6. F distribution showing the p-value.

2.7.3. Post-Hoc tests

ANOVA is an omnibus test, i.e., it does indicate if there is a significant difference between the means of the groups, but not which means in particular are different [111]. For that, Post-Hoc test is needed. There are different types of Post-Hoc tests depending on which criteria they are mathematically based on to determine the differences on the means of the groups being compared. In this thesis, two Post-Hoc tests were used: Bonferroni and Tukey HSD, which perform pairwise comparisons between all groups of the ANOVA to find precisely which groups are different among them.

Bonferroni approach:

Developed by Olive Jean Dunn, sometimes it is named Dunn's multiple comparison test [111]. However, the groundwork was performed by Carlos Emilio Bonferroni [111]. This approach deals with the issue that the probability of committing a type I error increases with each comparison performed to the same dataset. In other words, if $\alpha = 5\%$, 1 out of 20 comparisons will commit a type I error. Consequently, if many comparisons of the same dataset are performed, significant results will appear by pure chance.

The Bonferroni approach solved this issue by decreasing the α to balance the increase of probability for performing large number of comparisons. More precisely, this approach consists of dividing α by the total number of comparisons being carried out. Thereby, the final α for the total number of comparisons will be 5%. An inconvenience of this method is that the individual α for each comparison is lowered, resulting in a very conservative test, i.e., it increases the probability of committing a type II error [111, 115].

Tukey Honestly Significant Difference (HSD) procedure:

The aim of this test is to calculate the minimum mean difference that will cause a significant result, i.e. minimum mean difference to reject H_0. The minimum difference according to Tukey (d_{Tukey}) is defined by Equation 2.20 [111]:

$$d_{Tukey} = \frac{q_T \cdot \sqrt{MS_{error}}}{\sqrt{n}} \tag{2.20}$$

Where q_T is the studentized range [116] statistic based on the desired α threshold for the total of all comparisons, MS_{error} is obtained from the ANOVA analysis, and n is the sample size of each pairwise comparison.

Consequently, if the means of two groups differ more than d_{Tukey}, the two groups are significant different between themselves.

2.7.4. Correlation

Correlation tests are used to check the relationship between two different variables. The most widely known test is the calculation of Pearson's correlation coefficient [111]. Pearson's coefficient (r) [117] ranges from -1 to 1, being closer to the extremes the stronger the relationship between the variables, whereas 0 indicates no correlation. The sign indicates the direction of the relationship: positive if both variables have the same tendency, while the tendency is opposite when the sign is negative. However, Pearson's coefficient is very sensitive to outliers because the model was developed assuming normal distribution [117]. In addition, r only indicates the strength of the linear relationship between the variables. If the correlation follows a curvilinear relationship, such as an exponential function, the r value will not be as high as if it is linear.

For datasets that do not follow these assumptions, several non-parametric tests are available. The main advantage of these non-parametric tests is that any type of monotonic relationship is reflected in the correlation coefficient being measured. Not only linear, but exponential and other curvilinear relationships will result in coefficient values close to 1 (in absolute value). Spearman's rank correlation coefficient (ρ) has been the most widely used in the 20th century [111]. However, Spearman's ρ is more sensitive to errors than other non-parametric tests such as Kendall's correlation coefficient [118]. Kendall's coefficient (τ) has always being avoided due to the tedious and complicated calculations required, especially for large datasets. However, thanks to the software development, Kendall's τ is becoming very popular nowadays; not only due to its robustness (low error sensitivity), but to its simple and direct interpretation on the data [111].

For τ calculation, one variable is ordered, either from largest to smallest value or vice versa. Then, the number of concordant (same rank position) and discordant (different rank position) values are calculated from the second variable. An example is given in Table 2-5 with data

from Paper II presented in this thesis, where the volume and maximum depth of crevice attacks were measured.

From Table 2-5, the variable "Volume" is ordered, from smallest to largest value, resulting in Table 2-6.

Table 2-5. Measured stable crevice attacks on UNS S32760 after the PD-GS-PD tests in 3.5 wt.% NaCl at 60ºC.

Crevice attack number	Volume (mm^3)	Maximum depth (µm)
1	$3.24 \cdot 10^{-5}$	37.5
2	$1.26 \cdot 10^{-2}$	83.9
3	$1.13 \cdot 10^{-4}$	18.4
4	$3.25 \cdot 10^{-3}$	59.3
5	$7.41 \cdot 10^{-4}$	72.8

Table 2-6. Table 2-5 data ordered from smallest to largest according to their volume size.

Crevice attack number	Volume (mm^3)	Maximum depth (µm)
1	$3.24 \cdot 10^{-5}$	37.5
3	$1.13 \cdot 10^{-4}$	18.4
5	$7.41 \cdot 10^{-4}$	72.8
4	$3.25 \cdot 10^{-3}$	59.3
2	$1.26 \cdot 10^{-2}$	83.9

Table 2-7. Calculation of concordant (C) and discordant (D) values from Table 2-6 data.

Crevice attack number	Volume (mm^3)	Maximum depth (μm)	C	D
1	$3.24 \cdot 10^{-5}$	37.5	3	1
3	$1.13 \cdot 10^{-4}$	18.4	3	0
5	$7.41 \cdot 10^{-4}$	72.8	1	1
4	$3.25 \cdot 10^{-3}$	59.3	1	0
2	$1.26 \cdot 10^{-2}$	83.9	-	-

From Table 2-6, the concordant and discordant pairs for the second variable "Maximum depth" are calculated. Since the values were ordered from smallest to largest, concordant is defined in this case as the number of values larger than the value being analyzed placed in a higher rank position. On the other hand, discordant values are defined in this case as the number of values smaller than the value being analyzed in a higher rank position. As result, Table 2-7 is obtained.

By normalizing the difference in the order of the variables to be +1 when they are identical and -1 when they are exactly opposite, the coefficient τ is defined by the formula shown in Equation 2.21 [119]:

$$\tau = \frac{C-D}{\binom{n}{2}} \tag{2.21}$$

Where *n* is the total number of ranks of each variable, i.e. the total number of values of each variable. $\binom{n}{2}$ is the binomial coefficient indicating the total number of combinations possible between two variables and is mathematically calculated following Equation 2.22:

$$\binom{n}{2} = \frac{n \cdot (n-1)}{2} \tag{2.22}$$

In the case of ties, i.e. there is exactly the same value in a higher rank, it does not count as concordant nor discordant, but it is counted as a possible combination in the denominator as shown in Equation 2.23 [119]:

$$\tau = \frac{C-D}{\sqrt{(C+D+T_1) \cdot (C+D+T_2)}} \tag{2.23}$$

Where T_i is the number of ties for each variable. When there are no ties, Equation 2.23 is equal to Equation 2.21. In the example given above in Table 2-7, $\tau = 0.6$.

A significant test is always performed at the end of the correlation calculation to verify if the null hypothesis $\tau = 0$ (i.e., the variables are independent) can be rejected. If the p-value obtained from the significant test is smaller than 0.05, the null hypothesis is rejected. Thus, the variables are dependent in the same degree as the τ value indicates. The significant test is a function of n. Larger n, smaller τ values are statistically significant [111].

It is a good practice to plot the scatter plot of the variables being studied, especially in the case of Pearson's correlation, to corroborate visually the relationship obtained with the correlation coefficient and, in case of mismatch, identify possible sources of errors.

CHAPTER 3: HEAT TREATMENTS AND MICROSTRUCTURE CHARACTERIZATION

This chapter includes the experimental procedure and tertiary phase characterization results from the isothermally aged materials in Paper I included in the Appendix.

3.1. Experimental methods

3.1.1. Materials

Three SDSSs differing mainly in W content were included in this PhD work. The three materials were: UNS S32750 (W-free), UNS S32760 (0.6 wt.% W) and UNS S39274 (2.1 wt.% W). Table 3-1 summarizes the chemical composition of the three materials together with their respective PRE_N and $PRE_{N,W}$ values. UNS S32750 was used as a reference material since it did not contain any W. All materials were received as extruded pipes with 30 mm wall thickness and 203.2 mm (8 inches) in diameter. The materials were machined in the workshop at the Department of Mechanical and Industrial Engineering (NTNU), resulting in disc specimens with 3 mm thickness and a diameter of 25 mm for UNS S32750 and UNS S32760, whereas the diameter was 30 mm for UNS S39274.

Table 3-1. Chemical composition in wt.%.

Material (UNS)	PRE_N / $PRE_{N,W}$	C	Si	Mn	Cu	Ni	Cr	Mo	N	W	Fe
S32750	43 / 43	0.03	0.27	0.51	0.14	6.42	25.6	3.83	0.295	-	62.9
S32760	41 / 42	0.03	0.50	0.60	0.60	7.1	25.2	3.6	0.254	0.62	61.5
S39274	40 / 43	0.02	0.24	0.71	0.52	6.3	24.9	3.1	0.29	2.1	61.8

3.1.2. Heat treatments

The specimens were SA at 1100ºC for 15 minutes in an air furnace, followed by water quenching, as recommended by the material provider. Additionally, extra IHTs, systematically chosen to study the precipitation of different tertiary phases in SDSS [14], were performed as well in the same air furnace and followed by water quenching. Only two specimens at the time were introduced into the furnace. A K-type temperature sensor was attached to one of the specimens to measure the temperature during the IHT. Table 3-2 shows all temperature-time combinations (Txty) carried out. These were chosen from the TTT curve values for UNS S32750 published by Nilsson [14] and shown in Figure 2-3.

Table 3-2. Isothermal heat treatment temperature-time (Txty) combinations.

Temperature (°C)	Time (s)
T1 = 790	t1 = 60
	t2 = 120
	t3 = 240
	t4 = 600
	t5 = 1200
T2 = 846	t1 = 60
	t2 = 90
	t3 = 120
	t4 = 240
	t5 = 600
	*t6 = 1200
T3 = 920	t1 = 60
	t2 = 120
	t3 = 240
	t4 = 600
	t5 = 1200

*heat treatment only performed on UNS S39274 for the TEM analyses due to the low density of secondary phases present at shorter times.

3.1.3. Sample preparation

Different sample preparation steps were performed depending on the technique or test used. Table 3-3 indicates which steps were used for each technique. The steps were in the following order:

Step 1: Grinding down to 600 US-grit with SiC paper.

Step 2: Polishing down to mirror-face surface with 1 μm diamond particles. For the transmission electron microscopy (TEM) specimens, vibratory polishing was used.

Step 3: Electro-etching following Statoil technical note MAT-2010080 [120]. The etching procedure consisted of two steps. In the first step, a 15 wt.% KOH solution was used, and a potential of 3 V applied for 12 s. In the second step, the solution was 20 wt.% NaOH with an applied potential of 1.5 V for 10 s.

Step 4: Electropolishing using a solution of 5.3 vol.% H_2SO_4 - 94.7 vol.% methanol at 18V for 30 s; followed by a final polishing step using an oxide polishing suspension (OPS) of a 0.02 μm colloidal silica [121, 122].

Step 5: Focused-ion beam (FIB) milling to obtain thin foils of the specimens [123, 124].

Step 6: Rinsing with acetone and distilled water and ultrasonic bath cleaning immersed in ethanol for 5 min.

Table 3-3. Sample preparation steps for each test and technique used in this thesis.

Technique/test	Steps
Light optical microscopy (LOM)	1, 2, 3, 6
Back scattered electron (BSE) imaging	1, 2, 3, 6
Energy dispersive x-ray spectroscopy (EDS)	1, 2, 3, 6
Electron backscatter diffraction (EBSD)	1, 2, 4, 6
Transmission electron microscopy (TEM)	1, 2, 5
Critical Pitting Temperature (CPT)	1, 2, 6

3.1.4. Microscopy characterization techniques

After the IHT, different microscopy techniques were employed in order to characterize the intermetallic phases present in the microstructure. More details of each technique can be found in Paper I.

- Light optical microscopy (LOM): An infinite focus microscope (IFM) was used as an optical microscope. The electro-etching procedure caused the γ, α and deleterious phases to appear in different colors.
- Back scattered electron (BSE) imaging: The scanning electron microscope (SEM) was employed in the BSE mode to identify the different types of intermetallic phases based on their chemical composition. This was possible because heavier chemical elements appear brighter in the BSE mode [14, 38, 125].
- Energy dispersive x-ray spectroscopy (EDS): This method was used to determine the chemical composition of the different phases seen in the BSE mode. At least 10 measurements were taken per phase. Nevertheless, EDS is not a precise quantification method, especially for small phases (< 1 μm), as the size and depth of the area analyzed are unknown. Therefore, the results from this technique are considered to be qualitative.
- Electron backscatter diffraction (EBSD): This technique was used to identify the phases seen in BSE. However, in many cases, the quantification of α and χ-phase was not reliable since these phases have the same type of crystal structure, BCC.
- Transmission electron microscopy (TEM): The intermetallic phases were analyzed by transmission electron microscopy (TEM), high-resolution (HR) TEM, scanning transmission electron microscopy (STEM), TEM-EDS, and selected area electron diffraction (SAD). These techniques were used to verify the identification of the deleterious phases performed by EBSD.

By combining all these microscopy techniques, identification of the precipitated phases and corresponding volume fraction quantification was possible. For the quantification, at least 10 measurements were performed on each specimen. The γ and σ volume fractions were obtained directly from the EBSD analyses. However, since EBSD could not distinguish successfully between χ and α, an open-access image processing software was employed to determine the total vol.% of deleterious phases from the BSE pictures, i.e., the sum of σ and χ. Thereby, χ could be determined by subtraction, since σ vol.% was known from the EBSD. Once the χ

vol.% was known, α could be calculated by subtraction from the EBSD. Figure 3-1 illustrates schematically the quantification process described.

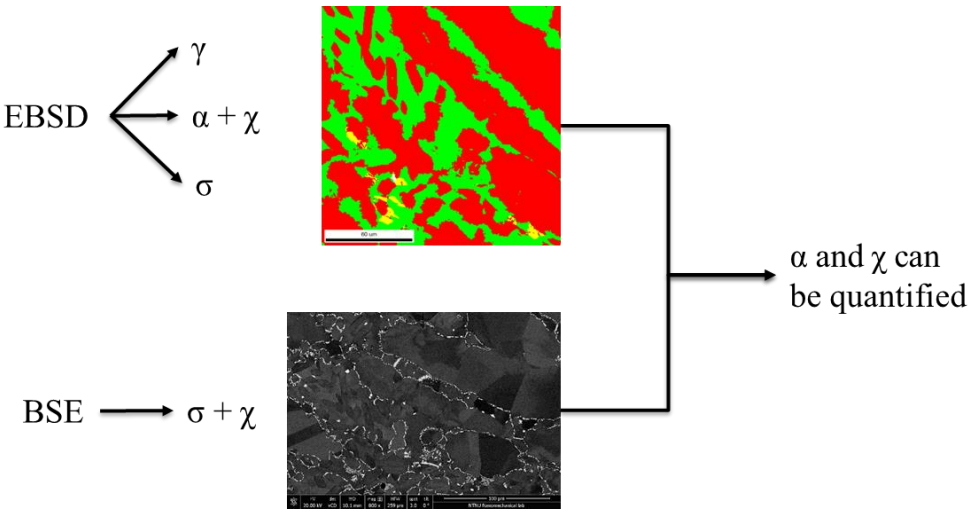

Figure 3-1. Schematic illustration of the quantification process followed to calculate the vol.% of every phase present in the IHT specimens.

3.2. Results

3.2.1. Microscopy characterization

Figure 3-2 shows an example of the LOM images after etching the specimens. There was a clear contrast between γ and α phases since they were colored differently. Samples containing tertiary phases were easily identified since the intermetallic phases were blue colored, or black if the specimen was over-etched.

Figure 3-3 illustrates a BSE image result of UNS S39274 where the intermetallic phases are distinguishable as they appear brighter than the matrix. Two different tertiary phases can be seen: (i) a smaller but brighter phase that precipitated mostly on the grain boundaries and at longer IHT times inside the α-phase, and (ii) a larger but duller phase, that precipitated at the grain boundaries and grew towards the α-phase. EDS results, summarized in Table 3-4, indicated that the smaller but brighter precipitate was richer in Mo and W, whereas the larger but duller phase was richer in Cr. Both were richer in Cr, Mo and W than the matrix, proving their brighter appearance in the BSE mode. Comparing the chemical composition to literature

values, the smaller but brighter precipitate could be χ-phase, whereas the larger and duller phase corresponded to σ.

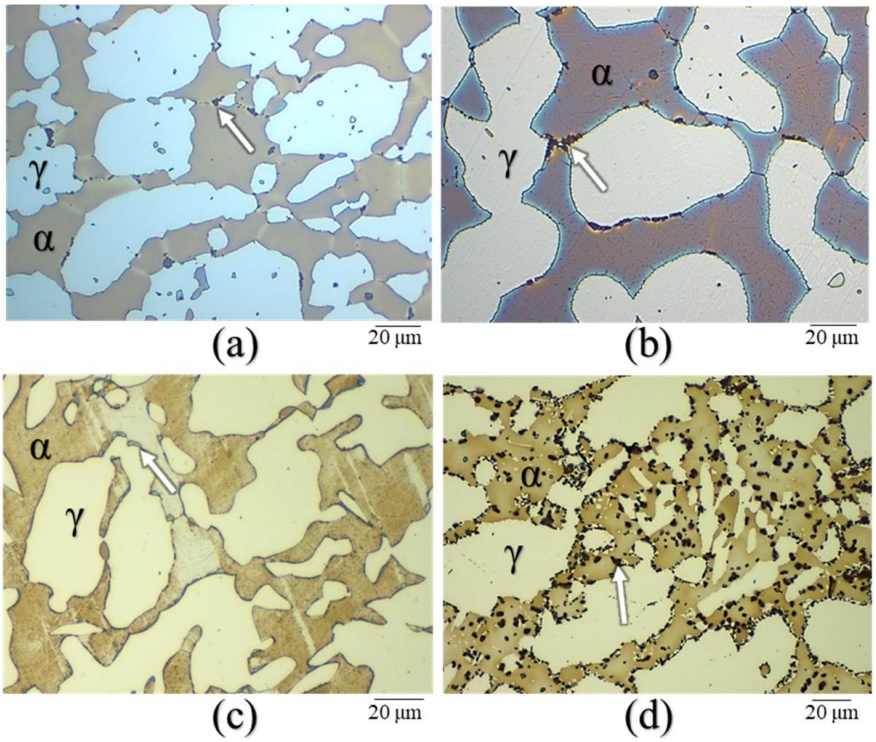

Figure 3-2. Light optical microscopy after isothermal aging (a) UNS S32750 at 846°C for 240 s, (b) UNS S32760 at 920°C for 240 s, (c) UNS S39274 at 846°C for 600 s and (d) UNS S39274 at 920°C for 1200 s. White arrows point at deleterious phases. Bright and dark phases correspond to austenite and ferrite, respectively.

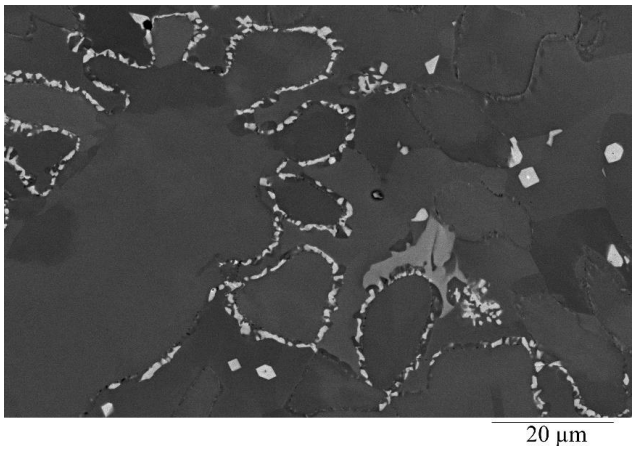

Figure 3-3. BSE image of UNS S39274 IHT at 920°C for 1200 s. Two different types of tertiary phases can be observed.

Table 3-4. Average chemical composition of each phase in wt.% for T3t5 IHT.

Material (UNS)	Phase	Fe	Cr	Ni	Mo	W
S32750	Ferrite (α)	63.9	28.1	4.6	3.6	-
	Austenite (γ)	64.9	25.2	7.5	2.3	-
	Sigma (σ)	59.0	30.0	4.4	6.4	-
	Chi (χ)	56.0	28.9	3.7	11.5	-
S32760	Ferrite (α)	62.2	27.0	5.3	3.1	0.75
	Austenite (γ)	63.3	23.9	8.3	2.1	0.6
	Sigma (σ)	57.7	29.9	4.4	5.2	1.0
	Chi (χ)	53.9	27.2	4.3	10.8	2.1
S39274	Ferrite (α)	63.5	26.4	4.7	2.9	2.5
	Austenite (γ)	64.7	24.1	7.3	1.9	1.9
	Sigma (σ)	55.2	29.7	3.7	6.6	4.5
	Chi (χ)	52.0	25.2	3.7	10.8	9.5

EBSD results confirmed that the smaller and brighter intermetallic phase corresponded to be χ-phase, whereas the larger and duller precipitate was σ-phase. One example is given in Figure 3-4, where one SDSS shows higher precipitation of σ-phase (Figure 3-4a), while χ-phase was the main intermetallic phase present in the other material (Figure 3-4b). This conclusion was also confirmed by the TEM results. Additionally, a nanosized phase rich in Cr and N was observed within σ-phase. Given its chemical composition, the phase was consistent with Cr_2N commonly found in SDSS [14, 21, 33, 34]. However, the detection of the nitrides was limited by the resolution of the chosen characterization methods. In this regard, the detection limit of SEM is good enough to identify <1μm precipitates. Even though small nitrides might affect negatively the corrosion resistance of the material [126], their effect is negligible compared to the higher density and bigger size of the χ- and σ-phases.

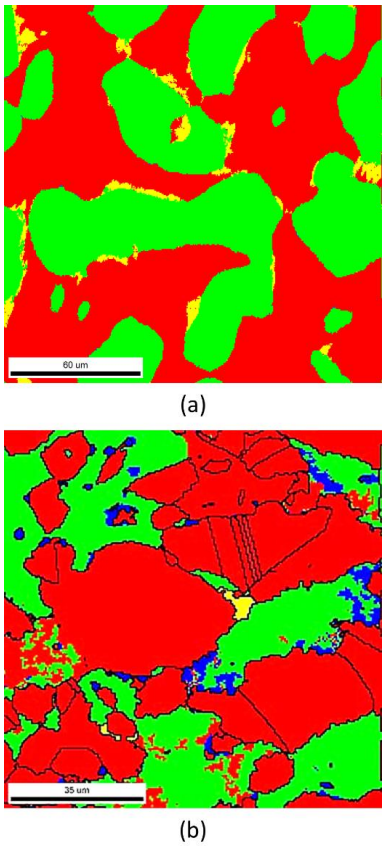

Figure 3-4. EBSD map of heat treated (a) UNS S32760 at 846°C for 1200 s and (b) UNS S39274 at 920°C for 1200 s (red = austenite, green = ferrite, blue = chi, yellow = sigma).

3.2.2. Tertiary phase quantification

Once identification of the intermetallic precipitates was complete, volume fraction quantification in each specimen was calculated following the procedure explained in section 3.1.4. The results are summarized in TTT diagrams in Figure 3-5, Figure 3-6 and Figure 3-7. In the TTT diagrams, a white circle indicates no tertiary phases present in the microstructure, i.e., the microstructure was the same as in the SA condition. Half white, half black circle symbolizes either: (i) the tertiary phases were small and could not be identify with the employed microscopy techniques, or (ii) small but similar vol.% of σ and χ were present in the microstructure, showing no clear preference for any of the phases. Circle with the cross indicates that χ was preferentially nucleated, whereas a black circle symbolizes that σ was the main precipitate present in the microstructure. Below the circles, the average vol.% of each phase is indicated.

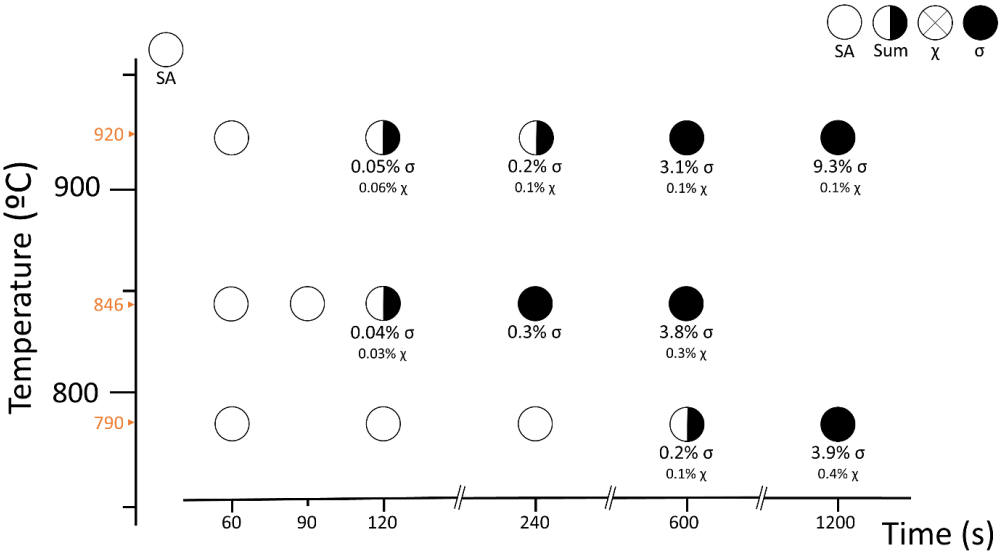

Figure 3-5. TTT-diagram for UNS S32750 including vol.% of tertiary phases.

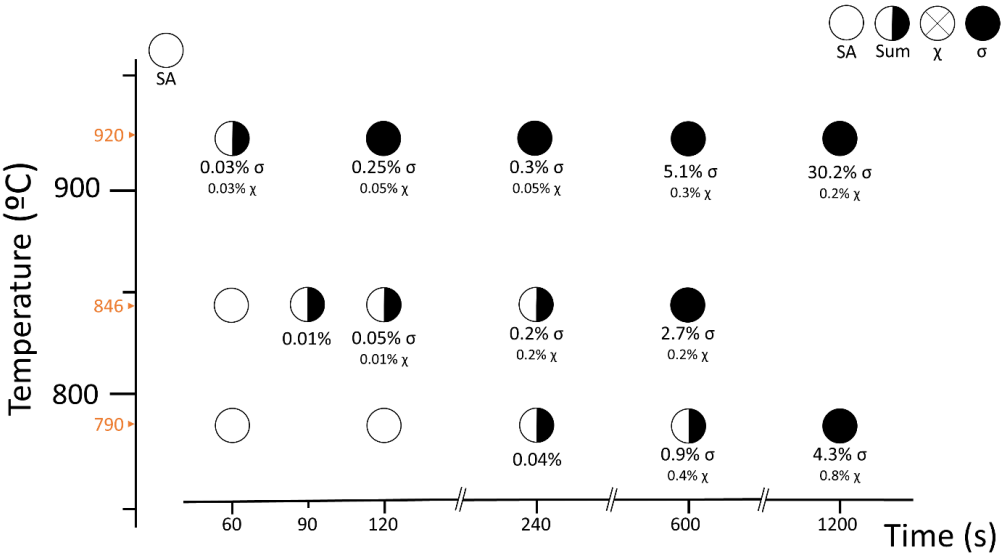

Figure 3-6. TTT-diagram for UNS S32760 including vol.% of tertiary phases.

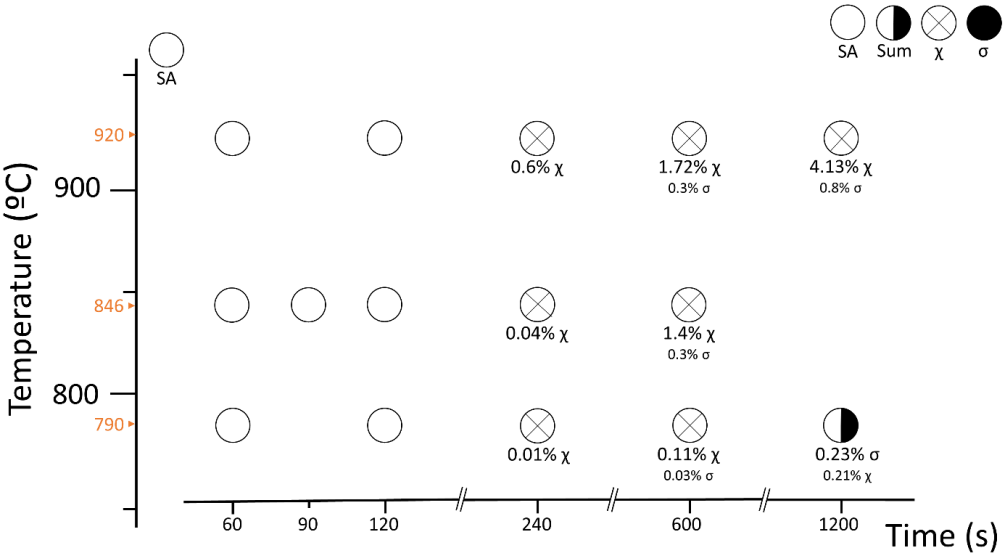

Figure 3-7. TTT-diagram for UNS S39274 including vol.% of tertiary phases.

Volume fraction of tertiary phases increased in the three materials with higher IHT temperature. The density of precipitates increased also with longer IHT times. Nevertheless, the total amount of intermetallic phases precipitated in the three materials for a given Txty was different and increased in the following order: UNS S39274, UNS S32750 and UNS S32760.

CHAPTER 4: CORROSION TEST METHODS

This chapter includes a detail explanation of all the corrosion techniques employed in this thesis.

4.1. Critical Pitting Temperature Test

The CPT test consisted on immersing the specimens in 6 wt.% $FeCl_3$ (pH = 1.2) and monitor the open circuit potential (OCP) while the temperature was increased stepwise. Figure 4-1 illustrates the set-up employed with the different elements numbered. The specimens were fully immersed in the solution by drilling a 2 mm diameter hole close to the edge of the sample and attaching a 200 µm Pt wire to the sample. Two freely exposed samples per condition were exposed simultaneously to check for repeatability in a 1 L glass container. The container was place on top of a hot plate, connected to a PID controller which kept the temperature within ±1°C from the set temperature. The temperature sensor of the PID controller was placed close to the specimens in the cell. The specimens were polished down with 1 µm diamond particles until achieving a mirror-face surface. The surface exposed to the electrolyte was 12.1 cm^2 for UNS S32750 and UNS S32760, and 16.9 cm^2 for UNS S39274.

The samples were exposed for 24 hours at 40°C before the temperature was increased stepwise 5°C every 24 hours. The OCP was monitored continuously against a standard calomel reference electrode (SCE), which was connected to the solution through a salt bridge to keep it at room temperature. The test stopped when the specimen suffered from localized corrosion, which was determined by the value of OCP decreasing below +500 mV_{SCE} [127].

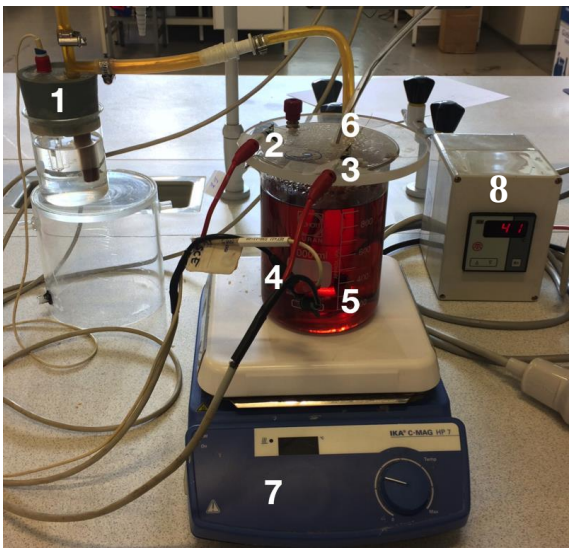

Figure 4-1. CPT set-up with the following elements: 1) reference electrode connected to the cell by a salt bridge, 2) connector to specimen 1, 3) connector to specimen 2, 4) specimen 1, 5) specimen 2, 6) temperature sensor, 7) hot plate, and 8) PID controller.

4.2. Crevice Corrosion tests

4.2.1. Sample preparation

UNS S32750 and UNS S32760 were solution annealed in an air furnace at 1110°C for 15 min, followed by quenching in water, as suggested by the material provider. UNS S39274 extruded pipe and rolled plate were provided in the SA condition. The specimens were prepared following steps 1 and 6 (section 3.1.3).

Multi-crevice assemblies as described in ISO18070 [128] and shown in Figure 4-2 were prepared with the specimens. The crevice formers were made of polytetrafluoroethylene (PTFE) and consisted of 12 artificial crevices, i.e., 24 in total for the two sides of the sample. The crevice formers were wrapped in PTFE tape to improve repeatability, as indicated by ASTM G192 [85]. The applied torque was 5 N·m [3]. A 200 µm Pt wire was connected through a 2 mm in diameter hole drilled closed to the edge of the specimen. The samples were immersed in the solution by hanging from the Pt wire. In this manner, the total exposed area (outside the crevice former) of the UNS S32750 and UNS S32760 samples was approximately 6.5 cm^2, whereas the area in contact with the solution for UNS S39274 was approximately 11 cm^2. In contrast, the area covered by the crevice former was 4.9 cm^2 for all specimens.

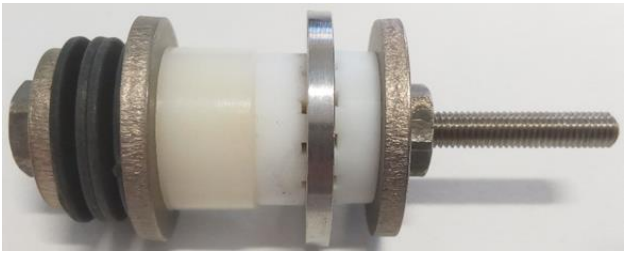

Figure 4-2. Multi-crevice assembly used in this thesis, as described in ISO18070 [128].

4.2.2. PD-GS-PD technique

In this thesis, the PD-GS-PD was performed to obtain the $E_{R,Crev}$ values for the specimens at different temperatures, defining $T_{R,Crev}$ as the temperature at which the $E_{R,Crev}$ experienced a sudden drop to low potential values [6, 76]. The $E_{R,Crev}$ was determined in two different ways: (i) the cross-over between the forward and reverse PD scans, and (ii) the potential at which the reverse PD scan reached 1 $\mu A/cm^2$ (approximately the passive current density of SDSSs).

A total of 160 ml volume of 3.5 wt.% NaCl (pH = 6.5) solution was used in each test. The solution volume/specimen surface ratio was 14.5 cm^3/cm^2 for the largest UNS S39274 samples. Different temperatures were tested: room temperature (22±1ºC), 40ºC, 50ºC and 60ºC. A double-glass cell connected to a recirculating water bath was used to control the temperature in all cases, apart from the room temperature condition which was performed with no heating element. The solution was deaerated for 2 h with N_2 gas before immersing the multi-crevice assembly into the solution. The purging continued during the test. A condenser glass tube filled with tap water (10 ºC approximately) was used at the inlet/outlet of the N_2 gas to avoid evaporation of the solution. An optical oxygen-meter was used during all the tests to verify that the dissolved oxygen concentration in the solution was below 10 ppb from the moment the specimen was in contact with the solution.

A three-electrode cell set-up was employed, with an Ag/AgCl KCl saturated reference electrode and a Pt mesh as the counter electrode. Starting with the immersion of the specimen into the solution, the OCP was monitored for 15 minutes. Then, a small cathodic current density (1 $\mu A/cm^2$) was applied for 15 minutes to remove possible surface contamination [3]. Afterwards, the OCP was monitored for 30 minutes, followed by the PD-GS-PD technique. The PD scans were performed at 0.167 mV/s, starting at 30 mV below the OCP. Two different i_{GS} were employed: 25 (taken from the work of Kappes et al. [3]) and 100 $\mu A/cm^2$. The lower i_{GS} was reached by metastable events and current noise, triggering the initiation of the GS step at potentials lower than CCT. The higher i_{GS} avoided this issue. The tests were duplicated to corroborate repeatability.

4.2.3. Natural Seawater exposure

Natural seawater from the Trondheim Fjord taken from 80 m depth was used. Two parallel specimens were exposed in the same 5 L glass container placed on a hot plate. The seawater inlet was placed at the bottom of the 5 L container, whereas the outlet was placed at the top of the container to have the seawater flowing continuously. A valve was placed at the inlet to control renewal of the seawater with a flowrate of 4 ml/min, which was sufficient slow to avoid turbulences inside the glass container and to secure heating of the seawater in the actual temperature range. The temperature was measured by placing a K-type temperature sensor close to the specimens. The temperature sensor was connected to a PID which controlled the

hot plate, keeping the temperature inside the glass container within ±1°C. Figure 4-3 illustrates the set-up described for this test.

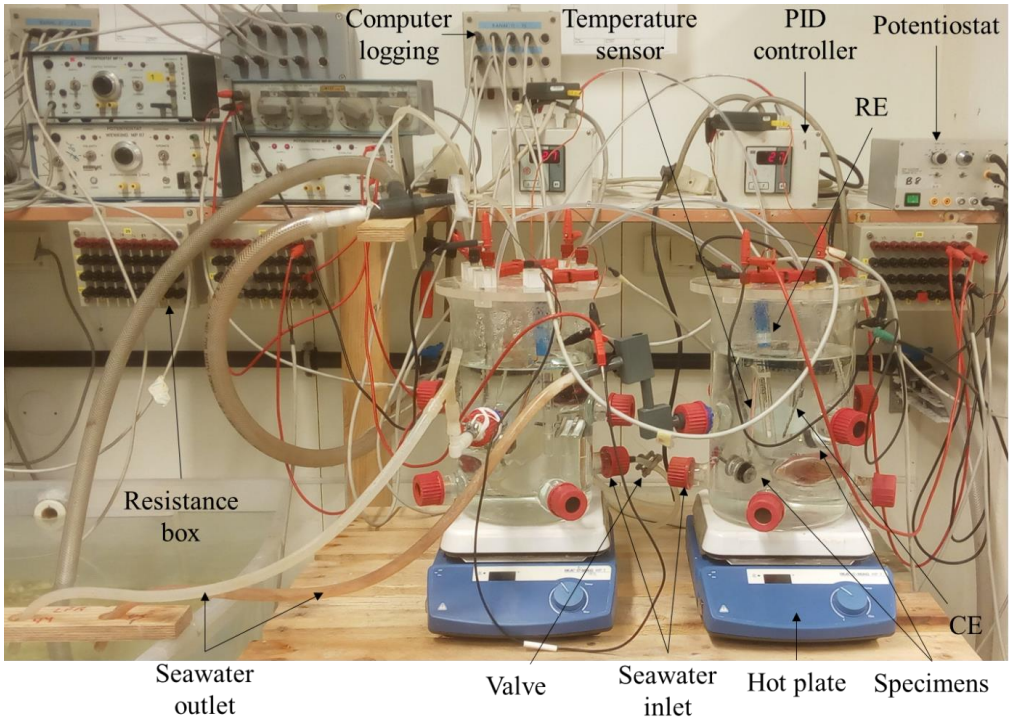

Figure 4-3. Set-up for the long-term exposure in natural seawater.

The SA specimens were tested at three different potentials: (i) OCP, (ii) +300 $mV_{Ag/AgCl}$, and (iii) +600 $mV_{Ag/AgCl}$. For the polarized samples (+300 and +600 $mV_{Ag/AgCl}$), the specimens were exposed at OCP for 24 h before applying the corresponding potential. The specimens were initially exposed at 50ºC and the temperature was increased in steps of 5ºC every fortnight. Crevice corrosion was assumed to initiate when the OCP suffered a sharp drop in the potential for the freely exposed specimens, or when the current density was above a threshold value of 25 $\mu A/cm^2$ (same value as the i_{GS} of the PD-GS-PD technique) for the polarized samples. The CCT was considered to be the temperature at which corrosion initiation was observed. However, for the samples polarized to +600 $mV_{Ag/AgCl}$, crevice corrosion initiated immediately at 50ºC. Therefore, the start temperature was decreased to 40ºC for these samples. Additionally, it was observed that corrosion initiated within the first day when the critical temperature was

reached. Consequently, the temperature step was changed to once a week, to shorten the total length of the test program.

Once crevice corrosion was initiated, the specimens were kept for at least 48 hours at the initiation temperature followed by a stepwise temperature decrease of 2.5ºC every 48 h until repassivation was observed. This temperature was determined to be the $T_{R,Crev}$. For freely exposed specimens, repassivation was considered when the OCP returned to its value before crevice corrosion initiated. For the polarized samples, $T_{R,Crev}$ was defined as the temperature when the current density dropped below 25 $\mu A/cm^2$ (same limit as the PD-GS-PD technique).

The tests for the isothermally aged specimens started at 20ºC, since the CCT values were expected to be lower due to the precipitates. These specimens were tested at two different conditions: (i) OCP, and (ii) +600 $mV_{Ag/AgCl}$. The temperature was increased in steps every week for both conditions. CCT and $T_{R,Crev}$ were measured following the same criteria as for the SA specimens.

4.3. Simulated localized environments

4.3.1. Galvele's critical acidification model

Galvele's critical acidification model [8], described in Equation 2.5, can be used to estimate the E_{crit} when the concentration of aggressive specimens in the electrolyte is known. Henceforth, to simplify the model, E_{inh} is considered negligible to the contribution of E_{crit} [3]. Although this assumption was arbitrary, it is considered acceptable as the E_{crit} value estimated in this manner is more conservative, i.e., lower E_{crit}. Thus, E_{crit} can be expressed as:

$$E_{crit} = E_{corr}^{*} + \eta + \phi \tag{4.1}$$

The ohmic potential drop term was estimated after Bocher et al. (Equation 4.2) [3, 97]:

$$\Phi = \frac{\rho \cdot i_{crit} \cdot x^2}{2w} \tag{4.2}$$

where ρ is the resistivity of the solution and is assumed to be 10 $\Omega \cdot$cm [97], w is the crevice gap which was given a value of 1 μm [3], x is the diffusion distance considered to be 10^{-4} cm [129], and i_{crit} was obtained from the pit stability product (Equation 4.3) [130]:

$$x \cdot i_{crit} = k \tag{4.3}$$

where k is a constant that is function of the metal and pH of the solution. In this work and based on Kappes et al., the value of 10^{-6} A/cm was adopted [129]. Equations 4.2 and 4.3 yield an $i_{crit} = 10^{-2}$ A/cm^2 and $\phi = 5$ µV. Since the $\phi << E_{corr}^*$, E_{crit} can be simplified to:

$$E_{crit} = E_{corr}^* + \eta \quad (4.4)$$

E_{corr}^* can be found by measuring the corrosion potential in an electrolyte simulating the inside of a corroding pit or crevice. Consequently, the E_{crit} can be obtained from Equation 4.4 by performing anodic potentiodynamic polarizations in crevice-like-solutions and obtaining the E_{corr} and η (i.e., the applied overpotential needed to reach $i_{crit} = 10^{-2}$ A/cm^2).

4.3.2. Anodic potentiodynamic polarizations in crevice-like-solutions

Two different solutions simulating crevice corrosion environments were used: (i) 1M HCl, used as a reference solution for 0 pH; and (ii) 7M LiCl (chosen from the results of Kappes et al. [3]) adjusted to 0 pH by adding concentrated HCl following the relationship between H^+ and Cl^- activity coefficients given by Bocher et al. [97]. The pH value of both solutions was confirmed to be 0 by titration with 1N NaOH (supplied as reagent of the European Pharmacopoeia [131]) and phenolphthalein as pH indicator, since pH-meters are not able to measure extreme pH values accurately [132, 133].

Anodic potentiodynamic polarizations were performed in a 3-electrode set-up, with an Ag/AgCl KCl saturated reference electrode and a Pt mesh as counter electrode. The tests were performed in an Avesta cell [91] with a working electrode area of 1.54 cm^2. The original Avesta cell was designed specifically to prevent crevice corrosion during testing [91]. This is achieved by adding a piece of filter paper below the sealing in contact with the specimen. During the test, this filter paper is wetted with fresh distilled water to avoid an aggressive acidic environment below the sealing that could provide an initiation point for crevice corrosion. The distilled water is pumped into the cell by a peristaltic pump which provides a low flow. The original Avesta cell does not include an outlet for the distilled water out of the cell. Instead, it connects the distilled water vent to the main chamber where the electrolyte is placed as illustrated in Figure 4-4a. Nevertheless, dilution of the electrolyte is negligible due to the low flow provided by the peristaltic pump [91]. Many studies have used the Avesta cell to successfully prevent crevice corrosion during testing and it is becoming a popular electrochemical cell nowadays [5, 90, 91, 134-137].

In this study, after performing some tests with the original Avesta cell, its design was changed. The main reason for this change was that the minimum flow provided by the peristaltic pump during the anodic potentiodynamic polarizations was high enough to cause a significant change in the volume of the electrolyte, implying that the dilution of the solution was not negligible. The modified Avesta cell (Figure 4-4b) solved this problem. By opening a new vent, the distilled water outlet is placed outside the cell, not into the electrolyte. Consequently, the distilled water flow does not affect the solution and the set-up prevented successfully crevice corrosion.

OCP was monitored for 1 hour once the specimen was in contact with the deaerated solution, followed by the anodic potentiodynamic polarization with a sweep rate of 0.167 mV/s, starting at OCP and ending at 1.2 $V_{Ag/AgCl}$. The tests were performed at different temperatures: room temperature (22±1°C), 40°C, 50°C and 60°C. A water bath connected to the jacketed cell was used to control the temperature of the solution, except for the room temperature condition which corresponded to the actual room temperature.

The solution was purged with N_2 gas for 1 hour before immersion of the specimen. Since the test specimen in the Avesta cell is placed at the bottom of the cell (Figure 4-4), the solution was pre-deareated in an external glass container. This glass container was connected to the interior of the Avesta cell with a valve as illustrated in Figure 4-5. The interior of the Avesta cell was simultaneously deaerated to avoid the deaerated solution to have contact with air. An optical O_2-meter was used to monitor the dissolved oxygen concentration in the solution during the test and to verify that the oxygen concentration was lower than 10 ppb from the moment the specimen came in contact with the solution. A condenser glass tube filled with cold water (10°C) was placed at the inlet/outlet of the N_2 gas to avoid evaporation of the solution during the test.

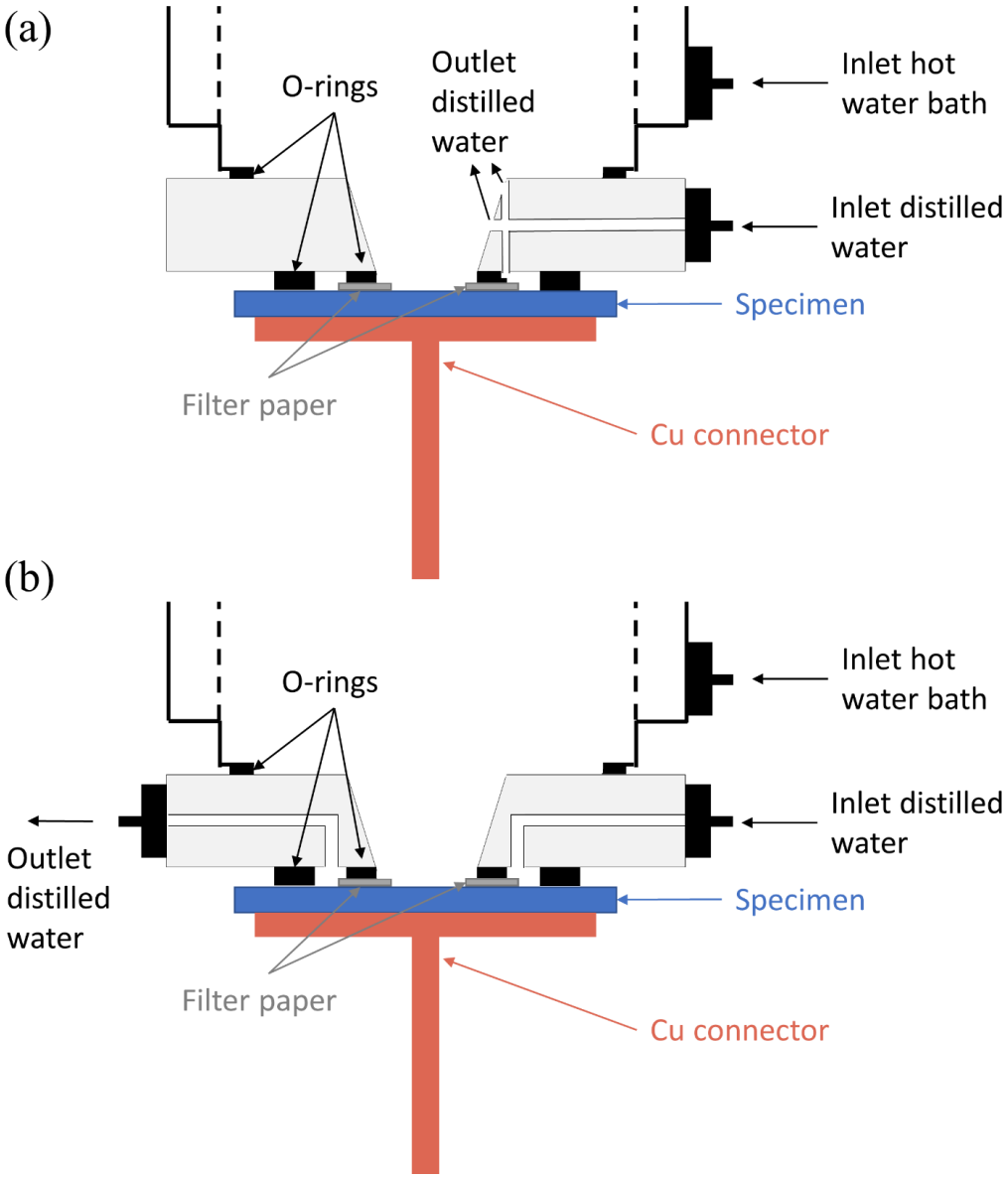

Figure 4-4. (a) Avesta cell and (b) modified Avesta cell sample holder design.

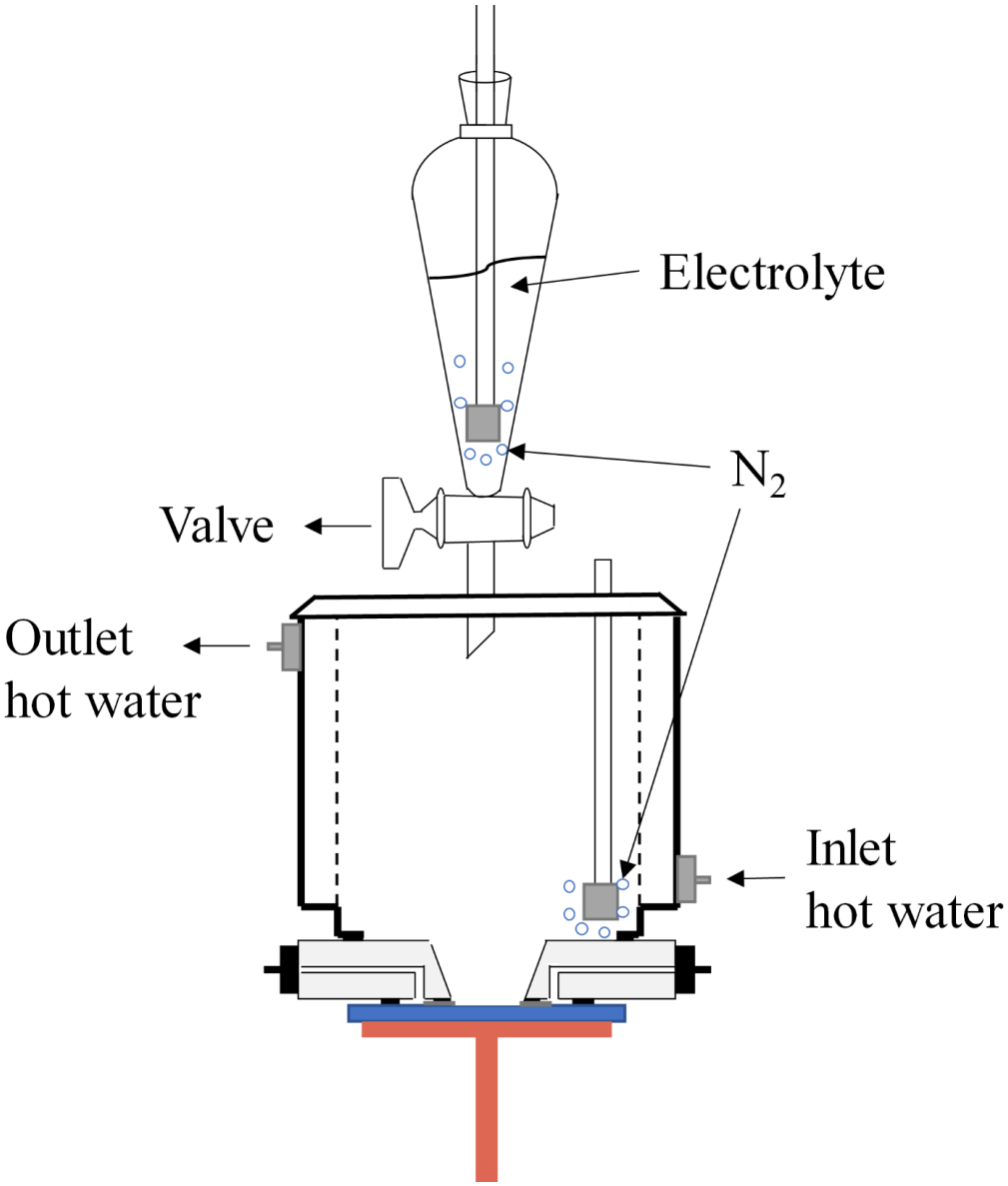

Figure 4-5. Full electrochemical test set-up showing the glass vessel employed to deaerate the electrolyte before introducing it into a pre-deaerated Avesta cell.

CHAPTER 5: CORROSION ATTACK CHARACTERIZATION

This chapter includes the experimental procedure following the corrosion tests to analyze the specimens and characterize the corrosion attacks.

5.1. Light optical microscopy

An IFM was used as an optical microscope to capture the full surface of the specimen after the corrosion tests. An overview of the extension of corrosion was the result of this procedure, as in the example illustrated in Figure 5-1.

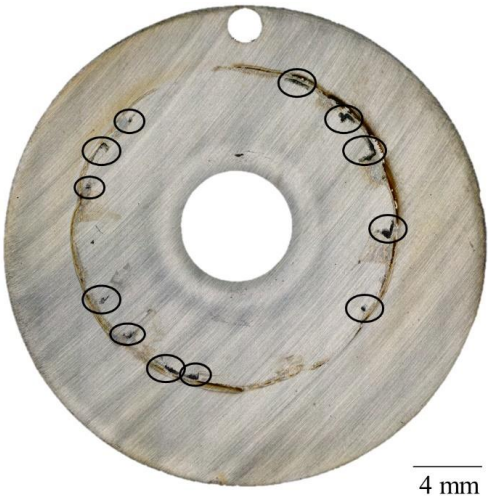

Figure 5-1. LOM capture of UNS S39274 specimen after crevice corrosion test with the PD-GS-PD technique in 3.5 wt.% NaCl at 60°C. Circles indicate crevice corrosion attacks identified with the IFM.

The IFM is a 3D microscopy technique allowing the measurement of the depth of the attacks. Thereby, the individual number of attacks were quantified and characterized by measuring the maximum depth. Figure 5-2 shows an example of the characterization performed in the IFM to a corrosion attack in UNS S32760 after the PD-GS-PD test in 3.5 wt.% NaCl at 60°C. The characterization includes a normal optical capture of the attack (Figure 5-2a), visualization of the attack with a color depth scale (Figure 5-2b), and the profile of the cross-section of the attack (Figure 5-2c). The maximum depth of the attack was measured from the cross-section profile. However, due to the irregular shape of the corrosion attacks, the area and the volume could not be measured with the IFM.

A commercial image analysis software called MountainsMap [138] was used to measure the area and volume of the corrosion attacks by importing the 3D image from the IFM. The

maximum depth was also measured and compared with the value calculated with the IFM, which resulted in only minor variations for large attacks that could be negligible.

An example of the characterization carried out with MountainsMap of the same corrosion attack as in Figure 5-2 is shown in Figure 5-3. In a similar manner as the IFM, MountainsMap shows the image in a color depth scale (Figure 5-3a), and can also show the attack in 3D (Figure 5-3b). Nevertheless, the main feature is the area and volume calculation which is performed by delimiting the outline of the attack (Figure 5-3c). Then, the software identifies which points of the image are above the surface of the material, indicated by a reference plane in Figure 5-3a and which point are below the surface. The points above the surface are measured as peaks, whereas the points below the surface are measured as holes. In Figure 5-3c, the total area, volume and maximum depth of the corrosion attack are calculated as the values from the "*Hole*".

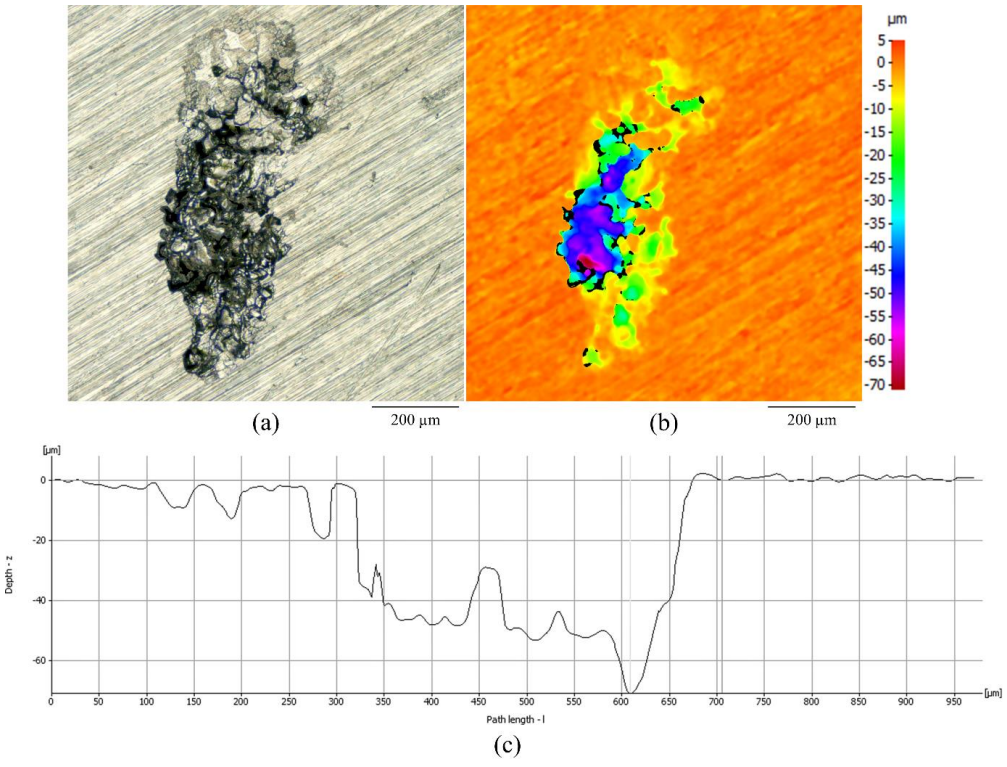

Figure 5-2. IFM characterization of a crevice attack in UNS S32760 after PD-GS-PD testing in 3.5 wt.% NaCl at 60°C: (a) normal optical capture, (b) optical color depth visualization, and (c) cross-section of the attack.

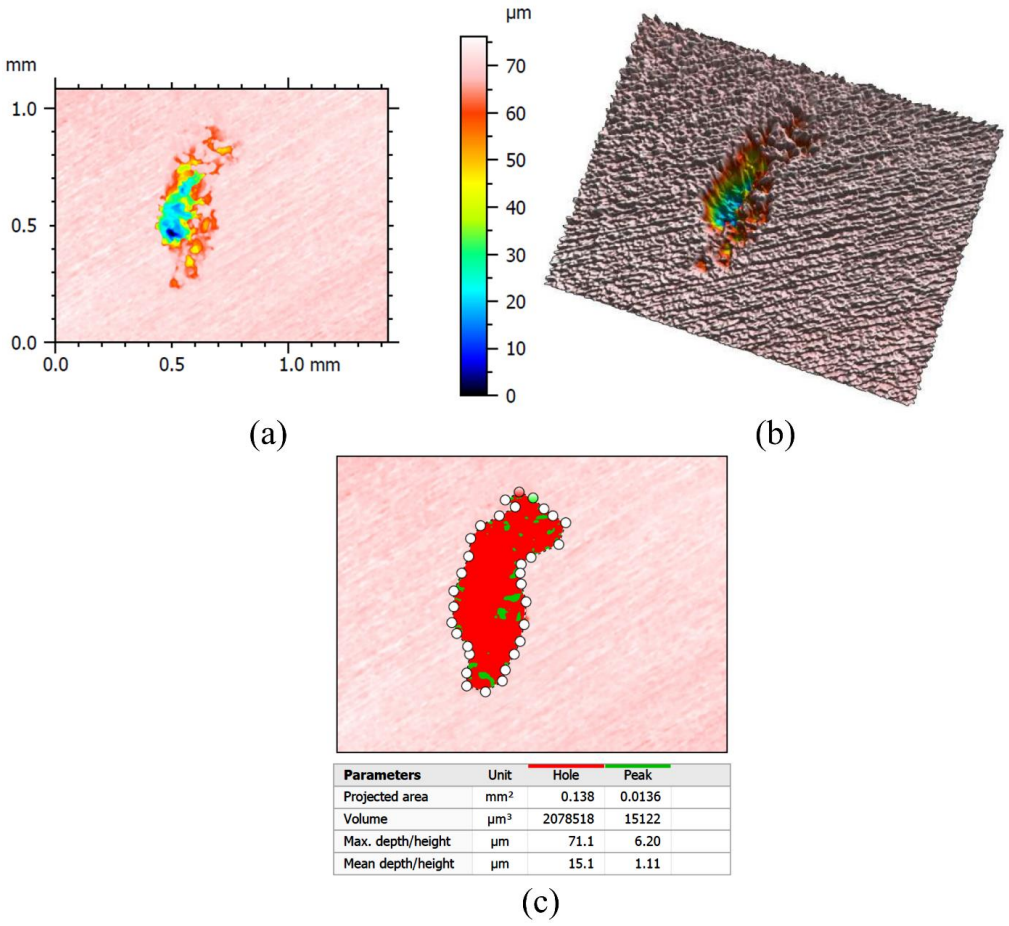

Parameters	Unit	Hole	Peak
Projected area	mm²	0.138	0.0136
Volume	µm³	2078518	15122
Max. depth/height	µm	71.1	6.20
Mean depth/height	µm	15.1	1.11

Figure 5-3. MountainsMap characterization of the same crevice attack as Figure 5-2: (a) optical color depth visualization, (b) 3D view of the corrosion attack, and (c) area, volume and maximum depth calculation.

5.2. SEM and EDS

In some cases, the corrosion attacks were analyzed in SEM to observe the initiation of the localized attack, or to analyze the morphology of the attack, i.e., whether γ and α were uniformly dissolved or, otherwise, one phase was selectively corroded. In the latter case, the EDS, by means of the point analysis tool, was used to identify which phase was selectively dissolved by measuring the chemical composition. At least 5 measurements were performed per phase and picture. The identification was sufficient with the EDS as γ is richer in Ni, whereas α is richer in Cr, Mo and W as was seen in Table 3-4.

5.3. Chemical dissolution

The solution at the end of selected tests was collected and stored in plastic containers. The samples were brought to the Department of Chemistry at NTNU where the chemical composition was analyzed by Inductively Coupled Plasma Mass Spectrometry (ICP-MS).

Congruent or incongruent dissolution for each element, M, was determined from the ICP-MS results by means of the dissolution ratio (d'_M). This parameter is defined as the ratio between the dissolution measured by ICP-MS ($d_{M.experimental}$) and the dissolution required to be considered congruent ($d_{M.congruent}$) with respect to the dissolution of Fe, which is the base element for the SDSS materials studied in this thesis. Thereby, d'_M is calculated according to Equation 5.1:

$$d'_M = \frac{d_{M.experimental}}{d_{M.congruent}} = \frac{d_M}{\frac{C_M \cdot d_{Fe}}{C_{Fe}}} \quad (5.1)$$

Where d_M is the dissolution quantity of metal M measured by ICP-MS, C_M is the concentration in solid solution of metal M in the material (shown in Table 3-1), C_{Fe} is the concentration in solid solution of Fe in the material (shown in Table 3-1), and d_{Fe} is the dissolution quantity of Fe obtained by ICP-MS for the same condition as that of the measured metal M.

Consequently, if $d'_M > 1$, the metal M was selectively dissolved compared to the bulk material. If $d'_M < 1$, the metal M was concentrated at the surface of the specimen. Finally, if $d'_M = 1$, the metal M uniformly corroded with the bulk of the material, i.e., the dissolution was congruent.

CHAPTER 6: SUMMARY OF THE JOURNAL PAPERS

This chapter includes an overview of the main objective of each journal paper included in the Appendix, in addition to a schematic view of the experimental procedure followed to achieve the goal of each paper and the main results and conclusions.

6.1. Paper I

6.1.1. Introduction

Paper I, with the title: "The Role of Tungsten on the Phase Transformation Kinetics and its Correlation with the Localized Corrosion Resistance of 25Cr Super Duplex Stainless Steels", was published in Journal of The Electrochemical Society and is included in the Appendix.

The main objective of Paper I was to determine the effect of W on precipitation kinetics of deleterious phases, quantify their volume fraction and correlate the quantification with the localized corrosion resistance of the materials. Consequently, the experimental procedure consisted of isothermally aging the three SDSSs shown in Table 3-1 and correlate the volume fraction of tertiary phase precipitation (explained in Chapter 3) with a CPT test (explained in section 4.1). Some statistical analyses were performed to study the correlation between volume fraction of intermetallic precipitates and CPT values. Figure 6-1 illustrates the schematic experimental procedure followed for Paper I.

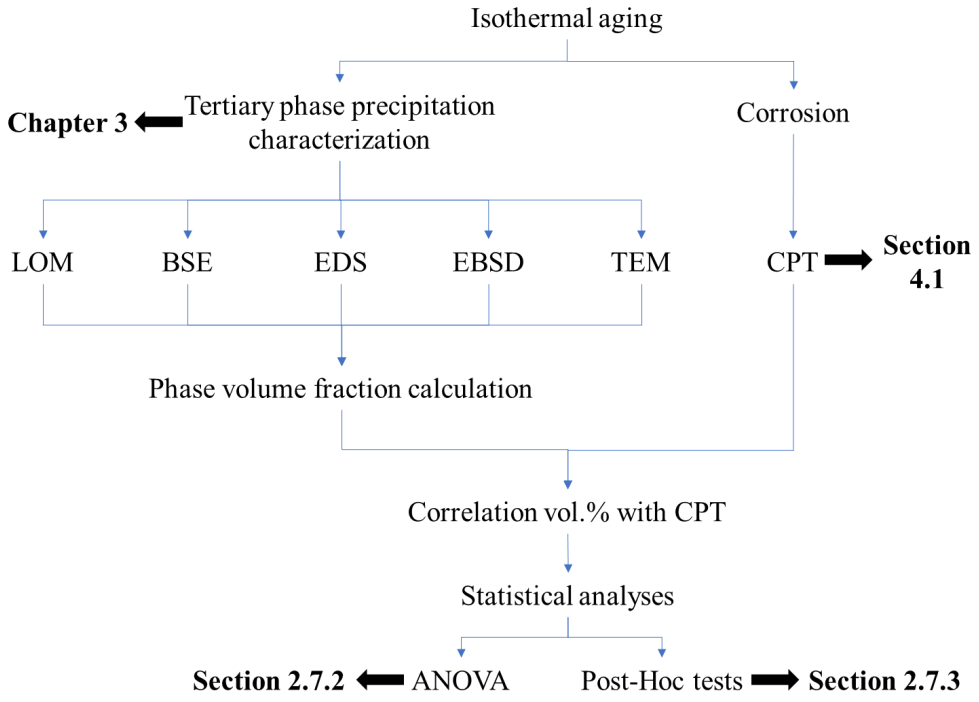

Figure 6-1. Schematic experimental procedure followed in Paper I to correlate the volume fraction of tertiary phases with the corrosion resistance.

6.1.2. Results and discussion

The volume fraction of tertiary phase precipitates for all the Txty for the three SDSSs were shown in TTT diagrams in Chapter 3 (Figure 3-5 to Figure 3-7). Visual Time-Temperature-Transformation-Corrosion (TTTC) diagrams were constructed from the TTT diagrams by including on top of each circle the minimum CPT value measured from the CPT test described in section 4.1.

Comparing the TTTC of the three SDSSs, the tertiary phase precipitation kinetics differed greatly depending on the W content in solid solution. The SDSS with 0.6 wt.% W content had the fastest σ-phase precipitation kinetics, as this deleterious phase precipitated at shorter times and in higher quantity than for the other SDSSs. In contrast, the SDSS with 2.1 wt.% W had the slowest σ-phase precipitation kinetics, as σ-phase only precipitated at longer IHT times. Additionally, UNS S39274 preferentially nucleated χ-phase, instead of σ-phase being the main precipitate as in the other two SDSSs. The total density of intermetallic phases was reduced for UNS S39274 in comparison with the other two SDSSs.

The CPT values were correlated to the vol.% of the deleterious phases, since CPT decreased with the increment of intermetallic phases precipitated in the microstructure. The initiation of the localized attack differed depending on the type of tertiary phase present in the microstructure. In specimens with tertiary phase precipitation, the attacks initiated in the vicinity of the precipitates, the well-known depleted zone. Thereby, localized attacks initiated in the secondary austenite generated next to σ-phase or next to χ-phase. In specimens with no tertiary phase precipitation, the initiation of the attacks followed a random nature.

The two-way ANOVA with replication and the Post-Hoc tests performed on the CPT values of all IHT indicated the vol.% of tertiary phases that caused the largest drop in CPT. UNS S32750 and UNS S32760 experienced the largest drop in CPT at shorter times at 846°C IHT. The time was the same for the three materials at 790°C IHT, whereas UNS S39274 had the critical shortest time at 920°C IHT. Nevertheless, this latter case was due to the minor CPT drop for UNS S39274 isothermally aged at 920°C causing the CPT reduction to 60ºC to be the largest experienced by this material. In contrast, UNS S32750 and UNS S32760 suffered a larger reduction in CPT, 25°C and 20°C, respectively, at 920°C IHT. These results indicate that UNS S39274 showed the highest corrosion resistance of the three SDSSs.

6.1.3. Main conclusions

- Precipitation kinetics of deleterious phases differed greatly depending on the W content of the material. 2.1 wt.% W retarded σ-phase precipitation by promoting χ-phase nucleation, in addition to a reduction in the total volume of intermetallic phases. On the other hand, 0.6 wt.% W accelerated σ-phase precipitation and obtained the higher precipitation density of tertiary phases.
- There exists a W content range in IHT materials within which W decreases and retards intermetallic phase precipitation. Outside this range, σ-phase precipitation is accelerated, and the total density of deleterious phases increases.
- Total density of tertiary phases was strongly correlated to the localized corrosion resistance of the material determined by the CPT values. Effect of σ- or χ-phase on the CPT values could not be isolated, but the decrease of CPT seemed more drastic on the specimens with higher σ vol.% than χ.
- 1 vol.% of tertiary phase precipitation was sufficient to cause a drastic reduction in the CPT. Critical vol.% of deleterious phases was dependent on IHT temperature; higher vol.%, the higher the temperature.

6.2. Paper II

6.2.1. Introduction

Paper II, with the title: “Crevice Corrosion of Solution Annealed 25Cr Duplex Stainless Steels: Effect of W on Critical Temperatures”, was submitted to Corrosion Science and is included in the Appendix.

The main objective of this paper was to quantify the crevice corrosion resistance of SA materials as a function of their W content. Consequently, the PD-GS-PD technique (explained in section 4.2.2) was employed in the three SDSSs included in Table 3-1. Additionally, UNS S39274 as rolled plate from Haugan et al. [6] was included to study the influence of the product form on the corrosion resistance of SDSS. The UNS S39274 plate was 100 mm by 150 mm by 9.5 mm, and disc specimens with 3 mm thickness and a diameter of 30 mm (same size as for the UNS S39274 samples from the extruded pipe (see section 3.1.1)) were machined. Multi-crevice assembled test specimens were used (see section 4.2.1). Table 6-1 summarizes the chemical composition obtained by EDS of all the materials used in this part of the work.

Table 6-1. Chemical composition in wt.% and PRE-values.

Material (UNS)	PRE_N/ $PRE_{N,W}$	Si	Mn	Cu	Ni	Cr	Mo	N	W	Fe
S32750	43 / 43	0.27	0.51	0.14	6.42	25.6	3.83	0.30	-	62.9
S32760	41 / 42	0.50	0.60	0.60	7.1	25.2	3.6	0.25	0.62	61.5
S39274 extruded pipe	40 / 43	0.24	0.71	0.52	6.3	24.9	3.1	0.29	2.1	61.8
S39274 rolled plate	40 / 43	0.20	0.71	0.48	7.6	24.6	2.9	0.35	2.1	61.1

The second objective of this paper was to verify the crevice corrosion resistance results obtained by the PD-GS-PD technique. With this aim, the materials were exposed long-term in natural seawater as explained in section 4.2.3. However, only SA specimens of UNS S32750 and UNS S39274 extruded pipe were tested at two constant potentials: (i) OCP, and (ii) +600 $mV_{Ag/AgCl}$. Figure 6-2 illustrates the schematic experimental procedure followed for Paper II.

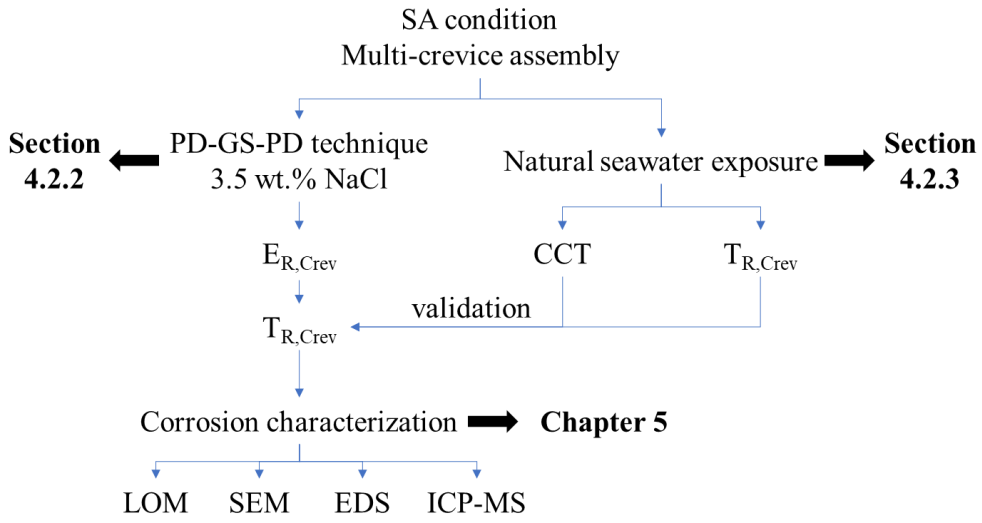

Figure 6-2. Schematic experimental procedure followed in Paper II to quantify the corrosion resistance of the materials and validate the results in natural seawater.

6.2.2. Results and discussion

The same $E_{R,Crev}$ values were measured with the two i_{GS} and with the two repassivation criteria used. The temperature at which $E_{R,Crev}$ experienced a sudden drop to lower potentials is considered the $T_{R,Crev}$. In this manner, the $T_{R,Crev}$ was 40°C, 50°C, ≈ 55°C and 60°C for UNS S32750, UNS S32760, UNS S39274 extruded pipe and UNS S39274 rolled plate, respectively. $T_{R,Crev}$ increased with the content of W in solid solution of the materials. Additionally, the rolled plate product form obtained slightly higher $T_{R,Crev}$ than the extruded pipe, even though their chemical compositions were similar and had equal PRE_N and $PRE_{N,W}$.

The total number of attacks found on the specimens was quantified. The density of attacks was approximately constant for UNS S32760, also for temperatures above $T_{R,Crev}$. UNS S32750 had the highest number of attacks for all temperatures, whereas the amount of attacks only increased at temperatures higher than $T_{R,Crev}$ for UNS S39274. Nevertheless, CCT was not reached for any of the temperatures for any material. Consequently, the crevice corrosion initiated in all cases due to transpassive dissolution, since all specimens reached potentials higher than the oxygen evolution reaction during the GS step.

The volume, area and maximum depth of all localized attacks on the specimens were measured and compared with the corresponding $E_{R,Crev}$ or transpassive potential (E_{Trans}) measured with the PD-GS-PD technique for the specimens. The results indicated that the transpassive attack needed to reach a specific size, $x_{Crit,Trans}$, before it stabilized and became a crevice corrosion site. Consequently, $x_{Crit,Trans}$ was quantified as the deepest attack in specimens with repassivation potential within the transpassive region, i.e., E_{Trans}. The higher the W content in the material, the deeper the $x_{Crit,Trans}$, in addition to an increase in temperature at which $x_{Crit,Trans}$ was observed.

SEM characterization showed that all attacks started at the phase boundary. Afterwards, the α-phase was selectively corroded. As the attacks grew, γ started dissolving and, finally, both phases were completely dissolved as the attack deepened.

From the natural seawater exposure, the CCT results obtained for the SA samples polarized to +600 $mV_{Ag/AgCl}$ were approximately the same as the $T_{R,Crev}$ obtained with the PD-GS-PD technique.

6.2.3. Main conclusions

- The $T_{R,Crev}$ measured by the PD-GS-PD method increased with increased W content in solid solution. Therefore, UNS S39274 showed the best corrosion resistance among the three SDSSs.
- The product form influenced the localized corrosion resistance. The rolled plate material obtained slightly higher $T_{R,Crev}$ than the extruded pipe material, although the reason is unknown.
- The crevice attack initiated at α/γ boundaries. In all cases, α selectively corroded; whereas dissolution of γ occurred at a later stage during crevice propagation.
- The CCT values obtained in the long-term natural seawater exposure polarized to +600 $mV_{Ag/AgCl}$ were approximately the same as the $T_{R,Crev}$ measured with the PD-GS-PD technique.

6.3. Paper III

6.3.1. Introduction

Paper III, with the title: "Use of the Critical Acidification Model to Estimate the Influence of W in the Localized Corrosion Resistance of 25Cr Super Duplex Stainless Steels", was submitted to Electrochimica Acta.

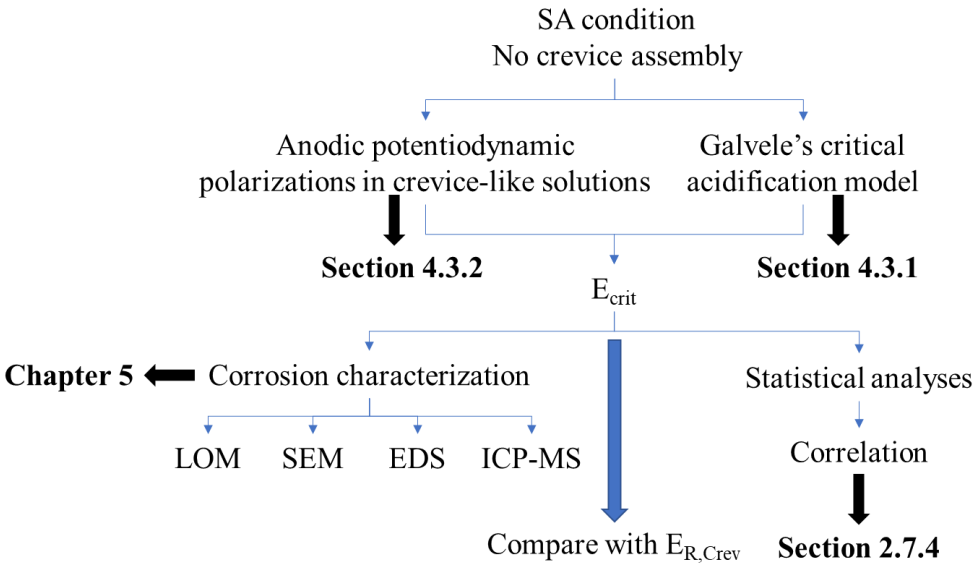

Figure 6-3. Schematic experimental procedure followed in Paper III to estimate E_{crit} with Galvele's critical acidification model and compare with $E_{R,Crev}$ values from Paper II.

The main objective of this paper was to analyze the role of W in localized corrosion environments by estimating E_{crit} according to Galvele's critical acidification model and compare the values with $E_{R,Crev}$ from Paper II. UNS S32750 (W-free) and UNS S39274 (2.1 wt.% W) from Table 3-1 were tested in this part of the project. See section 3.1.1. for more information about the two materials. The specimens were SA as described in section 4.2.1, although the specimens were not tested in a multi-crevice assembly. Figure 6-3 illustrates the schematic experimental procedure followed for Paper III.

6.3.2. Results and discussion

The modified Avesta cell avoided successfully crevice corrosion as no attacks were seen on the edges of the specimens. Additionally, the surface of the specimens did not suffer corrosion in the 1N Cl^- environment, whereas uniform corrosion was seen for the specimens exposed in the 7N Cl^- solution.

The dissolution attack differed between the two SDSSs after testing in 7M LiCl at 60ºC. The surface of UNS S32750 was uniformly corroded, whereas α-phase was selectively corroded in UNS S39274.

The dissolution ratio of each element was calculated from the average concentration measured by ICP-MS. All elements dissolved congruently in 1N Cl^-, corroborating the hypothesis that the dissolution of the elements occurred mainly at transpassive potentials. Contrarily, in 7M LiCl, W dissolution ratio (d'_W) indicated that the only element that dissolved incongruently was W, indicating a possible enrichment of W on the surface as $d'_W < 1$. According to Pourbaix [139], W is able to form a passive WO_3 film in the actual test conditions (pH = 0). A yellow reflection (the color of WO_3 [139]) was observed on the UNS S39274 specimens at the end of test. Nevertheless, at 60ºC, the calculated d'_W had its largest value, i.e., the ratio of dissolved W increased; even though all elements (including W) released less amount of metallic cations.

Additionally, no enrichment of W was detected by EDS, most probably because the enrichment film might be too thin for this technique. More surface-sensitive techniques such as x-ray photoelectron spectroscopy (XPS) or Auger electron spectroscopy (AES) are needed to verify the W enrichment on the surface of the UNS S39274 specimens.

Applying Galvele's model as described in section 4.3.1, E_{crit} was calculated and showed approximately the same value at all temperatures in both solutions. In 1M HCl, all E_{crit} were

E_{Trans}, since the potentials were more positive than the oxygen evolution reaction and within the transpassive region [139]. In 7N Cl^- environment, the two SDSSs differed in E_{corr}^* and η, balancing each other and, thus, obtaining similar low E_{crit} values. Only at 60ºC, UNS S39274 obtained an estimated E_{crit} approximately 100 mV more noble than UNS S32750. This difference was due to a more noble η in the W-rich material, indicating that the improvement in corrosion resistance was due to a lower dissolution rate [101].

According to Kendall's correlation coefficient, in 1N Cl^- environment, all d'_M followed the same trend and were correlated to the estimated theoretical E_{crit}. However, Kendall's coefficient indicated that dissolution of W in 7M LiCl did not depend on E_{crit}. All the other elements increased the quantity of ions released as the E_{crit} decreased in 7M LiCl.

In summary, Kendall's coefficient, together with the reduction of E_{Flade}, i_{max} and the dissolution quantity of all elements in 7M LiCl at 60ºC, indicated that W played an important role in improving corrosion resistance of SDSS, which was indicated by the shift of η to more noble values.

The E_{crit} values obtained at room temperature for UNS S32750 in this work and by Kappes et al. [3] differed 70 mV. For UNS S32750, the theoretical E_{crit} estimated in this work was similar to the $E_{R,Crev}$ obtained in neutral-chloride environment for $T \geq 50$ ºC. On the other hand, E_{crit} was similar to $E_{R,Crev}$ for UNS S39274 only at 60ºC. Considering the $T_{R,Crev}$ values obtained in the neutral-chloride environment in Paper II, 40ºC and 55ºC for UNS S32750 and UNS S39274, respectively, the estimated E_{crit} calculated with Gavele's critical acidification model was similar to $E_{R,Crev}$ for temperatures $> T_{R,Crev}$.

6.3.3. Main conclusions

- None of the materials suffered corrosion at 0 pH in the presence of 1N Cl^-. In 7N Cl^- solution, active stable propagating attacks were seen.
- In 7M Cl^- environment and 0 pH, the W-free material suffered uniform corrosion, whereas only α dissolved in UNS S39274.
- Lower i_{Flade} and E_{Flade} values obtained on UNS S39274 in 7N Cl^- at 60ºC indicated an enhancement of localized corrosion resistance due to W reducing the dissolution rate of the material, proven by the reduction of the released metallic cations measured by ICP-MS, the increment of η, and the incongruent dissolution of W suggesting

enrichment on the surface. Additionally, statistical analyses indicated that W was the only element in 7N Cl^- to be independent of the estimated E_{crit}.

- The estimated E_{crit} with Galvele's critical acidification model was independent of the temperature, inferring a significant role of passive film stability below critical temperatures according to Li-Scully-Frankel framework. Additionally, the values of E_{crit} were in good agreement with the $E_{R,Crev}$ measured with the PD-GS-PD in neutral-chloride environment for $T > T_{R,Crev}$.

CHAPTER 7: VALIDATION OF CORROSION RESISTANCE RESULTS IN NATURAL SEAWATER

This chapter includes the experimental procedure, results and main conclusions obtained from the investigation regarding crevice corrosion during long-term exposure of the specimens in natural seawater. Some information of this chapter is included in more detail in Paper II in the Appendix.

7.1. Introduction

In this part of the study, only UNS S32750 (W-free) and UNS S39274 (2.1 wt.% W) from Table 3-1 were investigated. See section 3.1.1. for more information about the two materials.

The main objective of this study was to verify the corrosion resistance obtained with the CPT test and the PD-GS-PD technique in Paper I and Paper II, respectively. Figure 7-1 illustrates schematically this part of the study from the outline of the thesis (from Figure 1-1).

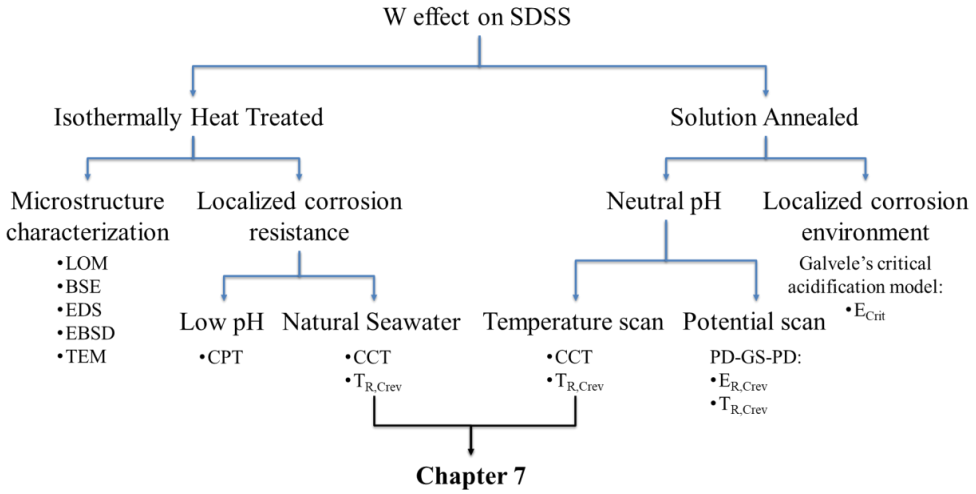

Figure 7-1. Schematic outline of Chapter 7 within the thesis.

7.2. Experimental method

The specimens were SA as described in section 4.2.1. Additionally, two IHT conditions were chosen from the investigation performed in Chapter 3. The IHT conditions were T2t3 and T2t4 corresponding to 846ºC IHT for 120 s and 240 s, respectively, as they differed greatly regarding vol.% of tertiary phases and CPT for the selected materials as seen in Table 7-1. Therefore, some specimens were isothermally aged at T2t3 and T2t4 following the same procedure as explained in section 3.1.2. After the corresponding heat treatment, the specimens were prepared following steps 1 and 6 (section 3.1.3) and assembled in a multi-crevice set-up as explained in section 4.2.1.

The corrosion test procedure was explained in detail in section 4.2.3. Each IHT condition was tested in duplicate to check repeatability.

Table 7-1. UNS S32750 and UNS S39274 characterization for T2t3 and T2t4 IHTs from Paper I.

UNS	Txty	σ vol.%	χ vol.%	CPT (°C)
S32750	**T2t3**	0.04	0.03	70
	T2t4	0.3	-	50
S39274	**T2t3**	-	-	75
	T2t4	-	0.04	65

Table 7-2. CCT and $T_{R,Crev}$ values obtained in the long-term exposure test in natural seawater.

Material (UNS)	IHT	Potential	CCT (°C)	$T_{R,Crev}$ (°C)
S32750	**SA**	**OCP**	> 80	-
		+300 mV$_{Ag/AgCl}$	80	42.5
		+600 mV$_{Ag/AgCl}$	45	42.5
	T2t3	**OCP**	> 80	-
		+600 mV$_{Ag/AgCl}$	65	52.5
	T2t4	**OCP**	> 80	-
		+600 mV$_{Ag/AgCl}$	40	30
S39274	**SA**	**OCP**	> 80	-
		+300 mV$_{Ag/AgCl}$	> 80	-
		+600 mV$_{Ag/AgCl}$	55	50
	T2t3	**OCP**	> 80	-
		+600 mV$_{Ag/AgCl}$	65	62.5
	T2t4	**OCP**	75	65
		+600 mV$_{Ag/AgCl}$	50	32.5

7.3. Results and discussion

Table 7-2 summarizes the results, where the lowest CCT and $T_{R,Crev}$ values obtained for each condition are reported. The monitored OCP and current density during exposure of one SA specimen for each material at OCP and +600 $mV_{Ag/AgCl}$ with indications of determination of CCT and $T_{R,Crev}$ are shown in Figure 7-2. Figure 7-3 shows images captured by LOM of some specimens after the tests.

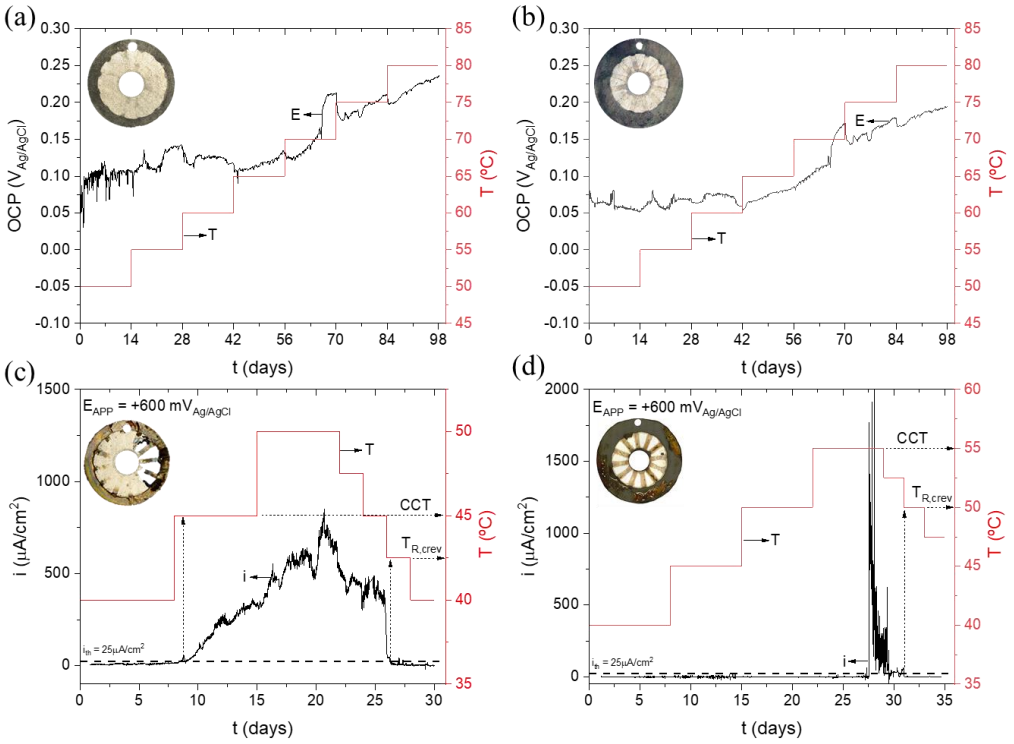

Figure 7-2. CCT and $T_{R,Crev}$ tests in natural seawater of one specimen of (a) UNS S32750 at OCP, (b) UNS S39274 at OCP, (c) UNS S32750 polarized to +600 $mV_{Ag/AgCl}$, and (d) UNS S39274 polarized to +600 $mV_{Ag/AgCl}$, the picture inserts show a specimen after exposure to illustrate the attack.

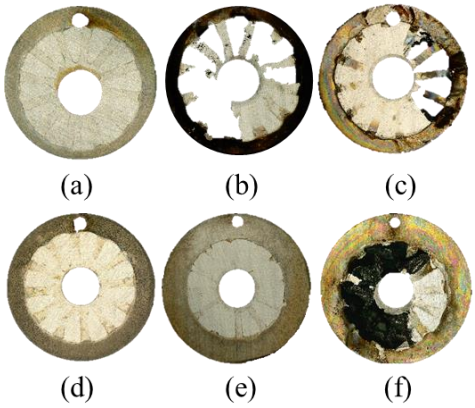

Figure 7-3. Crevice assembled specimens after exposure in natural seawater of (a) T2t4 UNS S32750 at OCP, (b) SA UNS S32750 polarized to +300 $mV_{Ag/AgCl}$, (c) SA UNS S32750 polarized to +600$mV_{Ag/AgCl}$, (d) T2t3 UNS S39274 at OCP, (e) SA UNS S39274 polarized to +300$mV_{Ag/AgCl}$, and (f) T2t4 UNS S39274 polarized to +600$mV_{Ag/AgCl}$. The hole in the middle measures 7 mm for all the specimens.

The CCT and $T_{R,Crev}$ values showed a clear trend as a function of potential: the higher the applied polarization potential, the lower the CCT and $T_{R,Crev}$. The specimens freely exposed, i.e., at OCP, did not suffer crevice corrosion as seen in Figure 7-3a and Figure 7-3d, even though some localized attacks were found using LOM on the samples after testing. The only exception was UNS S39274 IHT at T2t4 which obtained a CCT of 75ºC and a $T_{R,Crev}$ of 65ºC. This result contradicts the CPT value shown in Table 7-1, which was higher for UNS S39274. This was the only condition where the CCT and $T_{R,Crev}$ were lower for UNS S39274 than for UNS S32750. In all other cases, UNS S32750 showed a lower crevice corrosion resistance. For instance, for the SA specimens polarized to +300 $mV_{Ag/AgCl}$, UNS S32750 suffered crevice corrosion whereas UNS S39274 did not initiate up to 80ºC. Similarly, UNS S39274 SA specimens polarized to +600 $mV_{Ag/AgCl}$ obtained a 10ºC increase in CCT and 7.5ºC increase in $T_{R,Crev}$ compared to UNS S32750. Likewise, UNS S39274 IHT to T2t4 and polarized to +600 $mV_{Ag/AgCl}$ obtained a 10ºC increase in CCT and a 2.5ºC increase in $T_{R,Crev}$ compared to UNS S32750. This is in agreement with the results from Paper I and Paper II, where the CPT for the IHT specimens and the $T_{R,Crev}$ for the SA specimens were always higher for the UNS S39274 than for the UNS S32750. Additionally, the results obtained in this case for the SA samples polarized to +600 $mV_{Ag/AgCl}$ were approximately the same as the $T_{R,Crev}$ obtained with the PD-GS-PD technique in Paper II.

Higher temperature values were unexpectedly obtained for T2t3 specimens compared to SA specimens polarized to +600 $mV_{Ag/AgCl}$ as shown in Table 7-2. The only difference between the two test conditions was the start temperature of the test. For the SA specimens, the exposure started at 40ºC, whereas the T2t3 specimens started at 20ºC. According to Bardal et al. [140], stainless steel corrosion resistance increases with exposure time in natural seawater. This behavior was correlated to an enhancement of the oxide layer, although Bardal and coauthors did not detail the exact mechanism. UNS S39274 IHT at T2t3 had a SA microstructure, i.e., no presence of tertiary phases as seen in Table 7-1. Therefore, it is plausible that a thicker and stronger passive layer could shift the CCT and the $T_{R,Crev}$ approximately 10ºC as shown in Table 7-2. However, UNS S32750 IHT at T2t3 included some tertiary phase precipitation in the microstructure as indicated in Table 7-2. This should indicate a reduced corrosion resistance compared to SA condition.

7.4. Main conclusions

- In general, 2.1 wt.% W showed better localized corrosion resistance proven by higher CCT and $T_{R,Crev}$ values than the W-free material.
- More positive applied potential, lower the CCT and $T_{R,Crev}$ values.
- The CCT values measured in SA condition at +600 $mV_{Ag/AgCl}$ for both materials were very close to the $T_{R,Crev}$ values measured by PD-GS-PD in Paper II; validating the PD-GS-PD methodology to measure critical temperature values by means of $T_{R,Crev}$.

CHAPTER 8: GENERAL CONCLUSIONS

This chapter includes general conclusions obtained from all investigations on the effect of W on the localized corrosion resistance of SDSS.

8.1. Conclusions

In this thesis, three SDSSs with different W content in solid solution were compared to investigate the role of W as alloying element in SA and IHT specimens. Simulated and natural neutral-chloride environments and artificial acidic-chloride solutions simulating the localized corrosion environment were used in this study. Different techniques based on potentiodynamic and temperature scans were employed to compare and validate the results. Finally, the following conclusions were drawn from this thesis:

- W retarded and reduced the precipitation of tertiary phases within a given W range (e.g. 2.1 wt.%). Outside this range (e.g. 0.6 wt.%), W accelerated σ precipitation and the total density of deleterious phases increased.
- Localized corrosion resistance was strongly correlated to the tertiary phase vol.%. Effect of σ or χ on the CPT values could not be isolated, but the decrease in CPT seemed more drastic on those specimens with higher σ vol.% than χ.
- 1 vol.% of tertiary phase precipitation was sufficient to cause a drastic reduction of the CPT in some IHT conditions. However, the critical vol.% of deleterious phases inducing a significant drop of CPT depended on IHT temperature. At higher IHT temperatures, larger vol.% of intermetallic phases were required to provoke a significant decrease of CPT.
- CCT and $T_{R,Crev}$ determined with the PD-GS-PD technique and long-term immersion testing in natural seawater increased with the W content in the material. The difference in value with the W-free material was between 7.5 and 15ºC, depending on the technique used.
- $T_{R,Crev}$ measured with the PD-GS-PD technique obtained similar values as the CCT measured in the long-term immersion test in natural seawater. The difference was in the range 2.5 and 5ºC, depending on the material.
- The crevice corrosion attacks initiated at the phase boundaries between γ and α, followed by selectively corrosion of α. Dissolution of γ occurred at a later stage of the propagation.
- A minor difference in crevice corrosion resistance was measured by the PD-GS-PD technique between the two product forms of UNS S39274, resulting in a higher corrosion resistance for rolled plate samples.

- Dissolution rate of UNS S39274 (2.1 wt.% W) was significantly reduced at 60ºC in a propagating attack environment most probably due to W, as indicated by Galvele's critical acidification model and quantity of metallic cations released by the material.

8.2. Future work

There are still many questions regarding the role of W on localized corrosion resistance that have not been resolved. Therefore, further investigation would be needed to address this topic. Below are some suggestions:

- Investigation of the precipitation kinetics of commercially available SDSS with higher W content, to study if there is an upper limit to the optimal W content range.
- Investigate the corrosion performance of welds and correlate the results with the IHT data obtained in Paper 1.
- Testing UNS S32760 in natural seawater, to determine whether there is a W content range in SA conditions.
- Testing UNS S32760 in simulated localized corrosion environments to determine whether the W content plays a different role in an active pit/crevice.
- Testing a W-free material (like UNS S32750) in a solution containing tungstates to study the role of W dissolved in the solution.
- Analyzing the passive layer of the SDSS to study whether the oxide layer includes W.
- Investigate the composition and properties of the passive layer as function of temperature and exposure time in a corrosive solution.
- Using Synchrotron based techniques to study in-situ passivity breakdown.
- More detailed investigation of the effect of other alloying elements whose quantities were not exactly the same in the three SDSSs studied in this thesis. Especially elements such as Cu that could contribute to the corrosion resistance of the material.
- Performing tribocorrosion tests to study the repassivation role of W.

CHAPTER 9: REFERENCES

This chapter includes all references used in this thesis.

Chapter 9: References

[1] G.S. Frankel, N. Sridhar, Understanding localized corrosion, Materials Today, 11 (2008) 38-44, DOI: 10.1016/s1369-7021(08)70206-2.

[2] N.J. Laycock, J. Stewart, R.C. Newman, The initiation of crevice corrosion in stainless steels, Corros. Sci., 39 (1997) 1791-1809, DOI: 10.1016/s0010-938x(97)00050-4.

[3] M.A. Kappes, M.R. Ortíz, M. Iannuzzi, R.M. Carranza, Use of the Critical Acidification Model to Estimate Critical Localized Corrosion Potentials of Duplex Stainless Steels, Corros., 73 (2017) 31-40, DOI: 10.5006/2142.

[4] Z. Szklarska-Smialowska, Pitting and Crevice Corrosion, NACE International, Houston, TX, 2005.

[5] P.T. Jakobsen, E. Maahn, Temperature and potential dependence of crevice corrosion of AISI 316 stainless steel, Corros. Sci., 43 (2001) 1693-1709, DOI: 10.1016/s0010-938x(00)00167-0.

[6] E.B. Haugan, M. Næss, C. Torres Rodriguez, R. Johnsen, M. Iannuzzi, Effect of Tungsten on the Pitting and Crevice Corrosion Resistance of Type 25Cr Super Duplex Stainless Steels, Corros., 73 (2017) 53-67, DOI: 10.5006/2185.

[7] M. Iannuzzi, M. Salasi, E. Hornus, Crevice Corrosion, in, 2019, DOI: 10.31224/osf.io/fj3xq.

[8] J.R. Galvele, Transport Processes and the Mechanism of Pitting of Metals, J. Electrochem. Soc., 123 (1976) 464, DOI: 10.1149/1.2132857.

[9] R.M. Carranza, M.A. Rodríguez, Crevice corrosion of nickel-based alloys considered as engineering barriers of geological repositories, npj Mater. Degrad., 1 (2017) 1-9, DOI: 10.1038/s41529-017-0010-5.

[10] A.J. Sedriks, Plenary Lecture—1986: Effects of Alloy Composition and Microstructure on the Passivity of Stainless Steels, in: Corros., 1986, pp. 376-389, DOI: 10.5006/1.3584918.

[11] V.K. Lorenz, G. Médawar, Über das Korrosionsverhalten austenitischer Chrom-Nickel-(Molybdän-) Stähle mit und ohne Stickstoffzusatz unter besonderer Berücksichtigung ihrer Beanspruchbarkeit in chloridhaltigen Lösungen., Thyssenforschung, 1 (1969) 97-108.

[12] J.E. Truman, Effects of composition on the resistance to pitting corrosion of stainless steels, in: UK Corrosion'87, Brighton, 1987, pp. 111-129.

[13] R.F.A. Jargelius-Pettersson, Application of the Pitting Resistance Equivalent Concept to Some Highly Alloyed Austenitic Stainless Steels, Corros., 54 (1998) 162-168, DOI: 10.5006/1.3284840.

[14] J.O. Nilsson, Super duplex stainless steels, Mater. Sci. Technol., 8 (1992) 685-700, DOI: 10.1179/mst.1992.8.8.685.

[15] N. Fuertes, Use of local electrochemical techniques for corrosion studies of stainless steels, Thesis for the degree of Phlisophiae Doctor, KTH Royal Institute of Technology, Stockholm, Sweden, 2016, Document number: TRITA-CHE Report 2016:24.

[16] M. Knyazeva, M. Pohl, Duplex Steels: Part I: Genesis, Formation, Structure, Metallography, Microstructure, and Analysis, 2 (2013) 113-121, DOI: 10.1007/s13632-013-0066-8.

[17] J. Charles, Super duplex stainless steels: structure and properties, in: Duplex Stainless Steels '91, Proceedings. Les Éditions de Physique Les Ulis, Beaune, Bourgogne, France, 1991, pp. 151-168.

[18] ISO, Petroleum, petrochemical and natural gas industries -- Materials selection and corrosion control for oil and gas production systems, in, International Organization for Standardization, Geneva, Switzerland, 2010.

[19] NORSOK, Materials selection. Rev. 4, in: NORSOK M-001, Standards Norway, Lysaker, Norway, 2004.

[20] K. Ogawa, T. Osuki, Effects of Alloying Elements on Sigma Phase Precipitation in Duplex Stainless Steel (1) - Modelling of Effects of Chrovmium, Molybdenum and Tungsten on Sigma Phase Growth Rate in Super Duplex Stainless Steel, ISIJ Int., 59 (2019) 122-128, DOI: 10.2355/isijinternational.ISIJINT-2018-477.

[21] N. Llorca-Isern, H. López-Luque, I. López-Jiménez, M.V. Biezma, Identification of sigma and chi phases in duplex stainless steels, Mater. Charact., 112 (2016) 20-29, DOI: 10.1016/j.matchar.2015.12.004.

[22] K. Ogawa, H. Okamoto, M. Ueda, M. Igarashi, T. Mori, T. Kobayashi, Effects of tungsten on pitting corrosion resistance and impact toughness in the HAZ of duplex stainless steel - study of weldability of high-tungsten duplex stainless steel (1st Report), Weld. Int., 10 (1996) 466-472, DOI: 10.1080/09507119609549032.

[23] J.M. Pardal, S.S.M. Tavares, M.C. Fonseca, J.A. de Souza, R.R.A. Côrte, H.F.G. de Abreu, Influence of the grain size on deleterious phase precipitation in superduplex stainless steel UNS S32750, Mater. Charact., 60 (2009) 165-172, DOI: 10.1016/j.matchar.2008.08.007.

[24] J.M. Pardal, S.S.M. Tavares, M.d.P.C. Fonseca, J.A.d. Souza, L.M. Vieira, H.F.G.d. Abreu, Deleterious phases precipitation on superduplex stainless steel UNS S32750: characterization by light optical and scanning electron microscopy, Mater. Res., 13 (2010) 401-407, DOI: 10.1590/s1516-14392010000300020.

[25] J.M. Pardal, S.S.M. Tavares, M.P. Cindra Fonseca, M.R. da Silva, M.L.R. Ferreira, Study of deleterious phase precipitation under continuous cooling of superduplex stainless steel UNS S32750, Mater. Sci. Technol., 28 (2012) 295-302, DOI: 10.1179/1743284711y.0000000040.

[26] S.I. Cristini, B. Sacchi, E. Guerrini, S. Trasatti, S.P. Trasatti, Detection of sigma phase in 22% Cr duplex stainless steel by electrochemical methods, Russ. J. Electrochem., 46 (2010) 1094-1100, DOI: 10.1134/s1023193510100034.

[27] C. Örnek, D.L. Engelberg, Correlative EBSD and SKPFM characterisation of microstructure development to assist determination of corrosion propensity in grade 2205 duplex stainless steel, J. Mater. Sci., 51 (2016) 1931-1948, DOI: 10.1007/s10853-015-9501-3.

[28] J. Michalska, B. Chmiela, Phase analysis in duplex stainless steel: comparison of EBSD and quantitative metallography methods, IOP Conf. Ser.: Mater. Sci. Eng., 55 (2014), DOI: 10.1088/1757-899x/55/1/012010.

[29] R. Magnabosco, Kinetics of sigma phase formation in a Duplex Stainless Steel, Mater. Res., 12 (2009) 321-327, DOI: 10.1590/s1516-14392009000300012.

[30] D.Y. Kobayashi, S. Wolynec, Evaluation of the low corrosion resistant phase formed during the sigma phase precipitation in duplex stainless steels, Mater. Res., 2 (1999) 239-247, DOI: 10.1590/s1516-14391999000400002.

[31] D.M.E. Villanueva, F.C.P. Junior, R.L. Plaut, A.F. Padilha, Comparative study on sigma phase precipitation of three types of stainless steels: austenitic, superferritic and duplex, Mater. Sci. Technol., 22 (2006) 1098-1104, DOI: 10.1179/174328406x109230.

[32] D.M. Escriba, E. Materna-Morris, R.L. Plaut, A.F. Padilha, Chi-phase precipitation in a duplex stainless steel, Mater. Charact., 60 (2009) 1214-1219, DOI: 10.1016/j.matchar.2009.04.013.

[33] N. Pettersson, R.F.A. Pettersson, S. Wessman, Precipitation of Chromium Nitrides in the Super Duplex Stainless Steel 2507, Metall. Mater. Trans. A, 46 (2015) 1062-1072, DOI: 10.1007/s11661-014-2718-y.

[34] I. Calliari, M. Pellizzari, E. Ramous, Precipitation of secondary phases in super duplex stainless steel ZERON100 isothermally aged, Mater. Sci. Technol., 27 (2011) 928-932, DOI: 10.1179/174328409x463243.

[35] H. Kokawa, E. Tsory, T.H. North, Nitride Precipitation in Duplex Stainless Steel Weld Metal, ISIJ Int., 35 (1995) 1277-1283, DOI: 10.2355/isijinternational.35.1277.

[36] J. Liao, Nitride Precipitation in Weld HAZs of a Duplex Stainless Steel, ISIJ Int., 41 (2001) 460-467, DOI: 10.2355/isijinternational.41.460.

[37] C.-C. Hsieh, W. Wu, Overview of Intermetallic Sigma () Phase Precipitation in Stainless Steels, ISRN Metall., 2012 (2012) 1-16, DOI: 10.5402/2012/732471.

[38] J.O. Nilsson, T. Huhtala, P. Jonsson, L. Karlsson, A. Wilson, Structural stability of super duplex stainless weld metals and its dependence on tungsten and copper, Metall. Mater. Trans. A, 27 (1996) 2196-2208, DOI: 10.1007/bf02651874.

[39] K.Y. Kim, P.Q. Zhang, T.H. Ha, Y.H. Lee, Electrochemical and Stress Corrosion Properties of Duplex Stainless Steels Modified with Tungsten Addition, Corros., 54 (1998) 910-921, DOI: 10.5006/1.3284810.

[40] J.S. Kim, H.S. Kwon, Effects of Tungsten on Corrosion and Kinetics of Sigma Phase Formation of 25% Chromium Duplex Stainless Steels, Corros., 55 (1999) 512-521, DOI: 10.5006/1.3284014.

[41] H.J. Park, H.W. Lee, Effect of Alloyed Mo and W on The Corrosion Characteristics of Super Duplex Stainless Steel Weld, Int J Electrochem Sc, 9 (2014) 6687-6698.

[42] N. Llorca-Isern, I. López-Jiménez, H. López-Luque, M.V. Biezma, A. Roca, Study of the Precipitation of Secondary Phases in Duplex and Superduplex Stainless Steel, Mater. Sci. Forum, 879 (2016) 2537-2542, DOI: 10.4028/www.scientific.net/MSF.879.2537.

[43] J.O. Nilsson, A. Wilson, Influence of isothermal phase transformations on toughness and pitting corrosion of super duplex stainless steel SAF 2507, Mater. Sci. Technol., 9 (1993) 545-554, DOI: 10.1179/mst.1993.9.7.545.

[44] K. Ogawa, H. Okamoto, M. Igarashi, M. Ueda, T. Mori, T. Kobayashi, Effects of tungsten on precipitation behaviour of intermetallic compounds in the HAZ of duplex stainless steel: Study of weldability of high-tungsten duplex stainless steel (2nd Report), Weld. Int., 11 (1997) 14-22, DOI: 10.1080/09507119709454409.

[45] S. Hertzman, T. Huhtala, L. Karlsson, J.O. Nilsson, M. Nilsson, R. Jargelius-Pettersson, A. Wilson, Microstructure–property relations of Mo- and W-alloyed super duplex stainless weld metals, Mater. Sci. Technol., 13 (1997) 604-613, DOI: 10.1179/mst.1997.13.7.604.

[46] Y.H. Lee, K.T. Kim, Y.D. Lee, K.Y. Kim, Effects of W substitution on σ and χ phase precipitation and toughness in duplex stainless steels, Mater. Sci. Technol., 14 (1998) 757-764, DOI: 10.1179/mst.1998.14.8.757.

[47] Y.S. Ahn, J.P. Kang, Effect of aging treatments on microstructure and impact properties of tungsten substituted 2205 duplex stainless steel, Mater. Sci. Technol., 16 (2000) 382-388, DOI: 10.1179/026708300101507965.

[48] C.-J. Park, M.-K. Ahn, H.-S. Kwon, Influences of Mo substitution by W on the precipitation kinetics of secondary phases and the associated localized corrosion and embrittlement in 29% Cr ferritic stainless steels, Materials Science and Engineering: A, 418 (2006) 211-217, DOI: 10.1016/j.msea.2005.11.053.

[49] A.R. Akisanya, U. Obi, N.C. Renton, Effect of ageing on phase evolution and mechanical properties of a high tungsten super-duplex stainless steel, Materials Science and Engineering: A, 535 (2012) 281-289, DOI: 10.1016/j.msea.2011.12.087.

[50] J.S. Kim, T.H. Ha, K.Y. Kim, Effect of Tungsten Substitution on Precipitation Retardation and Stress Corrosion Cracking Properties of 25%Cr-6%Ni Duplex Stainless Steel, Corros., 57 (2001) 452-464, DOI: 10.5006/1.3290369.

[51] D.M.E. Villanueva, F.C.P. Junior, R.L. Plaut, A.F. Padilha, Comparative study on sigma phase precipitation of the three types of stainless steels: austenitic, superferritic and duplex, 22 (2006) 1098-1104.

[52] A.F. Miranda Pérez, Solid state phase transformations in advanced steels, Thesis for the degree of Industrial Engineering, Università Degli Studi di Padova, Padova.

[53] K. Ogawa, T. Osuki, Effects of Alloying Elements on Sigma Phase Precipitation in Duplex Stainless Steel (2) - Effects of Alloying Chromium, Molybdenum and Tungsten on C-curve of Sigma Phase Precipitation in Duplex Stainless Steel, ISIJ Int., 59 (2019) 129-135, DOI: 10.2355/isijinternational.ISIJINT-2018-478.

[54] R. Magnabosco, L. da Costa Morais, D.C. dos Santos, Use of composition profiles near sigma phase for assessment of localized corrosion resistance in a duplex stainless steel, Calphad, 64 (2019) 126-130, DOI: 10.1016/j.calphad.2018.12.004.

[55] R. Magnabosco, N. Alonso-Falleiros, Pit Morphology and Its Relation to Microstructure of 850°C Aged Duplex Stainless Steel, Corros., 61 (2005) 130-136, DOI: 10.5006/1.3278167.

[56] D. Caluscio dos Santos, R. Magnabosco, C. de Moura-Neto, Influence of Sigma Phase Formation on Pitting Corrosion of an Aged UNS S31803 Duplex Stainless Steel, Corros., 69 (2013) 900-911, DOI: 10.5006/0768.

[57] S.-H. Jeon, S.-T. Kim, I.-S. Lee, J.-S. Kim, K.-T. Kim, Y.-S. Park, Effects of W substitution on the precipitation of secondary phases and the associated pitting corrosion in hyper duplex stainless steels, J. Alloys Compd., 544 (2012) 166-172, DOI: 10.1016/j.jallcom.2012.07.129.

[58] B. Deng, Z. Wang, Y. Jiang, H. Wang, J. Gao, J. Li, Evaluation of localized corrosion in duplex stainless steel aged at 850°C with critical pitting temperature measurement, Electrochim. Acta, 54 (2009) 2790-2794, DOI: 10.1016/j.electacta.2008.11.038.

[59] I. Calliari, M. Pellizzari, E. Ramous, Precipitation of secondary phases in super duplex stainless steel ZERON100 isothermally aged, 27 (2011) 928-932.

[60] I. Calliari, M. Zanesco, E. Ramous, Influence of isothermal aging on secondary phases precipitation and toughness of a duplex stainless steel SAF 2205, 41 (2006) 7643-7649.

[61] J.W. Simmons, J.B.S. Covino, J.A. Hawk, J.S. Dunning, Effect of Nitride (Cr2N) Precipitation on the Mechanical, Corrosion, and Wear Properties of Austenitic Stainless Steel, ISIJ Int., 36 (1996) 846-854, DOI: 10.2355/isijinternational.36.846.

[62] M.F. McGuire, Stainless Steels for Design Engineers, ASM International, Materials Park, Ohio, 2008.

[63] T.-H. Lee, S.-J. Kim, Phase identification in an isothermally aged austenitic 22Cr-21Ni-6Mo-N stainless steel, Scr. Mater., 39 (1998) 951-956, DOI: 10.1016/s1359-6462(98)00269-3.

[64] A.P. Miodownik, N. Saunders, Modelling of materials properties in duplex stainless steels, Mater. Sci. Technol., 18 (2002) 861-868, DOI: 10.1179/026708302225004694.

[65] T. Mathiesen, C. Jensen, Rapid Corrosion Test for Detecting Intermetallic Phases in Duplex Stainless Steels, in: CORROSION 2013, NACE International, Orlando, Florida, 2013.

[66] M. Pourbaix, L. Klimzack-Mathieiu, C. Mertens, J. Meunier, C. Vanleugenhaghe, L. de Munck, J. Laureys, L. Neelemans, M. Warzee, Potentiokinetic and corrosimetric investigations of the corrosion behaviour of alloy steels, Corros. Sci., 3 (1963) 239-259, DOI: 10.1016/s0010-938x(63)80030-x.

[67] K.K. Starr, E.D. Verink, M. Pourbaix, The Significance of the Protection Potential for Fe-Cr Alloys at Room Temperature, Corros., 32 (1976) 47-51, DOI: 10.5006/0010-9312-32.2.47.

[68] H.P. Leckie, H.H. Uhlig, Environmental Factors Affecting the Critical Potential for Pitting in 18–8 Stainless Steel, J. Electrochem. Soc., 113 (1966) 1262-1267, DOI: 10.1149/1.2423801.

[69] T. Shibata, T. Takeyama, Stochastic Theory of Pitting Corrosion, Corros., 33 (1977) 243-251, DOI: 10.5006/0010-9312-33.7.243.

[70] H. Yashiro, K. Tanno, The effect of electrolyte composition on the pitting and repassivation behavior of AISI 304 stainless steel at high temperature, Corros. Sci., 31 (1990) 485-490, DOI: 10.1016/0010-938x(90)90150-4.

[71] M. Akashi, G. Nakayama, T. Fukuda, Initiation Criteria for Crevice Corrosion of Titanium Alloys Used for HLW Disposal Overpack, in: Corrosion 98, NACE International, 1998.

[72] C. Vanleugenhaghe, L. Klimczak-Mathieu, J. Meunier, M. Pourbaix, INFLUENCE OF CHLORIDES AND OXIDIZERS ON THE BEHAVIOUR OF STAINLESS STEELS IN BI-CARBONIC SOLUTION. Report No. 725, in, Centre Belge d'Etude de la Corrosion, Brussels, 1961.

[73] S. Tsujikawa, Y. Hisamatsu, On the Repassivation Potential for Crevice Corrosion, Corros. Eng., 29 (1980) 37-40, DOI: 10.3323/jcorr1974.29.1_37.

[74] N.G. Thompson, B.C. Syrett, Relationship Between Conventional Pitting and Protection Potentials and a New, Unique Pitting Potential, Corros., 48 (1992) 649-659, DOI: 10.5006/1.3315985.

[75] D.S. Dunn, G.A. Cragnolino, N. Sridhar, An Electrochemical Approach to Predicting Long-Term Localized Corrosion of Corrosion-Resistant High-Level Waste Container Materials, Corros., 56 (2000) 90-104, DOI: 10.5006/1.3280526.

[76] L.L. Machuca, S.I. Bailey, R. Gubner, Systematic study of the corrosion properties of selected high-resistance alloys in natural seawater, Corros. Sci., 64 (2012) 8-16, DOI: 10.1016/j.corsci.2012.06.029.

[77] ASTM International, Standard Test Method for Conducting Cyclic Potentiodynamic Polarization Measurements for Localized Corrosion Susceptibility of Iron-, Nickel-, or Cobalt-Based Alloys, in, West Conshohocken, PA, 2018, DOI: 10.1520/G0061-86R18.

[78] C.M. Giordano, M. Rincón Ortíz, M.A. Rodríguez, R.M. Carranza, R.B. Rebak, Crevice corrosion testing methods for measuring repassivation potential of alloy 22, Corros. Eng. Sci. Technol., 46 (2011) 129-133, DOI: 10.1179/1743278210y.0000000014.

[79] Q.J. Meng, A. Adeleke, S. Derrickson, Localized Corrosion Resistance Of Uns S32750 And Uns S33207 Duplex Umbilical Tubes In Synthetic Seawater, in: Corrosion 2010, NACE International, 2010.

[80] I.L. Rosenfeld, Breakdown of the Passive State and Repassivation of Stainless Steels, J. Electrochem. Soc., 125 (1978) 1729-1735, DOI: 10.1149/1.2131284.

[81] R.C. Newman, E.M. Franz, Growth and Repassivation of Single Corrosion Pits in Stainless Steel, Corros., 40 (1984) 325-330, DOI: 10.5006/1.3593930.

[82] T. Nakayama, K. Sasa, Effect of Ultrasonic Waves on the Pitting Potentials of 18-8 Stainless Steel in Sodium Chloride Solution, Corros., 32 (1976) 283-285, DOI: 10.5006/0010-9312-32.7.283.

[83] E.C. Hornus, M.A. Rodríguez, R.M. Carranza, R.B. Rebak, Effect of Temperature and Chloride Concentration on the Crevice Corrosion Resistance of Austenitic Stainless Steels, in: Corrosion 2016, NACE International, 2016.

[84] N. Sridhar, G.A. Cragnolino, Applicability of Repassivation Potential for Long-Term Prediction of Localized Corrosion of Alloy 825 and Type 316L Stainless Steel, Corros., 49 (1993) 885-894, DOI: 10.5006/1.3316014.

[85] ASTM International, Standard Test Method for Determining the Crevice Repassivation Potential of Corrosion-Resistant Alloys Using a Potentiodynamic-Galvanostatic-Potentiostatic Technique, in, ASTM International, West Conshohocken, PA, 2014, DOI: 10.1520/G0192-08R14.

[86] A.K. Mishra, G.S. Frankel, Crevice Corrosion Repassivation of Alloy 22 in Aggressive Environments, Corros., 64 (2008) 836-844, DOI: 10.5006/1.3279917.

[87] M.R. Ortíz, M.A. Rodríguez, R.M. Carranza, R.B. Rebak, Determination of the Crevice Corrosion Stabilization and Repassivation Potentials of a Corrosion-Resistant Alloy, Corros., 66 (2010) 105002-105002-105012, DOI: 10.5006/1.3500830.

[88] S. Valen, P.O. Gartland, Crevice Corrosion Repassivation Temperatures of Highly Alloyed Stainless Steels, Corros., 51 (1995) 750-756, DOI: 10.5006/1.3293552.

[89] B. Deng, Y. Jiang, J. Gong, C. Zhong, J. Gao, J. Li, Critical pitting and repassivation temperatures for duplex stainless steel in chloride solutions, Electrochim. Acta, 53 (2008) 5220-5225, DOI: 10.1016/j.electacta.2008.02.047.

[90] G.S. Frankel, Pitting Corrosion, in: S.D. Cramer, B.S. Covino (Eds.) Corrosion: Fundamentals, testing, and Protection, ASM International, Ohio, 2003, pp. 236-241, DOI: 10.1361/asmhba0003612.

[91] G.S. Frankel, Pitting Corrosion of Metals, J. Electrochem. Soc., 145 (1998) 2186-2198, DOI: 10.1149/1.1838615.

[92] R.C. Newman, M.A.A. Ajjawi, H. Ezuber, S. Turgoose, An experimental confirmation of the pitting potential model of galvele, Corros. Sci., 28 (1988) 471-477, DOI: 10.1016/0010-938x(88)90069-8.

[93] F. Bocher, R. Huang, J.R. Scully, Prediction of Critical Crevice Potentials for Ni-Cr-Mo Alloys in Simulated Crevice Solutions as a Function of Molybdenum Content, Corros., 66 (2010) 055002-055001 to 055002-055015, DOI: 10.5006/1.3430462.

[94] E.C. Hornus, C.M. Giordano, M.A. Rodriguez, R.M. Carranza, R.B. Rebak, Effect of Temperature on the Crevice Corrosion of Nickel Alloys Containing Chromium and Molybdenum, J. Electrochem. Soc., 162 (2015) C105-C113, DOI: 10.1149/2.0431503jes.

[95] E.C. Hornus, M.A. Rodríguez, R.M. Carranza, R.B. Rebak, Comparative Study of the Crevice Corrosion Resistance of UNS S30400 and UNS S31600 Stainless Steels in the Context of Galvele's Model, Corros., 73 (2017) 41-52, DOI: 10.5006/2179.

[96] J. Srinivasan, R.G. Kelly, On a Recent Quantitative Framework Examining the Critical Factors for Localized Corrosion and Its Impact on the Galvele Pit Stability Criterion, Corros., 73 (2017) 613-633, DOI: 10.5006/2334.

[97] J.R. Galvele, J.B. Lumsden, R.W. Staehle, Effect of Molybdenum on the Pitting Potential of High Purity 18% Cr Ferritic Stainless Steels, J. Electrochem. Soc., 125 (1978) 1204, DOI: 10.1149/1.2131650.

[98] T. Li, J.R. Scully, G.S. Frankel, Localized Corrosion: Passive Film Breakdown vs. Pit Growth Stability: Part III. A Unifying Set of Principal Parameters and Criteria for Pit Stabilization and Salt Film Formation, J. Electrochem. Soc., 165 (2018) C762-C770, DOI: 10.1149/2.0251811jes.

[99] T. Li, J.R. Scully, G.S. Frankel, Localized Corrosion: Passive Film Breakdown vs. Pit Growth Stability: Part IV. The Role of Salt Film in Pit Growth: A Mathematical Framework, J. Electrochem. Soc., 166 (2019) C115-C124, DOI: 10.1149/2.0211906jes.

[100] N. Bui, A. Irhzo, F. Dabosi, Y. Limouzin-Maire, On the mechanism for improved passivation by additions of tungsten to austenitic stainless steels, Corros., 39 (1983) 491-496, DOI: 10.5006/1.3577373.

[101] A. Belfrouh, C. Masson, D. Vouagner, A.M. de Becdelievre, N.S. Prakash, J.P. Audouard, The cumulative effect of alloying elements N, W, Mo and Cu on the corrosion behaviour of 17Cr-13Ni stainless steel in 2 N H2SO4, Corros. Sci., 38 (1996) 1639-1648, DOI: 10.1016/s0010-938x(96)00033-9.

[102] N.D. Tomashov, G.P. Chernova, O.N. Marcova, Effect of Supplementary Alloying Elements On Pitting Corrosion Susceptibility Of 18Cr-14Ni Stainless Steel, Corros., 20 (1964) 166t-173t, DOI: 10.5006/0010-9312-20.5.166t.

[103] M.K. Ahn, H.S. Kwon, H.M. Lee, Quantitative comparison of the influences of tungsten and molybdenum on the passivity of Fe-29Cr ferritic stainless steels, Corros. Sci., 40 (1998) 307-322, DOI: 10.1016/s0010-938x(97)00138-8.

[104] E.-A. Cho, C.-K. Kim, J.-S. Kim, H.-S. Kwon, Quantitative analysis of repassivation kinetics of ferritic stainless steels based on the high field ion conduction model, Electrochim. Acta, 45 (2000) 1933-1942, DOI: 10.1016/s0013-4686(99)00415-6.

[105] R. Goetz, J. Laurent, D. Landolt, The influence of minor alloying elements on the passivation behaviour of iron-chromium alloys in HCl, Corros. Sci., 25 (1985) 1115-1126, DOI: 10.1016/0010-938x(85)90057-5.

[106] H. Habazaki, A. Kawashima, K. Asami, K. Hashimoto, The corrosion behavior of amorphous Fe-Cr-Mo-P-C and Fe-Cr-W-P-C alloys in 6 M HCl solution, Corros. Sci., 33 (1992) 225-236, DOI: 10.1016/0010-938x(92)90147-u.

[107] N. Salkind, Encyclopedia of Measurement and Statistics, SAGE Publications, Thousand Oaks, California, 2007.

[108] S. Deviant, Statistics How to - ANOVA Test: Definition, types, Examples, https://www.statisticshowto.com/probability-and-statistics/hypothesis-testing/anova/, 2020 (accessed 29 May 2020).

[109] B. Illowsky, S. Dean, Collaborative Statistics, Maxfield Foundation, Online: http://cnx.org/content/col10522/1.40/, 2012.

[110] D.C. Montgomery, Design and Analysis of Experiments, John Wiley & Sons, Inc., Hoboken, NJ, 2009.

[111] T.V. Perneger, What's wrong with Bonferroni adjustments, BMJ, 316 (1998) 1236-1238, DOI: 10.1136/bmj.316.7139.1236.

[112] R.E. Lund, J.R. Lund, Algorithm AS 190: Probabilities and Upper Quantiles for the Studentized Range, Applied Statistics, 32 (1983), DOI: 10.2307/2347300.

[113] K. Pearson, Mathematical Contributions to the Theory of Evolution. III. Regression, Heredity, and Panmixia, Philos. Trans. R. Soc. London, Ser. A, 187 (1896) 253-318.

[114] C. Croux, C. Dehon, Influence functions of the Spearman and Kendall correlation measures, Statistical Methods & Applications, 19 (2010) 497-515, DOI: 10.1007/s10260-010-0142-z.

[115] T.S. King, R. Lengerich, S. Bai, 18.3-Kendall Tau-b Correlation Coefficient, in: STAT 509-Design and Analysis of Clinical Trials, https://online.stat.psu.edu/stat509/node/165/, 2018 (accessed 23 May 2020).

[116] Statoil ASA, Technical note – Metallographic etching of duplex stainless steels, in: MAT–2010080, Statoil ASA, Oslo, Norway, 2010.

[117] D. Wan, A. Barnoush, Plasticity in cryogenic brittle fracture of ferritic steels: Dislocation versus twinning, Materials Science and Engineering: A, 744 (2019) 335-339, DOI: 10.1016/j.msea.2018.12.038.

[118] D. Wang, X. Lu, D. Wan, Z. Li, A. Barnoush, In-situ observation of martensitic transformation in an interstitial metastable high-entropy alloy during cathodic hydrogen charging, Scr. Mater., 173 (2019) 56-60, DOI: 10.1016/j.scriptamat.2019.07.042.

[119] S. He, M. Saunders, K. Chen, H. Gao, A. Suvorova, W.D.A. Rickard, Z. Quadir, C.Q. Cui, S.P. Jiang, A FIB-STEM Study of Strontium Segregation and Interface Formation of Directly Assembled La0.6Sr0.4Co0.2Fe0.8O3-δCathode on Y2O3-ZrO2Electrolyte of Solid Oxide Fuel Cells, J. Electrochem. Soc., 165 (2018) F417-F429, DOI: 10.1149/2.0151807jes.

[120] D. Tomus, H.P. Ng, In situ lift-out dedicated techniques using FIB-SEM system for TEM specimen preparation, Micron, 44 (2013) 115-119, DOI: 10.1016/j.micron.2012.05.006.

[121] E.M.L.E.M. Jackson, P.E.d. Visser, L.A. Cornish, Distinguishing between Chi and Sigma phases in duplex stainless steels using potentiostatic etching, Mater. Charact., 31 (1993) 185-190, DOI: 10.1016/1044-5803(93)90061-y.

[122] T. Mathiesen, T.S. Nielsen, T. Haugen, B. Espelid, P. Hummelgaard, K. Vilpponen, NT Technical Report 548 - Improved Method for ASTM G48 Corrosion Testing of Welds, in, Force Technology, DNV, Esbjerg Oilfield Services, Kværner Oilfield Products, 2004, pp. 36.

[123] ISO, Corrosion of metals and alloys - Crevice corrosion formers with disc springs for flat specimens or tubes made from stainless steel, in, International Organization for Standardization, Geneva, Switzerland, 2015.

[124] J.R. Galvele, Tafel's law in pitting corrosion and crevice corrosion susceptibility, Corros. Sci., 47 (2005) 3053-3067, DOI: 10.1016/j.corsci.2005.05.043.

[125] J.R. Galvele, Transport processes in passivity breakdown—II. Full hydrolysis of the metal ions, Corros. Sci., 21 (1981) 551-579, DOI: 10.1016/0010-938x(81)90009-3.

[126] European Directorate for the Quality of Medicines & HealthCare, European Pharmacopoeia, https://www.edqm.eu/en/european-pharmacopoeia-background-50.html, 2020 (accessed 8 June 2020).

[127] I. Feldman, Use and Abuse of pH Measurements, Anal. Chem., 28 (1956) 1859-1866, DOI: 10.1021/ac60120a014.

[128] G. Orgovan, B. Noszal, Electrodeless, accurate pH determination in highly basic media using a new set of (1)H NMR pH indicators, J Pharm Biomed Anal, 54 (2011) 958-964, DOI: 10.1016/j.jpba.2010.11.022.

[129] R. Qvarfort, New electrochemical cell for pitting corrosion testing, Corros. Sci., 28 (1988) 135-140, DOI: 10.1016/0010-938x(88)90090-x.

[130] R. Ovarfort, Critical pitting temperature measurements of stainless steels with an improved electrochemical method, Corros. Sci., 29 (1989) 987-993, DOI: 10.1016/0010-938x(89)90088-7.

[131] H. Andersen, C.O.A. Olsson, L. Wegrelius, Critical Pitting Temperatures in Sodium Chloride and Ferric Chloride Solutions - Determined Using the 'Avesta Cell', Mater. Sci. Forum, 289-292 (1998) 925-932, DOI: 10.4028/www.scientific.net/MSF.289-292.925.

[132] J. Hildén, J. Virtanen, O. Forsén, J. Aromaa, Electrolytic pickling of stainless steel studied by electrochemical polarisation and DC resistance measurements combined with surface analysis, Electrochim. Acta, 46 (2001) 3859-3866, DOI: 10.1016/s0013-4686(01)00673-9.

[133] S.H. Mameng, R. Pettersson, J.Y. Jonson, Limiting conditions for pitting corrosion of stainless steel EN 1.4404 (316L) in terms of temperature, potential and chloride concentration, Mater. Corros., 68 (2017) 272-283, DOI: 10.1002/maco.201609061.

[134] M.N. Bajestani, J. Neshati, M.H. Siadati, Development of Time-Frequency Analysis in Electrochemical Noise for Detection of Pitting Corrosion, Corros., 75 (2018) 183-191, DOI: 10.5006/2900.

[135] Digital Surf, www.digitalsurf.com, 1996 (accessed 14 February 2020).

[136] M. Pourbaix, Atlas of Electrochemical Equilibria in Aqueous Solutions, National Association of Corrosion Engineers (NACE), Houston, Texas, USA, 1974.

[137] E. Bardal, J.M. Drugli, P.O. Gartland, The behaviour of corrosion-resistant steels in seawater: A review, Corros. Sci., 35 (1993) 257-267, DOI: 10.1016/0010-938x(93)90157-c.

CHAPTER 10: APPENDIX

In the Appendix, the three peer-reviewed papers (one published, two submitted) and the two conference proceedings are included.

PAPER I

The Role of Tungsten on the Phase Transformation Kinetics and its Correlation with the Localized Corrosion Resistance of 25Cr Super Duplex Stainless Steels

C. Torres, M. S. Hazarabedian, Z. Quadir, R. Johnsen, M. Iannuzzi

Journal of The Electrochemical Society, 167 (2020), 081510

DOI: 10.1149/1945-7111/ab90af

Journal of The Electrochemical Society, 2020 **167** 081510
1945-7111/2020/167(8)/081510/17/$40.00 © 2020 The Electrochemical Society ("ECS"). Published on behalf of ECS by IOP Publishing Limited

The Role of Tungsten on the Phase Transformation Kinetics and its Correlation with the Localized Corrosion Resistance of 25Cr Super Duplex Stainless Steels

Cristian Torres,[1,z] María Sofía Hazarabedian,[2] Zakaria Quadir,[3] Roy Johnsen,[1] and Mariano Iannuzzi[1,2,*]

[1]*Department of Mechanical and Industrial Engineering, Norwegian University of Science and Technology, 7491 Trondheim, Norway*
[2]*Curtin Corrosion Centre, Curtin University, Perth, WA 6845, Australia*
[3]*John de Laeter Centre, Curtin University, Perth, WA 6845, Australia*

Super Duplex Stainless Steels (SDSS) have excellent corrosion resistance due to their high concentration of alloying elements like Cr, Mo, and N. There is still, however, disagreement on the role of tungsten in the corrosion resistance of stainless steels. In this regard, the influence of tungsten on tertiary phase precipitation kinetics remains a chief source of controversy. In this study, three different SDSS with different tungsten contents have been investigated, namely, UNS S32750 (W-free), S32760 (0.6 wt% W), and S39274 (2.1 wt% W). Different isothermal aging conditions were studied, followed by microstructure characterization using scanning electron microscopy, energy dispersive X-ray spectroscopy, electron backscatter diffraction, and transmission electron microscopy to quantify the type and volume fraction of tertiary phases and intermetallic compounds. Time-Temperature-Transformation-Corrosion maps were constructed by quantifying the changes in pitting corrosion resistance caused by the precipitation of incremental amounts of deleterious phases. Results showed that 2.1 wt% W additions retarded the precipitation kinetics of all tertiary phases—including σ-phase—favoring the formation of χ-phase. Both χ- and σ-phase affected corrosion resistance, reducing the critical pitting temperature by 10 °C–20 °C at concentrations well below 1 vol%.
 [DOI: 10.1149/1945-7111/ab90af]

Manuscript submitted March 30, 2020; revised manuscript received May 4, 2020. Published May 15, 2020.

It is well established that the localized corrosion resistance of stainless steels can be improved by alloying with Cr, Mo, and N.[1–4] Lorenz and Medawar[5] and later Truman[6] proposed an empirically derived parameter referred to as Pitting Resistance Equivalent (PRE) to correlate the observed localized corrosion resistance of stainless steels with composition (Eq. 1). In Eq. 1, the sub-index N indicates that the original PRE formula proposed by Lorenz and Medawar was modified to include N.[7]

$$\mathrm{PRE_N} = \%\mathrm{Cr} + 3.3\%\mathrm{Mo} + 16\%\mathrm{N} \quad [1]$$

In practical terms, the higher the PRE, the higher the resistance to localized corrosion (pitting and crevice) of the material. However, PRE and similar expressions only consider that alloying elements are in solid solution and ignore the effects of deleterious phases such as chromium carbides and σ-phase, which can precipitate during welding or improper thermomechanical processing.[7–9]

Stainless steels with higher contents of Cr, Mo, and N are required as the corrosivity of the environment increases.[10] Super duplex stainless steels (SDSS) are defined as highly-alloyed stainless steels with a PRE $\geqslant$ 40.[4,11] Currently, according to ISO 21457 and NORSOK M-001, only stainless steels with a PRE $\geqslant$ 40 can be used in natural and chlorinated seawater service.[12,13] Consequently, SDSS are widely used in the Oil and Gas offshore industry[10,14] and in other aggressive environments due to their excellent corrosion resistance and mechanical properties, the latter a consequence of their fine-grained microstructure.[15–17]

Besides Cr, Mo, and N, there are other alloying elements that improve the localized corrosion resistance of stainless steels.[18,19] It has been suggested that tungsten (W) has the same beneficial effect on passivity as Mo.[20–23] Interestingly, W is included in the PRE expression (Eq. 2) in ISO 21457.[12] In Eq. 2, the sub-index W indicates that W was also added to the original PRE expression.

$$\mathrm{PRE_{N,W}} = \%\mathrm{Cr} + 3.3(\%\mathrm{Mo} + 0.5\%\mathrm{W}) + 16\%\mathrm{N} \quad [2]$$

*Electrochemical Society Member.
[z]E-mail: cristian.torres@ntnu.no

However, despite the demonstrated beneficial effects on nickel alloys,[24,25] the role of W on improving the localized corrosion resistance of stainless steels remain controversial.

Effects of tungsten in solid solution.—There are several studies on the effects of W on the localized corrosion resistance of austenitic,[21,23,26–28] ferritic,[29,30] amorphous,[22] duplex,[21,31–34] super duplex[19,35–44] and hyper duplex[45] stainless steels. Although most of these investigations concluded that W improves the corrosion resistance of stainless steels, the mechanisms are still uncertain. Findings showed that, even though pure W does not form a passive layer,[26] the passive film in Fe–Cr stainless steels is improved when W is added as an alloying element.[20,27,30,46] However, this effect is less pronounced than those of Mo, when added to the same stainless steel.[20,30,46]

Researchers found that when Mo is partly substituted by W (i.e., Cr + Mo + W), the corrosion resistance of certain stainless steels further increases, demonstrating a synergetic effect between Cr, Mo, and W.[20,21,28] Additionally, according to published data,[19,31–33,37,38,47] it seems that the maximum beneficial influence of W is achieved when added at about 2–4 wt%; becoming less effective as this quantity decreases or increases and, eventually, becoming detrimental. The influence of W is more noticeable in thermally aged than in solution annealed materials, indicating a strong link between tertiary phase and intermetallic compound (IMC) precipitation kinetics and corrosion resistance.

Effects of tungsten on the precipitation kinetics of deleterious phases.—Highly alloyed stainless steels, such as SDSS, are prone to the precipitation of secondary phases (tertiary phases in the case of (S)DSS as they are dual phase materials) including IMCs, carbides, and nitrides, given their high Cr and Mo content.[4,31,35,48] The most studied deleterious phases in stainless steels are sigma-phase (σ),[1,4,29,32–39,41–45,48–60] chi-phase (χ),[4,29,32,33,36–39,41–43,45] and chromium nitrides (usually as Cr_2N).[4,49,50,58,61–63] As shown in Table I, σ- and χ-phase are rich in Cr, Mo, and W. Several studies have confirmed that σ-phase has the largest Cr enrichment, whereas χ-phase is the richest in Mo and W.[33,36,38,42,43,45,57]

Regarding the effect of W on the precipitation kinetics of deleterious phases, published works suggest that χ-phase is the

Table I. Summary of the most relevant deleterious phases in DSS and SDSS.[2,5,29,32–39,41–45,48–69]

Deleterious phase	Nominal chemical formula	Crystal structure	Temperature range (°C)
Sigma (σ)	Fe–Cr–Mo (W, Mn, Si)	BCT	600–1000
Chi (χ)	Fe–Cr–Mo (W)	BCC	750–850
Nitrides	Cr_2N (CrN, less common)	HCP	700–900

primary secondary phase precipitating in W-rich stainless steels, while σ-phase is predominant in W-free SDSS.[32,37–39,41,42] Furthermore, W shifts the Time-Temperature-Transformation (TTT) curves of all deleterious phases to higher temperatures.[4,34] There is, however, a strong disagreement on the effect of W on σ-precipitation kinetics and the ability of W to reduce the total density of intermetallic precipitates.

Nilsson et al. and Hertzman et al.[36,41] concluded that W additions to stainless steels increased the density of intermetallic phases, both σ- and χ-phase. Wessman et al.[40,64] endorsed these results by means of computational simulations. These findings contrast with Kim and Kwon, Ogawa et al. and others[29,32,33,38,42,43,45] who experimentally showed that W retarded σ-phase precipitation by stabilizing χ-phase, which was later also verified by computational simulations.[34,35]

The main difference in the experimental methods between both positions lies in the heat treatment procedure. In this regard, Nilsson and Hertzman[36,41] investigated a W-free SDSS that was welded with fillers containing varying amounts of W. The samples were isothermally aged after welding. In contrast, Kim, Ogawa and others[29,32,33,38,42,43,45] isothermally treated alloys that contained W as a solid solution element.

An analysis of the results presented by Nilsson et al. and Hertzman et al.[36,41] shows that the deleterious phases nucleated faster in the W-free filler as the isothermal aging time increased in the 800 °C to 950 °C temperature range, surpassing the volume fraction of the W-rich filler at longer times. For example, at 900 °C and 1.5 min of isothermal aging, the W-free filler presented a higher density of precipitates than the W-rich filler. Therefore, it is plausible that χ-phase (mentioned by Nilsson[36] for the case treated at 900 °C and 0.5 min) was present in the W-rich filler at shorter times, delaying σ-phase formation and, thereby, reducing the total density of precipitates at longer aging times. Additionally, Wessman et al.,[40] who computationally verified that W increased tertiary phase precipitation, only considered in the simulations the growth of the intermetallic phases, not their nucleation. Consequently, it is plausible that W does play a role in the nucleation stage, but not during growth.

In contrast, Ogawa et al.[32] simulated the heat affected zone (HAZ) by controlling the heating and cooling rates of a thermal cycle performed on the samples, followed by isothermal aging. Kim and others[29,38,45] isothermally aged the samples, but they used very long aging times (up to 10 h[38]) that are not representative of the typical times involved in, e.g., welding of SDSS.[65] In addition, Park et al.[29] studied a ferritic stainless steel, Jeon et al.[45] tested a hyper duplex stainless steel (HDSS), Ahn et al.[33] focused on lab-prepared DSSs (22Cr) and Ogawa, Lee and Kim et al.[32,38,42] tested lab-prepared SDSSs. Only Akisanya et al.[43] investigated a commercial SDSS.

Correlation between the precipitation of deleterious phases and localized corrosion.—Most of the studies cited above focused separately either on the metallographic characterization of the materials[32–34,36,38,43,44] or on their corrosion properties.[19,21–23,26–28,30] Only a few investigations have linked the corrosion properties to the microstructural characterization.[29,31,37,39,41,45]

Because the precipitation of deleterious phases such as σ -phase is a diffusion-assisted transformation, a Cr-, Mo- and W-depleted zone forms around these precipitates.[4] Depleted zones have a lower localized corrosion resistance than the matrix and the precipitates, facilitating the initiation of localized corrosion in the material.[29,38,39,52–54] Among the IMCs precipitating in stainless steels, σ-phase is considered the most deleterious since it is the richest in Cr and leads to Cr and Mo depleted zones.[39]

Most studies on the effect of IMCs focused on their influence on mechanical properties rather than corrosion. It has been reported, for example, that the impact toughness of (S)DSS starts to decline when the volume of σ-phase exceeds 5–10 vol%.[4,33,43,49,66,67] In contrast, even though all studies agree on that the presence of σ-phase reduces corrosion resistance, very few investigations have reported a critical volume fraction of σ-phase responsible for the decrease in corrosion resistance of (S)DSS. Caluscio dos Santos et al.[54] found a drop in the pitting potential (E_{Pit}) of a 22Cr DSS (UNS S31803) when the volume of σ-phase was higher than 15 vol%. On the other hand, Mathiesen et al.[68] reported that corrosion resistance of DSSs (UNS S31803 and S32750), measured as changes in the critical pitting temperature (CPT), started to deteriorate when the presence of σ-phase was above 2 to 6 vol%. Deng et al.[60] observed a CPT drop of 10 °C when the σ-phase content was about 1 vol%, decreasing by more than 20 °C when the content increased above 5 vol%.

There has been, however, no systematic attempt to correlate and reconcile conflicting views on the effect of W on precipitation kinetics of SDSS and the corresponding influence in localized corrosion resistance. In this work, three SDSS with different W contents were studied, namely, UNS S32750 (W-free), S32760 (0.6 wt% W), and S39274 (2.1 wt% W). Isothermal heat treatments and advanced characterization techniques were used to investigate the role of W in the precipitation kinetics of intermetallic phases. Likewise, changes in pitting corrosion resistance were correlated with the type and volume fraction of deleterious phases. The results were combined in visual Time-Temperature-Transformation-Corrosion (TTC) maps and the implications of the findings discussed using statistical analysis.

Experimental

Materials.—Three commercial SDSS families were studied in this investigation, namely, UNS S32750, S32760, and S39274. The alloys were chosen due to their close chemical composition, except for the varying W content. As seen in Table II, UNS S32750 does not contain W, so it was used as reference material; while UNS S32760 and S39274 had 0.6 and 2.1 wt%. W, respectively. All SDSS were produced as extruded pipes with a 30 mm wall thickness and a 203.2 mm diameter.

Round samples were machined by first extracting long cylinders along the length of the pipe. The thickness of the coin-shaped

Table II. Chemical composition in wt%.

Material (UNS)	$PRE_N/PRE_{N,W}$	C	Si	Mn	Cu	Ni	Cr	Mo	N	W	Fe
S32750	43/43	0.03	0.27	0.51	0.14	6.42	25.6	3.83	0.295	—	62.9
S32760	41/42	0.03	0.50	0.60	0.60	7.1	25.2	3.6	0.254	0.62	61.5
S39274	40/43	0.02	0.24	0.71	0.52	6.3	24.9	3.1	0.29	2.1	61.8

Table III. Isothermal heat treatment temperature-time ($T_x t_y$) combinations.

Temperature (°C)	Time (s)
T1 = 790	t1 = 60
	t2 = 120
	t3 = 240
	t4 = 600
	t5 = 1200
T2 = 846	t1 = 60
	t2 = 90
	t3 = 120
	t4 = 240
	t5 = 600
	[a)]t6 = 1200
T3 = 920	t1 = 60
	t2 = 120
	t3 = 240
	t4 = 600
	t5 = 1200

a) heat treatment only performed in UNS S39274 for the TEM analyses due to the low density of tertiary phases present at lower times.

specimens was 3 mm and the diameter 25 mm for UNS S32750 and S32760 and 30 mm for S39274. Unless specified otherwise, all tests were performed in duplicate.

Heat treatments.— *Solution annealing (SA).*—Even though the pipes were received in the solution annealed condition, all samples were re-solution annealed at 1100 °C for 15 min in an air furnace and rapidly quenched in water according to the recommendations of the alloy suppliers. SA was performed to remove all possible undesirable phases, and to ensure the homogeneity of the microstructure. Light optical microscopy (LOM) and electron backscatter diffraction (EBSD) measurements—performed as described below—showed that the average ferrite and austenite volume fractions were within the specified range, namely, 57–43, 60–40, and 48–52 vol%, for the UNS S32750, S32760, and S39274 SDSS, respectively.

Isothermal heat treatments (IHT).—Isothermal aging was carried out on the SA samples in an air furnace followed by quenching in water. The isothermal aging conditions were chosen based on the work by Nilsson et al.[4] Table III summarizes the selected time and temperature combinations. The highest temperature (T_3 = 920 °C) was chosen to avoid χ-phase precipitation, which is critical to examine the independent effect of σ-phase. The intermediate temperature (T_2 = 846 °C) was chosen to achieve a rapid σ-phase precipitation as reported for SDSS.[4] Lastly, a larger density of χ-phase was expected[4] at the lowest temperature (T_1 = 790 °C), which helped emphasize and separate its impact from the other precipitates. T1, T2, and T3 represent the actual temperature measured on the samples to which a K-type thermocouple was attached during each IHT.

The specimens were introduced in the furnace after reaching the set-temperature. Only two coin-shaped samples were included per IHT batch to minimize the thermal mass introduced into the furnace. Additionally, handling two specimens at the time reduced the handling time and ensured that the furnace door was open for a very short time. The temperature was recorded by attaching a thermocouple to one of the samples. The temperature drop observed immediately after introducing the specimens was under 10 °C, and it took less than 1 min for the coupons to reach the target temperature.

Changes in the austenite and ferrite volume fractions caused by IHT were also measured by LOM and EBSD as detailed below. The austenite and ferrite content remained in the accepted range for SDSS, i.e. 40–60 vol% for all materials.

Sample preparation.— *Polishing.*—After IHT, the samples were wet-ground and polished down to 1 μm diamond suspension to obtain a mirror-like surface finish. Afterwards, the samples were rinsed with acetone, followed by rinsing with distilled water and cleaned with ethanol in an ultrasonic bath for 5 min.

Etching.—Samples analyzed with LOM, scanning electron microscopy (SEM), and energy-dispersive X-ray spectroscopy (EDS) were etched following Statoil technical note MAT-2010080[69] to facilitate the identification of tertiary phases during the sample characterization stage described below. The etching procedure consisted of two steps. In the first step, a 15 wt%. KOH solution was used, and a potential of 3 V applied for 12 s. In the second step, the solution was 20 wt%. NaOH with an applied potential of 1.5 V for 10 s.

Electropolishing.—Only for those samples analyzed with EBSD, extra surface preparation steps were followed after polishing to remove the deformation structure left by abrasive polishing, which is known to affect EBSD results.[70] After the 1 μm diamond particle polishing, the samples were electropolished using a solution of 5.3 vol% H_2SO_4–94.7 vol% methanol at 18 V for 30 s; followed by a final polishing step using an oxide polishing suspension (OPS) of a 0.02 μm colloidal silica.[71,72]

Transmission electron microscopy specimens.—The various types of precipitates were further analyzed by transmission electron microscopy (TEM), high-resolution (HR) TEM, scanning transmission electron microscopy (STEM), TEM-EDS, and selected area electron diffraction (SAD). Thin foils were prepared via focused-ion beam (FIB) milling using a Tescan Lyra dual beam FEG SEM platform from the UNS S32750 and S39274 samples treated at T2 for t4 and at T2 for t6, respectively. Detailed information on the sample preparation by FIB can be consulted elsewhere.[73,74]

Sample characterization.—Different microscopy techniques were employed to characterize the microstructure of the samples after the isothermal aging, as follows.

Light optical microscopy.—An infinite focus microscope (IFM) was used with magnifications that varied between 10× and 50× to observe the overall sample microstructure, i.e., austenite (γ), ferrite (α), and the presence of deleterious phases.

Back scattered electron (BSE) imaging.—All the samples were investigated using SEM in the BSE imaging mode. BSE was chosen as it is more sensitive to variations in composition, facilitating the identification of different phases. In this regard, heavier elements (e.g., W) appear brighter while lighter elements appear darker in BSE images.[4,36,75] The electron beam was used with an acceleration voltage of 20 kV, with a 30 μm diameter aperture and a spot size of 3, resulting in a beam current of approximately 0.16 nA.

Energy dispersive X-ray spectroscopy.—Once the tertiary phases were located by BSE imaging, their chemical composition was analyzed by EDS. The electron beam was changed to an accelerated voltage of 20 kV, with a 50 μm diameter aperture and a spot size of 5, giving a beam current of approximately 7.2 nA. The point analysis tool was used to acquire the composition of only the deleterious phase and not the surrounding area. At least 10 points were taken per phase. EDS results were compared as a function of IHT temperature and time. Nevertheless, since the actual depth and area affected by the electron beam are unknown, the composition obtained by SEM-EDS was regarded as qualitative. Consequently, a definite conclusion could not be drawn by EDS alone as the variance of some of the

results was considerable, particularly for small (<1 μm) deleterious phases.

Electron backscatter diffraction.—Volume fraction calculations of the different phases were obtained from the EBSD maps. All analyses were performed at an 800× magnification to ensure an area large enough to compare between samples. The electron beam was used with an acceleration voltage of 20 kV, with a 50 μm diameter aperture and a spot size of 5, resulting in a beam current of approximately 7.2 nA. The acquisition settings consisted of a frame rate of 40 fps, a resolution of 256 × 256 px and an exposure time of 24500 μs. The confidence index (CI) obtained was always higher than 0.1.

Transmission electron microscopy.—Bright-field (BF), high-resolution (HR) TEM and STEM were conducted using a FEI Talos FS200X G2 field emission gun (FEG) TEM operating with an electron beam at 200 kV acceleration voltage. Samples were tilted to a prominent zone axis with a double tilt holder and the selected area the diffraction pattern was obtained with a high-resolution camera. The SAD patterns were obtained using a 200 nm diameter aperture for selecting the area of interest, indexed manually and compared to the literature to confirm the crystal structure of the phases identified by EBSD. Additionally, the chemical composition of the precipitates was obtained in STEM mode using EDS mapping. EDS was conducted using two pairs of FEI Super X detectors. The EDS and STEM data were acquired and analyzed with Velox software.

Corrosion testing—critical pitting temperature.—Once the tertiary phases were identified and quantified for each sample, corrosion tests were carried out to evaluate the impact of the deleterious phases on the pitting corrosion resistance of the materials. Isothermally aged specimens were freely exposed in a 6 wt% $FeCl_3$ environment (pH = 1.2) while the temperature was increased in steps.[19,76] The surface exposed to the electrolyte (12.1 cm^2 for UNS S32750 and S32760, and 16.9 cm^2 for UNS S39274) was polished down to a 1 μm diamond suspension as explained above. The specimens were suspended using a 200 μm Pt wire to avoid crevice corrosion.[19] A small hole, approximately 2 mm in diameter, was drilled on the sample to pass the Pt wire. Then, the full sample was immersed in the electrolyte. If signs of crevice corrosion were found after testing, the sample was discarded, and the experiment repeated.

The tests started at 40 °C and the temperature was increased 5 °C every 24 h until observing localized corrosion. Between steps, the temperature was increased as quickly as possible. The temperature was controlled using a hot plate and kept within ±1 °C at each step. The open circuit potential (OCP) was monitored during exposure and used as an indication of pitting corrosion initiation, as explained elsewhere.[19,77] Mathiesen et al.[77] reported localized attacks on SDSS samples once the OCP decreased below +500 mV vs standard calomel electrode (SCE). Hence, this value was arbitrarily chosen as the threshold to define the CPT.

After exposure, samples were analyzed with IFM and SEM to document the location of the localized corrosion attacks. All corrosion tests were conducted in duplicate to verify reproducibility.

Statistical analysis.—Given the large number of conditions, statistical analysis was performed to evaluate whether the influence of the heat treatments and alloy composition on CPT values was significant. The statistical analysis considered two factors: (i) the type of material (i.e., UNS S32750, S32760, and S39274) and (ii) the isothermal heat treatment condition (i.e., the 15 different temperature-time combinations shown in Table III). Since each corrosion test was carried out in duplicate, a two-way ANOVA with replication[78,79] was chosen as the statistical tool to determine if there were significant differences between the three materials, the different heat treatments, or both with a 95% confidence (i.e., a p-value lower than 0.05).

Unfortunately, the ANOVA test cannot be used to determine the specific materials or heat treatments that result in the statistically significant differences in CPT. Hence, further analyses using the so-called Post-Hoc tests were required. Post-Hoc tests perform pairwise comparisons between different groups of the factors studied in the ANOVA. The goal of the Post-Hoc tests is to identify the group(s) that lead to a significant difference. A type I error, i.e., concluding that there is a significant difference when there is none, is a common issue that might appear when performing multiple comparisons using the same dataset. This is because a type I error (5% for p-values equal to 0.05) gets added for each comparison performed in the same dataset. Consequently, if enough comparisons are carried out, the type I error could reach 100% and, hence, cause a wrong result in the Post-Hoc test. For this study and given the large number of multiple comparisons, the Bonferroni test was chosen.[80] The Bonferroni test was developed to avoid data incorrectly appearing as statistically significant (type I error).[80] The Bonferroni analysis included a correction to the p-value, which consists of dividing the p-value (i.e., the type I error) by the total number of comparisons performed to the data. Thereby, the type I error for the total number of pairwise comparisons was 5%. The Bonferroni test has been, nonetheless, criticized for being overly conservative.[81] Thus, a second Post-Hoc test referred to as Tukey test[82] was also performed and the results compared with the Bonferroni approach. In contrast to the Bonferroni method, the Tukey approach used the so-called Honestly Significant Difference (HSD) parameter. The HSD test compares the differences between "means of values" rather than comparing pairs of values. The parameter HSD is calculated from the ANOVA result as shown elsewhere.[82] Thereby, if the averages of the conditions being compared differ by more than the HSD, the difference between them is considered significant. An example of the calculation can be consulted elsewhere.[79]

Results

Phase identification and microstructure evolution.—In light optical micrographs, σ- and χ-phases appeared, in most cases, as dark spots or small blue areas at the γ/α interfaces. Figure 1 illustrates the precipitation of tertiary phases in different conditions, as indicated by the arrows. In Fig. 1, bright and dark phases correspond to austenite and ferrite, respectively.[51,54,83–85]

Figures 2 to 4 present a series of BSE images that summarize the structures of the three SDSS samples at different IHT conditions, as indicated. The γ and α phases were identified from their relative bright and dark contrasts and checked later by EBSD phase identification. Deleterious phases appeared brighter than both matrix phases, indicating an enrichment of heavy elements in their composition.[4,36,75] In this regard, BSE imaging has been proposed as a reliable method to identify χ-phase given its higher W content.[4] In all cases, the amount and size of precipitates increased with higher temperature and longer aging times. In Figs. 2 and 3 (UNS S32750 and S32760, respectively), the precipitates preferentially grew from the γ/α interface into the α grains as the IHT time increased. In contrast, in Fig. 4 (UNS S39274), the density of precipitates increased at γ/α interfaces and, ultimately, precipitation occurred inside the α grains.

As seen in Figs. 5a–5c, there were two predominant phases precipitating in all three materials. One phase was brighter and smaller, whereas the second phase was larger and duller than the other phase, but still brighter than the matrix. The latter precipitate appeared in higher quantities in UNS S32750 and S32760, whereas the former was the main phase nucleating in S39274. Both phases formed at γ/α interfaces. At longer isothermal aging times, the bright phase nucleated inside the α grains as well, whereas the duller one grew from the grain boundaries into the α grains as seen in Fig. 5d.

Table IV summarizes the average chemical composition obtained by EDS of every phase observed in the BSE for the three SDSSs. The main differences were in their Mo and W (for those materials containing W) content. All tertiary phases (σ and χ) were richer in

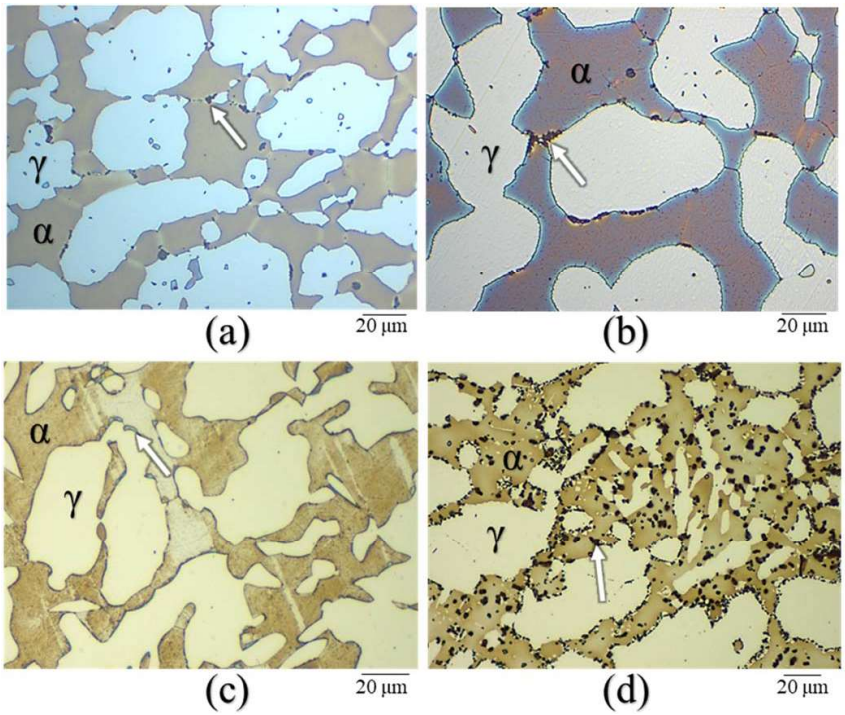

Figure 1. Light optical microscopy after isothermal aging (a) UNS S32750 at 846 °C for 240 s, (b) UNS S32760 at 920 °C for 240 s, (c) UNS S39274 at 846 °C for 600 s and (d) UNS S39274 at 920 °C for 1200 s. White arrows point at deleterious phases. Bright and dark phases correspond to austenite and ferrite, respectively.

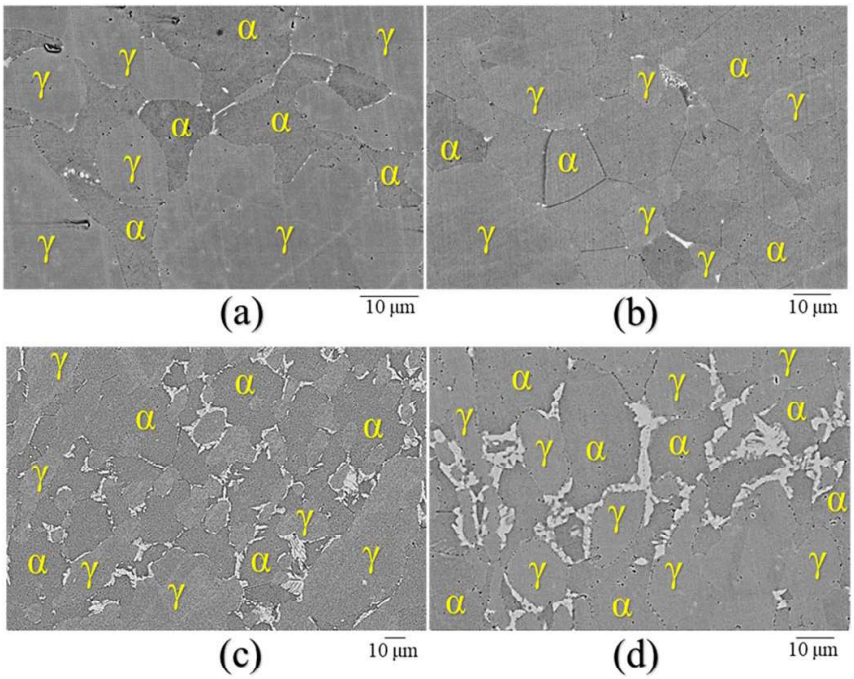

Figure 2. Scanning electron microscopy after isothermal aging of UNS S32750 at (a) 790 °C for 600 s, (b) 846 °C for 240 s, (c) 846 °C for 600 s and (d) 920 °C for 600 s.

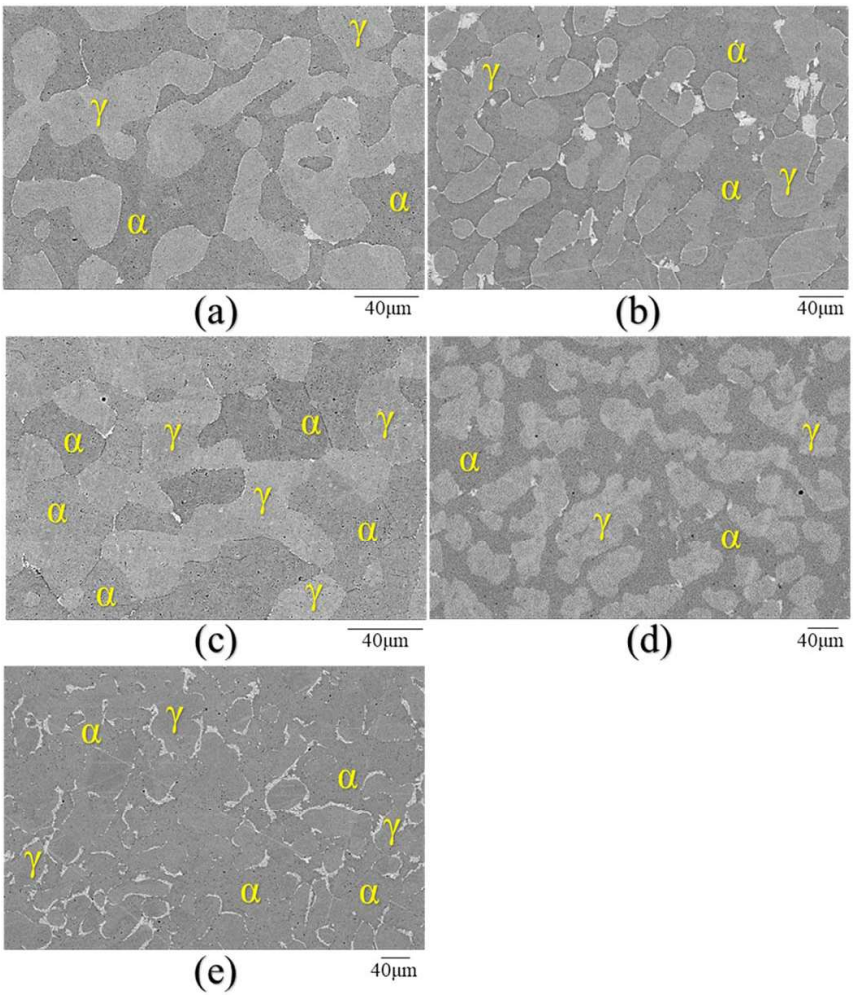

Figure 3. Scanning electron microscopy after isothermal aging of UNS S32760 at (a) 790 °C for 600 s, (b) 790 °C for 1200 s, (c) 846 °C for 240 s, (d) 920 °C for 240 s and (e) 920 °C for 600 s.

Cr, Mo, and W than the matrix (i.e., α and γ). In the case of the W-free SDSS, χ-phase was enriched only in Mo, while σ-phase had a higher Cr and Mo content than both γ and α. For the samples containing W, both tertiary phases were also enriched in W relative to the matrix. These findings confirmed that bright precipitates were χ-phase, while the other particles were σ-phase.[4,36] These results were consistent across all the samples investigated in this study.

EBSD results validated the SEM-EDS analysis. Figure 6 shows the main phases that precipitated in UNS S32760 and S39274 after isothermal aging, as indicated. σ-phase precipitated after short IHT times (i.e., 120 s) in both UNS S32750 and S32760. The size and amount of σ-phase increased with the duration of the IHT. While σ-phase was predominant in UNS S32750 and S32760, χ-phase was the main phase found in S32794. In fact, σ-phase was only detected in UNS S39274 after long (i.e., 1200 s) isothermal aging times and in very small quantities.

TEM was used to confirm EBSD results. Figures 7 to 10 show HR-TEM images, SAD patterns, and STEM-EDS data of the tertiary phases in the UNS S32750 and S39274 samples, respectively. The HR-TEM image and SAD pattern of the intergranular precipitate in the S39274 (Fig. 7) sample were consistent with the BCC χ-phase structure.[86] The corresponding chemical composition analysis of χ-phase in Fig. 8 showed a high Cr and Mo content, but no clear enrichment in W. This lack of a clear W enrichment was attributed to an experimental limitation, as EDS did reveal a clear W enrichment in larger precipitates. The higher W content leads to a brighter region in BSE SEM images. This difference in brightness was used to differentiate between χ and σ as explained by Jackson et al.[75] Furthermore, it was possible to qualitatively observe the depleted zone between both phases, i.e., a small area which was poorer in Cr and Mo adjacent to χ-phase as indicated, although no clear W gradient was found. Similarly, the SAD pattern obtained from the UNS S32750 tertiary phase (Fig. 9) was in good agreement with the tetragonal crystal structure of σ-phase.[87] The chemical analysis in Fig. 10 confirmed the Cr and Mo enrichment of the σ-phase. The formation of secondary austenite (γ_2) was verified as well by its low Cr and Mo content and the relative Ni enrichment.[55] Additionally, a nanosized phase rich in Cr and N was observed within σ-phase. Given its chemical composition, the phase was consistent with Cr_2N commonly found in SDSS.[4,48,57,61]

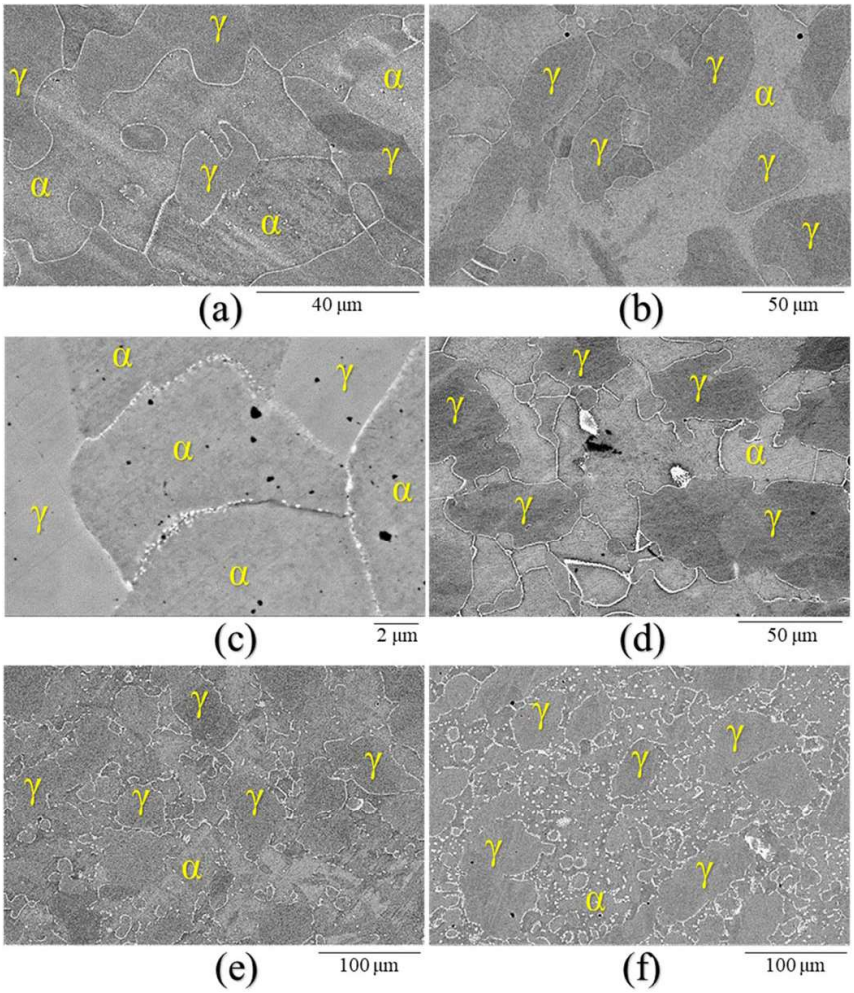

Figure 4. Scanning electron microscopy after isothermal aging of UNS S39274 at (a) 790 °C for 600 s, (b) 790 °C for 1200 s, (c) 846 °C for 240 s, (d) 846 °C for 600 s, (e) 920 °C for 600 s and (f) 920 °C for 1200 s.

Phase quantification.—Once the deleterious phases were identified, their volume fractions were measured for each IHT condition. Although EBSD analysis can provide the volume fraction of each phase directly, unfortunately, it failed to distinguish between α and χ-phase unambiguously as both have a BCC crystal structure. Thus, only the vol% of γ and σ-phase could be measured directly from the EBSD results. The α and χ-phase were quantified together as the sum of both phases. Subsequently, an open-access image processing software was used to obtain the total vol% of all deleterious phases from the BSE SEM pictures. The phase quantification was achieved by filtering the deleterious phases that appeared brighter in these BSE pictures from the background (γ and α). The χ vol% was quantified by subtracting the total vol% of deleterious phases from the σ vol% determined by EBSD. Lastly, once the amount of χ-phase was known, the α vol% could be obtained from the EBSD results. At least ten pictures of each microscopy technique were used for each IHT condition.

Corrosion testing.—Figure 11 illustrates an example of the pitting corrosion test results for the three SDSS in identical IHT conditions, whereas Fig. 12 shows the CPT values obtained for all specimens as a function of IHT time and temperature, as indicated. CPT values decreased with isothermal aging time for all samples at all temperatures, falling faster for UNS S32760, S32750, and S39274, in order. The decline in the CPT values was faster at 846 °C for all three materials. In all instances, localized corrosion started at the interface between the matrix and the different precipitates, as illustrated in Fig. 13.

Temperature–time–transformation-corrosion diagrams.—TTTC diagrams were constructed for each alloy considering the average vol% of the deleterious phases and the lowest CPT result for each condition, as illustrated in Figs. 14 to 16. Each point in the TTTC plots was drawn according to the type of microstructure observed, as follows. (i) An empty circle indicates no tertiary phase precipitation (within the resolution limits of the techniques used herein), i.e., the microstructure was similar to the SA sample; (ii) a half-full circle indicates that either (a) precipitates were found but their amount was small, and no quantitative identification was possible or (b) both types of precipitates (σ and χ) were present in small but similar quantities; (iii) a circle with a cross inside indicates that the main tertiary phase was χ-phase and, finally, (iv) a full black circle indicates that the main

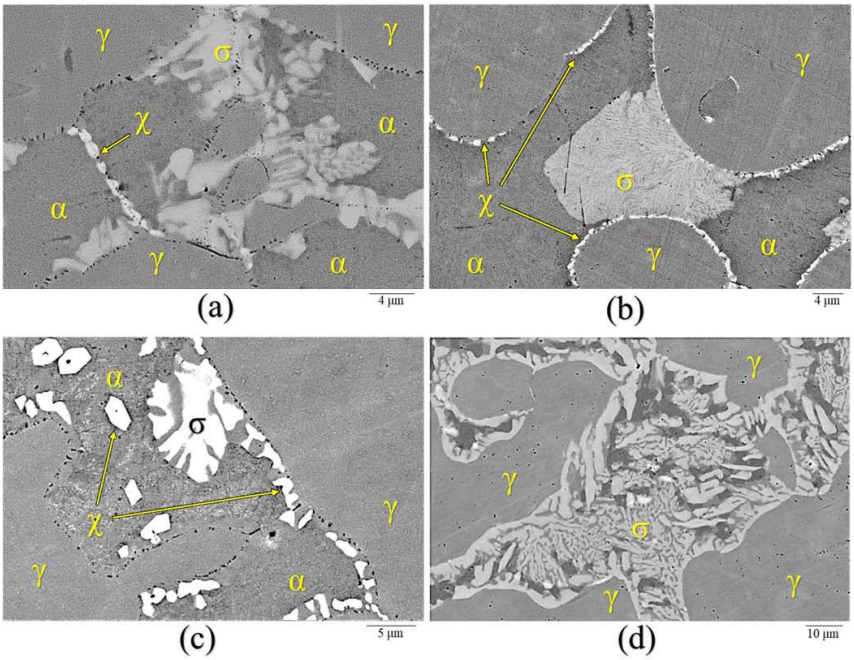

Figure 5. Scanning electron microscopy after isothermal aging of (a) UNS S32750 at 846 °C for 600 s, (b) UNS S32760 at 790 °C for 1200 s, (c) UNS S39274 at 920 °C for 1200 s and (d) UNS S32760 at 920 °C for 1200 °C.

Table IV. Average chemical composition of each phase in wt%.

Material (UNS)	Phase	Fe	Cr	Ni	Mo	W
S32750	Ferrite (α)	63.9	28.1	4.6	3.6	—
	Austenite (γ)	64.9	25.2	7.5	2.3	—
	Sigma (σ)	59.0	30.0	4.4	6.4	—
	Chi-phase (χ)	56.0	28.9	3.7	11.5	—
S32760	Ferrite (α)	62.2	27.0	5.3	3.1	0.75
	Austenite (γ)	63.3	23.9	8.3	2.1	0.6
	Sigma (σ)	57.7	29.9	4.4	5.2	1.0
	Chi-phase (χ)	53.9	27.2	4.3	10.8	2.1
S39274	Ferrite (α)	63.5	26.4	4.7	2.9	2.5
	Austenite (γ)	64.7	24.1	7.3	1.9	1.9
	Sigma (σ)	55.2	29.7	3.7	6.6	4.5
	Chi-phase (χ)	52.0	25.2	3.7	10.8	9.5

precipitate was σ-phase. The volume fraction of the phase calculated from the microscopy techniques was included below the circle, whereas the CPT value was added on top. In the case when the phases could not be successfully identified, the total volume fraction was reported together as the sum of all precipitates. In this manner, all data is gathered in the same plot, facilitating a visual and straightforward analysis.

Statistical analysis.—Table V shows the results of the ANOVA calculations. The p-value obtained for the interaction between the materials and the heat treatments was lower than 0.05, meaning that there was a statistically significant difference on the CPT values as a function of composition and heat treatment condition. Consequently, the Pot-Hoc tests were carried out to find the specific significant difference in CPT values

Both Post-Hoc tests yielded similar results for each pairwise comparison between the two factors. The first part of the tests consisted of pairwise comparisons between isothermal aging times within each material and temperature to find if a significant difference in the CPT values existed. The results are summarized in Table VI. UNS S32750 and S32760 showed that the CPT change was significantly different at the same aging times for the three different aging temperatures. On the other hand, UNS S39274 experienced a significant CPT drop at longer IHT times at 846 °C, whereas the drop occurred at the same IHT time at 790 °C. The significant drop obtained at 920 °C, although logical since it was a drop of 15 °C, cannot be compared with the other two alloys since the corresponding CPT was 60 °C, much higher than for the other two materials.

Table V. Results obtained from two-way ANOVA with replication of CPT values. (SS: sum of squares, df: degrees of freedom, MS: mean square).

Source of variation	SS	df	MS	F-ratio	P-value
Factor A: Material	1007	2	504	64.8	$5.2 \cdot 10^{-14}$
Factor B: Heat treatment	15132	14	1081	139.0	$3.5 \cdot 10^{-32}$
Interaction: Material * Heat treatment	1059	28	37.8	4.9	$1.4 \cdot 10^{-6}$
Error (within)	350	45	7.8		
Total	17549	89			

The second part of the Bonferroni and Tukey tests consisted of a pairwise comparison of each heat treatment condition between the three materials. Table VII shows the heat treatments that exhibited statistically significant differences between different materials. UNS S32750 and S32760 were only significantly different at one heat treatment (790 °C, 240 s). In contrast, S39274 was significantly different from the other two materials at two different heat treatments, namely, 846 °C, 240 s and 920 °C, 600 s.

Discussion

Precipitation kinetics.—Many publications[4,31,37,42,43,45,48,51,55–57] report that the precipitation of both σ- and χ-phase starts at the γ/α interface, similar to what has been observed in this work. The mechanism by which σ-phase precipitates has been described as an eutectoid reaction[51,55,59] (Eq. 3) where ferrite (α) splits into σ-phase and a γ_2, which has a lower Cr and Mo content than in the original γ-phase.[4,55,88] The α-stabilizing elements, such as Cr and Mo, form σ-phase, while the austenite stabilizing elements like Ni diffuse out, leading to the formation of γ_2. On the other hand, the austenite stabilizers are enriched in the γ_2, while the α stabilizers are expelled helping the growth of σ-phase.[55] This reaction gives σ a lamellar structure, which can be seen in Figs. 5a–5c. Even though the lamellar eutectoid morphology has been described only for temperatures under 900 °C[55]; in this work, lamellar eutectoid σ-phase formation occurred as well at 920 °C for UNS S39274 as shown in Fig. 5c. For the other SDSS, γ_2 developed below 900 °C, whereas above 900 °C σ-phase precipitation followed the divorced eutectoid mechanism described by Kobayashi et al.[55] and illustrated in Fig. 5d. This difference in the temperature range can be explained by the fact that W shifts the TTT curves to higher temperatures.[4,34] Therefore, it is reasonable to expect that the eutectoid σ-phase reaction occurred above 900 °C if the material contained enough W. In the case of UNS S32760, it seems that 0.6 wt% W was insufficient to affect the phase precipitation mechanism.

$$ferrite(\alpha) \rightarrow sigma(\sigma) + secondary\ austenite\ (\gamma_2) \qquad [3]$$

Another consequence of the shift of TTT curves caused by W is that the fastest precipitation kinetics takes place at higher temperatures, explaining why both W-rich materials had a higher density of intermetallic phases at 920 °C than the W-free UNS S32750. In contrast, the largest amount of precipitates was found at 846 °C for the W-free SDSS.

The main difference between the materials was, however, the effect of high-W additions (i.e., 2.1 wt%) on σ- and χ-phase precipitation. In this regard, while σ-phase was the main IMC present in UNS S32750 and S32760, χ-phase was almost the exclusive tertiary phase in S39274. Indeed, depending on the IHT condition, χ -phase precipitation inhibited or retarded the nucleation of σ-phase and decreased the total amount of deleterious phases.

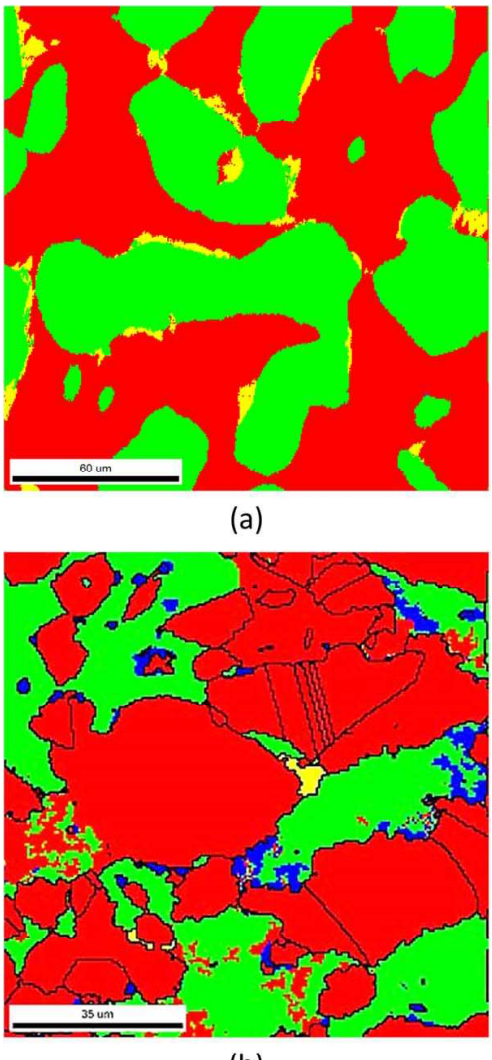

Figure 6. EBSD map of heat treated (a) UNS S32760 at 846 °C for 1200 s and (b) UNS S39274 at 920 °C for 1200 s (red = austenite, green = ferrite, blue = chi, yellow = sigma).

Table VI. Heat treatment times at which CPT was significantly different (p-value < 0.05) for each IHT temperature and material according to Bonferroni and Tukey tests.

	Heat treatment				
Material (UNS)	T (°C)	t (s)	CPT (°C)	CPT drop (°C)	Secondary phases (vol%)
S32750	790	600	<40	>30	0.2% σ, 0.1% χ
	846	240	50	20	0.3% σ
	920	600	45	25	3.1% σ, 0.1% χ
S32760	790	600	<40	>15	0.9% σ, 0.4% χ
	846	240	45	20	0.2% σ, 0.2% χ
	920	600	<40	>20	5.1% σ, 0.3% χ
S39274	790	600	50	10	0.11% χ, 0.03% σ
	846	600	<40	>15	1.4% χ, 0.3% σ
	920	240	60	15	0.6% χ

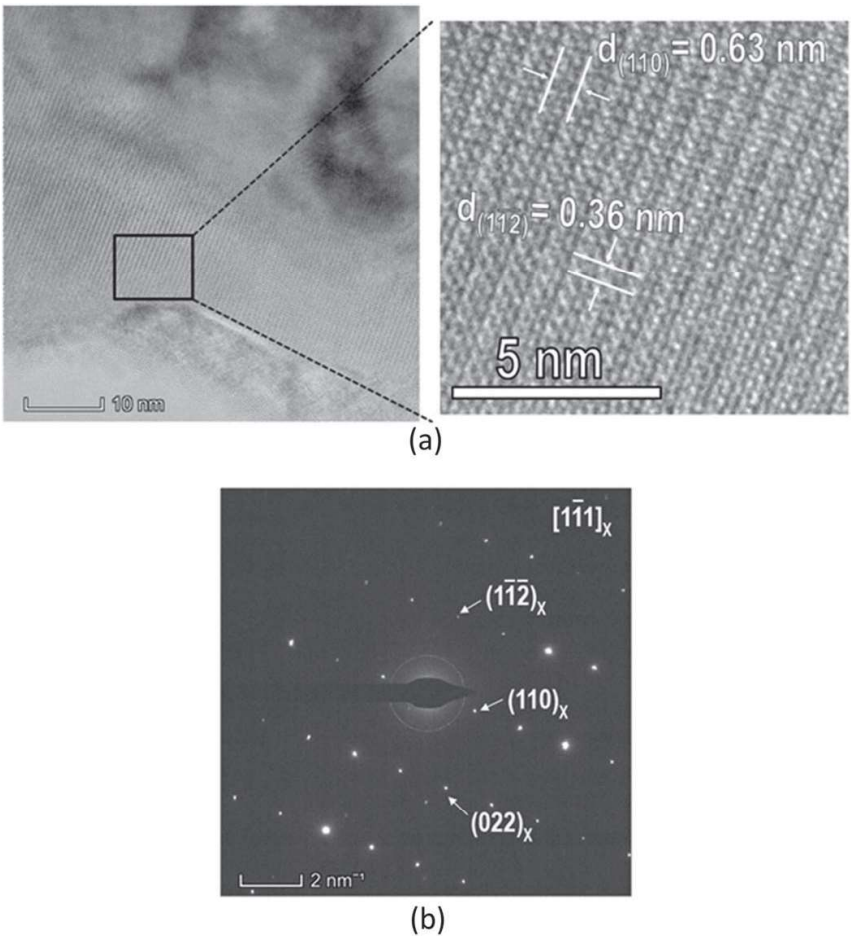

Figure 7. TEM analysis of χ-phase precipitate formed in UNS S39274 steel treated T2 for t6. (a) HR.TEM and (b) indexed SAD pattern of the χ-phase parallel to the [1$\bar{1}$1] zone axis.

Although the retardation of σ-phase precipitation kinetics by χ-phase has been attributed to the high W content, the mechanisms are unclear.[23,26,32,42,89] Some authors[32,37,39,41,42] have reported that, while stainless steels based on Fe–Cr–Mo promote σ-phase precipitation, χ-phase nucleates when Mo is partly substituted by W (Fe–Cr–Mo–W), slowing the kinetics of the σ-phase precipitation down. It has been suggested that the decomposition of α into σ (as shown in Eq. 3) is delayed given the much slower diffusion of W in ferrite than Mo.[32,42,90–93] In this regard, some researchers[42,90] have reported that Mo diffusivity in α was one order of magnitude faster than W, whereas others[32,91–93] obtained diffusivities two to three times slower for W compared to Mo. Consequently, α is stable longer when the alloy contains W and this undiffused W favors, instead, the nucleation of χ-phase.[42] Another explanation proposed by Ogawa et al. and Lee et al.[35,42] is that the interfacial energy between χ-phase and α is lower than that between σ-phase and α since χ and α both have BCC structures, while σ is tetragonal. Once χ-phase precipitates first, σ is delayed as the nucleation sites are occupied, i.e., there is not enough Cr and Mo to precipitate σ-phase.[32,38,45]

In this study, σ-phase was the predominant tertiary phase that nucleated in UNS S32760 despite its 0.6 wt%. W, suggesting that the W concentration was small to affect precipitation reactions. Results also suggested that there exists a W-content range where χ-phase becomes predominant, delaying σ-phase formation. Moreover, given that UNS S32760 exhibited the highest density of total deleterious phases in almost all the temperature-time combinations, W could become detrimental outside the suspected optimal range.

Pitting corrosion resistance.—The difference in precipitation kinetics resulted in a difference in the degree of corrosion attack. In the specimens where σ-phase was the main deleterious phase, the attack occurred in the γ_2 regions, as seen in Fig. 13b. In contrast, in samples where χ-phase was the primary precipitate, localized corrosion initiated at the χ-phase/matrix interface. Since χ-phase formed predominantly at grain boundaries, intergranular corrosion occurred on those specimens with a large vol% of χ-phase (Fig. 13c). Pitting corrosion was observed in the SA samples, which occurred predominantely in the austenite regions and in some ferrite grains, as illustrated in Fig. 13a.

CPT values decreased with isothermal aging due to the higher density of tertiary phases in the microstructure as the TTTC maps (Figs. 14 to 16) illustrate. As seen in Table VI, UNS S32750 and S32760 experienced the statistically significant CPT drop at the

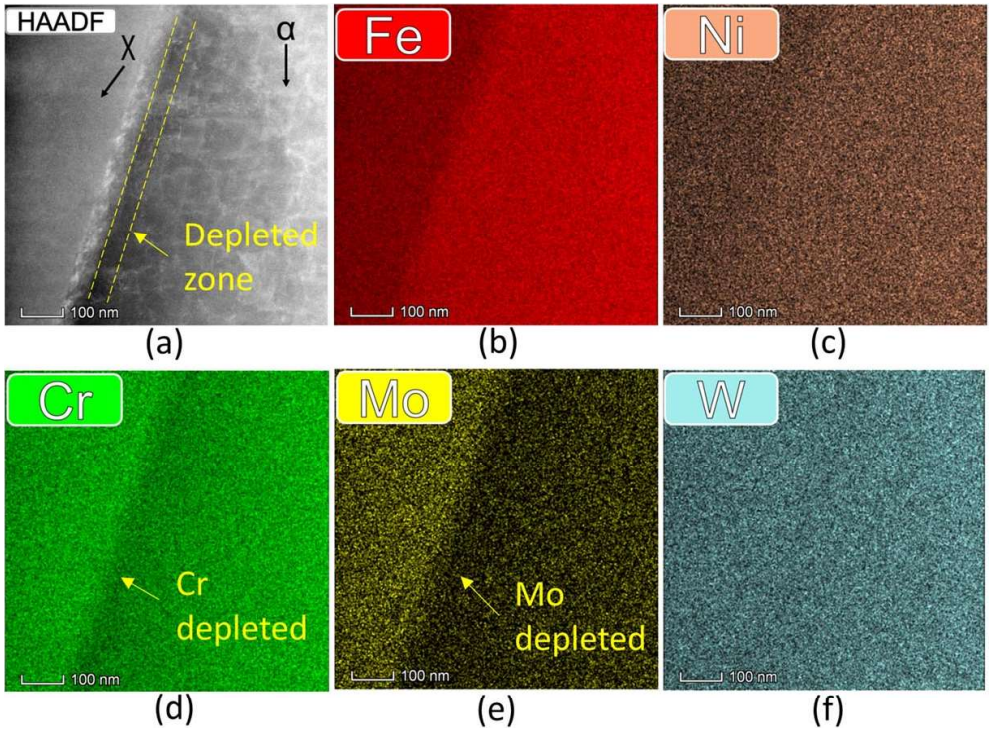

Figure 8. STEM images and elemental maps from EDS maps of χ-phase and α, as indicated. (a) HAADF image and (b) Fe, (c) Ni, (d) Cr, (e) Mo, and (f) W maps. TEM specimen extracted from UNS S39274 steel treated T2 for t6.

Table VII. Heat treatments showing statistically significant differences (p-value < 0.05) in CPT values depending on the material according to Bonferroni and Tukey tests.

Heat treatment T (°C), t (s)	Materials (UNS)	CPT (°C)	Secondary phases (vol%)
790, 240	S32750	65	No precipitates found by SEM
	S32760	55	0.04%
846, 240	S32750	50	0.3% σ
	S39274	65	0.04% χ
846, 240	S32760	45	0.2% σ, 0.2% χ
	S39274	65	0.04% χ
920, 600	S32750	45	3.1% σ, 0.1% χ
	S39274	55	1.72% χ, 0.3% σ
920, 600	S32760	<40	5.1% σ, 0.3% χ
	S39274	55	1.72% χ, 0.3% σ

same aging times for the three different aging temperatures. Those aging times corresponded to CPT values decreasing to below 40 °C and, for UNS S32750, involved a large difference from the previous CPT value. In contrast, UNS S39274 showed moderate CPT drops, as the CPT slowly decreased with IHT time (Fig. 16). As a result, S39274 had more statistically significant differences (p-value $<$ 0.05) with the other two SDSS as showed in Table VII.

The reason for the gradual decrease in CPT with vol% of precipitates observed for UNS S39274 was attributed to the preferential formation of χ-phase instead of σ-phase. The CPT was lower, 10 °C–20 °C depending on the IHT, when σ was the main phase present as seen in Table VII. Because σ-phase is richer in Cr, its precipitation leads to the lowest Cr content in the affected zone adjacent to the precipitates.[29] Consequently, σ-phase has been considered, a priori, the most deleterious IMC in (S)DSS.[29,41] Nevertheless, the presence of χ-phase also affected CPT values apparently to a similar degree than σ-phase when compared at the same volume fraction, which at the same aging temperature implies comparing different IHT times (e.g., Fig. 14 vs Fig. 16).

In all cases, the statistically significant differences in CPT involved only a small total amount of deleterious phases. Indeed, in most situations, the total volume of IMCs was less than 1 vol%, which was lower than the 2–6 vol% localized corrosion threshold reported by Mathiesen et al.[68] and Deng et al.[60]

If instead, the critical volume fraction of deleterious phases is arbitrarily defined according to the conditions at which CPT drops

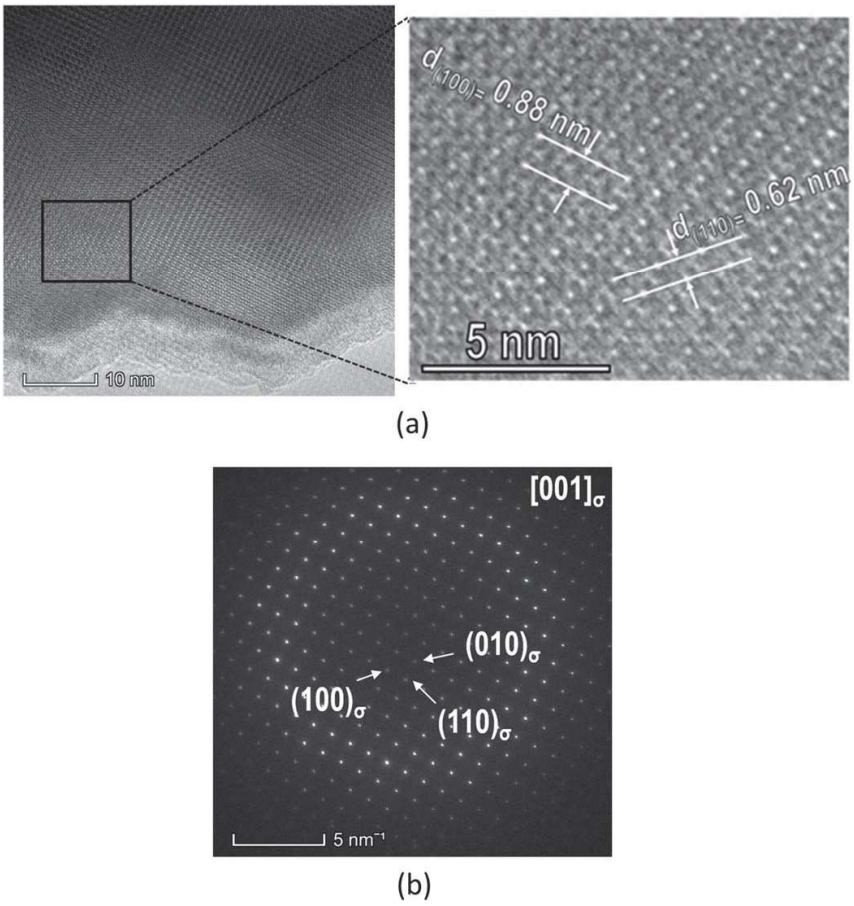

Figure 9. TEM analysis of σ-phase precipitate formed in UNS S32750 steel treated T2 for t4. (a) HR-TEM image and (b) indexed SAD pattern of the σ-phase parallel to the [001] zone axis.

below 40 °C, the quantities of σ- and χ-phase were higher. The volume fraction of tertiary phases that led to a CPT $\leqslant$ 40 °C are gathered in Table VIII for a simpler visualization. The three alloys followed the same trend, i.e., the higher the IHT temperature, the greater the density of intermetallic phases needed to lower the CPT below 40 °C. Furthermore, the same quantity of tertiary phases affected the CPT differently depending on the IHT temperature. For instance, in Fig. 14 there are two different IHT (790 °C, 600 s and 920 °C, 240 s) for UNS S32750 that had completely different CPT values (<40 °C and 70 °C, respectively) although they both contained a similar volume fraction of tertiary phases, i.e., 0.2% σ, 0.1% χ.

Table VIII. Volume fraction of deleterious phases and IHT time at which CPT was below 40 °C for each IHT temperature (values taken from Figs. 14 to 16).

	Heat treatment		
Material (UNS)	T (°C)	t (s)	Critical vol% of deleterious phases
S32750	790	600	0.2% σ, 0.1% χ
	846	600	3.8% σ, 0.3% χ
	920	1200	9.3% σ, 0.1% χ
S32760	790	600	0.9% σ, 0.4% χ
	846	600	2.7% σ, 0.2% χ
	920	600	5.1% σ, 0.3% χ
S39274	790	1200	0.23% σ, 0.21% χ
	846	600	1.4% χ, 0.3% σ
	920	>1200[a)]	>(4.13% χ, 0.8% σ)[a)]

a) CPT was over 40 °C for all IHT times.

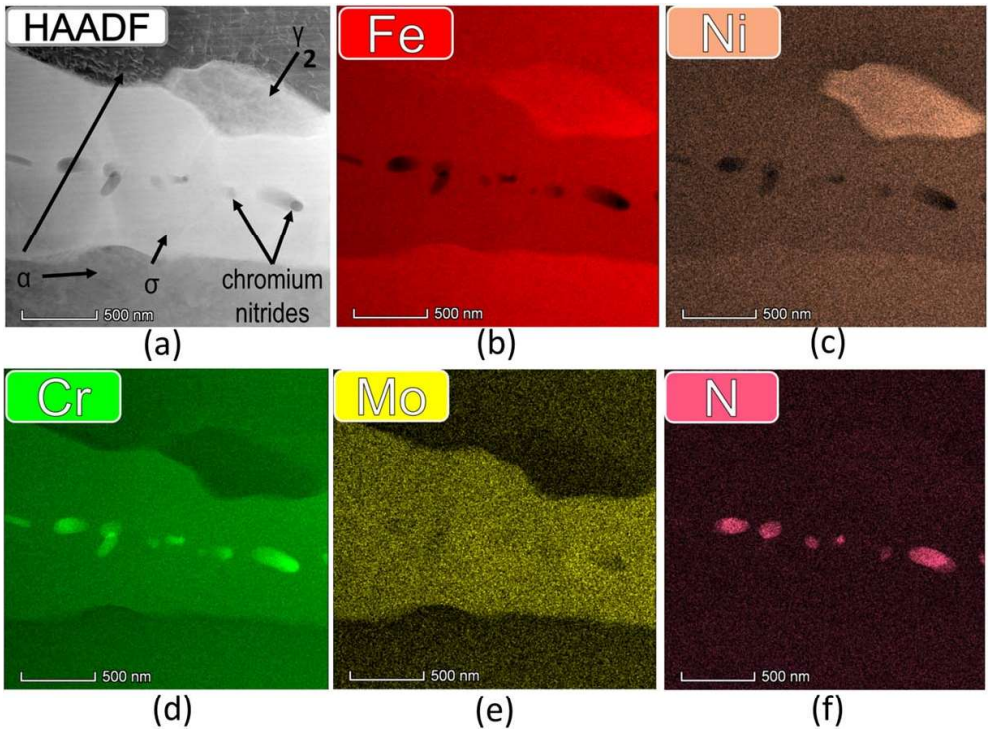

Figure 10. STEM images and elemental maps from EDS spectrum images of σ-phase, chromium nitrides, γ and α, as indicated. (a) HAADF image and (b) Fe, (c) Ni, (d) Cr, (e) Mo, and (f) N maps. TEM specimen extracted from UNS S32750 steel treated T2 for t4.

Nilsson et al.[49] reported similar observations, where different IHTs with the same volume fraction of σ-phase had different CPT values. In their work, the authors suggested that the reduction in localized corrosion resistance is not exclusively related to σ-phase, but the explanation might be related to the other intermetallic phases that were present. Other authors[94] suggested that the depleted zones are richer in Cr and Mo at higher IHT temperatures as the diffusion kinetics increases with temperature. Consequently, comparisons between IHT must be performed within the same temperature and, thus, reporting a unique critical volume fraction of tertiary phases per material is not possible. Instead, each material presented three critical volume fractions, one per IHT temperature, which are summarized in Table VIII. In Table VIII, it was assumed a CPT $\leqslant$ 40 °C to define the critical volume fraction.

Taking the IHT time as the critical parameter, Table VIII shows that UNS S32750 and S32760 shared the shortest critical IHT time at 790 °C. At 846 °C, all three materials attained the same critical IHT time. And finally, at 920 °C, UNS S32760 had the lowest critical IHT time whereas the CPT of S39274 did not drop below 40 °C even at the longest IHT time. Taking into consideration these critical IHT times, it was concluded that the localized corrosion resistance of UNS S39274 was the least affected by IHT; whereas S32760 was the most influenced by it.

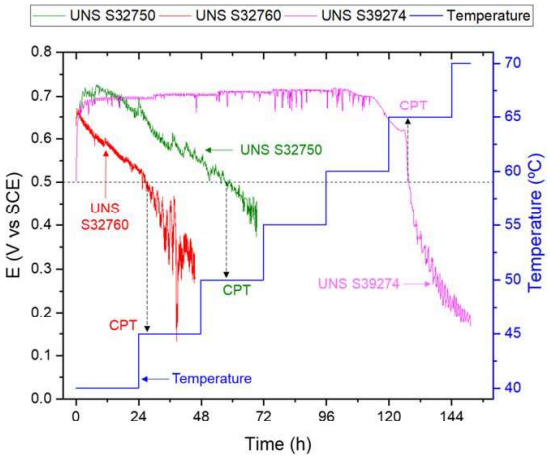

Figure 11. OCP in 6 wt%. $FeCl_3$ as a function of aging time and temperature for the three materials isothermally aged at 846 °C for 240 s, as indicated.

Implications.—The results of this work proved, by different types of analyses, that 2.1 wt% W drastically reduced the kinetics of σ-phase precipitation in UNS S39274, which also suffered the least deterioration of corrosion resistance by IHT. In contrast, UNS S32760 was the most impacted regarding both total precipitates and the corresponding corrosion resistance. Unlike UNS S32750,

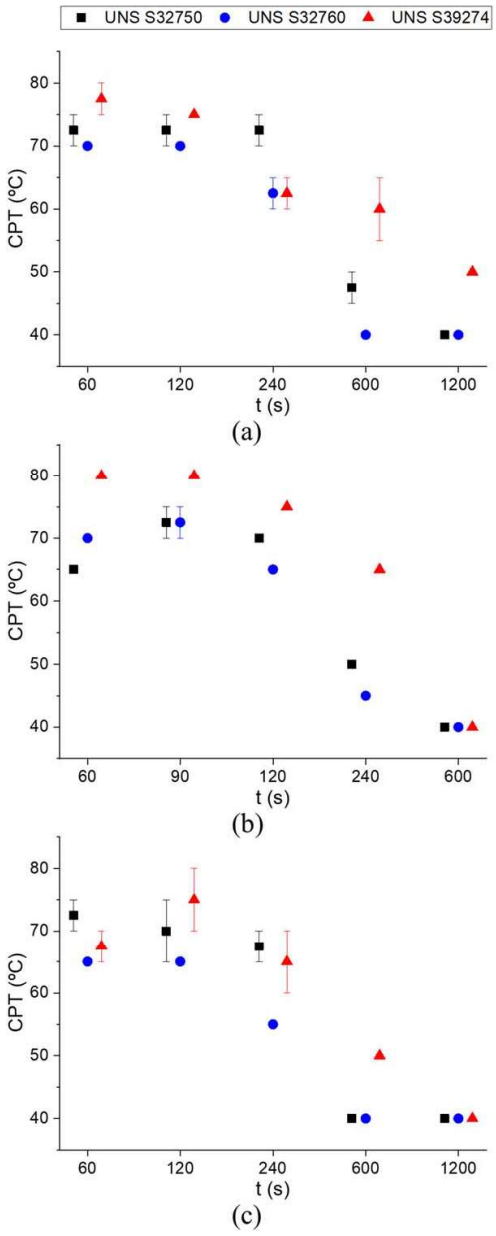

Figure 12. CPT values obtained in all specimens isothermally aged at (a) 920 °C, (b) 846 °C and (c) 790 °C. Error bars represent maximum and minimum values.

both S32760 and S39274 contain different quantities of W, suggesting the existence of an optimal W concentration.

Despite the exhaustive characterization performed herein, there are still some concerns that need to be addressed to quantify the role of W in solid solution and of each of the deleterious phases on the localized corrosion resistance of SDSS. The mechanisms by which W in solid solution influences localized corrosion resistance are yet to be demonstrated. Likewise, the reasons for the apparent optimal W range where the precipitation of σ-phase is kinetically retarded are unclear and contradict modeling work by, e.g., Wessman et al.[40,64] Additionally, although UNS S39274 appears to be within the optimal W concentration, the range within which W is beneficial cannot be inferred from this work.

The precipitation of both σ- and χ-phase led to a sharp decrease in CPT even in concentrations well below the 2–6 vol% threshold suggested by Mathiesen et al.[68] and observed by Deng et al.[60] It cannot be demonstrated conclusively from the results presented herein which phase, σ or χ, is more detrimental regarding corrosion resistance. Moreover, at a similar volume fraction of the same deleterious phase, the aging temperature had also an apparent effect as discussed above. A more detailed TEM, EDS and Auger spectroscopy investigation could shed light on possible compositional gradients at the precipitate/matrix interface as well as their influence on the local stability of the passive films, which could explain the observed corrosion behavior.

Despite these shortcomings, a comparison of UNS S32750 (W-free) and S39274 (high-W) indicated that similar reductions in CPT were measured in samples that had a similar volume fraction of precipitates, where σ-phase was predominant in UNS S32750 and χ-phase in S39274. The main advantage of the high-W SDSS appears to be the sharply slower precipitation kinetics of deleterious phases.

Although all SDSS had similar CPT in the SA condition, the slower precipitation kinetics of deleterious phases in UNS S39274 could be advantageous when welding SDSS components. In this regard, SDSS welding procedures require very low interpass temperatures—often below 150 °C[65]—to prevent the precipitation of deleterious phases. The low interpass temperature extends welding time and increases costs. Given the lower propensity to form deleterious phases of UNS S39274, welding procedures could be optimized by allowing higher interpass temperatures, which could, in turn, lead to economic benefits over other SDSS families. More research is, nonetheless, necessary to validate this hypothesis as the microstructure evolution during welding is more complex than that attained by IHT, and also contradicts the computational thermodynamics modeling work by Wessman et al.[64]

Conclusions

In this work, the effect of W on the precipitation kinetics of deleterious phases of three commercial SDSS was investigated. Additionally, the pitting corrosion resistance was quantified as a function of microstructure evolution after IHT. The following conclusions were drawn based on the evidenced provided above:

- A 2.1 wt% W addition to SDSS retarded σ-phase precipitation and promoted the nucleation of χ-phase. On the other hand, little χ-phase formation was observed in the alloy containing 0.6 wt%. W, which showed the fastest σ-phase precipitation.
- Despite the precipitation of χ-phase, the alloy containing 2.1 wt% W had the lowest total amount of intermetallic phases, whereas UNS S32760 (0.6 wt% W) contained the largest volume fraction of precipitates in almost all IHT conditions.
- CPT values dropped according to the concentration of deleterious phases within the same IHT temperature, indicating a strong correlation between corrosion resistance and tertiary phase precipitation kinetics.
- Both χ- and σ-phase lowered CPT, but the reduction appeared more drastic when σ-phase was the main precipitated phase (UNS S32750 and S32760), rather than χ-phase (10 °C–20 °C difference depending on the IHT).
- Results of the statistical analysis indicated that the decrease in CPT was significant when the concentration of deleterious phases was less than 1.0 vol%.

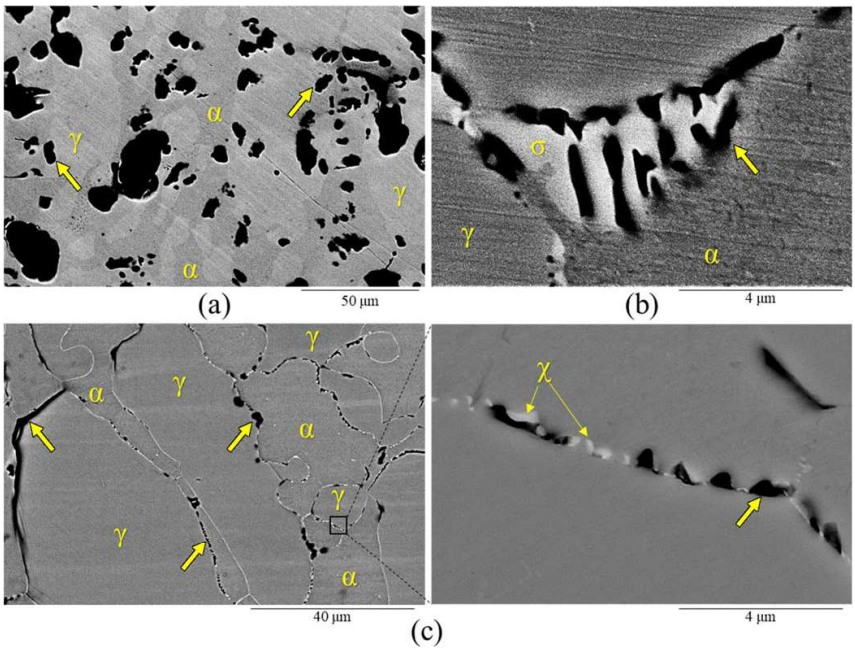

Figure 13. SEM pictures after CPT tests of samples (a) SA UNS 32750 and (b) 790 °C for 1200 s IHT UNS S32750, and (c) UNS S39274 heat treated at 790 °C for 1200 s. Arrows point at the location of some localized attacks.

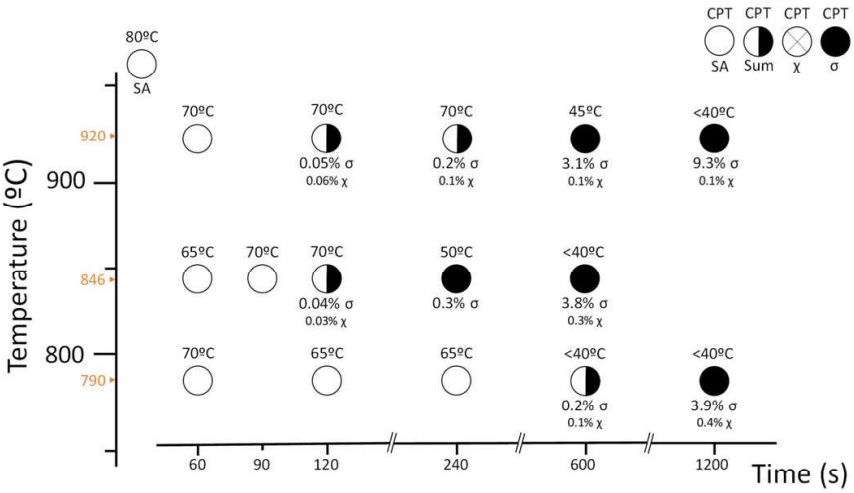

Figure 14. TTTC-diagram for UNS S32750 including vol% of tertiary phases and corresponding CPT values.

- The higher the IHT temperature, the higher the volume fraction of intermetallic phases needed to produce a decrease in CPT below 40 °C. Therefore, each material presented three critical volume fractions of deleterious phases, i.e., one per IHT temperature.
- Considering the IHT time as a critical parameter; UNS S39274 was the material affected the least by IHT, whereas S32760 was influenced the most.
- Results suggested the existence of an optimal W concentration range. Outside this range, W may become detrimental regarding corrosion resistance and precipitation kinetics. Although the optimal minimum and maximum W concentration cannot be inferred from the present study, the results indicated that 2.1 wt% W was inside the range, while 0.6 wt% W might have been outside of it.

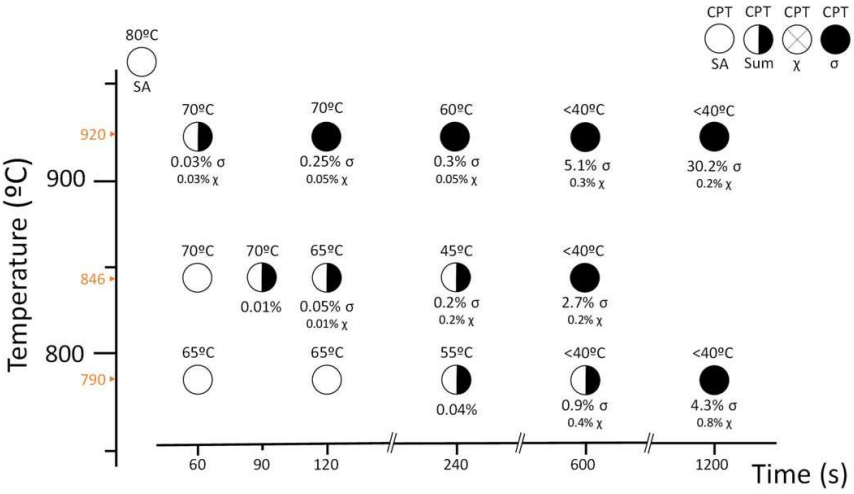

Figure 15. TTTC-diagram for UNS S32760 including vol% of tertiary phases and corresponding CPT values.

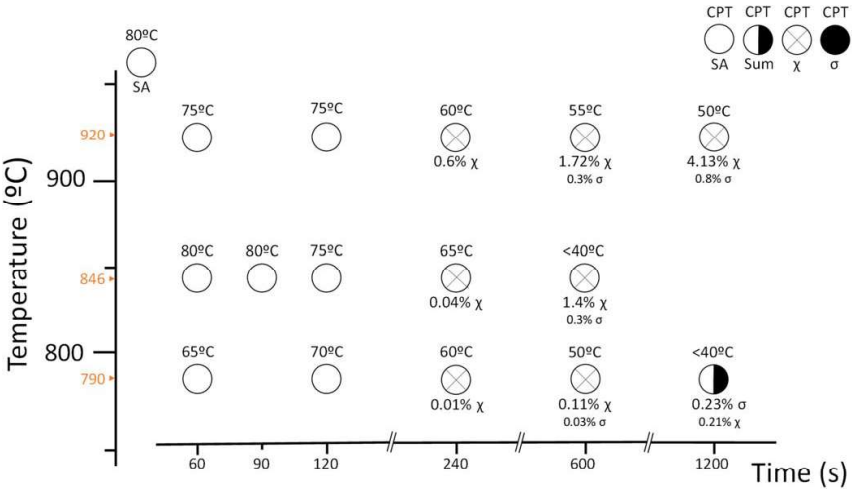

Figure 16. TTTC-diagram for UNS S39274 including vol% of tertiary phases and corresponding CPT values.

Acknowledgments

The authors thank professor Ida Westermann (NTNU), Di Wan (NTNU), Atle H. Qvale (GE O&G), and Anders Jernberg (GE O&G) for their guidance and the technical discussions. The authors also acknowledge Sumitomo Co. and Sandvik AS, who provided the various materials. This work was sponsored in part by General Electric, Co. (Oil and Gas, Norway) and NTNU and conducted at NTNU's Department of Mechanical and Industrial Engineering with the support of master students Hege Østvold, Mia Bernås, and Christian Lauritsen. Lastly, the authors acknowledge the support of the John de Laeter Centre at Curtin University during EBSD and TEM studies.

ORCID

Cristian Torres https://orcid.org/0000-0003-3793-6542
María Sofía Hazarabedian https://orcid.org/0000-0002-8220-3922
Zakaria Quadir https://orcid.org/0000-0003-1626-3748
Roy Johnsen https://orcid.org/0000-0002-5449-7396
Mariano Iannuzzi https://orcid.org/0000-0001-9202-3696

References

1. A. J. Sedriks, *Corrosion*, **42**, 376 (1986).
2. C. O. A. Olsson and D. Landolt, *Electrochim. Acta.*, **48**, 1093 (2003).
3. R. C. Newman, *Corros.*, **57**, 1030 (2001).
4. J. O. Nilsson, *Mater. Sci. Technol.*, **8**, 685 (1992).
5. V. K. Lorenz and G. Médawar, *Thyssenforschung*, **1**, 97 (1969).
6. J. E. Truman, *Proceedings UK Corrosion'87*, Brighton, UK, 111 (1987).
7. R. F. A. Jargelius-Pettersson, *Corros.*, **54**, 162 (1998).
8. E. Alfonsson and R. Qvarfort, *Mater. Sci. Forum*, **111–112**, 483 (1992).
9. J. H. Cleland, *Eng. Fail. Anal.*, **3**, 65 (1996).
10. P. Kangas and G. C. Chai, *Adv. Mater. Res.*, **794**, 645 (2013).
11. J. Charles, "Duplex stainless steels "91." *Proceedings. Les Éditions de Physique Les Ulis*, Beaune, Bourgogne, France, p. 151 (1991).
12. International Organization for Standardization, Switzerland, "ISO 21457:2010." *Petroleum, petrochemical and natural gas industries - Materials selection and corrosion control for oil and gas production systems* (2010).
13. NORSOK M-001, *Materials Selection*, Standards Norway, Lysaker, Norway (2014).
14. R. Francis, G. Byrne, and G. Warburton, *Corrosion 2011*, Houston, TX(NACE International), 11351 (2011).
15. J. Oredsson and S. Bernhardsson, *Mater. Perform.*, **22**35 (1983).
16. R. N. Gunn, *Duplex Stainless Steels: Microstructure, Properties and Applications* (Woodhead Publishing, Cambridge, U.K) (1997).

17. M. Sofia Hazarabedian, A. Viereckl, Z. Quadir, G. Leadbeater, V. Golovanevskiy, S. Erdal, P. Georgeson, and M. Iannuzzi, *Corros.*, **75**, 824 (2019).
18. L. F. Garfias-Mesias and J. M. Sykes, *Corros.*, **54**, 40 (1998).
19. E. B. Haugan, M. Næss, C. Torres Rodriguez, R. Johnsen, and M. Iannuzzi, *Corros.*, **73**, 53 (2017).
20. M. K. Ahn, H. S. Kwon, and H. M. Lee, *Corros. Sci.*, **40**, 307 (1998).
21. J. S. Kim, P. J. Xiang, and K. Y. Kim, *Corros.*, **61**, 174 (2005).
22. H. Habazaki, A. Kawashima, K. Asami, and K. Hashimoto, *Corros. Sci.*, **33**, 225 (1992).
23. C. Jia and W. Jiann Kuo, *Corros. Sci.*, **30**, 53 (1990).
24. A. K. Mishra and D. W. Shoesmith, *Corros.*, **70**, 721 (2014).
25. K. Lutton Cwalina, C. R. Demarest, A. Y. Gerard, and J. R. Scully, *Curr. Opin. Solid State Mater. Sci.*, **23**, 129 (2019).
26. N. Bui, A. Irhzo, F. Dabosi, and Y. Limouzin-Maire, *Corros.*, **39**, 491 (1983).
27. N. D. Tomashov, G. P. Chernova, and O. N. Marcova, *Corros.*, **20**, 166t (1964).
28. A. Belfrouh, C. Masson, D. Vouagner, A. M. de Becdelievre, N. S. Prakash, and J. P. Audouard, *Corros. Sci.*, **38**, 1639 (1996).
29. C.-J. Park, M.-K. Ahn, and H.-S. Kwon, *Materials Science and Engineering: A*, **418**, 211 (2006).
30. E.-A. Cho, C.-K. Kim, J.-S. Kim, and H.-S. Kwon, *Electrochim. Acta*, **45**, 1933 (2000).
31. K. Ogawa, H. Okamoto, M. Ueda, M. Igarashi, T. Mori, and T. Kobayashi, *Weld. Int.*, **10**, 466 (1996).
32. K. Ogawa, H. Okamoto, M. Igarashi, M. Ueda, T. Mori, and T. Kobayashi, *Weld. Int.*, **11**, 14 (1997).
33. Y. S. Ahn and J. P. Kang, *Mater. Sci. Technol.*, **16**, 382 (2000).
34. K. Ogawa and T. Osuki, *ISIJ Int.*, **59**, 129 (2019).
35. K. Ogawa and T. Osuki, *ISIJ Int.*, **59**, 122 (2019).
36. J. O. Nilsson, T. Huhtala, P. Jonsson, L. Karlsson, and A. Wilson, *Metall. Mater. Trans. A*, **27**, 2196 (1996).
37. K. Y. Kim, P. Q. Zhang, T. H. Ha, and Y. H. Lee, *Corros.*, **54**, 910 (1998).
38. J. S. Kim and H. S. Kwon, *Corros.*, **55**, 512 (1999).
39. H. J. Park and H. W. Lee, *Int J Electrochem Sc*, **9**, 6687 (2014).
40. S. Wessman and R. Pettersson, *Steel Res. Int.*, **86**, 1339 (2015).
41. S. Hertzman, T. Huhtala, L. Karlsson, J. O. Nilsson, M. Nilsson, R. Jargelius-Pettersson, and A. Wilson, *Mater. Sci. Technol.*, **13**, 604 (1997).
42. Y. H. Lee, K. T. Kim, Y. D. Lee, and K. Y. Kim, *Mater. Sci. Technol.*, **14**, 757 (1998).
43. A. R. Akisanya, U. Obi, and N. C. Renton, *Materials Science and Engineering: A*, **535**, 281 (2012).
44. J. S. Kim, T. H. Ha, and K. Y. Kim, *Corros.*, **57**, 452 (2001).
45. S.-H. Jeon, S.-T. Kim, I.-S. Lee, J.-S. Kim, K.-T. Kim, and Y.-S. Park, *J. Alloys Compd.*, **544**, 166 (2012).
46. R. Goetz, J. Laurent, and D. Landolt, *Corros. Sci.*, **25**, 1115 (1985).
47. T.-H. Lee and S.-J. Kim, *Scr. Mater.,*, **39**, 951 (1998).
48. N. Llorca-Isern, H. López-Luque, I. López-Jiménez, and M. V. Biezma, *Mater. Charact.,*, **112**, 20 (2016).
49. J. O. Nilsson and A. Wilson, *Mater. Sci. Technol.*, **9**, 545 (1993).
50. C. Örnek and D. L. Engelberg, *J. Mater. Sci.,*, **51**, 1931 (2016).
51. R. Magnabosco, *Mater. Res.*, **12**, 321 (2009).
52. R. Magnabosco, L. da Costa Morais, and D. C. dos Santos, *Calphad*, **64**, 126 (2019).
53. R. Magnabosco and N. Alonso-Falleiros, *Corros.*, **61**, 130 (2005).
54. D. Caluscio dos Santos, R. Magnabosco, and C. de Moura-Neto, *Corros.*, **69**, 900 (2013).
55. D. Y. Kobayashi and S. Wolynec, *Mater. Res.*, **2**, 239 (1999).
56. D. M. E. Villanueva, F. C. P. Junior, R. L. Plaut, and A. F. Padilha, *Mater. Sci. Technol.*, **22**, 1098 (2006).
57. I. Calliari, M. Pellizzari, and E. Ramous, *Mater. Sci. Technol.*, **27**, 928 (2011).
58. N. Llorca-Isern, I. López-Jiménez, H. López-Luque, M. V. Biezma, and A. Roca, *Mater. Sci. Forum*, **879**, 2537 (2016).
59. C.-C. Hsieh and W. Wu, *ISRN Metall.*, **2012**, 1 (2012).
60. B. Deng, Z. Wang, Y. Jiang, H. Wang, J. Gao, and J. Li, *Electrochim. Acta*, **54**, 2790 (2009).
61. N. Pettersson, R. F. A. Pettersson, and S. Wessman, *Metall. Mater. Trans. A*, **46**, 1062 (2015).
62. H. Kokawa, E. Tsory, and T. H. North, *ISIJ Int.*, **35**, 1277 (1995).
63. J. Liao, *ISIJ Int.*, **41**, 460 (2001).
64. S. Wessman, L. Karlsson, R. Pettersson, and A. Östberg, *Weld. World*, **56**, 79 (2013).
65. International Molybdenum Association, London, UK, *Practical guidelines for the fabrication of duplex stainless steels* (2009).
66. A. P. Miodownik and N. Saunders, *Mater. Sci. Technol.*, **18**, 861 (2002).
67. J. O. Nilsson, P. Kangas, A. Wilson, and T. Karlsson, *Metall. Mater. Trans. A*, **31**, 35 (2000).
68. T. Mathiesen and C. Jensen, *CORROSION 2013* (NACE International, Orlando, Florida) (2013).
69. Statoil ASA, "MAT-2010080." *Technical Note - Metallographic Etching of Duplex Stainless Steels* (2010).
70. M. M. Nowell, R. A. Witt, and B. W. True, *Microsc. Today*, **13**, 44 (2005).
71. D. Wan and A. Barnoush, *Materials Science and Engineering: A*, **744**, 335 (2019).
72. D. Wang, X. Lu, D. Wan, Z. Li, and A. Barnoush, *Scr. Mater.*, **173**, 56 (2019).
73. S. He, M. Saunders, K. Chen, H. Gao, A. Suvorova, W. D. A. Rickard, Z. Quadir, C. Q. Cui, and S. P. Jiang, *J. Electrochem. Soc.*, **165**, F417 (2018).
74. D. Tomus and H. P. Ng, *Micron*, **44**, 115 (2013).
75. E. M. L. E. M. Jackson, P. E. D. Visser, and L. A. Cornish, *Mater. Charact.*, **31**, 185 (1993).
76. M. Iannuzzi, C. Mendez, L. Avila-Gray, G. Maio, and H. Rincón, *Corros.*, **66**, 045003-1 (2010).
77. T. Mathiesen, T. S. Nielsen, T. Haugen, B. Espelid, P. Hummelgaard, and K. Vilpponen, *NT Technical Report - Improved Method for ASTM G48 Corrosion Testing of Welds*, Nordic Innovation Centre, Oslo, Norway (2004).
78. T. W. MacFarland, *Two-Way Analysis of Variance. Statistical Tests and Graphics Using R* (Springer, New York) (2012).
79. H. Abdi and L. J. Williams, *Encyclopedia of Research Design*, ed. N. J. Salkind (SAGE Publications, Thousand Oaks, CA) (2010).
80. J. P. Shaffer, *Annual Review of Psychology*, **46**, 561 (1995).
81. T. V. Perneger, *Brit. Med. J.*, **316**, 1236 (1998).
82. D. C. Montgomery, *Design and Analysis of Experiments* (John Wiley & Sons, Inc, Hoboken, NJ) (2009).
83. D. M. Escriba, E. Materna-Morris, R. L. Plaut, and A. F. Padilha, *Mater. Charact.*, **60**, 1214 (2009).
84. J. M. Pardal, S. S. M. Tavares, M. D. P. C. Fonseca, J. A. D. Souza, L. M. Vieira, and H. F. G. D. Abreu, *Mater. Res.*, **13**, 401 (2010).
85. J. M. Pardal, S. S. M. Tavares, M. P. Cindra Fonseca, M. R. da Silva, and M. L. R. Ferreira, *Mater. Sci. Technol.*, **28**, 295 (2012).
86. K. W. Andrews, *Nat.*, **164**, 1015 (1949).
87. G. Bergman and D. P. Shoemaker, *Acta Crystallogr.*, **7**, 857 (1954).
88. J. O. Nilsson, L. Karlsson, and J. O. Andersson, *Mater. Sci. Technol.*, **11**, 276 (1995).
89. A. Irhzo, Y. Segui, N. Bui, and F. Dabosi, *Corros. Sci.*, **26**, 769 (1986).
90. H. M. Lee, S. M. Allen, and M. Grujicic, *Metall. Trans. A*, **22**, 2869 (1991).
91. H. Nitta, T. Yamamoto, R. Kanno, K. Takasawa, T. Iida, Y. Yamazaki, S. Ogu, and Y. Iijima, *Acta Mater.*, **50**, 4117 (2002).
92. S. Takemoto, H. Nitta, Y. Iijima, and Y. Yamazaki, *Philos. Mag.*, **87**, 1619 (2007).
93. P. J. Alberry and C. W. Haworth, *Met. Sci.*, **8**, 407 (1974).
94. E. Angelini, B. De Benedetti, and F. Rosalbino, *Corros. Sci.*, **46**, 1351 (2004).

PAPER II

Crevice Corrosion of solution annealed 25Cr duplex stainless steels: Effect of W on critical temperatures

C. Torres, R. Johnsen, M. Iannuzzi

Accepted for publication in Corrosion Science

(date: 29.09.2020)

Crevice Corrosion of solution annealed 25Cr duplex stainless steels: Effect of W on critical temperatures.

Cristian Torres [a,*], Roy Johnsen [a], Mariano Iannuzzi [a,b]

[a] Department of Mechanical and Industrial Engineering, Norwegian University of Science and Technology, Richard Birkelands veg 2b, 7491, Trondheim, Norway

[b] Curtin Corrosion Centre, Curtin University, GPO Box U1987, Perth, WA, 6845, Australia

***Corresponding author:**

E-mail address: cristian.torres@ntnu.no

Phone number: +47 45126703

Abstract

In this work, the influence of tungsten on the crevice corrosion resistance of three super duplex stainless steels (SDSS) containing 0.0, 0.6, and 2.1 wt.% W was determined. The PD-GS-PD technique was used to estimate the critical crevice repassivation temperature by performing tests at different temperatures. Additionally, long-term potentiostatic experiments were conducted as a function of temperature in natural seawater to validate PD-GS-PD testing. Results showed that W improved crevice corrosion resistance as evidenced by the higher initiation and repassivation crevice temperatures, which were 7.5 to 15 °C higher in the 2.1 wt.% W SDSS than in the W-free case.

Keywords: A. Tungsten, A. Duplex Stainless Steel**,** B. PD-GS-PD, C. Crevice corrosion, C. Repassivation Potential

Abbreviations:

CCT: Critical Crevice Temperature

CPP: Cyclic Potentiodynamic Polarisation

CPT: Critical Pitting Temperature

CRA: Corrosion-resistant alloy

E_{corr}: Corrosion potential

E_P: Pitting potential

E_R: Repassivation potential

$E_{R,Crev}$: Crevice repassivation potential

E_{Trans}: Transpassive potential

EDS: Energy-Dispersive X-ray Spectroscopy

GS: Galvanostatic polarisation

ICP-MS: Inductively Coupled Plasma Mass Spectrometry

IFM: Infinite Focus Microscope

i_{GS}: Current density of galvanostatic polarisation step

i_{pass}: Passive current density

OCP: Open circuit potential

PD: Potentiodynamic polarisation

PD-GS-PD: Potentiodynamic-Galvanostatic-Potentiodynamic

PRE_N: Pitting Resistance Equivalent considering the N content

$PRE_{N,W}$: Pitting Resistance Equivalent considering the N and W content

PS: potentiostatic polarisation

PTFE: Polytetrafluoroethylene

Q: Electric charge

Q_{exp}: experimental electric charge

SA: Solution annealed

SEM: Scanning Electron Microscope

SDSS: Super Duplex Stainless Steel

THE: Tsujikawa-Hisamatsu Electrochemical

T_R: repassivation temperature

$T_{R,Crev}$: crevice repassivation temperature

α: Ferrite

γ: Austenite

1. Introduction

In the case of super duplex stainless steels (SDSS), it is known that increasing the Cr, Mo, and N content improves their localised corrosion resistance to chloride-containing electrolytes with a pH value ranging from slightly acidic to moderately alkaline [1-6]. Tungsten has also been shown to improve the localised corrosion resistance of SDSS, although the mechanisms and the extent to which W can improve pitting and crevice corrosion performance are still a cause of debate within the scientific community [7, 8].

Two different roles of W need to be considered when investigating its effect on corrosion resistance: (i) its influence as a solid solution element in the solution annealed (SA) condition; and (ii) its impact on the precipitation kinetics of deleterious phases in, e.g., isothermally aged materials. The scope of this work focuses on the former role, as the W effect on precipitation kinetics has been addressed elsewhere [8].

Literature published so far on SA stainless steel indicates that pure W does not form a passive layer [9]. However, there is disagreement as to whether W contributes to passivity when it is added to Fe-Cr stainless steels. Belfrouh et al. [10] reported a detrimental effect of W when added to austenitic stainless steels in the absence of Mo; however, the authors indicated that when combined with Mo, W could improve pitting corrosion resistance. In contrast, Bui et al. [9] performed potentiodynamic polarisations of austenitic stainless steels as a function of W content in acid and neutral chloride-containing-electrolytes. In some conditions, the authors included tungstates to study the inhibition effect of W both as a solid solution element and as an anodic inhibitor in the electrolyte. The results showed a clear improvement in the corrosion resistance of the material with increasing W content, and, according to the authors, W was present in the passive layer in the form of WO_3. The influence of W on improving passivity was a function of the pH of the bulk electrolyte. In acid media, W interacted with water to form insoluble WO_3. In neutral pH, WO_3 bonded to the substrate, increasing the

stability of the passive film. The tungstates added to the electrolyte inhibited corrosion by surface absorption without electrochemical reduction on the passive layer. Tomashov et al. [11] studied the influence of W additions from 0.18 to 2.67 wt.% to austenitic stainless steels. The authors obtained lower corrosion rates and higher pitting potentials (E_P) as the W content increased. However, the 0.18 wt.% W addition worsen the corrosion resistance when compared with the W-free base alloy.

For ferritic stainless steels, Ahn et al. [12] obtained a clear improvement in pitting corrosion resistance in neutral and acid chloride-containing electrolytes. W had the same beneficial effect as Mo when added at the same at.% (i.e., half the quantity of Mo in wt.%). However, the authors reported no synergistic effects when both elements were added together. Cho et al. [13] also studied ferritic stainless steels, analysing the influence of W on the repassivation kinetics. The authors observed a beneficial effect of W on the localised corrosion resistance of the materials, although an equal addition of Mo (in wt.%) had 1.6 times the effect of W, i.e., W and Mo would have had approximately the same beneficial influence if added at the same at.%. Goetz et al. [14] observed enrichment of Mo and W at the surface of ferritic stainless steels. However, the improvement in localised corrosion resistance was not attributed to this enrichment, but to a lower activity of Fe. The authors concluded that Mo had a higher beneficial effect than W, even at equal at.% additions.

Habazaki et al. [15] investigated additions of Mo and W to amorphous Fe-Cr alloys. Both elements, although W to a greater extent, improved corrosion resistance of the materials by inhibiting Cr dissolution during passivity. Thereby, the passive layer was enriched in Cr and localised corrosion was averted. Nevertheless, when the W and Mo were added in excess (10 at.%), the dissolution during passivation increased and the inhibiting effect was lost. Consequently, the results in the literature seem to indicate the existence of an optimal W concentration within which W improves the stability of the passive film. W might be

detrimental or ineffective outside this range; nevertheless, the optimal composition range is not well defined.

Despite the extent of the research presented above, all these investigations focused on single-phase stainless steels (either austenitic or ferritic) or amorphous alloys. Consequently, there is a lack of knowledge on the role of W on highly allowed dual-phase stainless steels such as duplex stainless steels. Recently, Haugan et al. [7] compared two different SDSS containing W, specifically 0.55 wt.% and 2.2 wt.%. The authors performed different electrochemical techniques to obtain the critical pitting temperature (CPT), the critical crevice temperature (CCT) and the repassivation temperature (T_R); the later one determined based on repassivation potentials (E_R) measured following ASTM G61 [16]. Although the authors found a marked improvement in crevice corrosion resistance with W content; a reference W-free alloy was not included in the test matrix, and the samples were extracted from components made using different forming methods (i.e., extruded pipe vs. rolled plate). Additionally, the cyclic potentiodynamic polarization (CPP) technique adapted from ASTM G61 has limitations that need to be considered when studying highly alloyed stainless steels.

1.1. Electrochemical techniques to determine crevice corrosion resistance

E_R and, for studies using crevice formers, $E_{R,Crev}$ are often obtained by means of potentiodynamic tests. ASTM G61 describes the CPP technique, which is the most widely used. The CPP technique consists of a slow potentiodynamic polarisation (PD) scan to a pre-specified current density value. The current density value must be high enough to initiate localised corrosion in the forward scan. As soon as this current density value is reached, the direction of the polarization is reverted during the backward PD. E_R is then defined as either a cross-over potential or when the backward scan reaches the passive current density (i_{pass}) [17]. However, several studies [18-21] have indicated the dependence of E_R with the extent of pit and crevice propagation, which can be related to the electrical charge (Q) passed during

the forward scan. For certain stainless steels and corrosion resistant alloys (CRAs), i.e., UNS S30400, S31603 and N08825, only when the propagation was deep enough (i.e., Q > 10-30 C/cm^2), E_R became independent of the size of the attack [21-25]. These findings imply the existence of a minimum pit or crevice depth to obtain reproducible E_R values. Especially for highly alloyed CRAs, the CPP method might allow insufficient time for localised corrosion propagation during the forward step, as the backward potentiodynamic scan starts as soon as the pre-defined current density is reached. Additionally, several investigations [23, 26] have shown an inherent large scatter in critical potentials since the extent of the localised corrosion attack might be insufficient to ensure a lower-bound E_R value.

Researchers have, thus, developed alternative methods to circumvent the limitations of the CPP technique. Tsujikawa and Hisamatsu [27] developed a new electrochemical test to study crevice corrosion of nickel-based CRAs, which is referred to as the Tsujikawa-Hisamatsu Electrochemical (THE) test. This multi-step technique is now standardised in the ASTM G192 standard and consists of the following steps [28]: (i) PD to a potential more positive than critical potential, (ii) galvanostatic polarisation (GS) for 2 h to let localised corrosion propagate, and (iii) iterative potentiostatic polarisation (PS), lowering the potential 10 mV every 2 h until repassivation is achieved. Thanks to the GS step, the total charge passed is better controlled as the current is held constant during the time of the galvanostatic step. As a result, a sufficiently deep localised attack can develop, which leads to more reproducible E_R values [21-24]. E_R is defined in this technique as the highest potential where the current stops increasing during the PS. Nevertheless, the THE method is slow and time consuming as E_R is normally found at low potentials. Thus, it often takes many iterations and a long time to reach E_R using 10 mV steps every 2 hours. Additionally, in some cases [29], it was difficult to discern when repassivation occurred due to the current behaviour during the PS step, complicating the determination of E_R.

Consequently, Mishra and Frankel [29] changed the third step of the THE test to a backward PD scan. As in the case of CPP, E_R is defined as the cross-over of both potentiodynamic scans or when the backward scan reaches i_{pass}. This technique was referred to as the PD-GS-PD method by the authors, named to reflect the three different steps, specifically: (i) potentiodynamic polarisation scan (PD), (ii) galvanostatic polarisation (GS), and (iii) reverse potentiodynamic polarisation scan (PD). Thereby, the issues mentioned above with the CPP and the THE techniques were resolved. In a PD-GS-PD scan, crevice corrosion develops during the GS step, resulting in a low scatter of the results while keeping the testing time short.

The PD-GS-PD has successfully been used to analyse the localised corrosion resistance of nickel-based alloys [29-35]. The PD-GS-PD technique has, as well, been used to test conventional [24] and highly-alloyed stainless steels, specifically UNS S32205 and S32750 [36, 37]. Results showed that the PD-GS-PD method gave the most conservative crevice repassivation potentials ($E_{R,Crev}$) values among the different methods, i.e., the lowest values in comparison to the CPP and THE tests [29-31]. In addition, these E_R values were independent of the scan rate used during the PD steps [29], torque applied to the crevice former (if greater than 2 N·m) [31], and the charge passed during the GS step [30]. These results indicated that the PD-GS-PD technique allowed sufficient localised attack propagation during the GS step to let E_R become independent of the experimental variables mentioned above. The PD-GS-PD method is, thus, a proven technique for testing localised corrosion resistant of highly alloyed CRAs, such as SDSS.

Since E_R is used to determine the localised corrosion resistance of an alloy, it can be used to analyse the role of different alloying elements on the resulting corrosion resistance [32, 33]. Additionally, by testing at different temperatures, the PD-GS-PD technique can be used to

determine the critical crevice temperature as well as the crevice repassivation temperature ($T_{R,Crev}$) [7, 38].

The objective of this investigation was to quantify the crevice corrosion resistance of commercial SDSS as a function of W content. Therefore, three SA materials differing mainly in their W content were compared. Firstly, PD-GS-PD tests were conducted at incremental temperatures to determine changes in $T_{R,Crev}$ as a function of W content. The results were, then, validated using long-term potentiostatic testing in natural seawater.

2. Experimental

Three different materials were employed in this work, i.e., UNS S32750, S32760, and S39274. Table 1 shows their chemical composition. UNS S32750, a W-free SDSS, was used as a reference material; whereas UNS S32760 and S39274 contained 0.6 wt.% W and 2.1 wt.% W, respectively. All materials were received as extruded pipes with a 30 mm wall thickness and a 203.2 mm diameter. Additionally, a 100 mm by 150 mm by 9.5 mm UNS S39274 rolled plate was included in the test program to compare the results to Haugan et al. [7] and analyse the influence of product form variations.

Round samples with a thickness of 3 mm were machined from all materials. The final diameter for UNS S32750 and S32760 specimens was 25 mm, whereas the diameter of the UNS S39274 specimens was 30 mm.

2.1. Sample preparation

Both extruded pipe and rolled plate UNS S39274 samples were received in the SA condition (heat-treated at 1085°C for 10 minutes). On the other hand, UNS S32750 and UNS S32760 were received as extruded and, thus, were solution annealed according to the manufacturer's specifications in an air furnaced at 1100°C for 15 minutes and rapidly quenched in water.

Figure 1 includes micrographs of the four materials studied in this work. All materials were within the acceptable austenite/ferrite ratio range [7, 8], i.e., 40-60%.

The specimens were subsequently wet ground down to 500 US-grit SiC paper, rinsed with acetone, followed by distilled water and ethanol, and cleaned in an ultrasonic bath with ethanol for 5 minutes.

The coupons were mounted in the multi-crevice assembly shown in Figure 2 as described in ISO18070 [39]. The crevice washers were made of polytetrafluoroethylene (PTFE) with 12 artificial crevice slots (i.e., 24 in total). The washers were covered with PTFE tape as indicated by ASTM G192, which improved the reproducibility of the results as determined by preliminary testing [28]. The applied torque was 5 N·m [37]. A small hole of 2 mm in diameter was drilled close to the edge of each specimen to pass a 200 μm Pt wire, which was used to suspend the multi-crevice assembly as illustrated elsewhere [40-43].

The total surface area of the specimens exposed to the electrolyte was approximately 6.5 cm^2 for UNS S32750 and S32760, and 11 cm^2 for S39274. The area covered by the crevice former was 4.9 cm^2 for all specimens.

2.2. Crevice corrosion tests in 3.5 wt% NaCl

The experiments were carried out in a double-wall cell filled with approximately 160 ml of 3.5 wt.% NaCl, pH 6.5 solution (a minimum volume/specimen area ratio of 14.5 cm^3/cm^2 for UNS S39274, which had the largest total surface area). The electrolyte was purged with N_2 for 2 h before the sample was immersed. The cell was continuously purged for the duration of the tests. The dissolved oxygen concentration, which was monitored during testing by means of a fibre optic oxygen meter, remained below 10 ppb from the moment the sample was immersed and until the end of the experiment.

The electrochemical tests were performed at different temperatures: room temperature (22±1 °C), 40°C, 50°C, and 60°C. The temperature was controlled by a water bath connected to the jacketed cell, except for the room temperature tests that were performed at the pre-set laboratory temperature. A condenser filled with continuously running cold tap water (approximately 10°C) was placed in the outlet of the gas port to avoid evaporation of the electrolyte during testing.

The PD-GS-PD tests were conducted in a conventional three-electrode setup. An Ag/AgCl KCl saturated electrode was used as the reference electrode and a Pt mesh as the counter electrode. All samples were freely exposed at the corrosion potential (E_{corr}) for 15 minutes after immersion and before polarisation. Subsequently, a small cathodic current density of 1 $\mu A/cm^2$ was applied to remove possible surface contamination [37]; followed by another 30 minutes of E_{corr} exposure to allow the surface to stabilise.

The following procedure for the PD-GS-PD technique was used [37]: (i) the PD step was conducted at a scan rate of 0.167 mV/s, starting 30 mV below E_{corr} and ending when a pre-defined current density (i_{GS}) was reached, (ii) the GS step was done at the pre-defined i_{GS} for 2 h, and (iii) the reverse PD step was done at a scan rate of 0.167 mV/s, starting at the last potential measured during GS and ending when repassivation was achieved. $E_{R,Crev}$ was defined in two different ways for comparison: (i) as the cross-over potential of the forward and backward PD scans, and (ii) as the potential at which i_{pass} reached 1 $\mu A/cm^2$ [17]. The i_{GS} values were: (i) 25 $\mu A/cm^2$ for all temperatures [37], and (ii) 100 $\mu A/cm^2$ for 50°C and 60°C. The highest current density, 100 $\mu A/cm^2$, was high enough to avoid metastable activity and current noise triggering the start of the following step in the PD-GS-PD technique, as explained below.

Once the $E_{R,Crev}$ was obtained for each material at each different temperature, the $T_{R,Crev}$ was defined as the temperature at which the $E_{R,Crev}$ experienced a sharp drop from potentials associated with transpassivity to lower, usually negative, potentials [7, 44].

All tests were conducted at least in duplicated, while additional experiments were conducted as needed when large variations in $E_{R,Crev}$ were found to confirm the repeatability of the results [23, 26]. In this regard, the number of tests conducted at temperatures in the vicinity of $T_{R,Crev}$ was up to 8 per condition.

2.3. Long-term experiments in natural seawater

UNS S32750 and UNS S39274 extruded pipe specimens were exposed in natural seawater with the same crevice assembly as described in section 2.1. The seawater was taken from the Trondheim fjord (Norway) from 80 m depth and brought into a 5 L glass container with an inlet close to the bottom and an outlet close to the top to let the natural seawater flow continuously during the test. The container was placed on top of a hot plate. The temperature was regulated using a PID controller connected to a thermocouple placed close to the specimens. The set temperature was maintained within a ±1°C variation. The seawater flow was approximately 4 ml/min to avoid turbulence while ensuring a uniform temperature within the container.

The specimens were exposed at: (i) open circuit potential (OCP), and (ii) polarised at +600 $mV_{Ag/AgCl}$, to simulate chlorinated seawater [7, 40]. An Ag/AgCl KCl saturated reference electrode was used, and in the case of the polarised samples, a Pt mesh served as the counter electrode. The tests with the specimens at OCP started at 50°C and the temperature was increased fortnightly at 5°C steps until crevice corrosion initiated. The initiation of crevice corrosion was determined as a sharp drop on the OCP as described by Oldfield and Sutton [45]. For the specimens polarised to +600 $mV_{Ag/AgCl}$, the initial temperature was 40°C and

was increased in 5°C steps weekly. Crevice corrosion initiation was assumed when the current density exceeded 25 µA/cm^2 for over 24 h. The temperature at which crevice corrosion initiated was considered the CCT. After crevice initiation, the specimens were kept at that temperature for at least 48 hours before decreasing the temperature at 2.5°C steps every 48 h until (i) the OCP value recovered for the freely exposed samples, or (ii) the current decreased below 25 µA/cm^2 for the polarised samples for over 24 h. This temperature was considered the $T_{R,Crev}$. Two specimens of the same material were exposed in the same container simultaneously for repeatability. Since the replicated polarized specimens were connected to the same potentiostat, the temperature scan was reversed once both samples showed crevice corrosion.

2.4. Characterisation

After testing, the specimens were analysed by means of an Infinite Focus Microscope (IFM) employed as optical microscope with the possibility of taking 3D pictures of the surface. The number of crevice attacks present on both sides of the specimens were identified and their depth measured. The volume and projected area on the surface of the crevices were calculated using a commercial surface and image analysis software (MountainMaps) [46]. In selected cases, the corrosion attack was further analysed in a scanning electron microscope (SEM) coupled with energy-dispersive x-ray spectroscopy (EDS).

At the end of the PD-GS-PD tests, the electrolyte was stored in plastic containers and brought to the Department of Chemistry at the Norwegian University of Science and Technology (NTNU) where the concentration of released ions in the solution were measured by Inductively Coupled Plasma Mass Spectrometry (ICP-MS).

The total Q measured during the PD-GS-PD tests (Q_{exp}) was calculated as well from the GS and reverse PD steps until repassivation was achieved, assuming that the Q provided by the

forward PD was negligible due to the low current densities measured and the short time of this step compared to the rest of the test.

3. Results

3.1. Critical Crevice Temperatures by the PD-GS-PD technique

Figure 3 illustrates two results obtained with the PD-GS-PD technique. In the case of Figure 3a, the specimen suffered crevice corrosion, indicated by a large hysteresis loop and a low $E_{R,Crev}$. In contrast, Figure 3b illustrates a case where the specimen did not suffer localised corrosion, displaying a small hysteresis loop at a high anodic potential. As discussed below, this small hysteresis loop is thought to be due to the depassivation of the specimen surface due to the high potentials reached in the forward PD scan, i.e., the specimen reached the transpassive region [47]. In the first case (Figure 3a), crevice corrosion was arrested due to repassivation and the term $E_{R,Crev}$ can be used. However, in the example shown in Figure 3b, the threshold symbolises the transpassive potential (E_{Trans}). Hereafter, to differentiate when the value obtained represented $E_{R,Crev}$ or E_{Trans}, the following criterion was followed. The values obtained were defined as E_{Trans} when the cross-over in the backward PD scan occurred at or above +0.7 $V_{Ag/AgCl}$ (i.e., the drop of potential during the GS step was negligible, resulting in a potential above the reversible potential of the oxygen evolution reaction in the conditions of the test [47]); otherwise, the potential was described as $E_{R,Crev}$.

Figure 4 illustrates unexpected results of the PD-GS-PD technique. In Figure 4a, the GS step was triggered due to a metastable attack and high current noise; whereas Figure 4b shows crevice corrosion starting during the backward PD scan instead of during the GS step. Figure 5 shows the potential evolution during the GS step for all extruded materials at 50 and 60°C for both i_{GS} conditions. All forward PD scans reached transpassive potentials, i.e., above the E_{corr} values that could be attained in, e.g., seawater due to the action of microorganisms or

chlorination [48]. Nevertheless, apparent metastable activity—evidenced by frequent current spikes—was present in all materials, increasing in intensity at higher temperatures. UNS S32750 and especially UNS S32760 started to show metastable events at room temperature with increasing severity at 40°C, 50°C (Figure 4a), and 60°C (Figure 5). On the other hand, UNS S39274 exhibited metastable activity only at temperatures above 50°C (Figure 5).

For UNS S32750 and UNS S32760, metastable activity and high current noise reached current densities higher than 25 $\mu A/cm^2$ at 50°C and 60°C, causing the GS step of the technique to start at lower potentials. As a result, the potential increased during the GS step as seen in Figure 5, and the reverse PD scan did not cross the forward PD scan (Figure 4a), making the determination of $E_{R,Crev}$ impossible. Consequently, the tests at 50°C and 60°C were repeated with an i_{GS} of 100 $\mu A/cm^2$. With the higher i_{GS} setting, the forward PD scan continued until reaching a stable critical current. In this regard, the potential during the GS step stayed relatively constant in the absence of crevice attack, while it exhibited a sharp decrease when crevice corrosion initiated, as shown in Figure 5.

Figure 6 illustrates the $E_{R,Crev}$ and E_{Trans} for the two i_{GS} values at 50 and 60°C, whereas Figure 7 shows $E_{R,Crev}$ and E_{Trans} as function of temperature. The $E_{R,Crev}$ and E_{Trans} values were unaffected by the choice of i_{GS} as shown in Figure 6. Only for UNS S32760, $E_{R,Crev}$ dropped to +0.15 $V_{Ag/AgCl}$ when using 100 $\mu A/cm^2$, whereas the drop remained at high anodic potentials, i.e., +0.6 $V_{Ag/AgCl}$ with a i_{GS} of 25 $\mu A/cm^2$. Only minor differences were observed in $E_{R,Crev}$ values when comparing the cross over and current criteria, as seen in Figure 6 and 5. Nevertheless, E_{Trans} obtained with the cross-over definition was slightly more positive than that measured at 1 $\mu A/cm^2$.

Crevice corrosion attack did not occur at room temperature in any of the three SDSS; thus, all the potentials were labelled as E_{Trans}. UNS S32750 transitioned from E_{Trans} to $E_{R,Crev}$ at 40°C. The transition temperature was 50°C for UNS S32760 and 60°C for the UNS S39274 rolled

plate. In contrast, UNS S39274 extruded pipe suffered stable crevice corrosion at 60°C with no clear transition temperature. Despite the absence of a clear transition region (Figure 6), the transition temperature was assumed to be between 50 and 60°C, i.e., approximately 55°C. At the transition temperature, some specimens showed signs of corrosion while others did not, resulting in a large dispersion in $E_{R,Crev}$ values. Therefore, the minimum number of tests was increased to 8 per condition. Additionally, this large fluctuation suggested that this temperature could be set as $T_{R,Crev}$, since it marked the change from transpassive attack to stable crevice propagation. Table 2 summarises the $T_{R,Crev}$ measured for all the extruded pipe materials.

3.2. Critical Crevice and Repassivation Temperatures in natural seawater

Figure 8 and Table 2 summarise the results of the long-term natural seawater exposure testing. Figures 8a and b show OCP and temperature as a function of exposure time, together with an insert presenting a picture of a specimen after the test to illustrate the severity of the crevice corrosion. Figures 8c and d show the current and temperature evolution for the specimens polarised to +600 $mV_{Ag/AgCl}$, alongside with pictures indicating the extent of crevice corrosion. In the case of UNS S32750 polarized to +600 $mV_{Ag/AgCl}$, the two specimens did not initiate crevice corrosion at the same temperature. Since both specimens were tested simultaneously in the same container, the temperature was increased until the second specimen also developed crevice attack (i.e., specimen 1 developed crevice at 45 °C while specimen 2 showed crevice corrosion at 50°C).

As seen in Figure 8, OCP remained in the 0.05 to 0.25 $V_{Ag/AgCl}$ range in all cases with no clear stepwise drop. At the end of the tests, the external surface was covered by a thin layer of calcareous deposits and only minor signs of attack were found under the crevice formers. In contrast, all specimens polarised at +600 $mV_{Ag/AgCl}$ suffered crevice corrosion. All samples repassivated during the backward temperature stepwise ramp. As seen in Table 2, $T_{R,Crev}$

values were lower than CCT, indicating a hysteresis in critical temperatures. In the particular case of UNS S32750 polarized to +600 $mV_{Ag/AgCl}$, the two specimens obtained different $T_{R,Crev}$ (corresponding to 2.5°C < CCT, respectively), as indicated in Table 2. UNS S39274 exhibited higher CCT and $T_{R,Crev}$ values than the W-free UNS S32750 (Table 2), suggesting a higher resistance to crevice corrosion.

3.3. Surface characterisation

The number of localised attacks was quantified by visual inspection after both PD-GS-PD and long-term exposure testing. Figure 9 summarises the total number of localised attacks after PD-GS-PD testing. In this regard, the number of attacks increased with temperature; although UNS S32760 had approximately the same quantity of crevice sites from 40°C to 60°C. UNS S39274 had the lowest number of attacks up to 50°C; while at 60°C, UNS S32760 and the UNS S32974 rolled plate samples exhibited the lowest number of crevice sites.

Figure 10 summarises the depth of each attack found on the specimens exposed to natural seawater at OCP, together with the total number of crevice sites, and micrographs of the deepest attack for each material. The average crevice depth was slightly higher in UNS S39274 than in UNS S32750, but in all cases the crevice depth remained below 35 μm. The crevice corrosion severity was drastically higher in the specimens polarised at +600 $mV_{Ag/AgCl}$, where through-thickness penetration of some crevice sites was found, as illustrated in Figure 8c for UNS S32750. In the case of UNS S39274, the crevice attacks were large, but did not penetrate through the thickness (Figure 8d).

The extent of all attacks in the PD-GS-PD tests was further quantified and illustrated in Figure 11 by (a) the total volume of the attack, (b) the projected area on the surface, and (c) the maximum depth of the crevices after PD-GS-PD testing. Some interesting findings can be

highlighted by comparing Figure 11 with the $E_{R,Crev}$ and E_{Trans} extracted from Figure 7. Below the critical temperature, the extent of transpassive attack was approximately similar in range for the three materials. The dispersion in depth, area, and volume increased as the temperature approached the critical value, with maximum values increasing with temperature for all materials. The large increase in dispersion and the differences in maximum values above and below the $T_{R,Crev}$ can be used to identify the transition from transpassive dissolution to crevice corrosion, as discussed below.

The maximum crevice depth, maximum crevice volume, and maximum corrosion area at the transition between E_{Trans} and $E_{R,Crev}$ were obtained from Figure 11 and are summarised in Table 3. The maximum crevice depth values gathered in Table 3 were considered the threshold to define the transition to stable crevice attack. Below this value, the attack was considered to be transpassive dissolution. On the contrary, above this value, crevice corrosion took place in the GS or backward PD steps and the potential threshold obtained was $E_{R,Crev}$. Accordingly, crevice corrosion in UNS S32750 stabilised at lower transpassive attack depths than the W-containing SDSS.

Selected samples were further analysed by SEM-EDS to gain a better understanding of the crevice dissolution process. Figures 12 and 13 illustrate crevice attacks found by SEM after the PD-GS-PD tests. SEM-EDS analysis revealed different degrees of corrosion depending on the propagation size. Selective dissolution of ferrite (α) occurred during the early stages of the attack whereas austenite (γ) corroded as corrosion propagated into the crevice. Thereby, the following 4 stages were identified, and they are numbered in Figure 12: (i) phase boundary attack, (ii) selective corrosion of α, (iii) initiation of γ dissolution, and (iv) complete dissolution of all phases.

3.4. Additional characterisations

The concentration of ions released after the PD-GS-PD tests was quantified by ICP-MS. Figure 14 shows the results for the specimens that exhibited crevice corrosion, i.e., low $E_{R,Crev}$ values. For most materials, Cr and Fe cations were the main elements dissolved into the electrolyte. The exception was UNS S39274 rolled plate, which had a preferential W, Ni, and Mo dissolution but a low Cr and Fe release when compared with the other tree materials.

Figure 15 illustrates the Q_{exp} calculated from the PD-GS-PD tests in C/cm^2, as it is typically reported in the literature. [21, 25] The Q_{exp} was four times larger in Figure 15b than in Figure 15a because the i_{GS} used was four times higher, as explained in the experimental section. UNS S32750 had a larger Q_{exp} at 50°C and the highest Q_{exp} in all cases with an i_{GS} = 100 $\mu A/cm^2$. Nevertheless, at 60°C and i_{GS} = 25 $\mu A/cm^2$, UNS S39274 showed the largest Q_{exp}.

4. Discussion

4.1. Disadvantages of the PD-GS-PD technique

Although the PD-GS-PD technique has been applied successfully to study the crevice corrosion of Ni-alloys [29-35] and some stainless steels [36, 37]; in this work, the technique showed limitations. The first issue was the effect of the metastable activity and high current noise experienced for some materials at all temperatures, but particularly near the transition temperature. The current density of these metastable events and the associated current noise was high enough to trigger the GS step before reaching the critical crevice potential or E_{Trans}, as seen in Figure 4a. As a result, the potential increased during the GS step (Figure 5) instead of remaining constant (in the case of no corrosion) or decrease with time (if corrosion initiated). Earlier published data [32, 35] showed a similar potential increase during the GS step, although it was attributed to the inhibiting effect of Cr or Cu ions in solution being studied and not to an experimental artefact. It was, thus, necessary to increase the value of the

i_{GS} from 25 to 100 μA/cm^2 to circumvent this problem. As seen in Figure 5, the initial potential achieved during the GS step was only slightly higher (approximately 10 mV) with 100 μA/cm^2 than with 25 μA/cm^2.

For samples that developed stable crevice corrosion, the $E_{R,Crev}$ was independent of the choice of i_{GS}, as illustrated in Figure 6, despite the differences in charge passed during testing (Figure 15). Even though the Q_{exp} values were lower than those reported for UNS S30400, S31603, and N08825 [21, 25], it is, thus, reasonable to assume that the crevices were large enough with both i_{GS} values [30].

The second observation is that, in all cases, the forward scan reached transpassive values, which a priori could influence the crevice initiation step. Even though Cr cannot passivate at transpassive potentials, thermodynamically Fe can [47], and it has been shown that UNS S32750 forms a Fe passive layer at those potentials [49]. Additionally, an insoluble Mo-rich layer has been found at transpassive potentials for Ni-alloys, suggested to form as result of a local decrease in pH due to the hydrolysis of Fe(III) ions dissolved in the crevice solution [50]. Additionally, it has been reported that the passive film on UNS S32750 is completely dissolved at 1.4 $V_{Ag/AgCl}$ [51]. Nevertheless, even if the passive film is not completely dissolved, it is Cr-depleted in comparison with the film at lower passive potentials. As result, the passive film is weaker and transpassive attack can occur [52-54]. Transpassive attack of (S)DSS leads to the preferential attack at phase boundaries [55, 56] followed by selective dissolution of the ferrite phase [51, 56]. Additionally, Jakobsen et al. [52] found that for temperatures below the CCT, transpassive attack propagates after initiation, but it is unstable.

The presence of a small hysteresis loop even in specimens that did not suffer crevice corrosion (Figure 3b) is a consequence of reaching transpassive potentials in the forward PD scan. Therefore, the term $E_{R,Crev}$ is not applicable in these situations. Instead, E_{Trans} should be used to indicate that the hysteresis loop was caused by transpassive dissolution. In this work,

$E_{R,Crev}$ and E_{Trans} were differentiated based on the E-log(i) behaviour followed by the specimen during the reverse PD scan. In the absence of crevice corrosion, the current density during the reverse PD scan rapidly decreased obtaining a new E_{corr} within the oxygen evolution potential range [47] (Figure 3b). This E_{corr} coincided with a change in the slope of the forward PD scan, indicating a change in the electrochemical reaction occurring on the surface (most likely signalling the onset of the transpassive region or the oxygen evolution reaction [47]).

Based on the observations presented above, it is, thus, reasonable to assume that crevice corrosion initiation on SDSS during PD-GS-PD testing at temperatures below CCT requires a minimum amount of transpassive attack in the forward PD scan or during the initial stage of the GS step. In this regard, repassivation will occur quickly and at high potentials if the depth of the transpassive attack is below a critical value, $x_{Crit,Trans}$. Contrarily, crevice corrosion will initiate and propagate during the GS and backward PD steps above $x_{Crit,Trans}$. The maximum depth of the transpassive attack found at the transition temperature, i.e., below the $T_{R,Crev}$, was considered as an estimator of $x_{Crit,Trans}$. As seen in Table 3, W increased the maximum depth of the transpassive attack, suggesting an increase in the critical depth required to stabilize crevice corrosion.

Another unexpected result was the delay in the crevice corrosion initiation for some of the specimens. In some instances, crevice corrosion initiated during the backward PD scan, instead of during the GS step as seen in Figure 4b. The same behaviour was observed in other works [36, 44, 57] for cases where the material suffered mild localised corrosion. This issue may be avoided by either extending the duration of the GS step, by using PTFE-covered ceramic crevice formers since they have been shown to produce more demanding crevices in highly corrosion resistant nickel-based alloys [31, 58, 59], or both. Nevertheless, $E_{R,Crev}$ values were independent of whether crevice corrosion started in the GS or backward PD step.

The Q_{exp} measured in both cases was similar, suggesting the same extent of the crevice attack.

During the backward PD scan, all specimens experienced a maximum in current density around 0.1 to 0.4 $V_{Ag/AgCl}$ (e.g., Figures 3a and 4b). In this regard, the reversible potential for the reduction of Cr(VI) to Cr(III) lies within this potential range for the tested conditions [47]. Therefore, the formation of a Cr-rich passive film is thermodynamically stable in this potential range and, consequently, the current density drops shortly after, stifling crevice corrosion propagation.

4.2. Effect of W on crevice corrosion resistance

Crevice corrosion did not initiate in the forward scan for any of the materials in the tested temperature conditions, making the determination of the CCT impossible. CCT values of UNS S32750 reported in the literature obtained from CPP tests are in the 65-70°C range both in simulated and natural seawater environments [7, 44], which are above the temperatures tested herein. The $T_{R,Crev}$ was determined as the temperature at which the results transitioned from E_{Trans} to $E_{R,Crev}$, as explained in section 3.1. Peguet et al. [55] described a transition temperature interval for CPT up to 10°C for the DSS UNS S32205. On the other hand, Sun et al. [60] suggested that only DSSs present the transition temperature interval because of their inhomogeneous microstructure, as the austenitic stainless steels tested by these authors showed a sharp CPT transition. Nevertheless, since the temperature interval used herein was ≥ 10°C, no clear transition temperature interval could be observed for the $T_{R,Crev}$.

The long-term experiments in natural seawater performed in this work showed that specimens freely exposed in natural seawater exhibited small attacks that did not affect the OCP up to 80°C, which made the determination of the critical temperature impossible. In contrast, the CCT measured at an applied potential of +600 $mV_{Ag/AgCl}$, which simulated chlorination

treatments [7, 40], was 45°C and 55°C for UNS S32750 and UNS S39274, respectively. Interestingly, the CCT values determined from the potentiostatic long-term exposure tests were similar to the $T_{R,Crev}$ results of the PD-GS-PD tests (Table 2), suggesting that, for SDSS, $T_{R,Crev}$ obtained by PD-GS-PD could be used as an estimator of crevice corrosion initiation in materials selection.

The $T_{R,Crev}$ of UNS S32750 obtained by PD-GS-PD testing and after long-term exposure (i.e., 40 and 42.4 °C, respectively) was lower than reported values in natural or simulated seawater environments (i.e., 56°C) [7, 44]. The differences in $T_{R,Crev}$ were attributed to the severity of the PD-GS-PD technique when compared to the CPP method and the extended duration of the temperature steps in the long-term test. Only one study [36] obtained a lower $T_{R,Crev}$ than in this work – the $T_{R,Crev}$ was below 30°C-, even though the electrolyte consisted of a more dilute NaCl solution (10,000 ppm Cl^-). The same PD-GS-PD technique was used, but the crevice formers were ceramic and covered with PTFE tape, resulting in a more aggressive localised attack [31, 58, 59].

Despite the experimental limitations discussed above, results indicated that tungsten increased the crevice corrosion resistance of SDSS, as determined by both CCT and $T_{R,Crev}$ values (Figures 7 and 8 and Table 2), and indirectly by the increase in $x_{Crit,Trans}$ (Table 3). In this regard, the W-free material (UNS S32750) had the lowest $T_{R,Crev}$ measured both by the PD-GS-PD method and potentiostatic testing at +600 $mV_{Ag/AgCl}$ in natural seawater (i.e., 40 and 42.5°C, respectively), whereas $T_{R,Crev}$ increased with incremental W content as summarised in Table 2. These findings are in agreement with a previous work [7] where only two SDSSs containing different degrees of W were investigated by performing CPP. By including a W-free SDSS as a reference, the enhancement of localized corrosion resistance due to the W could be inferred. Additionally, a higher extent of crevice corrosion propagation

was achieved by using the PD-GS-PD technique in comparison to the CPP, facilitating a better comparison among the materials in a wider temperature range.

It might be questioned, however, whether the small changes in the concentration of other alloying elements as seen in Table 1 could explain the differences observed in this investigation. In this regard, some of the elements have an important weight in the PRE formula such as Cr, Mo and N. Nevertheless, the impact of such changes in composition could be ruled out by comparing $T_{R,Crev}$ values of the different SDSS. In this regard, the W-free UNS S32750 contained the highest amount of Cr and Mo, yet showed the lowest $T_{R,Crev}$ values. Similarly, UNS S32760 contained the lowest amount of N among the SDSSs but gave an intermediate $T_{R,Crev}$ result. Another element—not included in the standard PRE expression—that has been shown to increase the CPT and the overall localized corrosion resistance in halide environments is Cu [61, 62]. However, as discussed by Haugan et al. [7] the improvement in CPT in DSS by Cu was much lower than that obtained by W, and, thus, the role of small changes in Cu content could be ignored.

4.3. Influence of the manufacturing route

Haugan et al [7], investigated the effect of W on the crevice corrosion resistance of two SDSS using a combination of methods that included CPP testing. However, the two SDSS studied also differed in product form. In this regard, the high-W UNS S32974 was produced as a rolled plate, whereas the UNS S32750 samples were extracted from an extruded pipe. Given that product form-to-product form variations can have an important effect on localised corrosion resistance [63], the influence of the manufacturing route was also studied herein, using samples extracted from the same plate as Haugan et al. [7].

As seen in Table 1, the rolled plate specimens had a higher Ni and N content than the extruded pipe specimens. Conversely, the Mo, Cu, and Fe contents were slightly lower in the

rolled plate. Even though Ni improves the corrosion resistance in acidic reducing environments, it does not influence localised corrosion resistance in oxidising chloride-containing solutions [3]. Despite the differences in N and Mo content, both materials had identical PRE values. Consequently, based on their chemical composition both materials were expected to exhibit similar crevice corrosion resistance. However, the results in this work (Figure 7) showed a small but measurable influence of the manufacturing process in the $T_{R,Crev}$ values. In this regard, the average $T_{R,Crev}$ of the extruded pipe was approximately 55°C whereas that of the rolled plate was 60°C. Additionally, the number of crevice sites (Figure 9) was higher in the extruded pipe, but the maximum crevice volume was larger in the rolled plate case (Figure 10). More research is needed to elucidate the influence of product form and heat-to-heat variations on crevice corrosion resistance.

5. Conclusions

In this work, the $T_{R,Crev}$ of three commercial SDSS containing incremental amounts of W was obtained by evaluating the $E_{R,Crev}$ values extracted from PD-GS-PD tests at different temperatures. Results were validated using long-term exposure in natural seawater at both the OCP and potentiostatically at +600 $mV_{Ag/AgCl}$, which allowed the estimation of CCT and $T_{R,Crev}$. The following conclusion were drawn based on the evidence provided in this work:

- The $T_{R,Crev}$ measured by the PD-GS-PD method increased with W content in solid solution.
- The 2.1 wt% UNS S39274 SDSS had the highest $T_{R,Crev}$ and the best crevice corrosion resistance as determined by both PD-GS-PD testing and long-term exposure to natural seawater. In this regard, the CCT and $T_{R,Crev}$ of UNS S39274 were 7.5 to 15 °C higher than the W-free control, depending on the measurement technique.

- A hysteresis in temperature was observed in the long-term potentiostatic tests at +600 $mV_{Ag/AgCl}$, indicating a difference between CCT and $T_{R,Crev}$ of 2.5. to 5°C depending on the material.
- The product form of UNS S39274 influenced corrosion resistance, with the rolled plate samples exhibiting a slightly better performance as determined by $T_{R,Crev}$.
- The crevice attack initiated at α/γ boundaries. In all cases, α selectively corroded; whereas dissolution of γ occurred at a later stage during crevice propagation.

6. Acknowledgments

The authors thank Dr. Edgar Hornus (Curtin University) for his contribution to the discussion of the results, and Dr. Syverin Lierhagen (NTNU) for performing the ICP-MS tests in the Department of Chemistry at NTNU. The authors also acknowledge Sumitomo Co. and Sandvik AS, who donated the various materials. This work was sponsored by NTNU's Department of Mechanical and Industrial Engineering.

7. Data availability

The raw/processed data generated in this work are available upon request from the corresponding author.

8. References

[1] J.M. Kolotyrkin, Pitting Corrosion of Metals, Corros., 19 (1963) 261t-268t, DOI: 10.5006/0010-9312-19.8.261.

[2] A.J. Sedriks, Plenary Lecture—1986: Effects of Alloy Composition and Microstructure on the Passivity of Stainless Steels, Corros., 42 (1986) 376-389, DOI: 10.5006/1.3584918.

[3] C.O.A. Olsson, D. Landolt, Passive films on stainless steels—chemistry, structure and growth, Electrochim. Acta, 48 (2003) 1093-1104, DOI: 10.1016/s0013-4686(02)00841-1.

[4] R.C. Newman, 2001 W.R. Whitney Award Lecture: Understanding the Corrosion of Stainless Steel, Corros., 57 (2001) 1030-1041, DOI: 10.5006/1.3281676.

[5] J.O. Nilsson, Super duplex stainless steels, Mater. Sci. Technol., 8 (1992) 685-700, DOI: 10.1179/mst.1992.8.8.685.

[6] R.F.A. Jargelius-Pettersson, Application of the Pitting Resistance Equivalent Concept to Some Highly Alloyed Austenitic Stainless Steels, Corros., 54 (1998) 162-168, DOI: 10.5006/1.3284840.

[7] E.B. Haugan, M. Næss, C. Torres Rodriguez, R. Johnsen, M. Iannuzzi, Effect of Tungsten on the Pitting and Crevice Corrosion Resistance of Type 25Cr Super Duplex Stainless Steels, Corros., 73 (2017) 53-67, DOI: 10.5006/2185.

[8] C. Torres, M.S. Hazarabedian, Z. Quadir, R. Johnsen, M. Iannuzzi, The Role of Tungsten on the Phase Transformation Kinetics and its Correlation with the Localized Corrosion Resistance of 25Cr Super Duplex Stainless Steels, J. Electrochem. Soc., 167 (2020) 081510, DOI: 10.1149/1945-7111/ab90af.

[9] N. Bui, A. Irhzo, F. Dabosi, Y. Limouzin-Maire, On the mechanism for improved passivation by additions of tungsten to austenitic stainless steels, Corros., 39 (1983) 491-496, DOI: 10.5006/1.3577373.

[10] A. Belfrouh, C. Masson, D. Vouagner, A.M. de Becdelievre, N.S. Prakash, J.P. Audouard, The cumulative effect of alloying elements N, W, Mo and Cu on the corrosion behaviour of 17Cr-13Ni stainless steel in 2 N H2SO4, Corros. Sci., 38 (1996) 1639-1648, DOI: 10.1016/s0010-938x(96)00033-9.

[11] N.D. Tomashov, G.P. Chernova, O.N. Marcova, Effect of Supplementary Alloying Elements On Pitting Corrosion Susceptibility Of 18Cr-14Ni Stainless Steel, Corros., 20 (1964) 166t-173t, DOI: 10.5006/0010-9312-20.5.166t.

[12] M.K. Ahn, H.S. Kwon, H.M. Lee, Quantitative comparison of the influences of tungsten and molybdenum on the passivity of Fe-29Cr ferritic stainless steels, Corros. Sci., 40 (1998) 307-322, DOI: 10.1016/s0010-938x(97)00138-8.

[13] E.-A. Cho, C.-K. Kim, J.-S. Kim, H.-S. Kwon, Quantitative analysis of repassivation kinetics of ferritic stainless steels based on the high field ion conduction model, Electrochim. Acta, 45 (2000) 1933-1942, DOI: 10.1016/s0013-4686(99)00415-6.

[14] R. Goetz, J. Laurent, D. Landolt, The influence of minor alloying elements on the passivation behaviour of iron-chromium alloys in HCl, Corros. Sci., 25 (1985) 1115-1126, DOI: 10.1016/0010-938x(85)90057-5.

[15] H. Habazaki, A. Kawashima, K. Asami, K. Hashimoto, The corrosion behavior of amorphous Fe-Cr-Mo-P-C and Fe-Cr-W-P-C alloys in 6 M HCl solution, Corros. Sci., 33 (1992) 225-236, DOI: 10.1016/0010-938x(92)90147-u.

[16] ASTM International, Standard Test Method for Conducting Cyclic Potentiodynamic Polarization Measurements for Localized Corrosion Susceptibility of Iron-, Nickel-, or Cobalt-Based Alloys, in, West Conshohocken, PA, 2018, DOI: 10.1520/G0061-86R18.

[17] R.M. Carranza, Environmental and metallurgical variables affecting crevice corrosion susceptibility of alloy 22 - A review, in: Corrosion 2008, NACE International, 2008, pp. 16.

[18] I.L. Rosenfeld, Breakdown of the Passive State and Repassivation of Stainless Steels, J. Electrochem. Soc., 125 (1978) 1729-1735, DOI: 10.1149/1.2131284.

[19] R.C. Newman, E.M. Franz, Growth and Repassivation of Single Corrosion Pits in Stainless Steel, Corros., 40 (1984) 325-330, DOI: 10.5006/1.3593930.

[20] N.G. Thompson, B.C. Syrett, Relationship Between Conventional Pitting and Protection Potentials and a New, Unique Pitting Potential, Corros., 48 (1992) 649-659, DOI: 10.5006/1.3315985.

[21] D.S. Dunn, G.A. Cragnolino, N. Sridhar, An Electrochemical Approach to Predicting Long-Term Localized Corrosion of Corrosion-Resistant High-Level Waste Container Materials, Corros., 56 (2000) 90-104, DOI: 10.5006/1.3280526.

[22] T. Nakayama, K. Sasa, Effect of Ultrasonic Waves on the Pitting Potentials of 18-8 Stainless Steel in Sodium Chloride Solution, Corros., 32 (1976) 283-285, DOI: 10.5006/0010-9312-32.7.283.

[23] H. Yashiro, K. Tanno, The effect of electrolyte composition on the pitting and repassivation behavior of AISI 304 stainless steel at high temperature, Corros. Sci., 31 (1990) 485-490, DOI: 10.1016/0010-938x(90)90150-4.

[24] E.C. Hornus, M.A. Rodríguez, R.M. Carranza, R.B. Rebak, Effect of Temperature and Chloride Concentration on the Crevice Corrosion Resistance of Austenitic Stainless Steels, in: Corrosion 2016, NACE International, 2016.

[25] N. Sridhar, G.A. Cragnolino, Applicability of Repassivation Potential for Long-Term Prediction of Localized Corrosion of Alloy 825 and Type 316L Stainless Steel, Corros., 49 (1993) 885-894, DOI: 10.5006/1.3316014.

[26] T. Shibata, T. Takeyama, Stochastic Theory of Pitting Corrosion, Corros., 33 (1977) 243-251, DOI: 10.5006/0010-9312-33.7.243.

[27] S. Tsujikawa, Y. Hisamatsu, On the Repassivation Potential for Crevice Corrosion, Corros. Eng., 29 (1980) 37-40, DOI: 10.3323/jcorr1974.29.1_37.

[28] ASTM International, Standard Test Method for Determining the Crevice Repassivation Potential of Corrosion-Resistant Alloys Using a Potentiodynamic-Galvanostatic-Potentiostatic Technique, in, ASTM International, West Conshohocken, PA, 2014, DOI: 10.1520/G0192-08R14.

[29] A.K. Mishra, G.S. Frankel, Crevice Corrosion Repassivation of Alloy 22 in Aggressive Environments, Corros., 64 (2008) 836-844, DOI: 10.5006/1.3279917.

[30] M.R. Ortíz, M.A. Rodríguez, R.M. Carranza, R.B. Rebak, Determination of the Crevice Corrosion Stabilization and Repassivation Potentials of a Corrosion-Resistant Alloy, Corros., 66 (2010) 105002-105002-105012, DOI: 10.5006/1.3500830.

[31] C.M. Giordano, M. Rincón Ortíz, M.A. Rodríguez, R.M. Carranza, R.B. Rebak, Crevice corrosion testing methods for measuring repassivation potential of alloy 22, Corros. Eng. Sci. Technol., 46 (2011) 129-133, DOI: 10.1179/1743278210y.0000000014.

[32] M. Rincón Ortíz, M.A. Rodríguez, R.M. Carranza, R.B. Rebak, Oxyanions as inhibitors of chloride-induced crevice corrosion of Alloy 22, Corros. Sci., 68 (2013) 72-83, DOI: 10.1016/j.corsci.2012.10.037.

[33] A.K. Mishra, D.W. Shoesmith, Effect of Alloying Elements on Crevice Corrosion Inhibition of Nickel-Chromium-Molybdenum-Tungsten Alloys Under Aggressive Conditions: An Electrochemical Study, Corros., 70 (2014) 721-730, DOI: 10.5006/1170.

[34] E.C. Hornus, C.M. Giordano, M.A. Rodriguez, R.M. Carranza, R.B. Rebak, Effect of Temperature on the Crevice Corrosion of Nickel Alloys Containing Chromium and Molybdenum, J. Electrochem. Soc., 162 (2015) C105-C113, DOI: 10.1149/2.0431503jes.

[35] A.K. Mishra, X. Zhang, D.W. Shoesmith, The Role of Copper on the Crevice Corrosion Behavior of Nickel-Chromium-Molybdenum Alloys in Aggressive Solutions, Corros., 72 (2016) 356-367, DOI: 10.5006/1876.

[36] P.A. Martínez, E.C. Hornus, M.A. Rodríguez, R.M. Carranza, R.B. Rebak, Crevice Corrosion Resistance of Super-Austenitic and Super-Duplex Stainless Steels in Chloride Solutions, in: Corrosion 2015, NACE International, Dallas, Texas, 2015.

[37] M.A. Kappes, M.R. Ortíz, M. Iannuzzi, R.M. Carranza, Use of the Critical Acidification Model to Estimate Critical Localized Corrosion Potentials of Duplex Stainless Steels, Corros., 73 (2017) 31-40, DOI: 10.5006/2142.

[38] E.A. Abd El Meguid, A.A. Abd El Latif, Electrochemical and SEM study on Type 254 SMO stainless steel in chloride solutions, Corros. Sci., 46 (2004) 2431-2444, DOI: 10.1016/j.corsci.2004.01.022.

[39] ISO, Corrosion of metals and alloys - Crevice corrosion formers with disc springs for flat specimens or tubes made from stainless steel, in, International Organization for Standardization, Geneva, Switzerland, 2015.

[40] R. Johnsen, H. Vingsand, Corrosion Properties Of UNS S32750, UNS N06022 And UNS N10276 In Seawater, in: CORROSION 2009, NACE International, Atlanta, Georgia, 2009, pp. 16.

[41] S. Valen, P.O. Gartland, Crevice Corrosion Repassivation Temperatures of Highly Alloyed Stainless Steels, Corros., 51 (1995) 750-756, DOI: 10.5006/1.3293552.

[42] U. Steinsmo, T. Rogne, J.M. Drugli, P.O. Gartland, Critical Crevice Temperature for High-Alloyed Stainless Steels in Chlorinated Seawater Applications, Corros., 53 (1997) 26-32, DOI: 10.5006/1.3280430.

[43] A.B. Høydal, E. Skavås, T. Hemmingsen, Crevice Corrosion on Super Duplex Stainless Steel – Effect of Potential on Critical Crevice Corrosion Temperature, in: Corrosion 2013, NACE International, 2013.

[44] L.L. Machuca, S.I. Bailey, R. Gubner, Systematic study of the corrosion properties of selected high-resistance alloys in natural seawater, Corros. Sci., 64 (2012) 8-16, DOI: 10.1016/j.corsci.2012.06.029.

[45] J.W. Oldfield, W.H. Sutton, Crevice Corrosion of Stainless Steels: II. Experimental studies, Br. Corros. J., 13 (1978) 104-111, DOI: 10.1179/000705978798276258.

[46] Digital Surf, www.digitalsurf.com, 1996 (accessed 14 February 2020).

[47] M. Pourbaix, Atlas of Electrochemical Equilibria in Aqueous Solutions, National Association of Corrosion Engineers (NACE), Houston, Texas, USA, 1974.

[48] E. Bardal, J.M. Drugli, P.O. Gartland, The behaviour of corrosion-resistant steels in seawater: A review, Corros. Sci., 35 (1993) 257-267, DOI: 10.1016/0010-938x(93)90157-c.

[49] G. Tranchida, F. Di Franco, M. Santamaria, Role of Molybdenum on the Electronic Properties of Passive Films on Stainless Steels, J. Electrochem. Soc., 167 (2020), DOI: 10.1149/1945-7111/ab7f8a.

[50] J.D. Henderson, X. Li, D.W. Shoesmith, J.J. Noël, K. Ogle, Molybdenum surface enrichment and release during transpassive dissolution of Ni-based alloys, Corros. Sci., 147 (2019) 32-40, DOI: 10.1016/j.corsci.2018.11.005.

[51] C. Örnek, M. Långberg, J. Evertsson, G. Harlow, W. Linpé, L. Rullik, F. Carlà, R. Felici, E. Bettini, U. Kivisäkk, E. Lundgren, J. Pan, In-situ synchrotron GIXRD study of passive film evolution on duplex stainless steel in corrosive environment, Corros. Sci., 141 (2018) 18-21, DOI: 10.1016/j.corsci.2018.06.040.

[52] P.T. Jakobsen, E. Maahn, Temperature and potential dependence of crevice corrosion of AISI 316 stainless steel, Corros. Sci., 43 (2001) 1693-1709, DOI: 10.1016/s0010-938x(00)00167-0.

[53] I. Betova, M. Bojinov, T. Laitinen, K. Mäkelä, P. Pohjanne, T. Saario, The transpassive dissolution mechanism of highly alloyed stainless steels, Corros. Sci., 44 (2002) 2675-2697, DOI: 10.1016/s0010-938x(02)00073-2.

[54] G. Song, Transpassivation of Fe–Cr–Ni stainless steels, Corros. Sci., 47 (2005) 1953-1987, DOI: 10.1016/j.corsci.2004.09.007.

[55] L. Peguet, A. Gaugain, C. Dussart, B. Malki, B. Baroux, Statistical study of the critical pitting temperature of 22-05 duplex stainless steel, Corros. Sci., 60 (2012) 280-283, DOI: 10.1016/j.corsci.2012.03.025.

[56] L. Peguet, A. Gaugain, Localized corrosion resistance of duplex stainless steels: methodology and properties; a review paper, Revue de Métallurgie, 108 (2011) 231-243, DOI: 10.1051/metal/2011062.

[57] G. Mori, D. Bauernfeind, Pitting and crevice corrosion of superaustenitic stainless steels, Mater. Corros., 55 (2004) 164-173, DOI: 10.1002/maco.200303746.

[58] X. Shan, J.H. Payer, Comparison of Ceramic and Polymer Crevice Formers on the Crevice Corrosion Behavior of Ni-Cr-Mo Alloy C-22, in: Corrosion 2007, NACE International, 2007.

[59] X. Shan, J.H. Payer, Effect of Polymer and Ceramic Crevice Formers on the Crevice Corrosion of Ni-Cr-Mo Alloy 22, Corros., 66 (2010) 105005-105005-105014, DOI: 10.5006/1.3500833.

[60] Y.T. Sun, J.M. Wang, Y.M. Jiang, J. Li, A comparative study on potentiodynamic and potentiostatic critical pitting temperature of austenitic stainless steels, Mater. Corros., 69 (2018) 44-52, DOI: 10.1002/maco.201709641.

[61] L.F. Garfias-Mesias, J.M. Sykes, C.D.S. Tuck, The effect of phase compositions on the pitting corrosion of 25 Cr duplex stainless steel in chloride solutions, Corros. Sci., 38 (1996) 1319-1330, DOI: 10.1016/0010-938x(96)00022-4.

[62] L.F. Garfias-Mesias, J.M. Sykes, Effect of Copper on Active Dissolution and Pitting Corrosion of 25% Cr Duplex Stainless Steels, Corros., 54 (1998) 40-47, DOI: 10.5006/1.3284827.

[63] F. Bocher, R. Huang, J.R. Scully, Prediction of Critical Crevice Potentials for Ni-Cr-Mo Alloys in Simulated Crevice Solutions as a Function of Molybdenum Content, Corros., 66 (2010) 055002-055001 to 055002-055015, DOI: 10.5006/1.3430462.

Figure captions

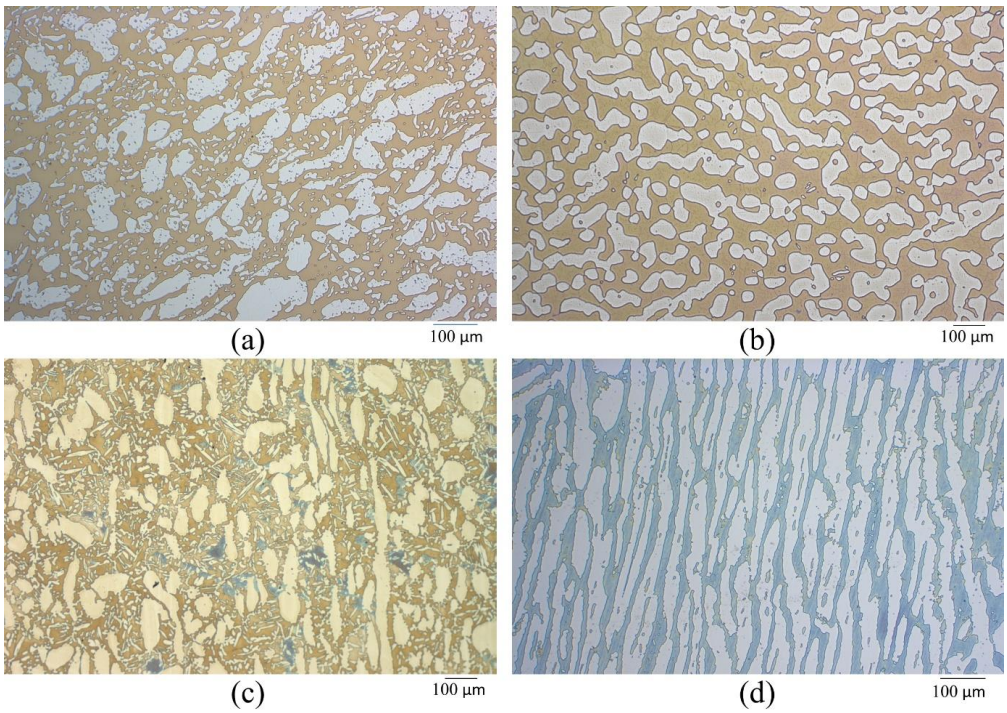

Figure 1. Micrograph taken by light optical microscope of (a) UNS S32750, (b) UNS S32760, (c) UNS S39274 extruded pipe, and (d) UNS S39274 rolled plate. The microstructure was revealed by applying two different etching steps. In the first step, a 15 wt.% KOH solution was used, and a potential of 3 V was applied for 12 s. In the second step, the solution was 20 wt.% NaOH with an applied potential of 1.5 V for 10 s.

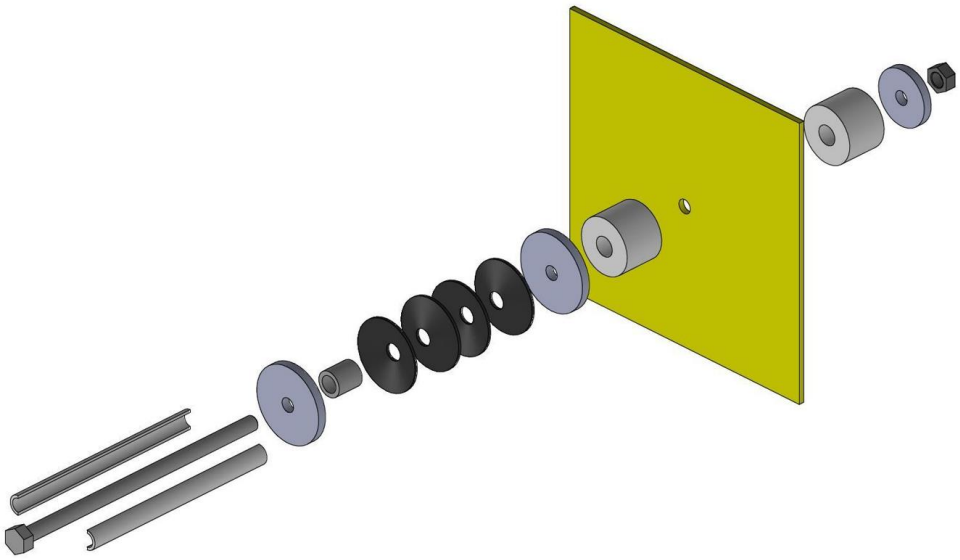

Figure 2. Schematic diagram of the multi-crevice assembly described in ISO18070 [128].

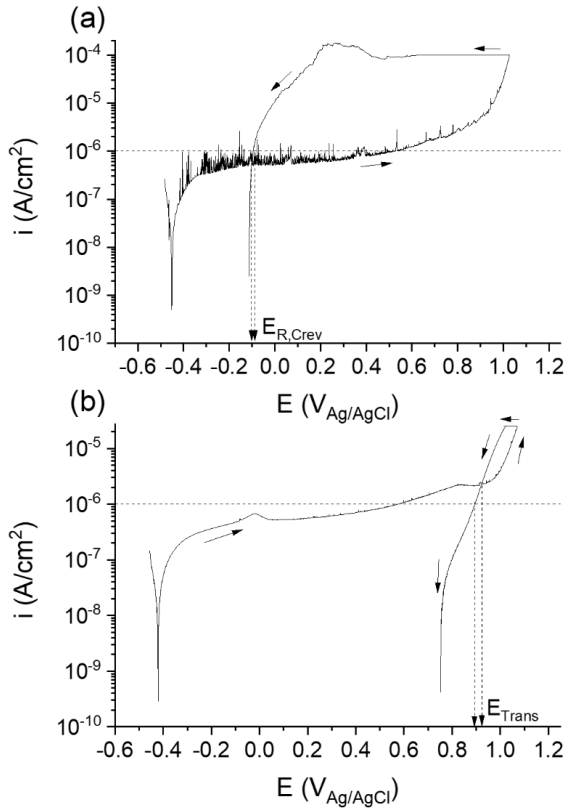

Figure 3. PD-GS-PD plots of (a) UNS S32750 at 60°C and (b) UNS S39274 extruded pipe at room temperature. Arrows indicate the direction of the scan. Dashed arrows indicate how $E_{R,Crev}$ and E_{Trans} were obtained from the cross-over potential and 1 µA/cm^2 definitions.

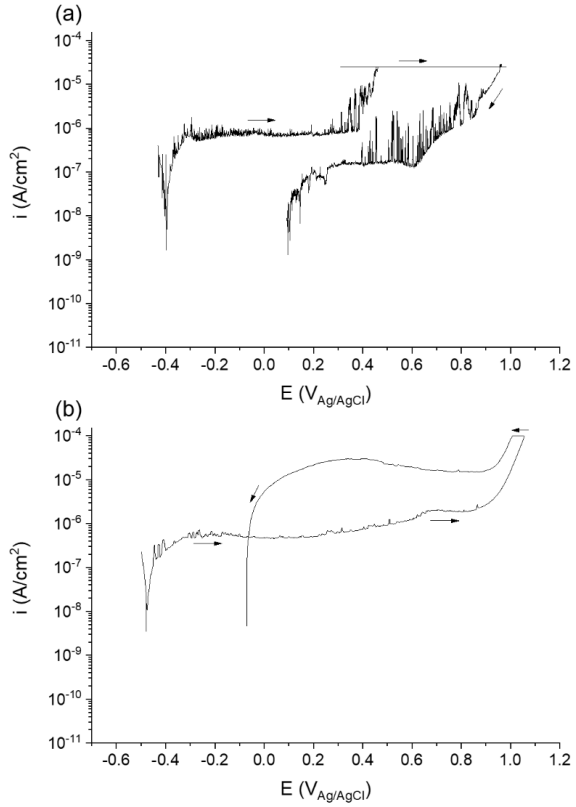

Figure 4. PD-GS-PD plots of (a) UNS S32760 at 50°C with an i_{GS} of 25 µA/cm^2 and (b) UNS S39274 extruded pipe at 60°C with an i_{GS} of 100 µA/cm^2. Arrows indicate the direction of the scan.

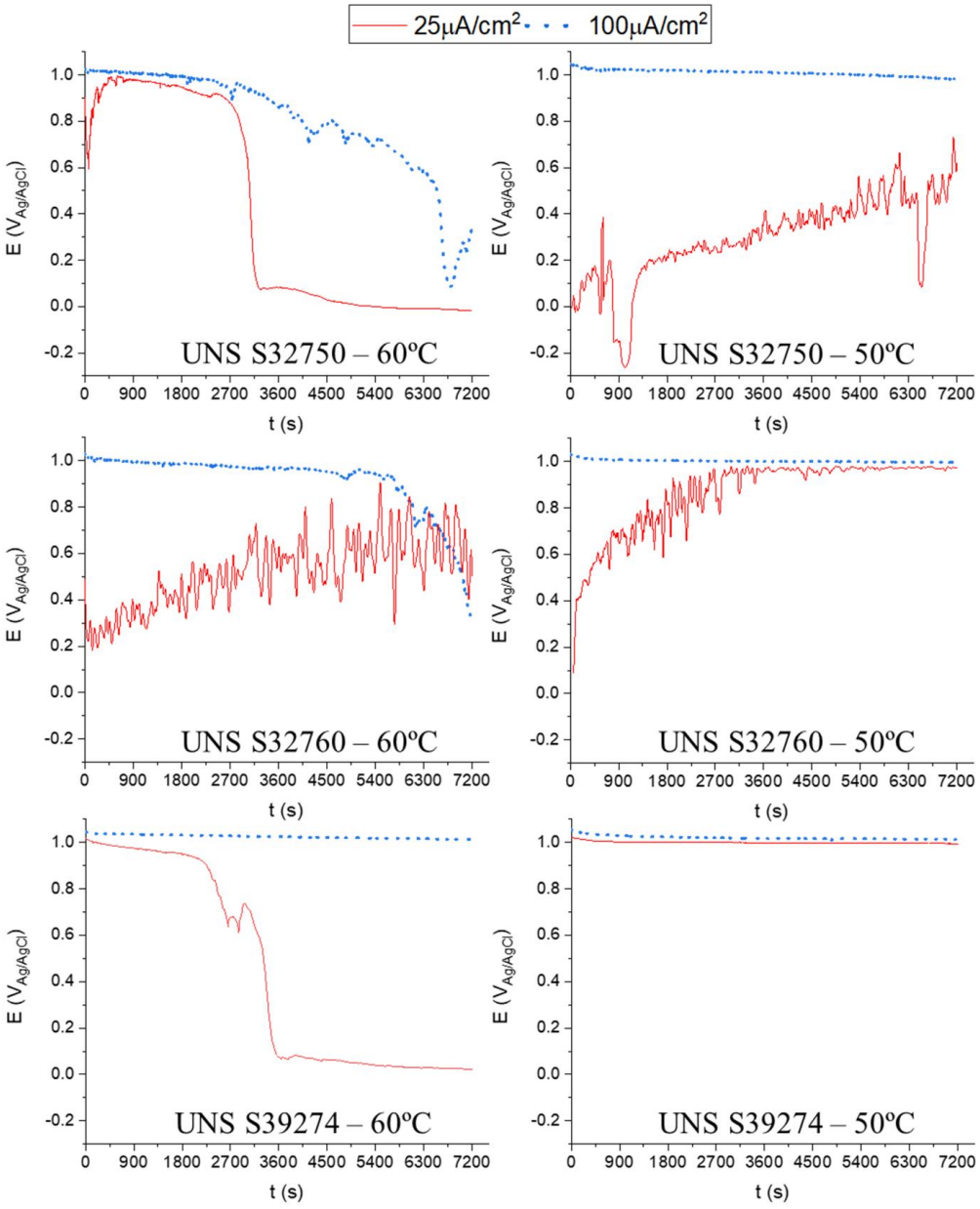

Figure 5. Potential evolution during the galvanostatic step of the PD-GS-PD tests for the extruded pipe materials tested at 50°C and 60°C at two i_{GS} values as indicated.

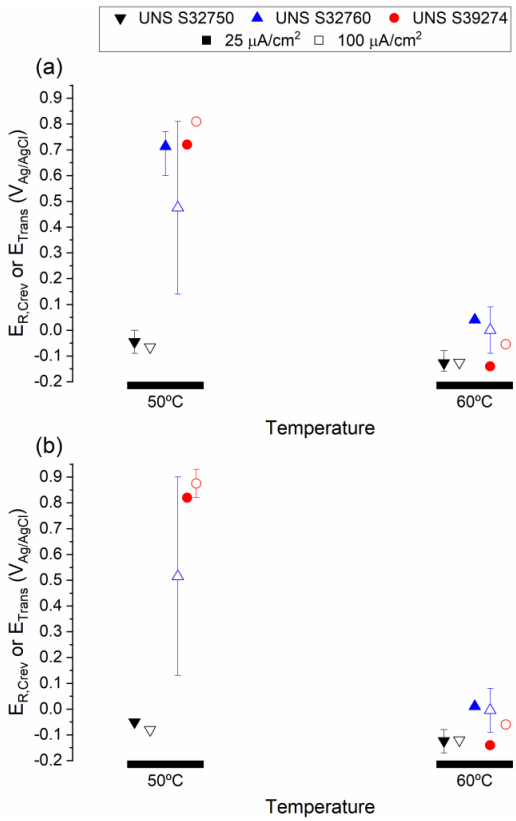

Figure 6. A comparison of the effect of i_{GS} on $E_{R,Crev}$ and E_{Trans}. The values were obtained for the extruded pipe materials from the PD-GS-PD tests at 50°C and 60°C; $E_{R,Crev}$ and E_{Trans} determined as (a) backward PD scan reaching 1 μA/cm^2 and (b) cross-over of forward and backward PD. Error bars show maximum and minimum values.

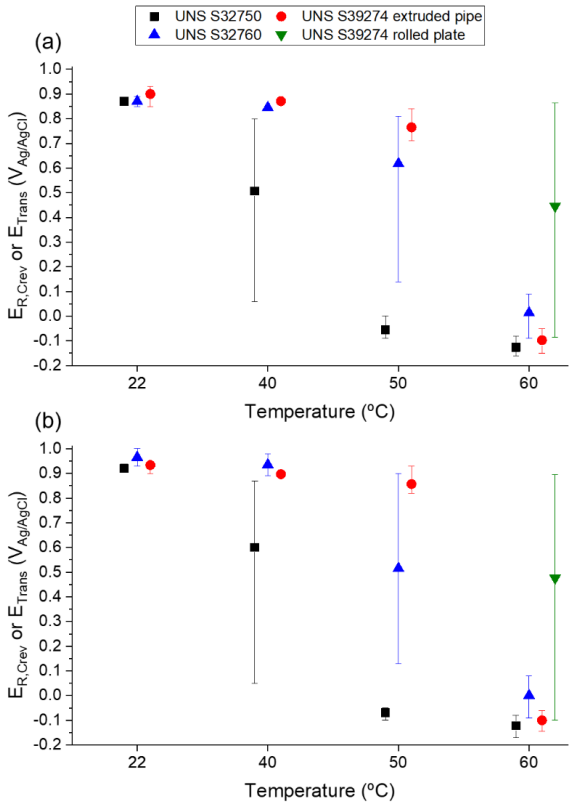

Figure 7. $E_{R,Crev}$ or E_{Trans} values obtained for all materials from all the PD-GS-PD tests, defined as (a) backward PD scan reaching 1 μA/cm^2, and (b) cross-over of forward and backwards PD. Error bars show maximum and minimum values.

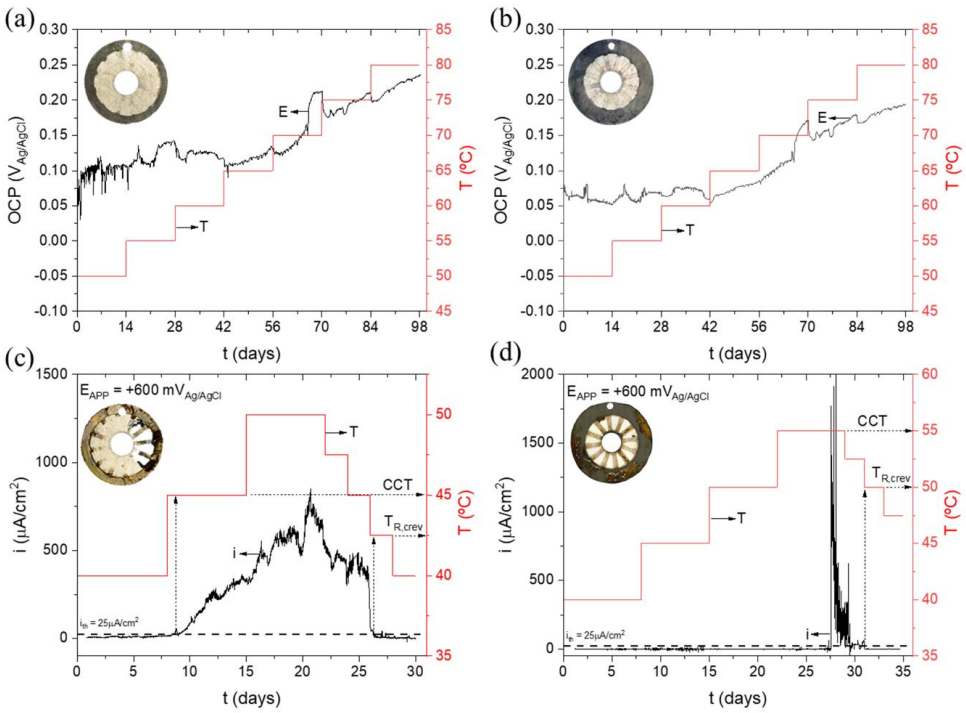

Figure 8. CCT and $T_{R,Crev}$ tests in natural seawater of extruded pipe materials (a) UNS S32750 at OCP, (b) UNS S39274 at OCP, (c) UNS S32750 polarised to +600 $mV_{Ag/AgCl}$, and (d) UNS S39274 polarised to +600 $mV_{Ag/AgCl}$, the picture inserts show a specimen after exposure to illustrate the attack.

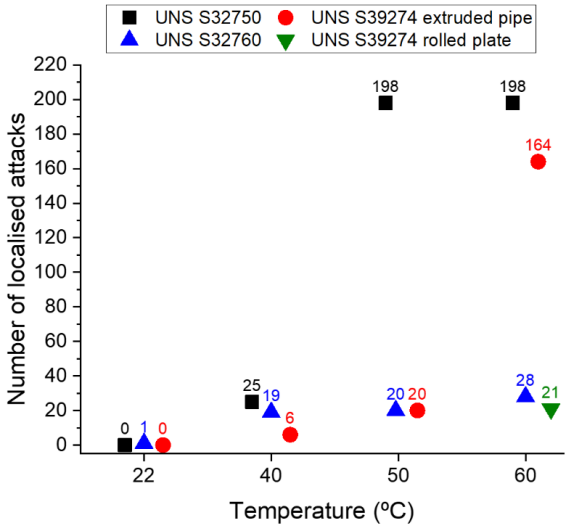

Figure 9. Total number of localised corrosion attacks in 2 specimens for each material and test temperature after the PD-GS-PD testing.

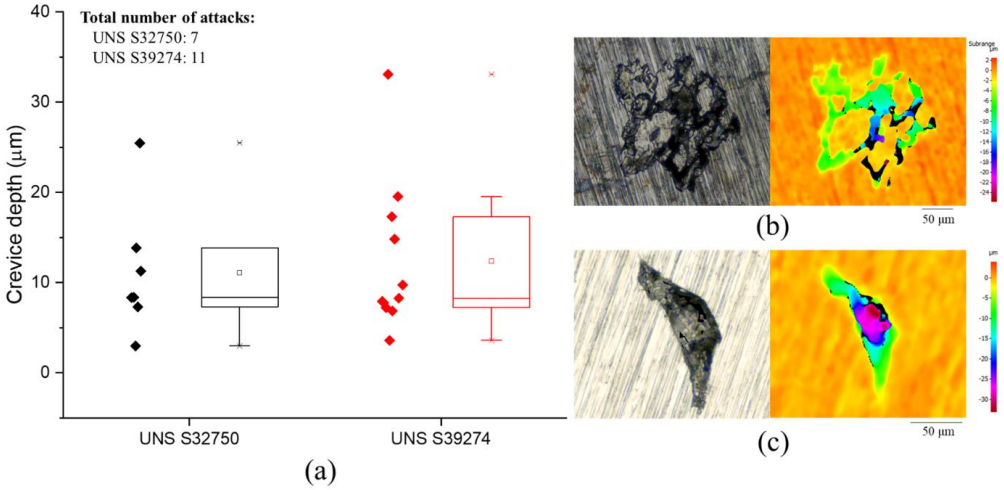

Figure 10. (a) All localized attacks depths, (b) pictures of deepest attack on UNS S32750, and (c) picture of deepest attack on UNS S39274 found on the specimens exposed at OCP in natural seawater.

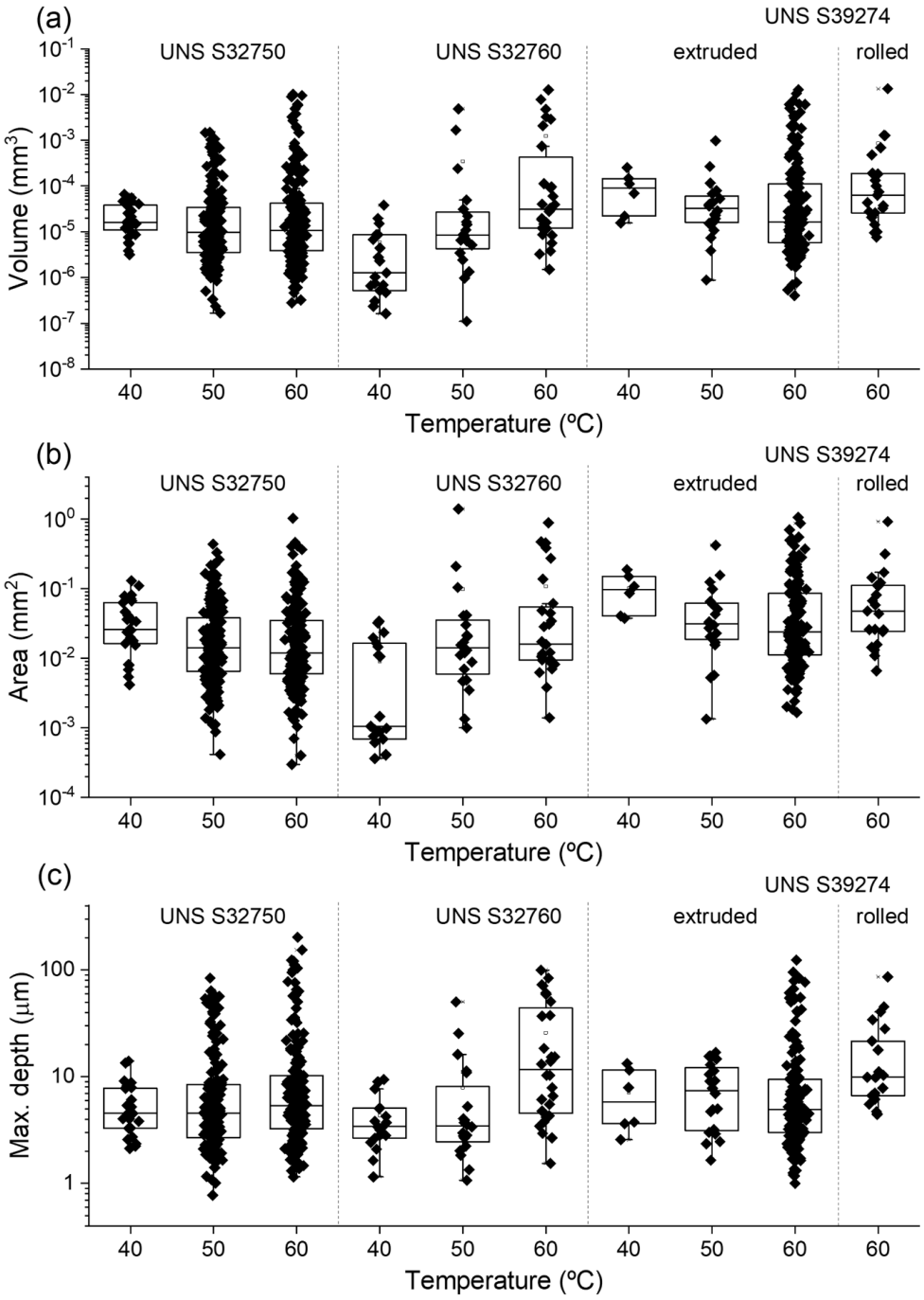

Figure 11. Crevice size measurements (a) volume, (b) area, and (c) maximum depth present in 2 specimens of all extruded materials after the PD-GS-PD tests at all temperatures.

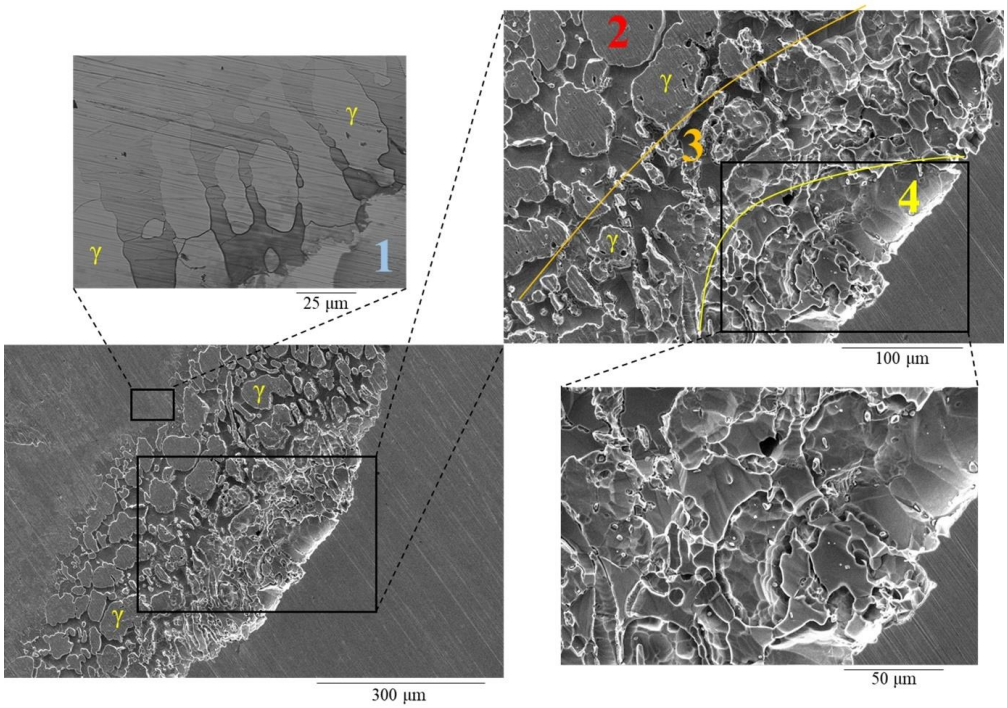

Figure 12. SEM pictures of a crevice attack found in UNS S32750 after the PD-GS-PD tests at 60°C. The numbers indicate the propagation stage: (1) phase boundary attack as the attack grows in area, (2) selective dissolution of α phase, (3) partial γ dissolution, and (4) γ is completely dissolved and the attack deepens.

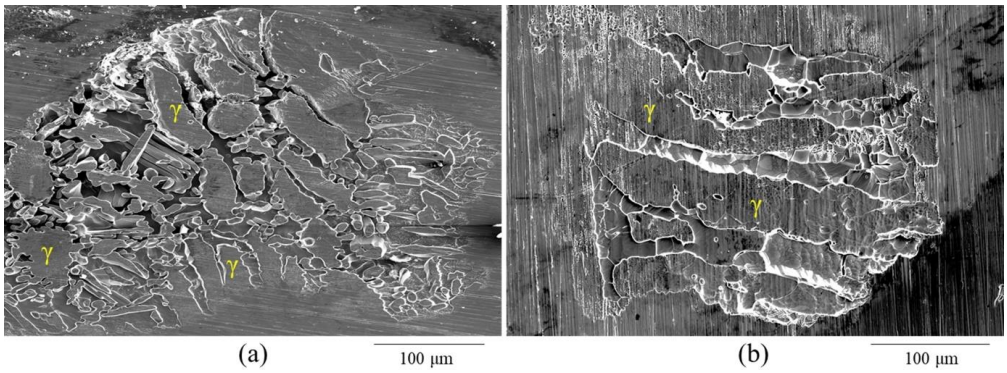

Figure 13. SEM pictures illustrating the crevice attack found in UNS S39274 (a) extruded pipe and (b) rolled plate after the PD-GS-PD tests at 60°C.

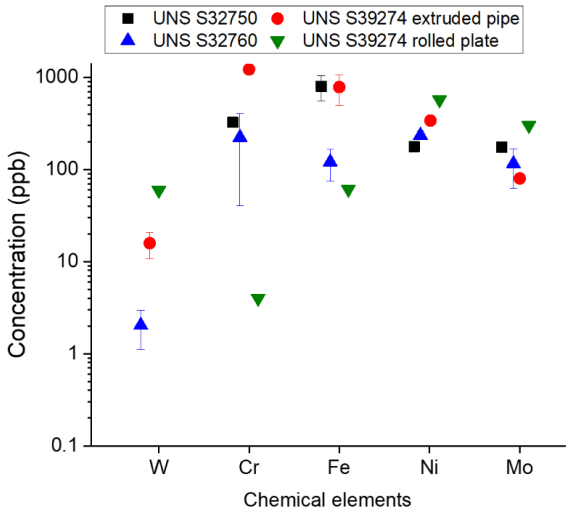

Figure 14. Concentration of ions released in the electrolyte after the PD-GS-PD tests at 60°C. Due to the logarithm scale of the concentration axis, error bars are not visible.

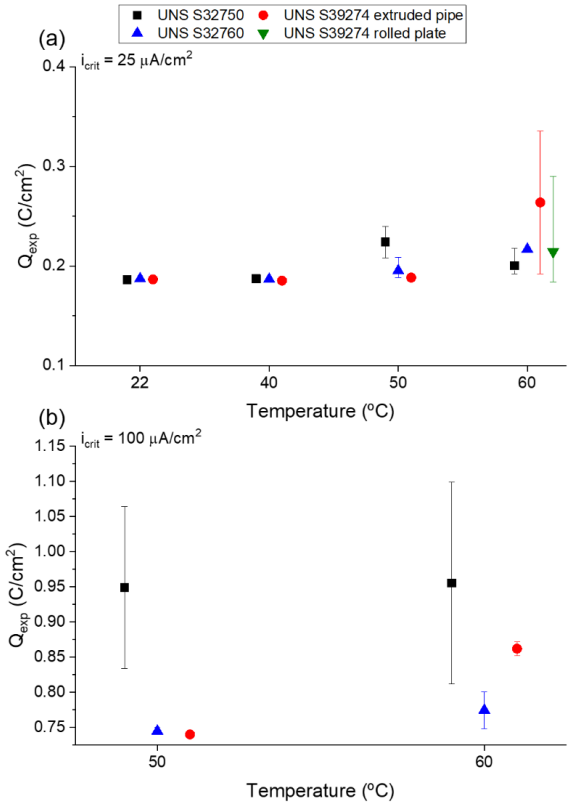

Figure 15. Q_{exp} calculated from the GS step and the reverse PD scan for all materials tested at (a) i_{GS} = 25 µA/cm^2, and (b) i_{GS} = 100 µA/cm^2. Error bars show maximum and minimum values.

Tables

Table 1. Chemical composition in wt.%

Material (UNS)	PRE_N^* / $PRE_{N,W}^{**}$	Si	Mn	Cu	Ni	Cr	Mo	N	W	Fe
S32750	43 / 43	0.27	0.51	0.14	6.42	**25.6**	**3.83**	**0.30**	-	62.9
S32760	41 / 42	0.50	0.60	0.60	7.1	**25.2**	**3.6**	**0.25**	**0.62**	61.5
S39274 extruded pipe	40 / 43	0.24	0.71	0.52	6.3	**24.9**	**3.1**	**0.29**	**2.1**	61.8
S39274 rolled plate	40 / 43	0.20	0.71	0.48	7.6	**24.6**	**2.9**	**0.35**	**2.1**	61.1

$^*PRE_N$ = %Cr + 3.3%Mo + 16%N
$^{**}PRE_{N,W}$ = %Cr + 3.3 (%Mo + 0.5 %W) + 16 %N

Table 2. CCT and $T_{R,Crev}$ values obtained with the PD-GS-PD technique and after long-term exposure in natural seawater for the extruded pipe materials.

UNS	Technique	Potential	CCT (°C)	$T_{R,Crev}$ (°C)
S32750	**PD-GS-PD**		> 60	40
	Natural seawater	**OCP**	> 80	-
		+600 $mV_{Ag/AgCl}$	45 / 50	42.5 / 47.5
S32760	**PD-GS-PD**		> 60	50
	Natural seawater	**OCP**	-	-
		+600 $mV_{Ag/AgCl}$	-	-
S39274	**PD-GS-PD**		> 60	~55
	Natural seawater	**OCP**	> 80	-
		+600 $mV_{Ag/AgCl}$	55	50

Table 3. Maximum depth, volume and surface area of transpassive attacks found in each material. The max. depth represents the depth of the transpassive attack at the transition temperature and it was taken as an estimator of $x_{Crit,Trans}$.

Material (UNS)	**E_{Trans} ($V_{Ag/AgCl}$)**	**T (°C)**	**Max. depth (μm)**	**Volume (mm^3)**	**Area (mm^2)**
S32750	0.80	40	7.9	$2.86 \cdot 10^{-5}$	0.067
S32760	0.81	50	16.1	$2.40 \cdot 10^{-4}$	0.105
S39274 extruded pipe	0.78	50	16.9	$9.77 \cdot 10^{-4}$	0.421
S39274 rolled plate	0.87	60	45.2	$1.29 \cdot 10^{-3}$	0.172

PAPER III

Use of the Critical Acidification Model to Estimate the Influence of W in the Localized Corrosion Resistance of 25 Cr Super Duplex Stainless Steels

C. Torres, M. Iannuzzi, R. Johnsen

Accepted for publication in Metals, special issue "Localized Corrosion of Metals and Alloys"

Article

Use of the Critical Acidification Model to Estimate the Influence of W in the Localized Corrosion Resistance of 25Cr Super Duplex Stainless Steels

Cristian Torres [1,*], Mariano Iannuzzi [1,2] and Roy Johnsen [1]

[1] Department of Mechanical and Industrial Engineering, Norwegian University of Science and Technology, Richard Birkelands veg 2b, 7491, Trondheim, Norway
[2] Curtin Corrosion Centre, Curtin University, GPO Box U1987, Perth, WA, 6845, Australia
* Correspondence: cristian.torres@ntnu.no

Received: date; Accepted: date; Published: date

Abstract: Two super duplex stainless steels (SDSS) with different W content, namely UNS S32750 (W-free) and UNS S39274 (2.1 wt.% W), were tested in simulated crevice corrosion environments to determine the influence of W on their corrosion resistance. Anodic potentiodynamic polarization experiments were performed in two different crevice-like-solutions: 1M HCl (as reference for a pH = 0 environment), and 7M LiCl adjusted to the same pH value. Galvele's critical acidification model was used to estimate the theoretical critical potential (E_{crit}) and comparatively evaluate the corrosion resistance of the two SDSS. The anodic potentiodynamic polarization results showed a statistically significant difference between the two materials only in one test condition, i.e., 7M Cl^- at 60°C. Additionally, the quantification of chemical dissolution of the metal cations after the tests suggested a surface enrichment in W only in the 7M chloride solution. SEM analysis indicated a uniform dissolution experienced by UNS S32750 in this environment, whereas UNS S39274 suffered selective corrosion of the ferrite-phase. These observations were reflected in a slight increase in the E_{crit} values of UNS S32974 estimated with Galvele's model.

Keywords: acidification model; tungsten; crevice-like-solutions; super duplex stainless steel

1. Introduction

Super duplex stainless steels (SDSS) have excellent corrosion resistance in neutral chloride-containing environments thanks to their high content of alloying elements like Cr, Mo, and N [1-4]. Tungsten (W) is another element that has been shown to improve corrosion resistance. However, the effect of W on localized corrosion resistance is still disputed, as discussed in detail elsewhere [5, 6].

A recent publication reviewed and studied the influence of W additions to SDSS on the precipitation kinetics of tertiary phases. In this regard, tertiary phases like σ- and χ-phase are well known to be deleterious to both mechanical properties and corrosion resistance [5]. The authors showed that about 2 wt.% W reduced the total concentration of deleterious phases, and retarded the precipitation of σ-phase, favoring the formation of χ-phase at grain and phase boundaries. When W was added at approximately 0.6 wt.%, W promoted deleterious phase precipitation and impacted the localized corrosion resistance of the material negatively.

Another recent publication [6] examined the influence of W as a solid solution element, i.e., in the absence of tertiary phases, on the crevice corrosion resistance of the same SDSS. The authors compared the critical crevice repassivation temperature ($T_{R,Crev}$) obtained by the potentiodynamic-galvanostatic-potentiodynamic (PD-GS-PD) technique with critical crevice temperature (CCT) and $T_{R,Crev}$ values from long-term exposure in natural seawater. The results showed that both the CCT and $T_{R,Crev}$ increased with W content, with a difference of up to 10 °C between the W-free and 2.1 wt% W cases, depending on the test conditions.

Despite quantifying the influence of W on localized corrosion resistance in neutral chloride environments and natural seawater, little is known about the mechanisms by which W influences corrosion resistance. It was, thus, desirable to investigate the performance of commercial SDSS in simulated crevice solutions, as done by Galvele [7], Newman [8], and others [9-12] for various alloys.

1.1. Crevice-like-solutions and the critical acidification model

Investigations in simulated pit/crevice environments can provide information about the role of alloying elements on the localized corrosion resistance of the materials, as first suggested by Galvele's critical acidification model [13] described in Equation 1.

$$E_{crit} = E_{corr}^{*} + \eta + \phi + E_{inh} \quad (1)$$

In Equation 1, E_{corr}^{*} is the corrosion potential of the material in the simulated pit or crevice electrolyte, η is the anodic polarization (overpotential) required to sustain an i_{crit} value at the bottom of the pit or crevice, ϕ is the ohmic potential drop along the pit or crevice, and E_{inh} is an additional polarization required in the presence of buffers or inhibitors. The critical potential (E_{crit}) is the theoretical pitting/crevice potential in a neutral chloride environment, obtained from measurements in the simulated acidic pit or crevice electrolyte [7].

Even though Galvele developed the critical acidification model for pure metals, the approach has been used for engineering alloys such as stainless steels and nickel-based alloys [7, 10, 11, 14, 15]. Galvele et al. [7] applied the critical acidification model to investigate the effect of Mo content in ferritic stainless steels (18Cr). Mo was found to decrease dissolution kinetics, changing the rate of pit propagation. Bocher et al. [14] investigated the influence of Mo additions to Ni-alloys using Galvele's model in two different crevice-like-solutions, i.e., localized environment inside a corroding crevice. The model was able to distinguish the performance of the same material (alloy 625) in two different product forms (plate and wire), even though their pitting resistance equivalent (PRE_N) was identical. Therefore, these authors concluded that the critical acidification model could be used to distinguish the influence of minor alloying elements on localized corrosion performance.

Srinivasan et al. [15] provided a detailed overview of Galvele's critical acidification model and the artificial 1D pit method, quantifying, among others, the minimum pH at which a protective oxide would precipitate. This critical minimum pH defined the repassivation of the active attack, i.e., pitting corrosion repassivation occurs when the critical metallic cation concentration and pH inside the pit/crevice stop being sustainable. Hornus et al. [10] measured the crevice repassivation potential ($E_{R,Crev}$) of two stainless steels (UNS S30400 and UNS S31600) and compared the difference in localized corrosion resistance using Galvele's model. By equating $E_{R,Crev}$ values measured with the PD-GS-PD technique to Equation 1, the authors concluded that the effect of a 2.5 wt.% Mo addition was related mainly to the ohmic potential drop (ϕ) term.

A detailed review of different solutions used to simulate active pits and crevices has been reported by Kappes et al. [11]. These authors compared a 22Cr duplex stainless steel (DSS) and a SDSS in pit-like-solutions as a function of the chloride content. The main difference between the two stainless steels was found at 7N Cl^-, a concentration considered to be the threshold for salt film precipitation [11]. Higher Cl^- concentrations caused a metal salt film precipitation on the material, seen by a diffusion limiting current in the active region of the anodic polarization curves [16]. Arguably, salt film precipitation suggested conditions of stable localized corrosion propagation [17, 18]. The estimated E_{crit} values differed by 20 mV with experimental $E_{R,Crev}$ measured with PD-GS-PD in neutral pH, demonstrating the ability of Galvele's model to estimate the critical potentials of commercially available alloys. Others [7, 10-12, 14] have also successfully distinguished the effect of other alloy elements by conducting anodic polarizations in acidic chloride environments.

The objective of this work was to investigate the possible role of W in a propagating localized attack as a function of temperature in simulated crevice electrolytes. For this purpose, two commercial SDSS differing mainly in their W content were tested in two different crevice-like environments as a function of temperature. Galvele's critical acidification model was employed to estimate theoretical E_{crit} values, which were compared with $E_{R,Crev}$ results obtained in neutral chloride solutions.

2. Materials and Methods

2.1. Materials

Two SDSS, differing mainly in their W composition, were studied in this work, namely UNS S32750 (W-free) and UNS S39274 (2.1 wt.% W). Table 1 summarizes their composition given by the provider and confirmed by EDS. Both materials were produced as extruded pipes with 30 mm wall thickness and 203.2 mm in diameter. Round samples were machined by first extracting cylinders along the length of the pipe. The thickness of the coin-shaped specimens was 3 mm and the diameter 25 mm for UNS S32750 and 30 mm for UNS S39274.

Table 1. Chemical composition in wt.%

Material (UNS)	PRE_N [1] / $PRE_{N,W}$ [2]	C [3]	Si	Mn	S [3]	Cu	Ni	Cr	Mo	N	W	Fe
S32750	43 / 43	0.03	0.27	0.5	0.02	0.14	6.42	25.6	3.83	0.3	-	62.9
S39274	40 / 43	0.02	0.24	0.7	0.02	0.52	6.3	24.9	3.1	0.29	2.1	61.8

[1] PRE_N = %Cr + 3.3%Mo + 16%N

[2] $PRE_{N,W}$ = %Cr + 3.3 (%Mo + 0.5 %W) + 16 %N

[3] Composition reported according to the alloy provider.

UNS S39274 was received in the solution annealed condition (heat-treated at 1085°C for 10 min). UNS S32750 was solution annealed after machining, in an air-furnace at 1100°C for 15 min and quenched in water, following the recommendations from the supplier.

Specimens were wet-ground down to 600 US-grit SiC paper, rinsed in acetone, followed by distilled water and ethanol, and cleaned in an ultrasonic bath for 5 min while they were immersed in ethanol.

Specimens of the two SDSSs were etched following Statoil technical note MAT-2010080 [19] to reveal the microstructure and distinguish the austenite (γ) and ferrite (α) phases by light optical microscopy (LOM) and scanning electron microscopy (SEM). The etching procedure consisted of two different steps. In the first step, a 15 wt. %. KOH solution was used, and a potential of 3 V was applied for 12 s. In the second step, the solution was 20 wt. %. NaOH with an applied potential of 1.5 V for 10 s. Figure 1 shows the microstructure of each material after the heat treatments. The γ and α ratio in these materials was measured by electron backscatter diffraction (EBSD) in a previous work [5], obtaining a 57.2 and 47.6 vol.% α for UNS S32750 and UNS S39274, respectively. These values are within the acceptable 40-60 vol.% range for each phase in SDSS. The average austenite region size of each material was determined by measuring the area of each austenite region in a minimum of three different areas and calculating the mean value by an open-access image processing software. The average austenite region size results for UNS S32750 and UNS S39274 were 577.9 μm^2 and 395.0 μm^2, respectively.

2.2. Galvele's critical acidification model

Galvele's critical acidification model [13], described in Equation 1, can be used to estimate the E_{crit} when the concentration of aggressive specimens in the electrolyte is known. Henceforth, to simplify the model, E_{inh} is considered negligible to the contribution of E_{crit} [11]. Despite the release of potential inhibiting species such as molybdates and tungstates from the alloys during dissolution [20-22], it is considered acceptable as the E_{crit} value estimated in this manner is more conservative, i.e., lower E_{crit}. Thus, E_{crit} can be expressed as:

$$E_{crit} = E_{corr}^{*} + \eta + \phi \quad (2)$$

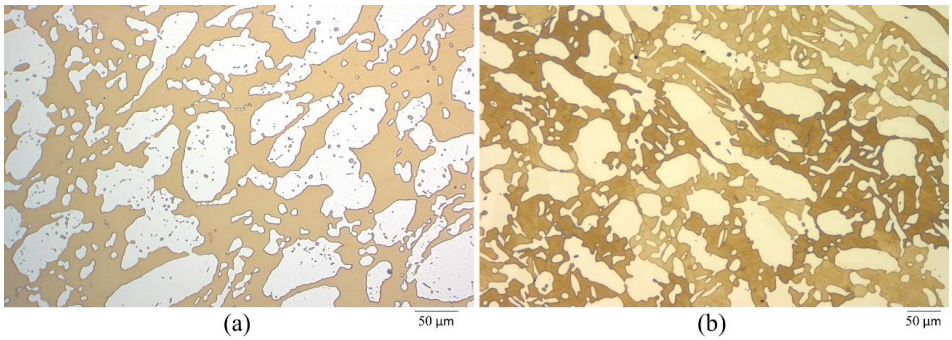

Figure 1. LOM micrographs of (**a**) UNS S32750, and (**b**) UNS S39274 after the heat treatments.

The ohmic potential drop term was estimated after Bocher et al. (Equation 3) [11, 14]:

$$\Phi = \frac{\rho \cdot i_{crit} \cdot x^2}{2w} \quad (3)$$

where ρ is the resistivity in the solution and is assumed to be 10 Ω·cm [14], w is the crevice gap which was given a value of 1 µm [11], x is the diffusion distance considered to be 10^{-4} cm [23], and i_{crit} was obtained from the pit stability product (Equation 4) [24]:

$$x \cdot i_{crit} = k \quad (4)$$

where k is a constant that is a function of the metal and pH of the solution. In this work and based on Kappes et al., the value of 10^{-6} A/cm was adopted [23]. Equation 3 and 4 yield an $i_{crit} = 10^{-2}$ A/cm^2 and $\phi = 5$ µV. Since the $\phi << E_{corr}^*$, E_{crit} can be obtained as:

$$E_{crit} = E_{corr}^* + \eta \quad (5)$$

E_{corr}^* can be found by measuring the corrosion potential in an electrolyte simulating the inside of a corroding pit or crevice. Consequently, the E_{crit} can be obtained from Equation 5 by performing anodic potentiodynamic polarizations in crevice-like-solutions and obtaining the E_{corr} and η (i.e., the applied overpotential needed to reach $i_{crit} = 10^{-2}$ A/cm^2).

2.3. Crevice-like-solutions

Anodic potentiodynamic polarization experiments were conducted in solutions simulating pit/crevice environments. Two different crevice-like-solutions were used: 1M HCl (as a reference solution at pH = 0) and 7M LiCl, which was chosen based on Kappes et al. [11] as 7N Cl^- presented the highest current density before salt precipitation occurred. The 7M LiCl solution was adjusted to 0 pH by adding concentrated HCl, following the relationship between H^+ and Cl^- activity coefficients given by Bocher et al. [14]. The volume used in each experiment was 160 ml, which was measured by a graduated cylinder. The solution resistances varied from the less conductive to the more conductive solutions from 0.3 to 0.1 Ω, which was also confirmed using OLI simulations and in line with the work of Artemov et al [25], who studied the conductivity of aqueous HCl, NaOH and NaCl solutions. Thus, the effect of IR drop was considered negligible for the comparative assessment of the two SDSSs.

A 3 electrode-cell consisting of an Ag/AgCl KCl saturated reference electrode (RE) (-199 mV vs Standard Hydrogen Electrode – SHE-) immersed in the solution through a glass tube and kept at room temperature was used to carry out the anodic polarization tests. The counter electrode (CE) consisted of a Pt mesh. A commercially available electrochemical Avesta cell was used to avoid crevice corrosion [26], which was modified, as shown in Figure 2. In the original design of the Avesta cell, the distilled water required to avoid crevice corrosion flows into the main chamber, which might affect the pH and Cl^- concentration at the surface. The modification consisted of creating an additional outlet for the distilled water supplied by the peristaltic pump (Figure 2) to avoid contact with the electrolyte.

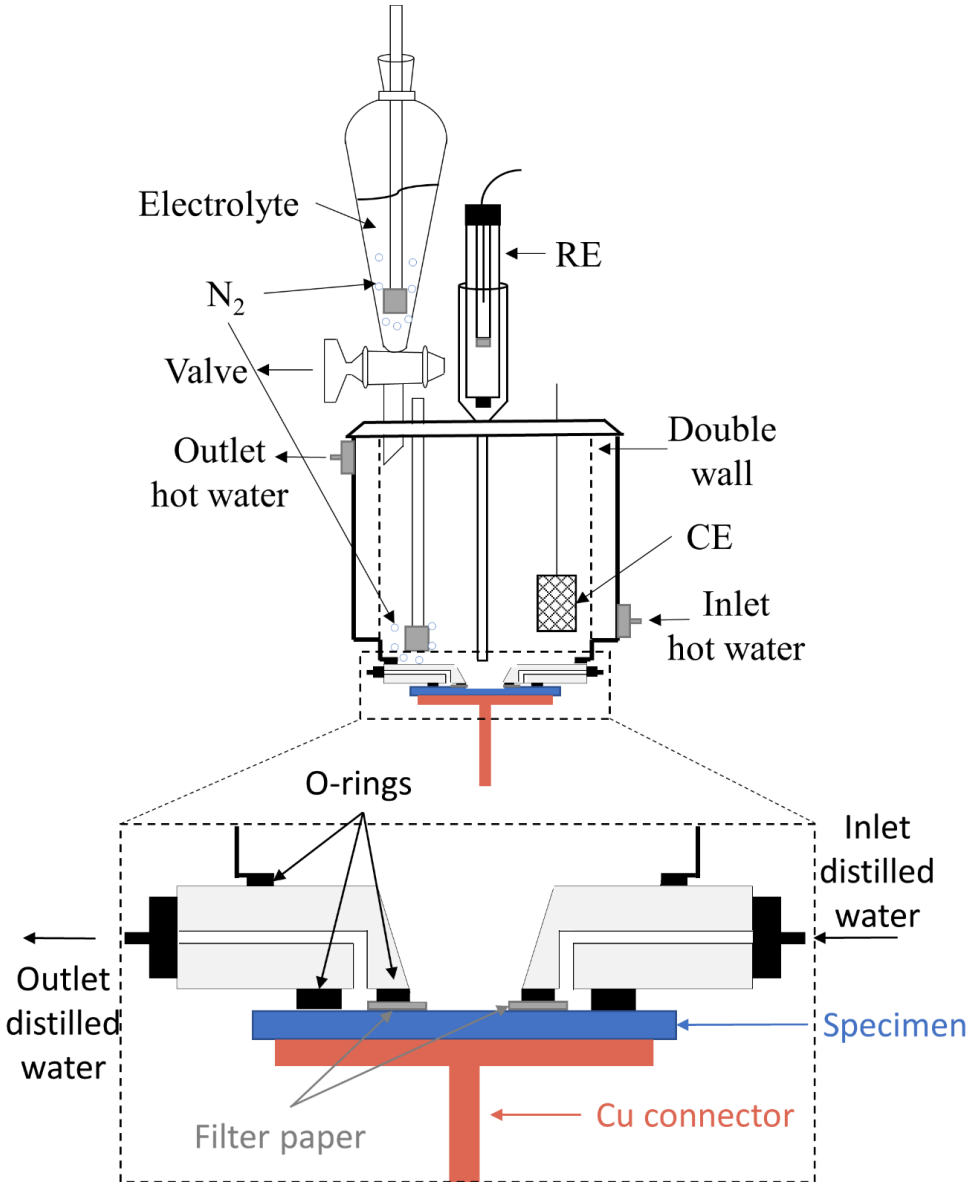

Figure 2. Full electrochemical test set-up showing the glass vessel employed to deaerate the electrolyte before introducing it into a pre-deaerated modified Avesta cell. The bottom part of the cell (the part with the inlet/outlet of the distilled water, the filter paper, the specimen and Cu connector) is zoomed in to show the particular features of the Avesta cell. The drawing is not to scale.

Consequently, the distilled water did not leak into the electrolyte, but circulated through the O-ring sealing, wetting the filter paper and, then, circulated outside the cell through a new vent. The area of the working electrode was 1.54 cm^2.

Anodic polarization experiments were performed at different temperatures: room temperature (22±1°C), 40°C, 50°C and 60°C. The temperature was controlled using a water bath connected to the

double glass wall of the cell, except for the room temperature condition in which testing was done at the temperature of the lab.

The tests were performed in an oxygen-free electrolyte since the localized environment inside active pits and crevices has a low oxygen content as it is consumed during the initial stages [27]. The electrolyte was purged with nitrogen gas for 1 h before exposing the specimen to ensure a low dissolved oxygen concentration. Since the specimen is placed at the bottom of the cell (Figure 2), the electrolyte had to be purged in a tight glass vessel mounted on top of the Avesta cell, as illustrated in Figure 2. The main Avesta cell chamber was simultaneously purged with N_2 to remove all air and ensure an O_2-free atmosphere from the moment the solution came in contact with the specimen. The tight glass vessel was connected through a valve directly into the Avesta cell, to avoid contact of the deaerated electrolyte with the air when transferring the solution from the vessel to the main cell. Deaeration of the electrolyte continued during the tests. The dissolved oxygen concentration was monitored continuously using a fiber optic oxygen meter, and its content was always below 10 ppb from the moment the material came in contact with the test solution.

The sequence of the anodic polarization tests was as follows. First, the E_{corr}^* was measured for 1 h (the asterisk indicates that E_{corr} was measured in a simulated crevice solution), followed by the anodic potentiodynamic polarization, starting at E_{corr}^* and finishing at 1.2 $V_{Ag/AgCl}$, with a sweep rate of 0.167 mV/s. All tests were performed at least in duplicate.

The passive current density (i_{pass}), the critical passive current density (i_{cp}), the corrosion potential (E_{corr}^*), the transpassive potential (E_{Trans}), and the primary passive potential (E_{pp}) were obtained from each anodic potentiodynamic polarization curve.

2.4. Characterization

After the tests, the electrolyte was stored in tight plastic containers and the ions released from the specimens were quantified using Inductively Coupled Plasma Mass Spectrometry (ICP-MS).

Congruent or incongruent dissolution was verified with the ICP-MS results by calculating the dissolution ratio of each metallic element M (d'_M). d'_M was defined as the ratio between the experimental dissolution ($d_{experimental}$) quantified by the ICP-MS analysis and the congruent dissolution ($d_{congruent}$) value. $d_{congruent}$ was calculated as the proportional dissolution of Fe, as it is the bulk element for the two materials, as shown in Equation 6:

$$d'_M = \frac{d_{M.experimental}}{d_{M.congruent}} = \frac{d_M}{\frac{C_M \cdot d_{Fe}}{C_{Fe}}} \quad (6)$$

Where d_M (in ppb) is the dissolution quantity of metal M measured by ICP-MS, C_M (in wt.%) is the concentration in solid solution of metal M in the material (shown in Table 1), C_{Fe} (in wt.%) is the concentration in solid solution of Fe in the material (shown in Table 1), and d_{Fe} (in ppb) is the dissolution quantity of Fe obtained by ICP-MS for the same condition as that of the measured metal M. In this regard, a $d'_M > 1$ suggests selective metal M dissolution [28]. Contrarily, a $d'_M < 1$ implies a relative surface enrichment in M [28]. Finally, $d'_M = 1$ indicates congruent dissolution [28].

The specimens were analyzed after the tests with an infinite focus microscope (IFM) used as a LOM, which can simultaneously acquire the 3D surface profile, enabling the estimation of the depth of localized attacks. The specimens were also analyzed by SEM together with energy-dispersive x-ray spectroscopy (EDS). An accelerated voltage of 20 kV, with a 50 μm diameter aperture and a spot size of 5 was employed, giving a beam current of approximately 7.2 nA. The point analysis tool was used to acquire the composition of the full area taken by the SEM. At least 5 measurements were performed per specimen.

2.5. Statistical analysis

A statistical study of the data was performed to examine whether the metal cations quantity released at the end of the electrochemical test was related to any of those parameters or the two parameters, η and E_{crit}, used in Galvele's model. The statistical study consisted of calculating the

Kendall correlation coefficient [29] in a pairwise comparison between all the mentioned variables. In contrast to other more known correlation parameters such as Pearson's, the Kendall correlation coefficient does not assume a normal distribution [30]. Thus, Kendall's coefficient indicates a general monotonic relationship, i.e., if both variables increase or decrease together [29]. Consequently, Kendall's coefficient will show a strong relationship even for non-linear relationships like exponential behaviors.

For this reason, this coefficient is becoming more popular within the scientific community [29, 31]. The closer the coefficient is to 1 (in absolute value), the stronger the variables are connected. The sign of the coefficient indicates the type of relationship: (i) positive; both variables increase or decrease together, or (ii) negative, one variable increases as the other decreases.

3. Results

3.1. Crevice-like-solutions

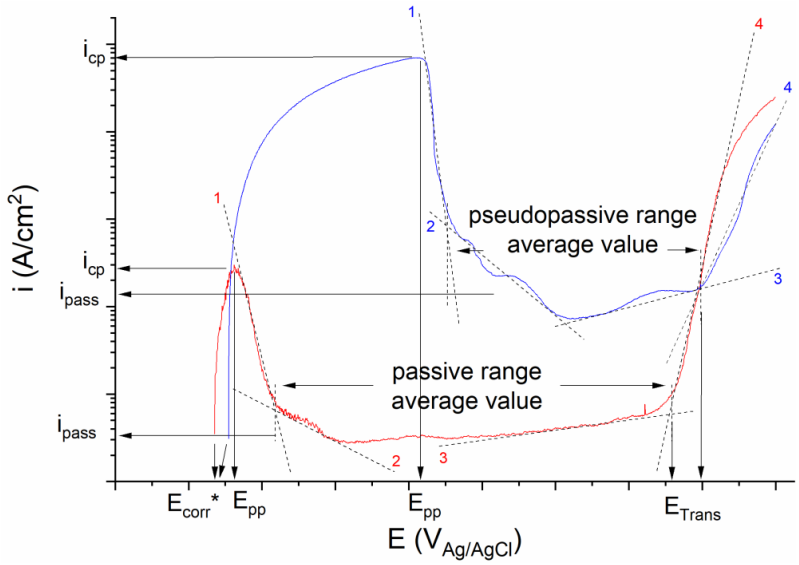

Figure 3. Illustration of the parameters obtained from anodic polarization curves for the tests performed in 1M HCl and 7M LiCl at pH 0.

Figure 3 illustrates how i_{pass}, i_{cp}, E_{pp}, E_{corr}^{*}, and E_{Trans} values were obtained from the anodic potentiodynamic polarization curves. Figure 4 summarizes the anodic potentiodynamic polarization curves obtained for one specimen of each alloy tested at each temperature, while Figure 5 presents all the critical parameters extracted from Figure 4. As indicated in Figure 3, i_{pass} was calculated as the average value between the intersections between lines 1 and 2 at low potentials and the intersection of lines 3 and 4 at high potentials. Although the limiting currents after the active/passive transition do not imply true passivation given the high values, i_{pass} was calculated as the average value of the current density measured during the pseudopassive region following the same criteria as for the normal passive range. In agreement with others [11, 32], i_{cp} was obtained as the maximum current density measured before the active/passive transition. Similarly, E_{pp} was defined as the potential at which the transition from active to passive took place. E_{corr}^{*} was considered as the value measured at the end of the 1 h open circuit potential measurement before polarization. After the active/passive transition, potentials reached values more positive than the oxygen evolution reaction and within the transpassive

area [33]. Consequently, the inflection point seen at high anodic potentials (the intersection between lines 3 and 4 in Figure 3) was defined as E_{Trans}.

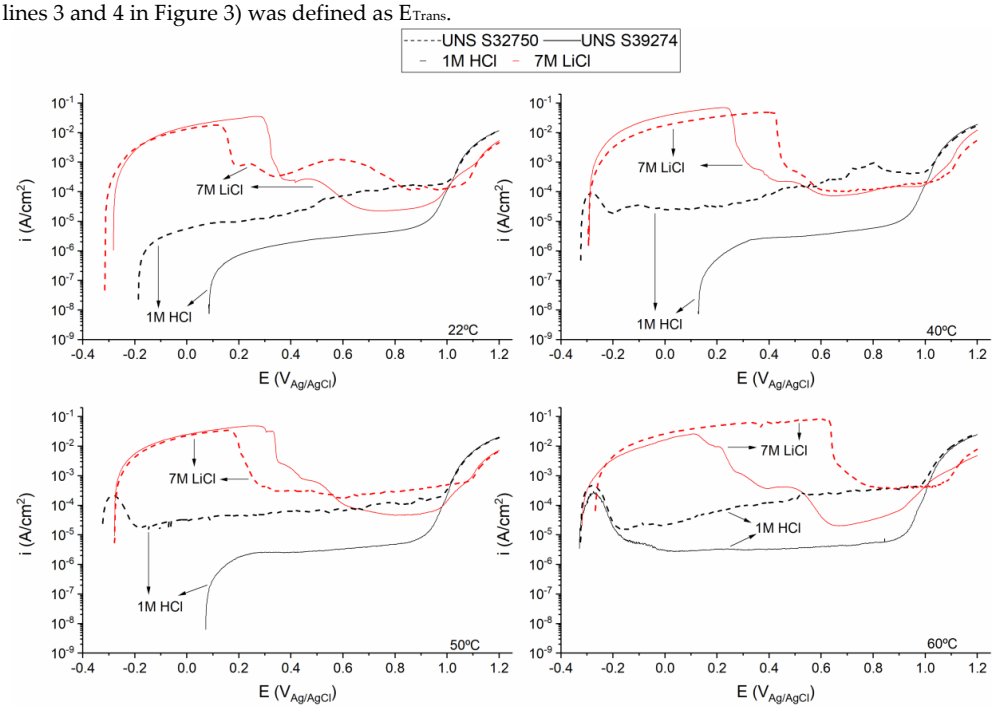

Figure 4. Anodic potentiodynamic polarization curves in two crevice-like-solutions as a function of temperature, as indicated.

As shown in Figures 4 and 5, a clear difference was observed between the two solutions. In this regard, the active/passive transition in 1 N Cl^- was only observed at T ≥ 40°C and T = 60°C for UNS S32750 and UNS S39274, respectively. In contrast, active dissolution followed by a high diffusion-limited current ($i_{lim} \approx i_{cp}$) and passivation at E_{pp} occurred in 7M LiCl for all specimens at all temperatures. Even though the current density did not achieve typical passive values, this area will be referred to as passive hereunder to compare i_{pass} between the solutions. Additionally, lower current densities (both i_{cp} and i_{pass}) were obtained in 1M HCl for potentials below the oxygen evolution reaction or below the transpassive region [33]. In contrast, i_{pass} was, in most cases, as high in 1M HCl as in 7M LiCl for UNS S32750. In 7M LiCl, the E_{pp} values were nobler than in 1M HCl. In fact, due to the high E_{corr}^* values in 1M HCl, the E_{pp} was not observed in several tests, as indicated in Figure 5.

Differences between the two materials were also observed. In 1M HCl, UNS S32750 had a higher i_{pass} than UNS S39274, whereas the E_{pp} of UNS S32750 was more positive in 7M LiCl, especially at 60°C. At that same temperature, there was a significant difference in i_{cp} between both materials in 7M LiCl.

Figure 6 illustrates the surface of two specimens after exposure, as observed by LOM. No crevice corrosion was found along the edges of the filter paper by both high IFM magnifications and SEM analysis. No evident corrosion attack was seen on the surface of the specimens tested in 1M HCl. In this case, the surface was slightly etched, revealing the grain structure of the samples. In contrast and as expected [11], the specimens tested in 7M LiCl experienced uniform dissolution.

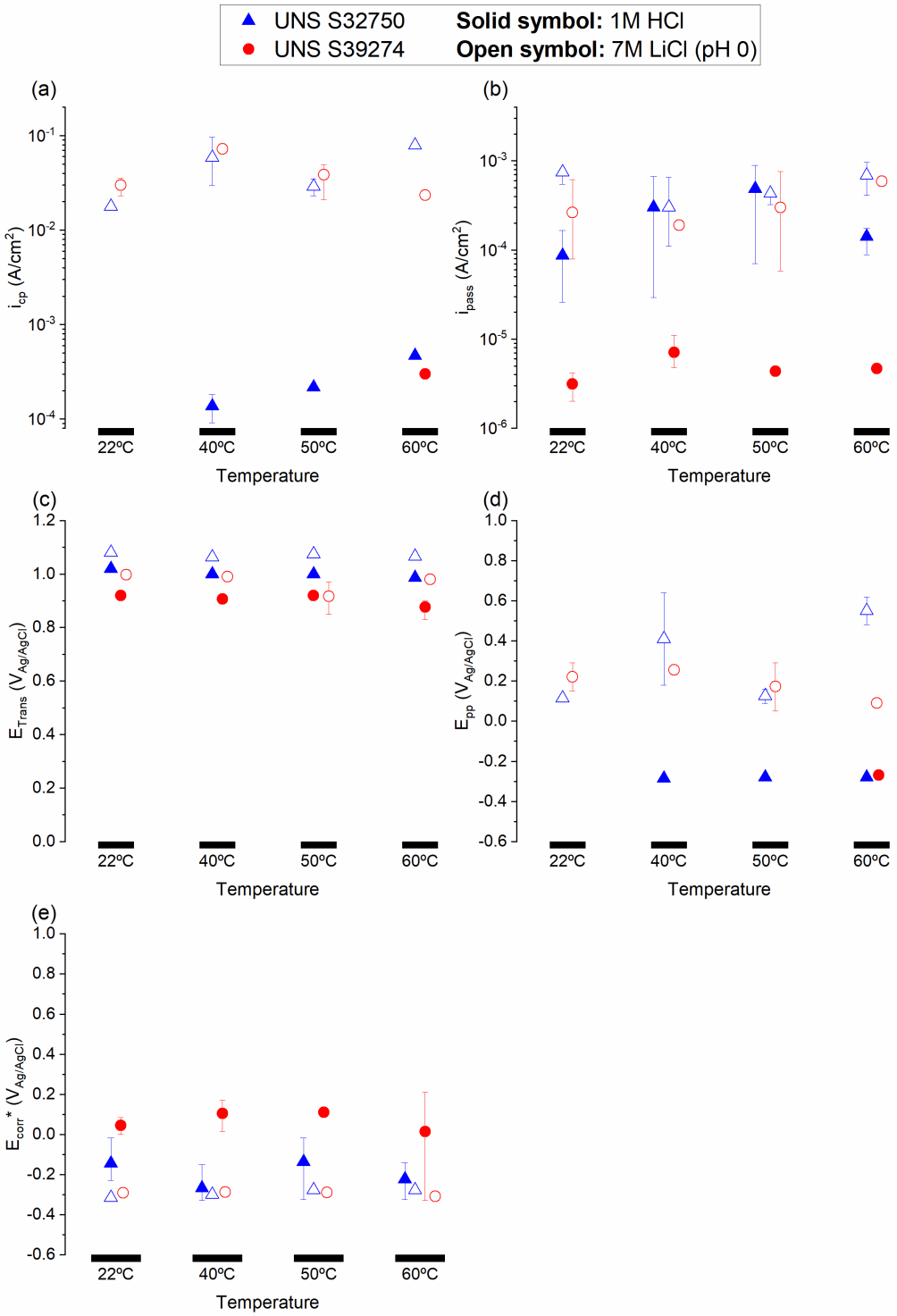

Figure 5. (**a**) i_{cp}, (**b**) i_{pass}, (**c**) E_{Trans}, (**d**) E_{pp}, and (**e**) E_{corr}^{*} measured from the anodic potentiodynamic polarization tests. Error bars indicate maximum and minimum values.

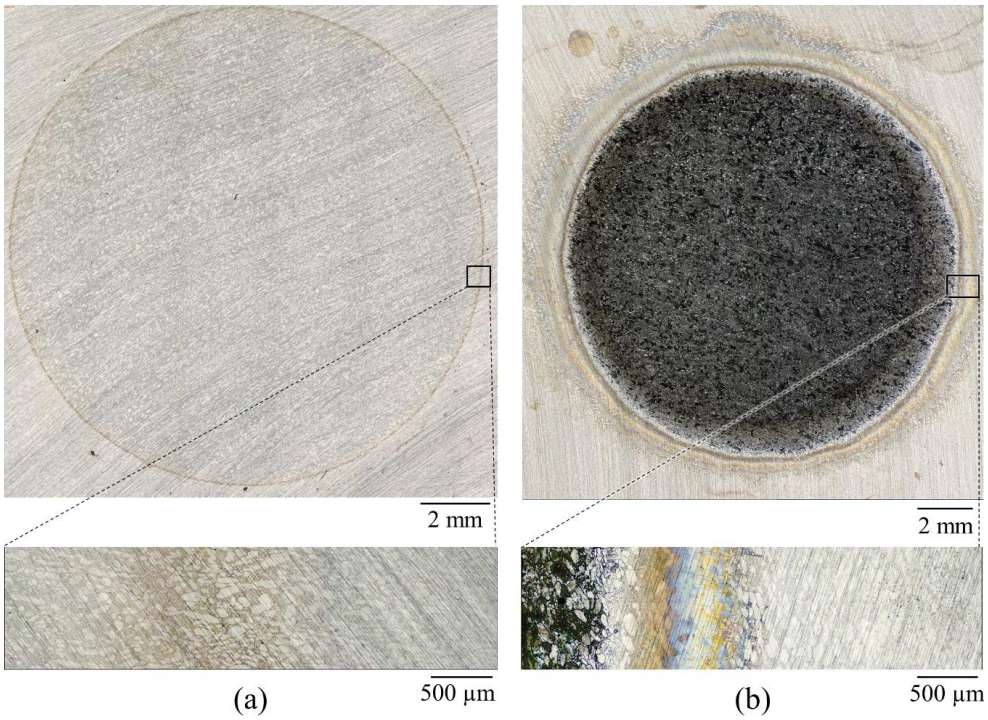

Figure 6. Optical visualization of UNS S39274 specimens after anodic potentiodynamic polarization at room temperature exposed to (**a**) 1M HCl, and (**b**) 7M LiCl. The exposed area -the circle- is equal in the two pictures.

The surface analysis performed by SEM and EDS of the corroded specimens in 7M LiCl revealed a clear difference in the attack morphology between both SDSS. Figure 7 shows the morphology of the attack after testing, as observed by SEM. While both phases corroded uniformly in the case of UNS S32750, S39274 suffered selective dissolution of the α-phase. In this regard, ferrite can be distinguished easily from austenite using EDS due to its lower Ni and higher Cr and Mo concentration [6, 34]. The surface chemical composition of each phase for both materials obtained by EDS before and after the corrosion testing is presented in Table 2. The W-free material showed a relative enrichment in O, Ni and Mo and an impoverishment in Cr and, especially Fe, when comparing the values before and after the corrosion testing. This behavior was observed for both austenite and ferrite phases. On the other hand, the W-rich material was richer in O and Mo, but poorer only in Fe. In comparison, Cr and Ni concentration was similar before and after corrosion. Nevertheless, there was a difference in the W content between the austenite and ferrite phases. W was enriched in the ferrite phase, but not in austenite after corrosion.

Figure 8 shows the concentration of dissolved metal cations as measured by ICP-MS after testing. As expected, the concentration of dissolved metal cations was larger in 7M LiCl than in 1M HCl for both materials, which increased with increasing temperature (except for UNS S39274 at 60°C in 7M LiCl). The amount of released metal cations by both materials in 1M HCl was similar. Contrarily, in 7M LiCl, the dissolved concentration of metal cations released by UNS S39274 was larger than that of UNS S32750, apart from the tests performed at 60°C, where UNS S39274 experienced a much lower dissolution than UNS S32750.

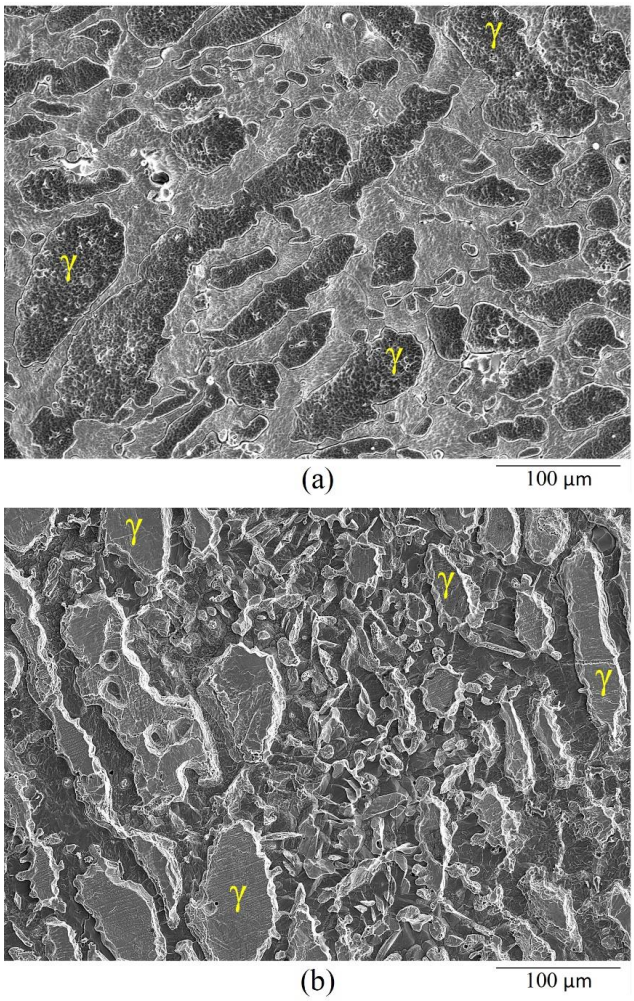

Figure 7. SEM secondary electron images of (**a**) UNS S32750, and (**b**) UNS S39274 specimens after the anodic potentiodynamic polarization in a 7M LiCl solution at 60°C. In the pictures, the austenite phase (γ) is indicated. The other phase is ferrite (α).

Table 2. Average surface chemical composition of the specimen in wt.% obtained by EDS before and after the anodic potentiodynamic polarization in 7M LiCl at 60°C.

Elements	Before corrosion testing				After corrosion testing			
	UNS S32750		UNS S39274		UNS S32750		UNS S39274	
	α	γ	α	γ	α	γ	α	γ
O	-	-	-	-	2.4	3.7	1.7	0.9
Cr	28.1	25.2	26.4	24.1	26.2	23.1	26.5	24.6
Fe	63.9	64.9	63.5	64.7	57.6	56.3	58.6	60.9
Ni	4.6	7.5	4.7	7.3	5.3	8.0	4.4	7.0
Mo	3.6	2.3	2.9	1.9	5.8	4.0	3.6	2.4
W	-	-	2.5	1.9	-	-	3.2	1.8

Table 3 shows the calculated dissolution ratio (d'_M) of each element for all specimens. Cr, Ni, and Mo showed dissolutions ratios close to 1, suggesting congruent dissolution with Fe. On the other hand, there were significant differences regarding the dissolution ratio of W. In 1M HCl, d'_W was close to 1; however, in 7M LiCl, the results indicated a possible surface enrichment of W, as $d'_W < 1$.

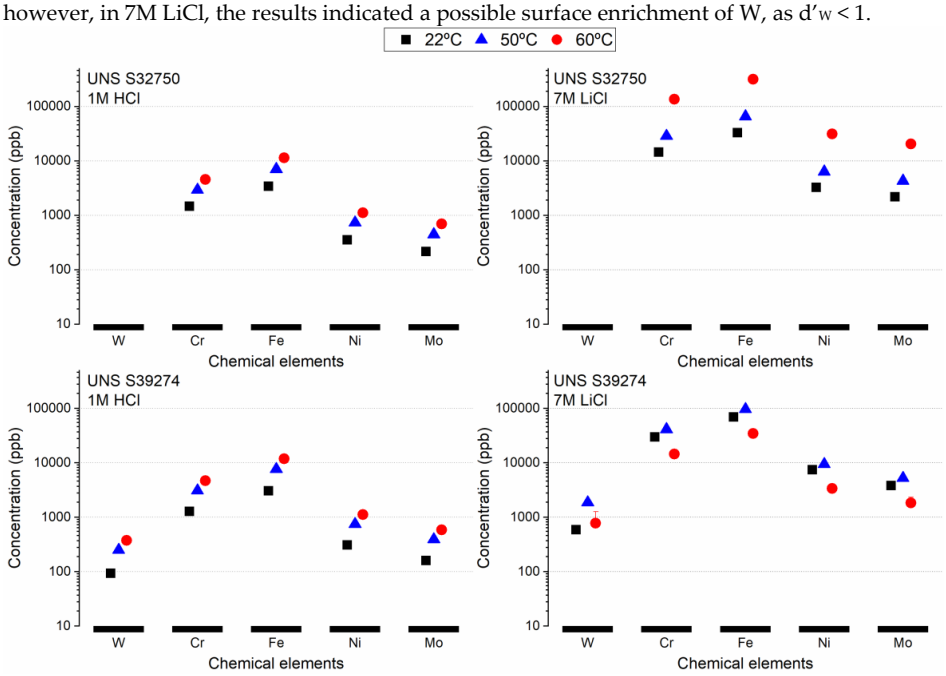

Figure 8. Concentration of dissolved metal cations measured by ICP-MS after performing the anodic potentiodynamic polarization tests. Error bars indicate maximum and minimum values. Due to the logarithmic scale, most of them are not visible.

Table 3. Normalized dissolution quantities (d'_M) for each element calculated from Equation 6, using the average concentration quantified by ICP-MS.

Material	Solution	T (°C)	d'_W	d'_{Cr}	d'_{Fe}	d'_{Ni}	d'_{Mo}
UNS S32750	1M HCl	22	-	1.05	1.00	1.01	1.03
		40	-	1.01	1.00	0.98	1.03
		50	-	1.03	1.00	1.02	1.04
		60	-	0.99	1.00	0.96	1.00
	7M LiCl	22	-	1.08	1.00	0.97	1.09
		40	-	1.02	1.00	0.97	1.06
		50	-	1.07	1.00	0.95	1.08
		60	-	1.05	1.00	0.96	1.06
UNS S39274	1M HCl	22	0.90	1.04	1.00	0.99	1.05
		40	1.01	1.03	1.00	1.01	1.02
		50	0.96	1.01	1.00	0.96	1.02
		60	0.93	0.98	1.00	0.93	0.98
	7M LiCl	22	0.25	1.07	1.00	1.06	1.10
		40	-	-	-	-	-
		50	0.57	1.06	1.00	0.96	1.08
		60	0.66	1.04	1.00	0.96	1.06

3.2. Galvele's acidification model

Figure 9 illustrates the E_{corr}^{*} and η obtained from the anodic potentiodynamic polarization curves used for Galvele's critical acidification model, together with the estimated E_{crit} calculated using Equation 5. Even though both materials differed in the E_{corr}^{*} and η, the resulting E_{crit} was similar for both materials in 1M HCl. Additionally, the estimated E_{crit} values were over the reversible potential of the oxygen evolution reaction and within the transpassive region [33], suggesting transpassive dissolution. As a result, in neutral chloride solutions, it could be expected that $E_{crit} \approx E_{Trans}$ at all temperatures. In 7N Cl^-, there were no differences in most cases, apart from 60°C where UNS S39274 obtained a slightly nobler E_{crit} than UNS S32750, due to the difference in η between materials. In all other conditions, E_{crit} decreased slightly with temperature, although the differences were within the experimental error.

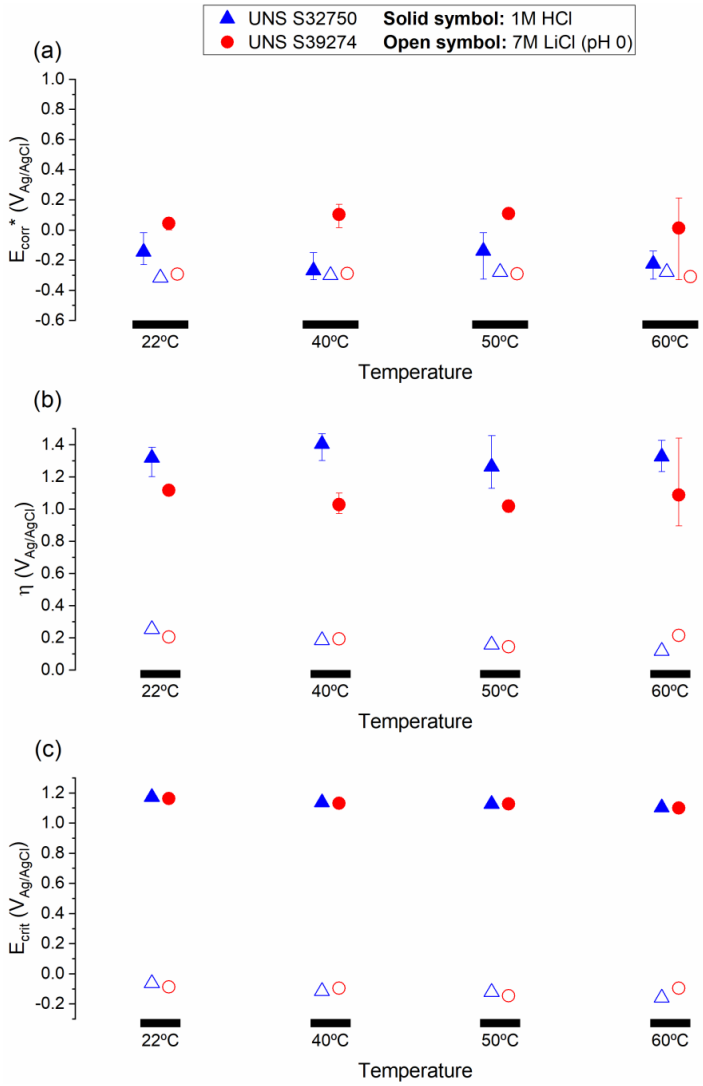

Figure 9. (**a**) E_{corr}^{*} and (**b**) η obtained from the anodic potentiodynamic polarization curves in crevice-like-solutions to estimate (**c**) E_{crit} obtained by Galvele's critical acidification model. Error bars indicate maximum and minimum values.

3.3. Statistical analysis

Tables 4 and 5 contain Kendall's correlation coefficients calculated for the pairwise parameters shown in the column and row of each cell for 1M HCl and 7M LiCl crevice-like-solutions, respectively. Additionally, statistically significant (p-value < 0.05) values are indicated in bold font.

In both electrolytes, the concentration of released metal cations of each element seemed to follow the same trend, either increasing or decreasing in quantity altogether. The only exception was W in 7M LiCl, which did not present any relationship with any parameter. The other elements had a strong significant positive relationship with i_{cp} and E_{pp} in 7M LiCl. In contrast, in 1M HCl, only a strong positive correlation was seen between the dissolution of the chemical elements and i_{cp}. The low correlation values obtained for E_{pp} were probably due to the low number of tests where the E_{pp} could be measured, as it was mentioned above. E_{crit} was correlated to the concentration of dissolved elements, especially in 1M HCl, indicating an increment of released cations of all elements, the more negative the E_{crit}. However, even though the correlation was weaker in 7M LiCl, there was a significant exception since W was the only element with no relationship to E_{crit}.

Table 4. Kendall's correlation coefficient obtained for all tests performed in 1M HCl. Bold numbers indicate a statistically significant (p-value < 0.05) correlation coefficient. (T stands for temperature).

	Cr	**Fe**	**Ni**	**Mo**	**T**	**i_{cp}**	**E_{Trans}**	**i_{pass}**	**E_{pp}**	**E_{corr}^***	**E_{crit}**	**η**
W	**0.93**	**0.93**	**0.93**	**1**	**0.91**	-	**-0.65**	0.00	-	0.07	**-0.71**	-0.21
Cr		**1**	**0.99**	**0.91**	**0.80**	**1**	-0.32	0.02	0.18	-0.09	**-0.84**	-0.02
Fe			**0.99**	**0.91**	**0.80**	**1**	-0.32	0.02	0.18	-0.09	**-0.84**	-0.02
Ni				**0.93**	**0.78**	**1**	-0.31	0.03	0.18	-0.10	**-0.82**	0.00
Mo					**0.78**	**1**	-0.24	0.10	0.18	-0.15	**-0.75**	0.04
T						0.82	**-0.40**	-0.05	0.67	0.00	**-0.73**	-0.10
i_{cp}							-0.55	-0.33	0.18	-0.33	**-1**	**-1**
E_{Trans}								**0.56**	-0.80	-0.42	0.35	**0.50**
i_{pass}									-0.91	-0.34	-0.09	**0.35**
E_{pp}										-0.18	-0.18	-0.18
E_{corr}^*											0.04	**-0.90**
E_{crit}												0.06

Table 5. Kendall's correlation coefficient obtained for all tests performed in 7M LiCl. Bold numbers indicate a statistically significant (p-value < 0.05) correlation coefficient. (T stands for temperature).

	Cr	**Fe**	**Ni**	**Mo**	**T**	**i_{cp}**	**E_{Trans}**	**i_{pass}**	**E_{pp}**	**E_{corr}^***	**E_{crit}**	**η**
W	0.52	0.52	0.52	0.52	0.11	0.52	-0.59	-0.62	0.20	0.14	-0.33	-0.33
Cr		**1**	**0.98**	**0.93**	0.16	**0.91**	0.06	-0.32	**0.75**	0.30	**-0.58**	**-0.63**
Fe			**0.98**	**0.93**	0.16	**0.91**	0.06	-0.32	**0.75**	0.30	**-0.58**	**-0.63**
Ni				**0.91**	0.14	**0.93**	0.03	-0.34	**0.77**	0.28	**-0.56**	**-0.60**
Mo					0.11	**0.85**	0.12	-0.30	**0.77**	0.32	**-0.52**	**-0.56**
T						0.22	-0.17	0.14	-0.03	0.29	-0.34	**-0.47**
i_{cp}							-0.03	-0.32	**0.75**	0.30	**-0.58**	**-0.63**
E_{Trans}								**0.43**	0.12	0.03	-0.03	-0.03
i_{pass}									-0.24	-0.10	0.08	0.12
E_{pp}										0.18	-0.33	-0.38
E_{corr}^*											-0.36	**-0.54**
E_{crit}												**0.82**

4. Discussion

4.1. Choice of parameters for the critical acidification model

During stable pit and crevice propagation, Cl^- anions migrate inside the pit/crevice to maintain electroneutrality as the metal cations are released at the bottom of the attack and undergo hydrolysis [27, 35]. Therefore, different Cl^- concentrations simulate different propagation degrees. The Cl^- concentration is limited by the metallic cation saturation concentration, above which a metallic salt film precipitates [11]. Some authors have reported maximum Cl^- concentration values in artificial and real pits of 6N [9] and 12N Cl^- [36], respectively. Additionally, Kappes et al. [11] reported the precipitation of the salt film in a 22Cr DSS and UNS S32750 to occur between 7N and 9N Cl^-, representing the 58% and 75% Cl^- saturation concentration, respectively. Other authors [15, 37] calculated the critical saturation concentration to be 50% for UNS S31600, i.e., approximately 7N Cl^- concentration required for stability of localized corrosion. Kappes and coauthors [11] observed as well that the maximum current density (i_{cp}) decreased with higher Cl^- content above the saturation concentration. On the other hand, i_{cp} increased with Cl^- concentration in the range below salt film formation. In this regard, the 7N Cl- concentration solution was chosen in this work to study the effect of W for being the crevice-like-solution with the highest i_{cp}. Similarly, the pH inside artificial pits has been reported to be close to 0 [9], becoming the pH value employed by Kappes et al. [11] and the chosen pH value in this work.

Galvele [13] developed the critical acidification model for pure metals; hence, the choice of parameters, especially for the stability product, must differ when estimating E_{crit} in alloys. Bocher et al. [14] employed a stability product value of $x \cdot i_{crit} = 0.01$ A/cm, with $x = 0.001$ cm for Ni-alloys. This choice of parameters results in $i_{crit} = 10$ A/cm^2, a current density value four orders of magnitude larger than the i_{crit} determined by Kappes [11] and in this work. Additionally, 10 A/cm^2 in the anodic potentiodynamic curves can only be reached in transpassive potentials, as seen in Figures 4 and 5, erroneously implying that both SDSS would be immune to crevice corrosion at all temperatures. In this regard, the i_{crit} obtained in this work, like the one calculated by Kappes [11], were considered to be more appropriate for the estimation of E_{crit} in DSS.

4.2. Role of W in crevice-like-solutions

The theoretical E_{crit} values obtained from Galvele's critical acidification model demonstrate the large difference in the aggressiveness of the solutions, as expected. The E_{crit} values obtained in 1M HCl where all more positive than the oxygen evolution reaction [33], implying that stable localized corrosion requires a higher chloride concentration and, thus, the material will suffer transpassive dissolution, i.e., E_{crit} in 1N Cl^- is, in reality, an E_{Trans}. In contrast, E_{crit} values for 7N Cl^- were low, suggesting that crevice corrosion could be possible in neutral chloride environments at all the temperatures investigated. Interestingly, Figure 8 clearly shows a significant difference in the concentration of dissolved ions in the two solutions, with much higher values for all elements in 7M LiCl.

Both materials behaved similarly in the 1N Cl^- environment. All parameters from the anodic potentiodynamic polarizations were in the same range (Figures 4 and 5), with the only exception of E_{corr}^* and i_{pass}, which were lower and higher, respectively, for UNS S32750, indicating a lower corrosion resistance in the pit/crevice solution. However, the concentration of dissolved metal cations was similar in both SDSSs (Figure 8). Since the anodic potentiodynamic polarization in all tests reached the transpassive region, it is suspected that most of the ions were released at these high potentials, causing negligible dissolution in the passive region or at E_{corr}^*.

In the more aggressive 7M LiCl solution, both materials showed larger differences, especially at 60°C. Even though all parameters extracted from the anodic potentiodynamic polarization curves (Figure 4) were in the same range up to 50°C, the concentration of released ions was higher in UNS S39274 than in UNS S32750. Nevertheless, at 60°C, UNS S39274 showed a somewhat better corrosion resistance as indicated by i_{cp}, E_{pp}, and the lower concentration of dissolved cations.

Based on the concentration of dissolved metal cations, the d'_M reported in Table 3 indicates an important difference that can be related to the difference achieved in E_{crit} for the two solutions. The only

values that changed significantly between the solutions were d'_W at all temperatures. In 1M HCl, d'_W was between 0.9 and 1, suggesting congruent W dissolution, like the other elements. In contrast, in 7M LiCl, d'_W fluctuated between 0.25 and 0.66, depending on the temperature, suggesting a surface enrichment in W. Indeed, W was the only element displaying incongruent dissolution, as all the other elements dissolved approximately uniformly at all temperatures. According to the Pourbaix diagrams [33], W is the only element capable of forming an oxide layer, WO_3, at pH 0. Indeed, a yellow (the color of WO_3 [33]) reflection was seen on UNS S39274 after the tests. Even though W is a ferrite stabilizer [38], ferrite dissolved selectively for UNS S39274, as seen in Figure 7. The dissolved W—in the form of tungstate ions—can precipitate forming a WO_3 layer, shown to reduce the corrosion rate [39]. A small enrichment was measured by EDS (Table 2) in ferrite, but not on austenite. Probably, given the small thickness of the deposit, a more surface-sensitive technique such as x-ray photoelectron spectroscopy (XPS) or Auger electron spectroscopy (AES) would be needed to confirm this assumption. On the other hand, the W-free material showed a uniform attack, as illustrated in Figure 7.

The analysis of the chemical composition of the phases before corrosion included in Table 2 showed that both α and γ phases of UNS S32750 are richer in Cr (> 1 wt.%) and Mo (approximately 0.5 wt.%) than the phases in UNS S39274. The total wt.% (Cr+Mo) difference between the two SDSSs for each phase was approximately the same as the content of W in UNS S39274 of that phase. Nevertheless, variances in chemical composition alone cannot explain the difference in the corrosion morphology observed by SEM (Figure 7). Local probe technique studies of passive film have concluded that, despite the higher PRE value of the ferrite phase in SDSS, austenite shows a more noble behavior, i.e., austenite is more corrosion resistant than ferrite [40]. However, when the material was exposed to a very aggressive environment (i.e., concentrated nitric acid), both austenite and ferrite adopted similar passive film properties and their differences disappeared. This observation is in line with the uniform corrosion observed in 7M LiCl solution at 60°C of UNS S32750 in this work. Nevertheless, the selective dissolution of ferrite observed for UNS S39274 is not in line with the SKPFM results obtained by Rahimi et al. [41], where ferrite showed a nobler behavior than austenite. On the other hand, selective dissolution of ferrite of SDSS was observed by Långberg et al. [42] as the data obtained by synchrotron XRR, XRF and XRD showed a higher dissolution quantity of Fe from ferrite than austenite. Additionally, this work observed the following order in element dissolution in UNS S32750 as the potentiodynamic polarization applied higher potentials: only Fe at $E < 1\ V_{Ag/AgCl}$, then dissolution of Fe and Cr at $E > 1.2\ V_{Ag/AgCl}$ causing an enrichment of Mo and Ni and, finally, dissolution of all elements at $E > 1.3\ V_{Ag/AgCl}$. This dissolution order fits the behavior seen for UNS S32750 in Table 2, where the surface was enriched in Ni and Mo and depleted in Cr and, especially, Fe. However, Rahimi et al. [41] stated that W promotes the stability of Mo, Cr and Fe. This statement can explain why the W-rich material experimented no Cr impoverishment and a much lower dissolution of Fe than the W-free material.

The improved localized corrosion resistance of UNS S39274 at 60°C—indicated by the lower metallic cation dissolution (Figure 8), the lower i_{cp}, and higher E_{pp} (Figures 4 and 5)—resulted in a higher E_{crit} calculated by Galvele's critical acidification model (Figure 9). The E_{crit} value obtained was nobler (approximately 100 mV) than that of UNS S32750, and nobler than the E_{crit} at previous temperatures. The increase of E_{crit} at 60°C was mainly due to the shift of η to more noble potentials. As stated by Galvele et al. [7], an increment of η indicates a slower dissolution rate.

Kendall's correlation coefficient calculated in Tables 4 and 5 also showed a significant difference between the quantity of W dissolved into the electrolyte and E_{crit} in 7M LiCl. The correlation between the dissolution of Cr, Fe, Ni, and Mo and E_{crit} is seen in Figures 8 and 9. Up to 50°C, the dissolution of these elements increased, whereas the E_{crit} decreased. However, at 60°C, this behavior changed for both parameters. The dissolution of the elements was reduced, whereas E_{crit} increased. In other words, at all temperatures, the dissolution quantity and the E_{crit} followed exactly the opposite trend, reflected by a strong negative value of Kendall's coefficient.

The fact that W was not correlated in the same way as the other elements might suggest that; either (i) W dissolution increased even though E_{crit} was nobler for UNS S39274 than for UNS S32750, or (ii) W

dissolution decreased as E_{crit} decreases for UNS S39274. Even though Figure 8 shows that W dissolution decreased at 60°C in 7M LiCl, as the other elements, whereas d'_W (Table 3) indicated that W was released in higher amounts at that condition. The only plausible explanation is that the dissolution of W was reduced, but not as much as the other elements at 60°C in 7M LiCl. This increment in d'_W despite the nobler E_{crit} at this particular condition for UNS S39274 is most probably the reason why the dissolution of W and E_{crit} were not correlated. Consequently, the combination of d'_W and Kendall's coefficient parameters infer a significant role of W on the improvement of corrosion resistance in propagating localized attacks, i.e., 7N Cl^- acidic environments, only at 60°C.

4.3. Prediction of crevice corrosion repassivation potential

In this work, Galvele's model was used to estimate the theoretical E_{crit} in different crevice-like-solutions and to study the validity of the model to predict crevice corrosion potentials, more specifically $E_{R,Crev}$ as it is widely used to define a protection potential [6]. Figure 10 compares E_{crit} values estimated by the critical acidification model in this work and by Kappes et al. [11] with experimental $E_{R,Crev}$ results of UNS S32750 and UNS S39274 measured by the PD-GS-PD technique in 3.5% NaCl (pH = 6.5) by Torres et al. [6]. In this regard, Torres et al. established a $T_{R,Crev}$ = 55°C for UNS S39274 in 3.5 wt.% NaCl by the PD-GS-PD technique. In the same study, UNS S39274 polarized at +600 $mV_{Ag/AgCl}$ (simulating chlorinated seawater [43, 44]) gave a CCT of 55°C in natural seawater. For UNS S32750, that same work measured a CCT of 45°C and a $T_{R,Crev}$ of 42.5°C in natural seawater polarized at +600 $mV_{Ag/AgCl}$.

As seen in Figure 10, the E_{crit} estimate by Kappes et al. [11] for UNS S32750 at room temperature in 7M LiCl was approximately 70 mV less noble than the one obtained in this work. Additionally, the difference between the E_{crit} value reported by Kappes and the $E_{R,Crev}$ of UNS S32750 in 1 wt.% NaCl environment at 30°C reported by Martinez et al. [45] is only of 20 mV, whereas the difference increases to 90 mV when compared to the E_{crit} obtained in this work. Nevertheless, many studies have tested SDSS, in particular UNS S32750, obtaining critical temperatures (T_{crit}) for localized corrosion well above 30°C [43, 46-49], i.e., E_{crit} is within the transpassive region at T ≤ 30°C, differing significantly from the E_{crit} values measured by Kappes and Martinez et al.

In this work, the E_{crit} values obtained using Galvele's model were independent of temperature and suggested the possibility of crevice corrosion at T ≥ 22 °C. In contrast, PD-GS-PD results gave E_{crit} values in the transpassive range for T < $T_{R,Crev}$, which was 40°C for UNS S32750 and 55°C for S39274. The discrepancy can be reconciled by the fact that Galvele's model describes stable localized corrosion propagation. The high potentials measured by the PD-GS-PD method in 3.5 wt.% NaCl suggested that crevice corrosion initiation is controlled by the breakdown of the passive film at T ≤ $T_{R,Crev}$ (or CCT) as suggested by the Li-Scully-Frankel framework [50, 51]. In this regard, while crevice corrosion could propagate stably if the concentration of the crevice environment reaches 7N Cl^-, in practice, the stability of the passive film at T < T_{crit} is rate-determining, preventing the development of the critical environment required for crevice corrosion propagation. To our knowledge, the effect of temperature on the critical acidification model has not been addressed to date. Despite these discrepancies, the E_{crit} obtained by Galvele's critical acidification model was in excellent agreement with $E_{R,Crev}$ values measured by the PD-GS-PD method in 3.5 wt.% NaCl (pH = 6.5) as seen in Figure 10, i.e., 33 mV difference at 60°C and a 66 mV difference at 50°C for UNS S32750, and no difference for UNS S39274 at 60°C. These findings, therefore, also suggest that the use of the critical acidification model to estimate the theoretical E_{crit} might require prior knowledge of T_{crit}.

5. Conclusions

In this work, simulated crevice environments were tested, and Galvele's critical acidification model applied to estimate E_{crit} values as a function of temperature and study the effect of W as an alloying element in solid solution. The following conclusions were drawn:

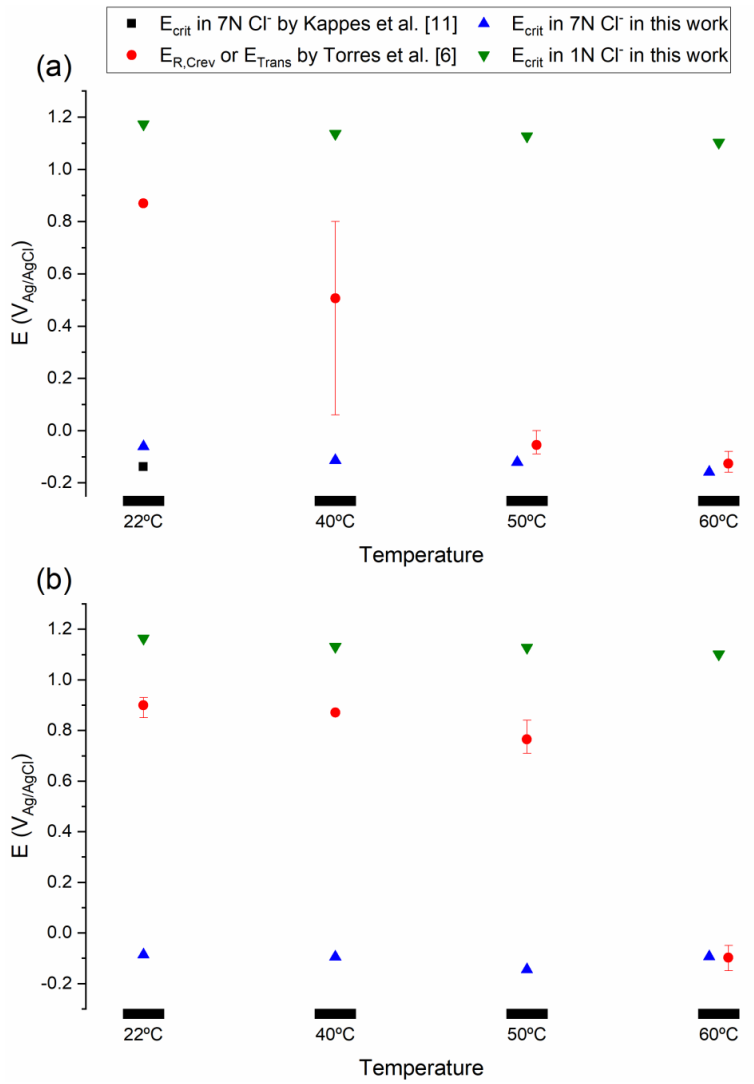

Figure 10. A comparison of estimated E_{crit} and measured $E_{R,Crev}$ for (**a**) UNS S32750, and (**b**) UNS S39274, as shown. Error bars indicate maximum and minimum values.

- A 7N Cl^- (pH = 0) crevice-like solution was necessary to simulate stable crevice propagation, suggesting that W additions could be beneficial only in situations of localized corrosion propagation under a salt film.
- The dissolution morphology was different between materials in 7N Cl^-. UNS S32750 experienced uniform corrosion of austenite and ferrite phases, whereas α-phase selectively dissolved in UNS S39274.
- Tungsten played a statistically significant role in the 7N Cl^- environment at 60°C. The incongruent dissolution of W suggested a possible surface enrichment. Both i_{cp} and E_{pp} indicated an improvement in corrosion resistance in the high-W SDSS. Additionally, the concentration of dissolved metal cations of all elements decreased significantly, and statistical analysis indicated that W was the only element whose dissolution was independent of E_{crit}.

- E_{crit} values obtained using the critical acidification model were independent of temperature, which contrasted with previous findings in simulated seawater environments. In line with the new Li-Scully-Frankel framework, the discrepancy was attributed to the stability of the passive film as a rate-determining step below a T_{crit}. Conversely, E_{crit} values obtained by the critical acidification model were in good agreement with $E_{R,Crev}$ results obtained by the PD-GS-PD technique in 3.5 wt.% NaCl for temperatures above $T_{R,Crev}$.

Author Contributions: Conceptualization, C.T., M.I. and R.J.; methodology, C.T., M.I., and R.J..; validation, C.T.; formal analysis, C.T.; investigation, C.T.; resources, C.T.; data curation, C.T.; writing—original draft preparation, C.T.; writing—review and editing, M.I. and R.J.; visualization, C.T.; supervision, M.I., and R.J.; project administration, R.J.; funding acquisition, R.J. All authors have read and agreed to the published version of the manuscript.

Funding: This research received no external funding.

Acknowledgments: The authors thank the help of Dr. Mariano Kappes (Comisión Nacional de Energía Atómica, CNEA, Argentina) for his guidance at the beginning of the project, especially with the crevice-like-solutions; Dr. Szymon Bernat (Sintef) for his help in the mechanical workshop with the modifications performed to the Avesta cell and Dr. Syverin Lierhagen (NTNU) for performing the ICP-MS analyses. This project was funded by the Norwegian University of Science and Technology (NTNU), and the experiments were performed at the Department of Mechanical and Industrial Engineering (MTP).

Conflicts of Interest: The authors declare no conflict of interest. The funders had no role in the design of the study; in the collection, analyses, or interpretation of data; in the writing of the manuscript, or in the decision to publish the results

References

1. A.J. Sedriks, Plenary Lecture—1986: Effects of Alloy Composition and Microstructure on the Passivity of Stainless Steels, *Corros.*, **1986**, *42*, 376-389. DOI: 10.5006/1.3584918.

2. C.O.A. Olsson, D. Landolt, Passive films on stainless steels—chemistry, structure and growth, *Electrochim. Acta*, **2003**, *48*, 1093-1104. DOI: 10.1016/s0013-4686(02)00841-1.

3. R.C. Newman, 2001 W.R. Whitney Award Lecture: Understanding the Corrosion of Stainless Steel, *Corros.*, **2001**, *57*, 1030-1041. DOI: 10.5006/1.3281676.

4. J.O. Nilsson, Super duplex stainless steels, *Mater. Sci. Technol.*, **1992**, *8*, 685-700. DOI: 10.1179/mst.1992.8.8.685.

5. C. Torres, M.S. Hazarabedian, Z. Quadir, R. Johnsen, M. Iannuzzi, The Role of Tungsten on the Phase Transformation Kinetics and its Correlation with the Localized Corrosion Resistance of 25Cr Super Duplex Stainless Steels, *J. Electrochem. Soc.*, **2020**, *167*, 081510. DOI: 10.1149/1945-7111/ab90af.

6. C. Torres, R. Johnsen, M. Iannuzzi, Crevice Corrosion of Solution Annealed 25Cr Duplex Stainless Steels: Effect of W on Critical Temperatures, *Corros. Sci.* accepted for publication.

7. J.R. Galvele, J.B. Lumsden, R.W. Staehle, Effect of Molybdenum on the Pitting Potential of High Purity 18% Cr Ferritic Stainless Steels, *J. Electrochem. Soc.*, **1978**, *125*, 1204. DOI: 10.1149/1.2131650.

8. R.C. Newman, M.A.A. Ajjawi, H. Ezuber, S. Turgoose, An experimental confirmation of the pitting potential model of Galvele, *Corros. Sci.*, **1988**, *28*, 471-477. DOI: 10.1016/0010-938x(88)90069-8.

9. T. Suzuki, M. Yamabe, Y. Kitamura, Composition of Anolyte Within Pit Anode of Austenitic Stainless Steels in Chloride Solution, *Corros.*, **1973**, *29*, 18-22. DOI: 10.5006/0010-9312-29.1.18.

10. E.C. Hornus, M.A. Rodríguez, R.M. Carranza, R.B. Rebak, Comparative Study of the Crevice Corrosion Resistance of UNS S30400 and UNS S31600 Stainless Steels in the Context of Galvele's Model, *Corros.*, **2017**, *73*, 41-52. DOI: 10.5006/2179.

11. M.A. Kappes, M.R. Ortíz, M. Iannuzzi, R.M. Carranza, Use of the Critical Acidification Model to Estimate Critical Localized Corrosion Potentials of Duplex Stainless Steels, *Corros.*, **2017**, *73*, 31-40. DOI: 10.5006/2142.

12. E.C. Hornus, C.M. Giordano, M.A. Rodriguez, R.M. Carranza, R.B. Rebak, Effect of Temperature on the Crevice Corrosion of Nickel Alloys Containing Chromium and Molybdenum, *J. Electrochem. Soc.*, **2015**, *162*, C105-C113. DOI: 10.1149/2.0431503jes.

13. J.R. Galvele, Transport Processes and the Mechanism of Pitting of Metals, *J. Electrochem. Soc.*, **1976**, *123*, 464. DOI: 10.1149/1.2132857.

14. F. Bocher, R. Huang, J.R. Scully, Prediction of Critical Crevice Potentials for Ni-Cr-Mo Alloys in Simulated Crevice Solutions as a Function of Molybdenum Content, *Corros.*, **2010**, *66*, 055002-055001 to 055002-055015. DOI: 10.5006/1.3430462.

15. J. Srinivasan, R.G. Kelly, On a Recent Quantitative Framework Examining the Critical Factors for Localized Corrosion and Its Impact on the Galvele Pit Stability Criterion, *Corros.*, **2017**, *73*, 613-633. DOI: 10.5006/2334.

16. R.D. Grimm, D. Landolt, Salt films formed during mass transport controlled dissolution of iron-chromium alloys in concentrated chloride media, *Corros. Sci.*, **1994**, *36*, 1847-1868. DOI: 10.1016/0010-938x(94)90023-x.

17. T. Li, J.R. Scully, G.S. Frankel, Localized Corrosion: Passive Film Breakdown vs. Pit Growth Stability: Part III. A Unifying Set of Principal Parameters and Criteria for Pit Stabilization and Salt Film Formation, *J. Electrochem. Soc.*, **2018**, *165*, C762-C770. DOI: 10.1149/2.0251811jes.

18. T. Li, J.R. Scully, G.S. Frankel, Localized Corrosion: Passive Film Breakdown vs. Pit Growth Stability: Part IV. The Role of Salt Film in Pit Growth: A Mathematical Framework, *J. Electrochem. Soc.*, **2019**, *166*, C115-C124. DOI: 10.1149/2.0211906jes.

19. *Technical note – Metallographic etching of duplex stainless steels*, Statoil ASA: Oslo, Norway, 2010, MAT–2010080.

20. W.D. Robertson, Molybdate and Tungstate as Corrosion Inhibitors and the Mechanism of Inhibition, *J. Electrochem. Soc.*, **1951**, *98*, 94-100. DOI: 10.1149/1.2778118.

21. C.R. Alentejano, I.V. Aoki, Localized corrosion inhibition of 304 stainless steel in pure water by oxyanions tungstate and molybdate, *Electrochim. Acta*, **2004**, *49*, 2779-2785. DOI: 10.1016/j.electacta.2004.01.039.

22. G. Mu, X. Li, Q. Qu, J. Zhou, Molybdate and tungstate as corrosion inhibitors for cold rolling steel in hydrochloric acid solution, *Corros. Sci.*, **2006**, *48*, 445-459. DOI: 10.1016/j.corsci.2005.01.013.

23. J.R. Galvele, Tafel's law in pitting corrosion and crevice corrosion susceptibility, *Corros. Sci.*, **2005**, *47*, 3053-3067. DOI: 10.1016/j.corsci.2005.05.043.

24. J.R. Galvele, Transport processes in passivity breakdown—II. Full hydrolysis of the metal ions, *Corros. Sci.*, **1981**, *21*, 551-579. DOI: 10.1016/0010-938x(81)90009-3.

25. V.G. Artemov, A.A. Volkov, N.N. Sysoev, A.A. Volkov, Conductivity of aqueous HCl, NaOH and NaCl solutions: Is water just a substrate?, *EPL (Europhysics Letters)*, **2015**, *109*. DOI: 10.1209/0295-5075/109/26002.

26. R. Qvarfort, New electrochemical cell for pitting corrosion testing, *Corros. Sci.*, **1988**, *28*, 135-140. DOI: 10.1016/0010-938x(88)90090-x.

27. G.S. Frankel, Pitting Corrosion, in *Corrosion: Fundamentals, testing, and Protection*, S.D. Cramer, B.S. Covino (Eds.); ASM International: Ohio, 2003, pp. 236-241.

28. J.D. Henderson, X. Li, D.W. Shoesmith, J.J. Noël, K. Ogle, Molybdenum surface enrichment and release during transpassive dissolution of Ni-based alloys, *Corros. Sci.*, **2019**, *147*, 32-40. DOI: 10.1016/j.corsci.2018.11.005.

29. N. Salkind, *Encyclopedia of Measurement and Statistics*; SAGE Publications: Thousand Oaks, California, 2007.

30. K. Pearson, Mathematical Contributions to the Theory of Evolution. III. Regression, Heredity, and Panmixia, *Philos. Trans. R. Soc. London, Ser. A*, **1896**, *187*, 253-318.

31. C. Croux, C. Dehon, Influence functions of the Spearman and Kendall correlation measures, *Statistical Methods & Applications*, **2010**, *19*, 497-515. DOI: 10.1007/s10260-010-0142-z.

32. T. Bellezze, G. Giuliani, G. Roventi, Study of stainless steels corrosion in a strong acid mixture. Part 1: cyclic potentiodynamic polarization curves examined by means of an analytical method, *Corros. Sci.*, **2018**, *130*, 113-125. DOI: 10.1016/j.corsci.2017.10.012.

33. M. Pourbaix, *Atlas of Electrochemical Equilibria in Aqueous Solutions*; National Association of Corrosion Engineers (NACE): Houston, Texas, USA, 1974.

34. M. Knyazeva, M. Pohl, Duplex Steels: Part I: Genesis, Formation, Structure, *Metallography, Microstructure, and Analysis*, **2013**, *2*, 113-121. DOI: 10.1007/s13632-013-0066-8.

35. G.S. Frankel, Pitting Corrosion of Metals, *J. Electrochem. Soc.*, **1998**, *145*, 2186-2198. DOI: 10.1149/1.1838615.

36. J. Mankowski, Z. Szklarska-Smialowska, Studies on accumulation of chloride ions in pits growing during anodic polarization, *Corros. Sci.*, **1975**, *15*, 493-501. DOI: 10.1016/0010-938x(75)90015-3.

37. J. Srinivasan, M.J. McGrath, R.G. Kelly, Mass Transport and Electrochemical Phenomena Influencing the Pitting and Repassivation of Stainless Steels in Neutral Chloride Media, *ECS Transactions*, **2014**, *58*, 1-11. DOI: 10.1149/05831.0001ecst.

38. J.E. Truman, Materials Science and Technology., in *Materials Science and Technology.*; John Wiley & Sons: Hoboken, NJ, 2006, pp. 529-581.

39. N. Bui, A. Irhzo, F. Dabosi, Y. Limouzin-Maire, On the mechanism for improved passivation by additions of tungsten to austenitic stainless steels, *Corros.*, **1983**, *39*, 491-496. DOI: 10.5006/1.3577373.

40. C. Örnek, C. Leygraf, J. Pan, Passive film characterisation of duplex stainless steel using scanning Kelvin probe force microscopy in combination with electrochemical measurements, *npj Mater. Degrad.*, **2019**, *3*. DOI: 10.1038/s41529-019-0071-8.

41. E. Rahimi, A. Kosari, S. Hosseinpour, A. Davoodi, H. Zandbergen, J.M.C. Mol, Characterization of the passive layer on ferrite and austenite phases of super duplex stainless steel, *Applied Surface Science*, **2019**, *496*. DOI: 10.1016/j.apsusc.2019.143634.

42. M. Långberg, C. Örnek, J. Evertsson, G.S. Harlow, W. Linpé, L. Rullik, F. Carlà, R. Felici, E. Bettini, U. Kivisäkk, E. Lundgren, J. Pan, Redefining passivity breakdown of super duplex stainless steel by electrochemical operando synchrotron near surface X-ray analyses, *npj Mater. Degrad.*, **2019**, *3*. DOI: 10.1038/s41529-019-0084-3.

43. R. Johnsen, H. Vingsand, Corrosion Properties Of UNS S32750, UNS N06022 And UNS N10276 In Seawater, Proceedings of CORROSION 2009. Atlanta, Georgia, 22-26 March 2009, 09195.

44. E.B. Haugan, M. Næss, C. Torres Rodriguez, R. Johnsen, M. Iannuzzi, Effect of Tungsten on the Pitting and Crevice Corrosion Resistance of Type 25Cr Super Duplex Stainless Steels, *Corros.*, **2017**, *73*, 53-67. DOI: 10.5006/2185.

45. P.A. Martínez, E.C. Hornus, M.A. Rodríguez, R.M. Carranza, R.B. Rebak, Crevice Corrosion Resistance of Super-Austenitic and Super-Duplex Stainless Steels in Chloride Solutions, Proceedings of Corrosion 2015. Dallas, Texas, 15-10 March 2015, 5740.

46. B. Deng, Y. Jiang, J. Gong, C. Zhong, J. Gao, J. Li, Critical pitting and repassivation temperatures for duplex stainless steel in chloride solutions, *Electrochim. Acta*, **2008**, *53*, 5220-5225. DOI: 10.1016/j.electacta.2008.02.047.

47. R.F.A. Jargelius-Pettersson, B. Pires Duarte, G. Duchamp, Pitting Corrosion in Austenitic and Duplex Stainless Steels, *Mater. Sci. Forum*, **1998**, *289-292*, 1029-1040. DOI: 10.4028/www.scientific.net/MSF.289-292.1029.

48. L.L. Machuca, S.I. Bailey, R. Gubner, Systematic study of the corrosion properties of selected high-resistance alloys in natural seawater, *Corros. Sci.*, **2012**, *64*, 8-16. DOI: 10.1016/j.corsci.2012.06.029.

49. Q.J. Meng, A. Adeleke, S. Derrickson, Localized Corrosion Resistance Of UNS S32750 And UNS S33207 Duplex Umbilical Tubes In Synthetic Seawater, Proceedings of Corrosion 2010. San Antonio, Texas, 14-18 March 2010, 10344.

50. G.S. Frankel, T. Li, J.R. Scully, Perspective—Localized Corrosion: Passive Film Breakdown vs Pit Growth Stability, *J. Electrochem. Soc.*, **2017**, *164*, C180-C181. DOI: 10.1149/2.1381704jes.

51. T. Li, J.R. Scully, G.S. Frankel, Localized Corrosion: Passive Film Breakdown vs Pit Growth Stability: Part II. A Model for Critical Pitting Temperature, *J. Electrochem. Soc.*, **2018**, *165*, C484-C491. DOI: 10.1149/2.0591809jes.

CONFERENCE PAPER I

Influence of Tungsten on Passivity Breakdown and Repassivation of 25Cr Super Duplex Stainless Steel

C. Torres, R. Johnsen, M. Kappes, M. Iannuzzi

CORROSION 2018, 15-19 April 2018, Phoenix, Arizona, USA

Paper No.
11102

NACE INTERNATIONAL CORROSION 2018 Conference & Expo

INFLUENCE OF TUNGSTEN ON PASSIVITY BREAKDOWN AND REPASSIVATION OF 25CR SUPER DUPLEX STAINLESS STEEL

Cristian Torres
Norwegian University of Science and Technology (NTNU), Department of Mechanical and Industrial Engineering
Richard Birkelands veg 2b
Trondheim, 7491, Norway

Roy Johnsen
Norwegian University of Science and Technology (NTNU), Department of Mechanical and Industrial Engineering
Richard Birkelands veg 2b
Trondheim, 7491, Norway

Mariano Kappes
Comisión Nacional de Energía Atómica, Instituto Sabato, UNSAM/CNEA-CONICET
Av. Gral. Paz 1499, San Martín, Buenos Aires, B1650KNA, Argentina

Mariano Iannuzzi
Curtin University
GPO BOX U1987
Perth, WA 6845, Australia

ABSTRACT

Super duplex stainless steels are ferritic-austenitic stainless steels with 25 wt% Cr and a pitting resistance equivalent (PRE) ≥ 40. Even though other elements, such as Cr and Mo, have been studied in much more detail than W, research has shown that an optimal composition exists, in which W in solid solution improves localized corrosion resistance. Outside this range, W is ineffective or even detrimental. However, the mechanisms by which W improves localized corrosion resistance in stainless steels are unclear. For example, debate still exists as to whether W enhances passivity or facilitates repassivation.

In this work, two super duplex stainless steels were investigated: a W-free (UNS S32750) and a 2.1 wt% W-containing (UNS S39274) grade. The first goal was to study differences in the overall localized corrosion resistance; while the second objective was to gain an insight into the mechanisms by which W affects the localized corrosion performance of super duplex stainless steels. The work was divided into two parts. Firstly, anodic potentiodynamic polarization curves were conducted in different simulated pit environments at various temperatures. Two simulated pit solutions were tested: 1 M HCl and 7 M LiCl adjusted to a pH of 0. In the second part, crevice repassivation potentials were measured using the potentiodynamic-galvanostatic-potentiodynamic technique in 3.5 wt% NaCl pH = 6.5 solution. This investigation will provide evidence regarding the influence of W in passive film stability and repassivation kinetics

Key words: localized corrosion, super duplex stainless steel, crevice repassivation potential, pit-like-solutions, tungsten

INTRODUCTION

Super duplex stainless steels (SDSS) are a type of highly alloyed stainless steels, with at least 25 wt% Cr. Additionally, SDSS have a dual austenitic and ferritic microstructure, with an ideal ratio between phases as close to one as possible.[1] Because of their high Cr, Mo, and N content, SDSS are widely used in corrosive environments where high corrosion resistance is required. However, SDSS can suffer localized corrosion in seawater and are limited to a maximum service temperature of 20ºC according to NORSOK M-001[2] and ISO 21457[3].

The literature on the effect of alloying elements in the corrosion resistance of duplex (22 wt% Cr) stainless steel and SDSS is vast. While most of the interest has been on Cr, Mo, and N, less attention has been traditionally paid to W. Haugan et al.[4] thoroughly reviewed the state of the art of stainless steels alloyed with W and their pitting and crevice corrosion performance in NaCl and seawater electrolytes. In short, according to the authors, there seems to be an optimal concentration range in which W, when present in solid solution, increases the localized corrosion resistance of the alloy. Outside this range, W can have either no effect or even become detrimental towards localized corrosion resistance, weldability, and mechanical properties. The authors investigated two SDSS materials that differed, primarily, in their W content; namely, 0.5 and 2.2 wt% W. Results showed a higher critical crevice temperature (CCT) and crevice repassivation potential ($E_{RP,Crev}$) values for the SDSS with 2.2 wt% W, which was confirmed by open circuit potential exposure (E_{OC}) in natural seawater.

Despite the documented improvements in localized corrosion resistance provided by W, there is no agreement regarding the mechanisms by which W increased pitting and crevice corrosion performance. Some authors[5] have suggested that W enhances passivity, while others[6-9] point out that W facilitates repassivation by means of tungstate ions once localized corrosion has taken place. Likewise, while there is consensus about the beneficial effect of W as a solid solution element, the influence of W in phase precipitation kinetics remains controversial. For example, some authors[6, 8-11] have found that W retards the formation of σ-phase precipitation, favoring instead the precipitation of χ-phase, which has been shown less detrimental towards corrosion resistance and mechanical properties than σ-phase. Contrarily, others[12, 13] claim that W enhances the precipitation kinetics of all tertiary phases, including σ-phase.

In practice, in the oil and gas industry, the controversy has led to different standards adopting different Pitting Resistance Equivalent (PRE) definitions as discussed elsewhere.[4] For example, NORSOK M-001[2] defines PRE by the weight percentages of Cr, Mo and N as shown in Equation 1, where the suffix N indicates that the original PRE formula proposed by Lorentz and Medawar[14] was modified to include nitrogen. On the other hand, ISO 21457[3] includes W in the PRE formula as shown in Equation 2, where the subscript W indicates that tungsten was added to the empirical expression.

$$PRE_N = \%Cr + 3.3\%Mo + 16\%N \quad (1)$$

$$PRE_{N,W} = \%Cr + 3.3\,(\%Mo + 0.5\%W) + 16\%N \quad (2)$$

Techniques to evaluate localized corrosion resistance

The choice of experimental technique to assess localized corrosion resistance also plays a role in pitting and crevice corrosion research. The different experimental approaches have shown both advantages and limitations. The cyclic potentiodynamic polarization (CPP) technique described in ASTM G61[15] is the most common methodology. Both the pitting or crevice initiation potentials (E_P and E_{Crev}, respectively) as well as the respective repassivation potential values (E_{RP} and $E_{RP,Crev}$) can be measured from CPP curves. However, for highly alloyed corrosion resistant alloys such as SDSS, localized corrosion does not occur within the water stability region and pitting or crevice corrosion can initiate concurrently with transpassive dissolution and oxygen evolution.[16, 17] The limited pitting or crevice corrosion growth in the forward scan represents and intrinsic limitation of the CPP method since E_{RP} values become independent of prior pit growth only above certain pit depth according to Sridhar and Cragnolino.[18] In this regard, the

authors associated this critical pith depth to a minimum charge density of 10 C/cm^2. Consequently, materials exhibiting a small hysteresis loop or no hysteresis often exhibit high E_{RP} values, making the proper analysis of their localized corrosion resistance difficult. This limitation is illustrated, for example, in the results of Haugan et al.[4] for the 2.2 wt% W SDSS below the critical crevice temperature (CCT).

The potentiodynamic-galvanostatic-potentiodynamic (PD-GS-PD) technique was developed by Mishra and Frankel[19] as an attempt to circumvent the issues associated with CPP in nickel-based alloys. The PD-GS-PD approach is a modification of the Tsujikawa-Hisamatsu Electrochemical (THE) technique, now implemented as ASTM G192.[20] The PD-GS-PD technique consists of three steps: i) a potentiodynamic anodic polarization until reaching a limit current density value, ii) a galvanostatic step where the limit current density value is held, and iii) a final potentiodynamic anodic backwards polarization. The aim of the galvanostatic step is to initiate localized corrosion, assuring the attack reached the critical pit depth and that a lower bound $E_{RP,Crev}$ value is obtained. Among many investigations, Ortiz et al.[21] and Giordano et al.[22] studied the results of $E_{RP,Crev}$ values obtained with different techniques for Alloy 22 (UNS N06022). Martinez at al.[23] did the same for UNS S32750 and other super-austenitic stainless steels. All of them concluded that the PD-GS-PD technique gave reproducible critical potentials, but it might be considered too conservative as it consistently gave low $E_{RP,Crev}$ values.

The critical acidification model

The critical acidification model first proposed by Galvele[24-26] can estimate the critical potential (E_{crit}) for either pitting or crevice corrosion initiation if the concentration of aggressive species of the electrolyte is known. In fact, there are a few studies where this model has been used to estimate critical potentials of stainless steels.[27-30]

When combined with polarization experiments in simulated pit or crevice electrolytes, Galvele's model can be used to obtain mechanistic information regarding localized corrosion propagation. Recently, Kappes et al.[30] thoroughly reviewed the composition of pit and crevice environments proposed for stainless steels and nickel alloys. In addition, the authors investigated artificial pit-like solutions of different chloride concentrations to determine the critical potentials of a duplex stainless steel and a SDSS. The authors found that salt film precipitation occurred at chloride concentrations 9 M or higher. Therefore, they concluded that the most representative pit-like solution was close to 7 M Cl^-. Furthermore, the authors defended the validity of the critical acidification model with field experience and laboratory experiments taking as a reference the 7M simulated pit solution and using the PD-GS-PD technique.

In the present work, the effect of W on SDSS has been investigated in simulated pit environments. Additionally, the PD-GS-PD technique was used to evaluate the crevice corrosion susceptibility of SDSS with and without W in neutral NaCl electrolytes.

EXPERIMENTAL PROCEDURE

Two different super duplex stainless steels were used in this study: a W free SDSS (UNS S32750) and a 2.1 wt% W SDSS (UNS S39274). Table 1 summarizes the composition of both samples. UNS S39274 was received in the solution annealed condition (10 minutes at 1085ºC) whereas UNS S32750 was received as extruded without proper heat treatment. For this reason, UNS S32750 was solution annealed for 15 minutes at 1110ºC, followed by water quenching as recommended by the manufacturer.

Samples were wet ground to 500 US-grit SiC paper using deionized water as lubricant immediately before starting the set-up of the test. Specimens were subsequently rinsed with acetone, followed by distilled water and ethanol and cleaned in an ultrasonic bath with ethanol for 5 minutes. All experiments included in this study were performed at least in duplicate.

Anodic Potentiodynamic Polarization in Pit-Like-Solutions

Anodic potentiodynamic polarization curves were performed in solutions that simulated those present inside pits and crevices. Different temperatures were tested: 10ºC, room temperature (i.e., 22ºC) and 40ºC. The temperature was controlled by means of a cooling/heating bath in which the set-up was immersed. Temperature was not controlled in the tests performed at room temperature. Two different pit-like-solutions were tested: 1M HCl and 7M LiCl. Tests in 1 M HCl were performed to characterize the behavior of the materials at pH 0 in the absence of additional chloride ions. The 7M LiCl concentration was chosen from the results obtained by Kappes et al.[30], since the highest current density was obtained at this concentration. The pH of the 7M LiCl solution was adjusted to 0 with concentrated HCl, following Bocher et al.[31] relationship between activity coefficient for H^+ and chloride concentration.

An Ag/AgCl KCl saturated electrode was used as reference and a mesh of Pt as counter electrode. Samples were immersed in the solution by hanging them with Pt wire. Nitrogen (N_2) gas was purged for 1 hour before immersing the sample in the electrolyte and maintained through all the experiment. Then, samples were freely exposed at E_{OC} for 1 hour, followed by anodic polarization with a scan rate of 0.167 mV/s. The dissolved oxygen content was measured using an optical oxygen probe, which indicated a maximum oxygen content of 0.1 ppb.

Crevice Corrosion Tests in Simulated Seawater

A double-wall cell filled with 160 ml of 3.5 wt% NaCl pH 6.5 solution was used for these tests. The samples were mounted in a multi-crevice assembly and exposed to the test solution following the description for flat specimens in ISO18070.[32] Each crevice washer had 12 artificially creviced teeth and were covered with a PTFE tape as indicated by ASTMG192.[20] The applied torque was 5 N·m.[22]

The total surface area exposed to the electrolyte was approximately 3 and 11 cm^2 for UNS S32750 and UNS S39274, respectively. In contrast, the area covered by the crevice former was 4.9 cm^2 for both materials.

Nitrogen gas was purged for 2 hours before immersing the sample in the electrolyte and it was kept through all the experiment. In addition, the dissolved oxygen concentration was measured by means of an optical oxygen sensor to verify that the electrolyte was properly deaerated before immersing the samples. The oxygen concentration before polarization was below 0.1 ppb. The temperature was controlled by means of a cooling and heating bath connected to the double wall of the set-up. Test temperatures were 10ºC, room temperature (22ºC), 40ºC and 60ºC. Temperature was not controlled in the tests performed at room temperature.

The electrochemical tests were performed in a three-electrode configuration using a commercially available potentiostat. An Ag/AgCl KCl saturated electrode, kept at room temperature and connected to the cell via a salt bridge, was used as the reference while a Pt mesh was chosen as counter electrode. Specimens were freely exposed at E_{OC} for 15 minutes. After the initial E_{OC} stabilization, a 15 min cathodic cleaning step was performed at a cathodic current density of -1 μA/cm^2, followed by a 30 min stabilization at E_{OC}. The PD-GS-PD technique was performed as detailed by Kappes et al.[30] The forward anodic potentiodynamic polarization was conducted at a scan rate of 0.167 mV/s, starting at 30 mV below E_{OC} and ending once a current density of 25 μA/cm^2 was reached. The current was held at 25 μA/cm^2 for 2 hours. After 120 minutes, the potential was reversed at a scan rate of 0.167 mV/s, starting from the potential at which the GS step finished, until the repassivation of the material. The $E_{RP,Crev}$ was determined as a cross-over potential.[19]

Characterization

After the tests, all samples were rinsed with distilled water and ethanol and were analyzed in an infinite focus optical microscope.

RESULTS

Anodic Potentiodynamic Polarization in Pit-Like-Solutions

Figure 1 shows the anodic potentiodynamic polarizations obtained in two different crevice-like-solutions: 1M HCl and 7M LiCl at all the temperatures tested in this project. A chief difference between both crevice-like-solutions was the current density measured at any potential. In this regard, current densities were at least one order of magnitude higher at all temperatures in the 7M LiCl electrolyte for both materials. In addition, all results in 7M LiCl presented an active-to-passive transition, whereas 1M HCl had an spontaneously passive behavior. The absence of an active-to-passive transition in the 1 M HCl electrolyte contrasts with the findings of Kappes et al.[30] At room temperature and 40ºC in 7M LiCl, there was a decrease in the current density values; however, current densities did not decrease to the passive current range found in the 1M HCl solution. Therefore, above the flade potential (E_{Flade}), corrosion was likely diffusion-limited but it would be incorrect to state that passivation occurred at these temperatures. The critical current density obtained before passivation, i_{Flade}, was the same for both materials in all conditions, although E_{Flade} was lower for UNS S39274 at room temperature and 40ºC in 7M LiCl. In addition, i_{Flade} increases with temperature in 7M LiCl and passive current density (i_p) increases as well with temperature in 1M HCl.

Prediction of Crevice Corrosion Potential

Galvele's critical acidification model[24-26], described by Equation 3, can be used to estimate critical potentials (E_{crit}) if the concentration of aggressive species in the solution is known.

$$E_{crit} = E_{corr}^{*} + \eta + \phi + E_{inh} \qquad (3)$$

Where E_{corr}^{*} is the corrosion potential of the material inside the pit or crevice, η is the anodic polarization required to reach a critical current (i_{crit}) at the bottom of the pit or crevice, ϕ is the ohmic potential drop along the pit or crevice and E_{inh} is an additional polarization required in the presence of buffers or inhibitors. Henceforth, in order to simplify the model, E_{inh} is considered negligible to the contribution of E_{crit}. Although this assumption was arbitrary, it is considered acceptable since the E_{crit} value obtained with this simplified model is more conservative, i.e. lower E_{crit}.

The ohmic potential drop term is estimate by means of Equation 4:[30, 31]

$$\Phi = \frac{\rho \cdot i_{crit} \cdot x^2}{2w} \qquad (4)$$

where ρ is the resistivity and is assumed to be 10 Ω·cm[31], w is the crevice gap which is 1 μm[30], x is the diffusion distance considered to be 10^{-4} cm.[33] i_{crit} is the critical current mention above and can be estimated by following the relationship in Equation 5 given by Galvele:[25]

$$x \cdot i_{crit} = k \qquad (5)$$

where k s a constant that is function of the metal and pH of the solution and which is given the value of 10^{-6} A/cm in this case.[33]

The i_{crit} obtained with Equation 5 is 10^{-2} A/cm^2. This value of current density was reached in all cases except in 1M HCl at room temperature and 40ºC for UNS S39274 as can be seen in Figure 1. According to Equation 4, ϕ was 5 μV. This value is so low compared with the other terms that it was neglected. Finally, E_{crit} can be calculated by means of Equation 3. Values of E_{corr}^{*} and η are obtained from the anodic potentiodynamic curves and are shown together with the calculated E_{crit} in Table 2.

Crevice Corrosion Tests in Simulated Seawater

The results obtained with the PD-GS-PD technique are illustrated in Figure 2 for all tested conditions. Because of the nearly-neutral pH of the solution, there was no active-passive transition for any of the samples. As seen in Figure 2, the passive current density was the same for both materials at 10ºC, room temperature (22ºC), and 60ºC. However, the passive current was higher for UNS S32750 at 40ºC. Furthermore, small fluctuations in current density were present in the results for UNS S32750 and only at 60ºC for UNS 39274. These small fluctuations might be related to metastable pitting prior to crevice propagation.[34]

Crevice corrosion initiated concurrent with transpassive dissolution in all cases as evidenced by the high breakdown potential values of 0.8 – 1.05 $V_{Ag/AgCl}$ for UNS S32750 and 1.0 – 1.1 $V_{Ag/AgCl}$ for UNS S39274. The decrease in potential during the galvanostatic step was small in all cases apart from the samples tested at 60ºC as illustrated in Figure 3.

Figure 4 shows the $E_{RP,Crev}$ obtained for each material as a function of test temperature. Both SDSS had identical $E_{RP,Crev}$ potential values as determined by the PD-GS-PD technique. In addition, both alloys gave the same temperature dependence, with a sharp drop in $E_{RP,Crev}$ above 40ºC. The largest difference between the two alloys was seen at 10ºC and 40ºC, where the repassivation potential of UNS S39274 was in the order of 20 mV more positive than that of UNS S32750.

Crevice corrosion was observed on both materials at 40ºC and 60ºC as seen in Figure 5. In addition, Figure 6 and Figure 7 illustrate the number of crevices and the corresponding depths for each material. At 40ºC UNS S32750 had a larger number of crevice corrosion areas than UNS S39274 as indicated by the higher number of crevices, even though their depth was in the same range for both alloys. At 60ºC, the number of crevices was higher and the attack deeper on UNS 39274 than on UNS S32750. However, the median crevice depth of UNS S39274 was smaller compared to that of UNS S32750.

In contrast, only minor discoloration was found at 10ºC and room temperature (22 ºC). These results are in accordance with the temperature limit in NORSOK M-001[2] and ISO 21457[3], but seem to contradict Haugan's et al.[4]

DISCUSSION

Anodic Potentiodynamic Polarization in Pit-Like-Solutions

Anodic current density was much higher in 7M LiCl than in 1M HCl at all temperatures for both alloys. In other words, the chloride concentration directly affected the corrosion resistance of both alloys, decreasing with increasing chloride concentrations as it has been shown previously by others.[21, 28, 35, 36]

In 1M HCl, both materials behaved similarly at 10ºC and at room temperature. However, passive current densities were higher for UNS S32750 at 40ºC than UNS S39274. In 7M LiCl, both materials performed similarly at 10ºC, but UNS S39274 had a lower E_{Flade} at room temperature and 40ºC than UNS S32750, even though current density decreased more in the case of UNS S32750. Kappes et al.[30] tested UNS S32750 in 7M LiCl at room temperature. They obtained a much lower E_{Flade} and passive current density values than the ones obtained in this study. Nevertheless, the UNS S32750 samples studied by those authors had slightly different composition than the one studied here, being the main difference the fact that it had 0.55 wt% W. Therefore, it might lead to think that W helps to get lower passivation current at lower potentials. However, in this study, the higher W content material did not follow this behavior, only the fact that the decrease in current density was achieved at lower potentials.

Prediction of Crevice Corrosion Potential

Table 2 shows the E_{crit} values obtained for all temperatures by means of Galvele's model.[24-26] The discussion regarding the values chosen for the terms used in the model can be found elsewhere.[30, 31, 33]

Kappes et al.[30] followed the same procedure for UNS S32750 in 7M LiCl concentration pit-like-solutions at room temperature and obtained a value of E_{crit} that differed only in 63 mV from the one obtained in this study for the same alloy in same environment at same temperature. Thereby, Galvele's model was able to estimate similar E_{crit}, despite the fact that the anodic potentiodynamic polarization did not look similar as mentioned in the paragraph above. The reason is that Galvele's model does not take into account the passive behavior of the material, but the potential at which the i_{crit} is reached which is before the passivation region.

The estimated values of E_{crit} in 7M LiCl were different from the $E_{RP,Crev}$ values obtained with the PD-GS-PD technique in this project. Only the $E_{RP,Crev}$ obtained at 60ºC was similar to the values obtained of E_{crit}, even though E_{crit} was not estimated at 60ºC. In other words, the critical acidification model predicted that crevice corrosion should have initiated at low potentials. However, below 60 °C, crevice corrosion started at transpassive potentials. It is possible that experimental setup or the choice of experimental technique were not aggressive enough to obtain $E_{RP,Crev}$ values comparable to Galvele's model. Since the choice of crevice former has been shown to affect anodic polarization results.[22, 37, 38] In fact, Martinez et al.[23] used ceramic wrapped crevice formers and obtained $E_{RP,Crev}$ at 40ºC comparable to the estimated E_{crit} obtained here. Likewise, evaluating the CCT using alternative techniques such as the ASTM G-48 methodology could yield useful comparisons, which is planned as future work.

On the other hand, the estimated values of E_{crit} in 1M HCl were closer to $E_{RP,Crev}$ obtained at the same temperatures, even though the difference was still significant since it was about 250 mV between them. As seen in the results, as crevice corrosion was not aggressive at 10ºC, room temperature or 40ºC, 1M HCl crevice-like-solution estimated closer E_{crit} than 7M LiCl.

Crevice Corrosion Tests in Simulated Seawater

The crevice repassivation values obtained in the PD-GS-PD tests in 3.5 wt% NaCl solution with 6.5 pH summarized in Figure 4 suggested that W did not have a measurable role in the crevice repassivation kinetics since both alloys had comparable $E_{RP,Crev}$ values at all temperatures. Only small differences were seen at 10ºC and 40ºC, where the crevice repassivation potential of UNS S39274 was about 20 mV higher than that of UNS S32750. However, $E_{RP,Crev}$ values were within the transpassive region in both cases. Thereby, it is necessary to perform more test at temperature intervals of 5ºC between 40ºC and 60ºC to verify whether W plays an important role in the crevice repassivation potential. In addition, testing the materials at higher temperatures such as 75ºC and 95ºC which are the critical crevice temperatures (CCT) obtained by Haugan et al.[4] for these alloys might show bigger differences in the repassivation kinetics.

Tungsten seemed, nonetheless, to improve passivity at 40ºC as reflected by the lower passive current density and the absence of metastable events. However, W did not help in more aggressive conditions as at 60ºC, where the passive current density was similar in both alloys and both have presence of metastable pitting, besides the fact that the $E_{RP,Crev}$ drops to the same value.

Haugan et al.[4] observed the largest difference between both SDSS using the repassivation potential (E_{RP}) measured on crevice-free specimens as an estimator of the conditions leading to crevice corrosion initiation. In that case, the critical crevice temperature determined based on E_{RP} was 30 °C higher on the high-W SDSS. However, the difference in the critical crevice repassivation temperature (CCRT) estimated by $E_{RP,Crev}$ on creviced coupons was 10°C. The fact that they applied a lower torque (2 N·m) does not affect the comparison of results between both studies because Akashi et al.[39] demonstrated that crevice repassivation potential was independent of applied torque for torques above 1 N·m and, later, Giordano et al.[22] proved that crevice repassivation potential was independent for torques higher than 2 N·m using several different techniques, CPP and PD-GS-PD among them. The result for UNS S32750 was in accordance with the values obtained in this study as well, since in this test the drop in

$E_{RP,Crev}$ was observed only at 60ºC. In contrast, the decrease in $E_{RP,Crev}$ happened at 50ºC for UNS S39274. This nonconformity between the results from the two studies indicate that the PD-GS-PD technique could be more aggressive than CPP, blurring the influence of differences in chemical composition.

Martinez et al.[23] reported that the $E_{RP,Crev}$ values obtained by means of PD-GS-PD technique for UNS S32750 and other stainless steel alloys for solutions with a chloride concentration between 10.000 and 100.000 ppmwt tested between 30ºC and 90ºC, were independent of temperature and chloride concentration. The solution tested in this research falls in between said range of chloride concentration (3.5 wt% = 35.000 ppmwt). Consequently, results from both studies can be compared taking into account that the test parameters were the same. The only exception is the material of the crevice washers used, which were ceramic in the case of Martinez et al. Thereby, even though their $E_{RP,Crev}$ for 60ºC was in line with the one obtained in this study, Figure 4 indicates clearly a temperature dependence for both alloys. This difference might be explained by the fact that the crevice washers used by Martinez et al. were ceramic whereas the ones used in this research were made of PTFE as ceramic crevice formers result in more aggressive crevice corrosion, i.e., lower $E_{RP,Crev}$[22, 37, 38].

Despite the fact that there was not a clear difference in the $E_{RP,Crev}$ between both materials included in this test program, there are differences in the number of crevices as seen in Figure 6 and in the crevice depth distribution as illustrated in Figure 7. At 40ºC, both materials had similar median crevice depth values as shown in Table 3, i.e., there was no difference in the crevice sizes. However, UNS S32750 presented a higher density of crevices. On the other hand, at 60ºC, UNS S39274 exhibited higher density of crevices and, even though it has a lower median crevice depth value than UNS S32750, it produced the deepest crevice. Consequently, no clear conclusion can be made at 60ºC between both materials.

CONCLUSIONS

After studying the effect of W in solid solution in two different materials: a W-free SDSS (UNS S32750) and a 2.1 wt% W SDSS (UNS S39274); the following conclusions could be drawn from the results obtained in this paper:

- There were no differences in E_{crit} estimated by means of Galvele's critical acidification model between both materials in both crevice-like-solutions.
- Results in 1M HCl suggested that crevice corrosion should not occur between 10ºC and 40ºC, as the E_{crit} obtained was higher than E_{trans}.
- PD-GS-PD tests seemed to support the estimation made by the critical acidification model at 1M HCl, as the only $E_{RP,Crev}$ value obtained below E_{trans} was at 60ºC.
- The choice of electrochemical technique seems to play a crucial role on estimating crevice corrosion resistance. More work is ongoing to compare results with long-term OCP exposure in seawater.

ACKNOWLEDGEMENTS

This work has been financed through internal funds at the Norwegian University of Science and Technology (NTNU).

REFERENCES

1. J.O. Nilsson, *Materials Science and Technology* 8, 8 (1992): p. 685-700.
2. NORSOK M-001, "Materials selection. Rev. 4" (Lysaker, Norway: Standards Norway, 2004).
3. ISO 21457:2010, "Petroleum, petrochemical and natural gas industries -- Materials selection and corrosion control for oil and gas production systems" (Geneva, Switzerland: International Organization for Standardization, 2010).

4. E.B. Haugan, M. Næss, C. Torres Rodriguez, R. Johnsen, M. Iannuzzi, *Corrosion* 73, 1 (2017): p. 53-67.
5. N. Bui, A. Irhzo, F. Dabosi, Y. Limouzin-Maire, *Corrosion* 39, 12 (1983): p. 491-496.
6. J.S. Kim, H.S. Kwon, *Corrosion* 55, 5 (1999): p. 512-521.
7. J.S. Kim, P.J. Xiang, K.Y. Kim, *Corrosion* 61, 2 (2005): p. 174-183.
8. K.Y. Kim, P.Q. Zhang, T.H. Ha, Y.H. Lee, *Corrosion* 54, 11 (1998): p. 910-921.
9. S.-H. Jeon, S.-T. Kim, I.-S. Lee, J.-S. Kim, K.-T. Kim, Y.-S. Park, *Journal of Alloys and Compounds* 544 (2012): p. 166-172.
10. K. Ogawa, H. Okamoto, M. Ueda, M. Igarashi, T. Mori, T. Kobayashi, *Welding International* 10, 6 (1996): p. 466-472.
11. H.J. Park, H.W. Lee, *Int J Electrochem Sc* 9, 12 (2014): p. 6687-6698.
12. J.O. Nilsson, P. Kangas, A. Wilson, T. Karlsson, *Metallurgical and Materials Transactions A: Physical Metallurgy and Materials Science* 31, 1 (2000): p. 35-45.
13. S. Wessman, R. Pettersson, *steel research international* 86, 11 (2015): p. 1339-1349.
14. K. Lorentz, G. Medawar, *Tyssenforschung* 1, 3 (1969): p. 97-108.
15. ASTM G61-86(2014), "Standard Test Method for Conducting Cyclic Potentiodynamic Polarization Measurements for Localized Corrosion Susceptibility of Iron-, Nickel-, or Cobalt-Based Alloys" (West Conshohocken, PA: ASTM International, 2014).
16. D.D. Macdonald, *Pure and Applied Chemistry* 71, 6 (1999):
17. D.D. Macdonald, in *Theory of the Transpassive State*, ed.(San Francisco, CA: The Electrochemical Society Spring Meeting, 2001).
18. N. Sridhar, G.A. Cragnolino, *Corrosion* 49, 11 (1993): p. 885-894.
19. A.K. Mishra, G.S. Frankel, *Corrosion* 64, 11 (2008): p. 836-844.
20. ASTM G192 - 08(2014), "Standard Test Method for Determining the Crevice Repassivation Potential of Corrosion-Resistant Alloys Using a Potentiodynamic-Galvanostatic-Potentiostatic Technique" (West Conshohocken, PA: ASTM International, 2014).
21. M.R. Ortíz, M.A. Rodríguez, R.M. Carranza, R.B. Rebak, *Corrosion* 66, 10 (2010): p. 105002-105002-105012.
22. C.M. Giordano, M. Rincón Ortíz, M.A. Rodríguez, R.M. Carranza, R.B. Rebak, *Corrosion Engineering, Science and Technology* 46, 2 (2011): p. 129-133.
23. P.A. Martínez, E.C. Hornus, M.A. Rodríguez, R.M. Carranza, R.B. Rebak, "Crevice Corrosion Resistance of Super-Austenitic and Super-Duplex Stainless Steels in Chloride Solutions," Corrosion 2015, NACE International, 2015).
24. J.R. Galvele, *Journal of The Electrochemical Society* 123, 4 (1976): p. 464.
25. J.R. Galvele, *Corrosion Science* 21, 8 (1981): p. 551-579.
26. S.M. Gravano, J.R. Galvele, *Corrosion Science* 24, 6 (1984): p. 517-534.
27. J.R. Galvele, J.B. Lumsden, R.W. Staehle, *Journal of The Electrochemical Society* 125, 8 (1978): p. 1204.
28. E.C. Hornus, C.M. Giordano, M.A. Rodriguez, R.M. Carranza, R.B. Rebak, *Journal of the Electrochemical Society* 162, 3 (2015): p. C105-C113.
29. E.C. Hornus, M.A. Rodríguez, R.M. Carranza, R.B. Rebak, *Corrosion* 73, 1 (2017): p. 41-52.
30. M.A. Kappes, M.R. Ortíz, M. Iannuzzi, R.M. Carranza, *Corrosion* 73, 1 (2017): p. 31-40.
31. F. Bocher, R. Huang, J.R. Scully, *Corrosion* 66, 5 (2010): p. 055002-055002-055015.
32. ISO 18070:2015, "Corrosion of metals and alloys - Crevice corrosion formers with disc springs for flat specimens or tubes made from stainless steel" (Geneva, Switzerland: International Organization for Standardization, 2015).
33. J.R. Galvele, *Corrosion Science* 47, 12 (2005): p. 3053-3067.
34. G.S. Frankel, L. Stockert, F. Hunkeler, H. Boehni, *Corrosion* 43, 7 (1987): p. 429-436.
35. N.J. Laycock, R.C. Newman, *Corrosion Science* 39, 10-11 (1997): p. 1771-1790.
36. E.C. Hornus, M.A. Rodríguez, R.M. Carranza, R.B. Rebak, "Effect of Temperature and Chloride Concentration on the Crevice Corrosion Resistance of Austenitic Stainless Steels," Corrosion 2016, NACE International, 2016).
37. X. Shan, J.H. Payer, *Corrosion* 66, 10 (2010): p. 105005-105014.

38. X. Shan, J.H. Payer, "Comparison of Ceramic and Polymer Crevice Formers on the Crevice Corrosion Behavior of Ni-Cr-Mo Alloy C-22," Corrosion 2007, NACE International, 2007).
39. M. Akashi, G. Nakayama, T. Fukuda, "Initiation Criteria for Crevice Corrosion of Titanium Alloys Used for HLW Disposal Overpack," Corrosion 98, NACE International, 1998).

TABLES

Table 1: Chemical composition, including PRE values calculated, of the SDSS samples provided by the suppliers for the specific batches used in this project (in wt%)

Material	PRE_N / $PRE_{N,W}$	C	Si	Mn	P	S	Cu	Ni	Cr	Mo	N	W	Fe
UNS S32750	43 / 43	0.014	0.27	0.51	0.021	0.0009	0.14	6.42	25.6	3.83	0.295	-	Bal.
UNS S39274	40 / 43	0.018	0.24	0.71	0.021	0.002	0.52	6.3	24.9	3.1	0.29	2.1	Bal.

Table 2: Prediction of crevice critical potential based on Galvele's model, including E_{corr}* and η values obtained from the plot results.

		7M LiCl			1M HCl		
		10ºC	22ºC	40ºC	10ºC	22ºC	40ºC
E_{corr}* ($V_{Ag/AgCl}$)	UNS S32750	-0.283	-0.286	-0.324	-0.162	-0.142	-0.152
	UNS S39274	-0.289	-0.282	-0.292	-0.159	-0.167	-0.160
η ($V_{Ag/AgCl}$)	UNS S32750	0.265	0.166	0.091	1.341	1.297	1.267
	UNS S39274	0.289	0.146	0.079	1.354	1.337	1.295
E_{crit}	UNS S32750	-0.017	-0.120	-0.232	1.179	1.155	1.115
	UNS S39274	0.00	-0.137	-0.213	1.195	1.170	1.135

Table 3: Median values of crevice depth obtained from Figure 7

Material	UNS S32750				UNS S39274			
Temperature	10ºC	22ºC	40ºC	60ºC	10ºC	22ºC	40ºC	60ºC
Median Crevice depth (µm)	No crevices	No crevices	4.5	25	No crevices	No crevices	5.2	19.2

FIGURES

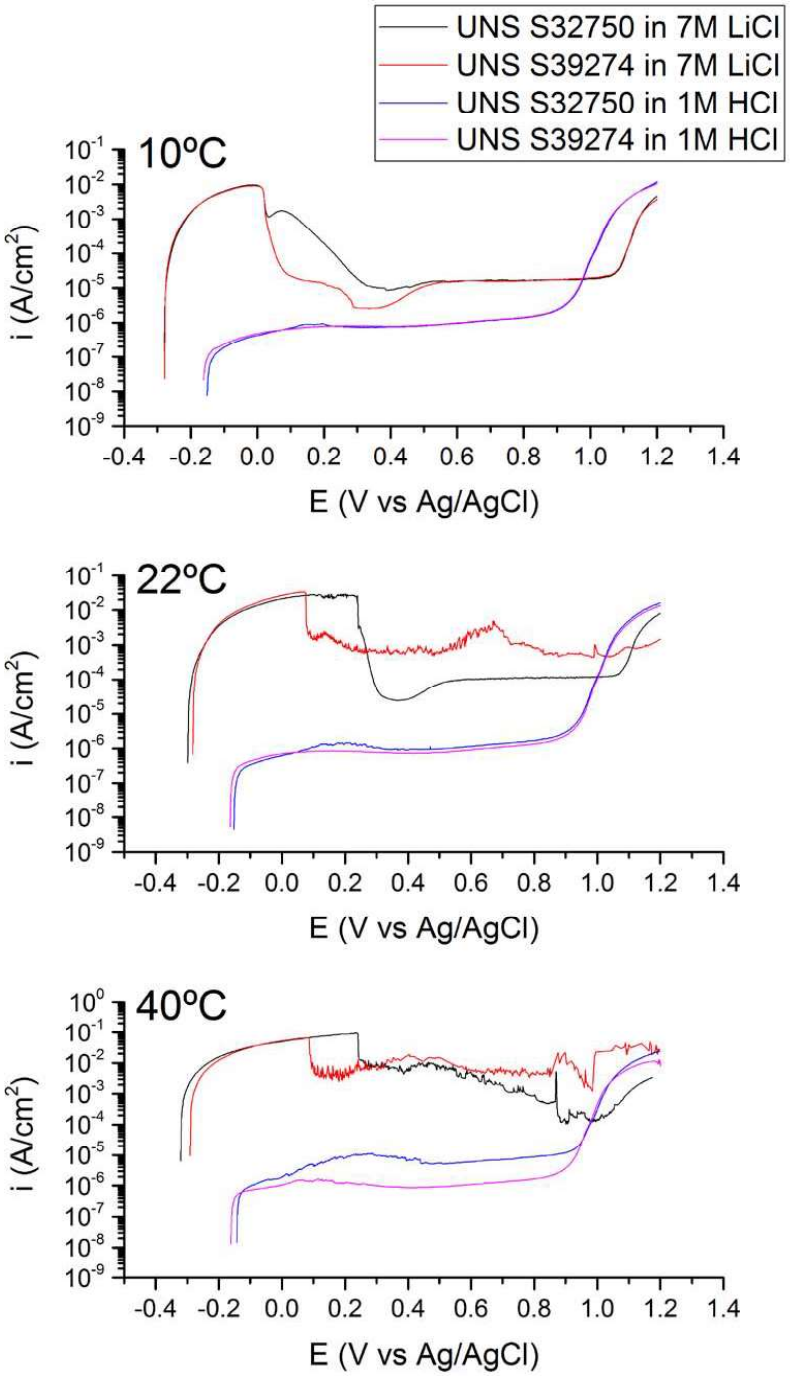

Figure 1-Potentiodynamic polarization curves measured in deaerated simulated crevice solutions at 10ºC, room temperature and 40ºC.

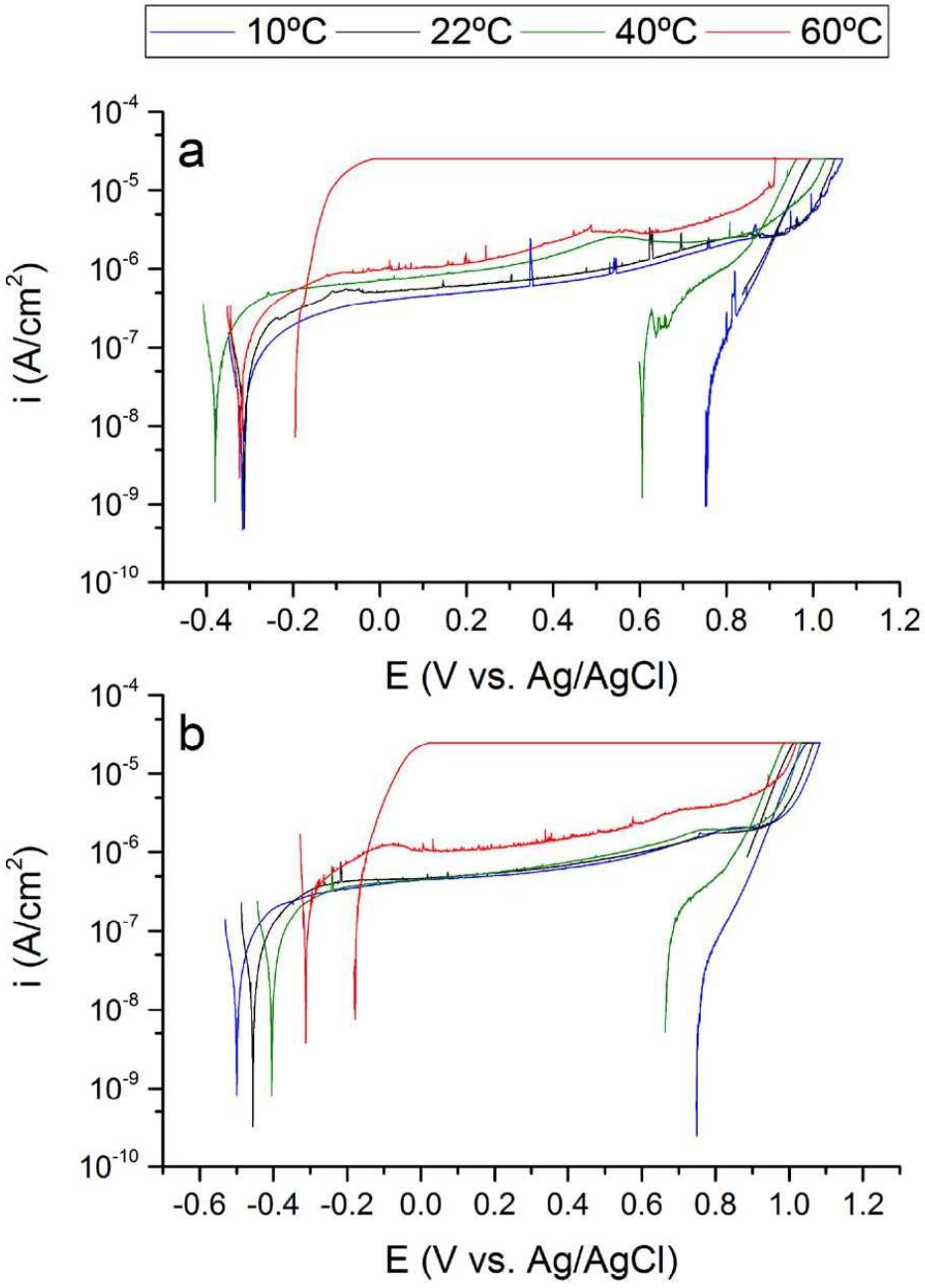

Figure 2-Current density vs potential measured during PD-GS-PD experiment for a) UNS S32750 and b) UNS S39274. Only one test was included in the plot for each condition since the test were reproducible.

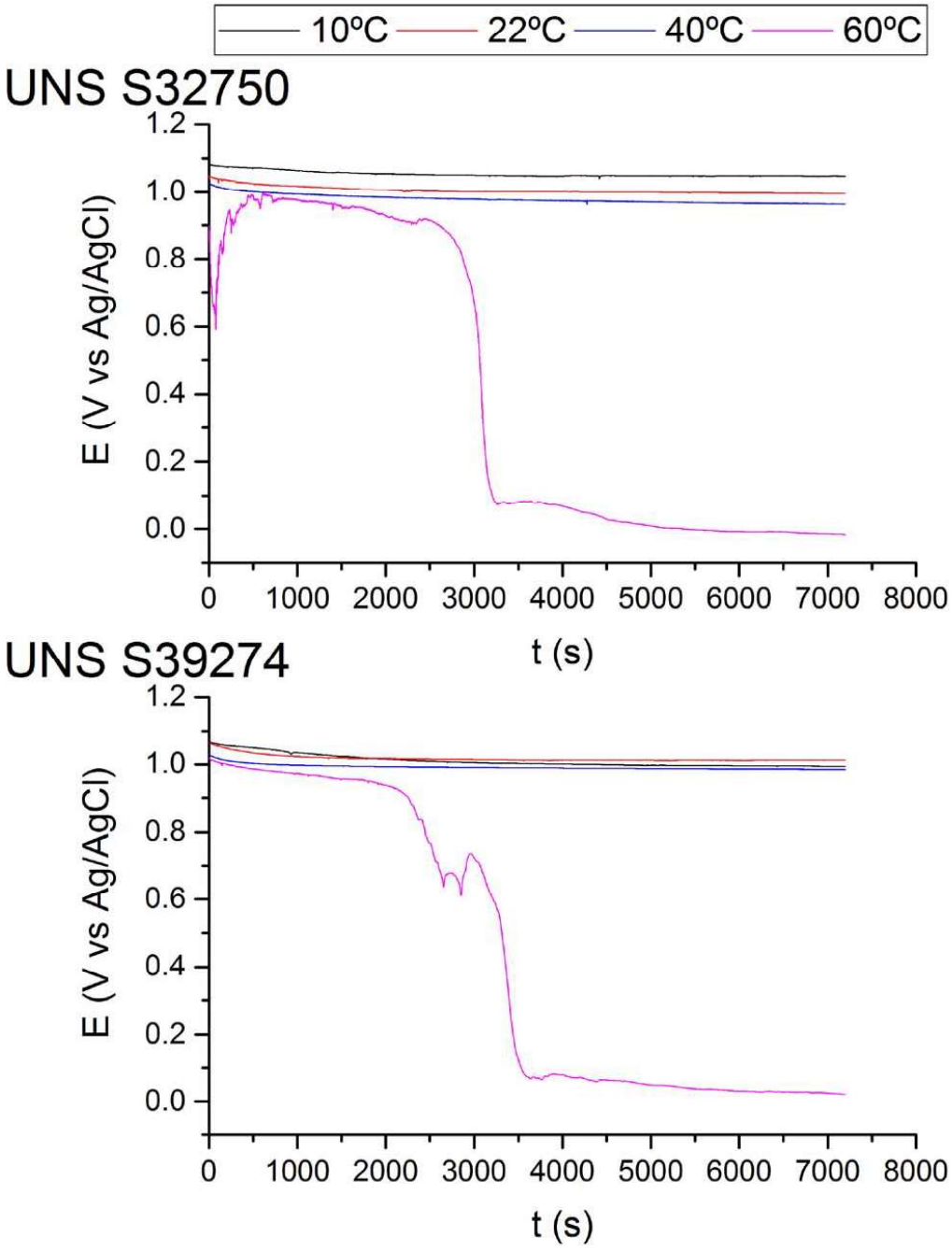

Figure 3-Potential evolution over time for all test conditions during the 2 hours galvanostatic step in the PD-GS-PD technique

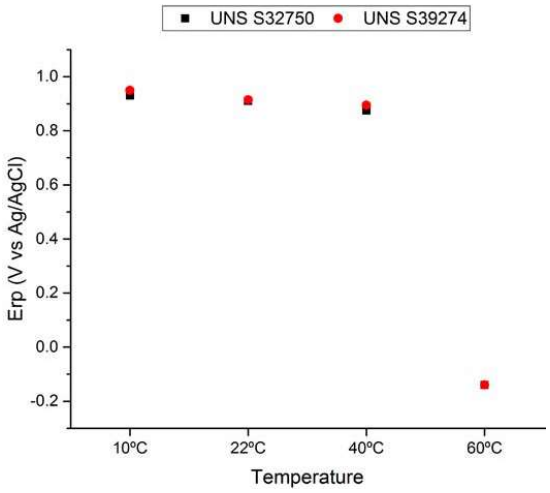

Figure 4-Crevice repassivation potentials for both SDSS as function of temperature. Each data point represents an average of two independent PD-GS-PD tests.

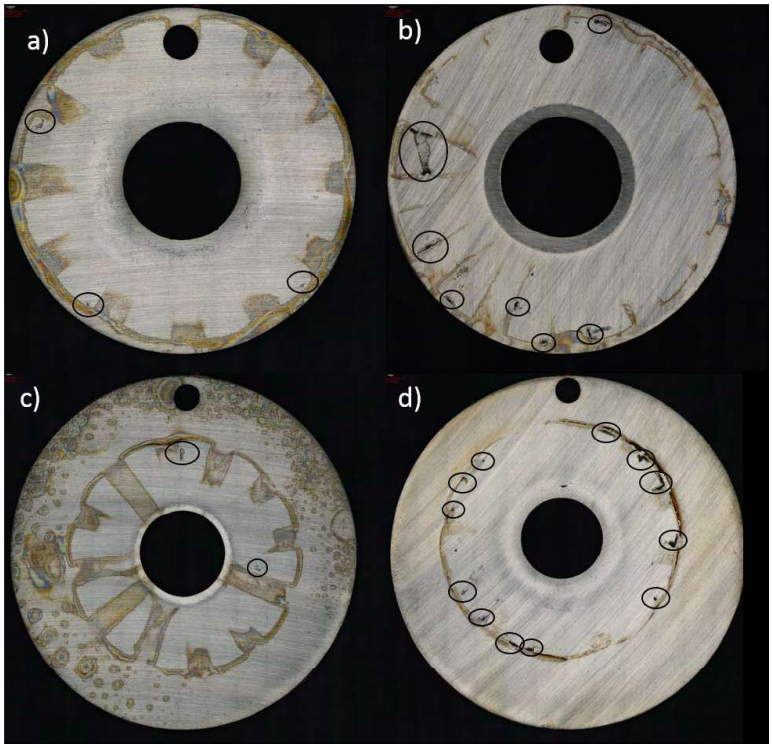

Figure 5-Sample surface indicating with black circles crevices present after PD-GS-PD tests for a) UNS S32750 at 40ºC, b) UNS S32750 at 60ºC, c) UNS S39274 at 40ºC and d) UNS S39274 at 60ºC.

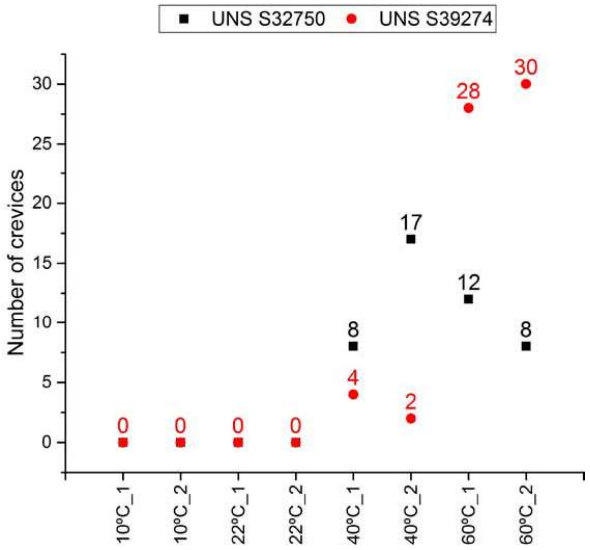

Figure 6-Number of crevices observed in each sample after PD-GS-PD tests

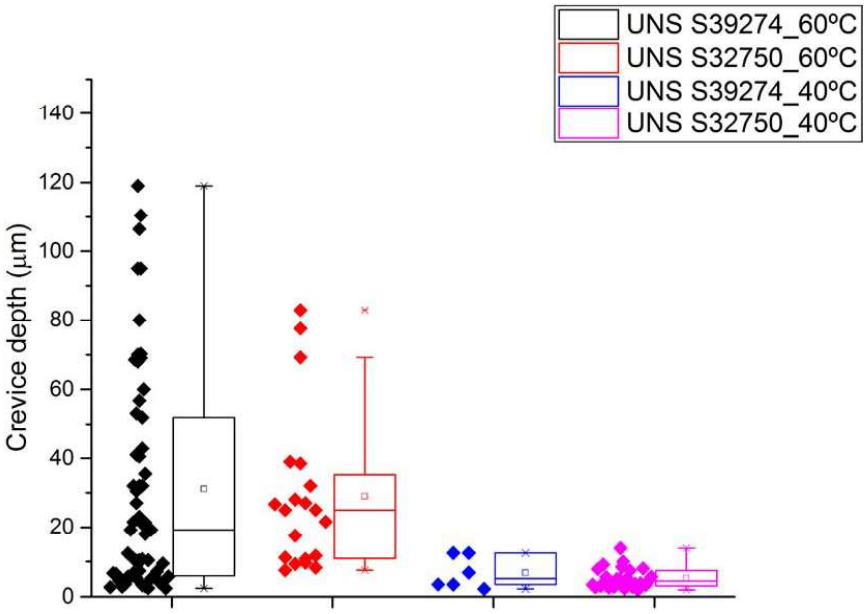

Figure 7-Box and whiskers plot showing the data distribution of crevice depth for both materials at 40ºC and 60ºC. The horizontal line inside each box represents the median of the distribution, i.e. the midpoint value of the distribution. Each box contains 50% of the distribution points (25% above and other 25% below the median). Each whisker represents other 25% of the distributions points. Each dataset includes both repetitions together.

CONFERENCE PAPER II

Effect of W on Phase Transformation Kinetics and its Correlation with Localized Corrosion Resistance for UNS S39274

C. Torres, R. Johnsen, H. Østvold, M. Bernås, M. Iannuzzi

CORROSION 2019, 24-28 March 2019, Nashville, Tennessee, USA

Paper No.
13233

NACE INTERNATIONAL CORROSION Conference & Expo 2019

Effect of W on Phase Transformation Kinetics and its Correlation with Localized Corrosion Resistance for UNS S39274

Cristian Torres, Roy Johnsen, Hege Østvold, Mia Bernås
Norwegian University of Science and Technology
Richard Birkelands vei 2
NO-7491 Trondheim, Norway.

Mariano Iannuzzi
Curtin University and Norwegian University of Science and Technology
GPO Box U1987
Perth, WA, 6845, Australia.

ABSTRACT

Previous research in 25Cr Super Duplex Stainless Steels (SDSS) has shown that an optimal W concentration—as an element in solid solution—exists, in which W improves localized corrosion resistance. Outside this range, W is either ineffective or even detrimental. However, debate still exists as to whether W accelerates or retards the precipitation of deleterious phases such as χ– and σ–phase.

The objective of this investigation is to elucidate the influence of W on phase transformation kinetics and its corresponding effect on corrosion resistance. Herein, a SDSS containing 2.1 wt. % W (UNS S39274) has been investigated and compared to a W-free SDSS (UNS S32750) studied previously. Different isothermal heat treatments were performed to precipitate tertiary phases in the microstructure. The alloy microstructure was analyzed and quantified by Scanning Electron Microscopy-Energy Dispersive X-ray Spectroscopy (SEM-EDS) and Electron Backscatter Diffraction (EBSD) and the type and volume fraction of deleterious phases quantified.

After characterization, critical pitting temperature (CPT) tests were performed in which samples were freely exposed (OCP) in 6 wt%. $FeCl_3$ solution starting at 40ºC. Then the temperature was increased 5ºC every 24 hours until corrosion was initiated. The temperature at which corrosion was initiated was taken as the CPT.

Key words: duplex stainless steels, critical pitting temperature, sigma phase, chi phase, chromium nitrides, time-temperature-transformation diagram.

INTRODUCTION

Corrosion resistance properties of super duplex stainless steels with secondary phases

Super duplex stainless steels (SDSS) are a type of high-alloyed stainless steel that has been described extensively in the literature.[1-7] They are widely used in the oil and gas industry due to their well-known high corrosion resistance properties. However, their properties deteriorate when secondary phases precipitate in the microstructure.[1, 2, 8] These deleterious phases are typically related to some type of heating processes such as e.g. welding or heat treatment. There are many different types of secondary phases that precipitate in SDSS. The most common ones are chi-phase (χ-phase), sigma-phase (σ-phase), chromium nitrides (Cr_2N) and secondary austenite (γ_2).[1, 9-12] Table 1 summarizes the temperature range in which some of these phases have been observed precipitating in duplex stainless steels (DSS) and SDSS. Even though these phases have already been described in detail elsewhere,[13] most emphasis is given to σ-phase since it is the most abundant in the microstructure and the most detrimental for both the mechanical and corrosion properties of the material.

Some authors[14-17] claim that the properties of SDSS can be improved with the presence of these deleterious phases if tungsten (W) is added in solid solution since W is able to delay the appearance of σ-phase which is the most detrimental phase. However, other authors[12, 18] claim that, in fact, W does not delay the precipitation of σ-phase, but also accelerates other secondary phases; resulting in a detrimental effect to the corrosion resistance properties.

As this controversial discussion continues, Haugan et al.[7] suggested that an optimal range of concentration for W in solid solution exits. Inside this range, W improves corrosion resistance in the material; otherwise it has a detrimental effect. The enhancement of the corrosion resistance properties is associated with the delay of σ-phase formation, as mentioned above.

Table 1: Summary of the most relevant deleterious phases in DSS and SDSS.

Secondary phase	Nominal chemical formula	Temperature range, °C
σ	Fe-Cr-Mo (W, Mn, Si)	600-1000
χ	$Fe_{32}Cr_{12}Mo_{10}$	750-850
Nitrides	Cr_2N (CrN, less common)	700-900

Motivation

In a previous study,[13] two SDSS with different W content (one of them was W-free and the other low-W content – 0.62 wt. %.) were exposed to different isothermal heat treatments and, afterwards, characterized by means of scanning electron microscopy (SEM), backscattered electron (BSE), energy dispersive x-ray spectroscopy (EDS), electron backscatter diffraction (EBSD) and light optical microscope (LOM). The combination of all these techniques allows the complete characterization of the microstructure and all precipitates present in it. In addition, critical pitting temperature (CPT) tests were performed for each isothermal heat-treatment in order to quantify the corrosion resistance property of the material at a given condition. As a result, temperature-time-transformation (TTT) diagrams with CPT data were plotted for each material. In this way, the time and temperature at which χ-phase and σ-phase appeared were easily observed, besides their effect on the corrosion resistance of each material for each isothermal heat treatment. Furthermore, a third SDSS with higher W content (2.1 wt. %.) was included, but only one isothermal temperature exposure was performed.

In this study, the same procedure has been applied to the SDSS with 2.1 wt. % W (UNS S39274) in order to complete the TTT diagram together with corrosion resistance data for the remaining isothermal aging temperatures.

EXPERIMENTAL

Materials

Table 2 shows the chemical composition of the alloy UNS S39274 studied in this paper. The material was received in the shape of a pipe with a wall thickness of 30 mm. Round samples were machined with a diameter of 25 mm and a thickness of 2 mm.

Table 2: UNS S39274 chemical composition in wt. %.

	C	Cr	Ni	Mo	Cu	W	N	PRE_N	$PRE_{N,W}$
UNS S39274	0.018	24.9	6.30	3.10	0.52	2.10	0.29	39.8	43.2

Heat treatment

Solution annealing (SA): Following the recommendation of the alloy manufacturer, all samples were solution annealed for 16 minutes (i.e., 1 minute temperature stabilization + 15-minutes annealing) at 1100°C in an air furnace to produce a homogeneous microstructure. The solution annealing step was followed by water quenching to room temperature. The objective of the solution annealing step was to remove prior heat treatment history.

Isothermal heat treatments: After solution annealing and quenching, the various sub-sets of samples were isothermally aged in an air furnace at three different temperatures: T_1 = 846°C, T_2 = 790°C, and T_3 = 920°C; followed by water quenching at room temperature. During each heat treatment, a K type thermocouple was inserted next to the sample in order to verify the correct temperature of the heat treatment. The value of T_1 was chosen close to the temperature at which the fastest precipitations kinetics of σ-phase and Cr_2N should be expected.[19] T_2 was chosen to separate the effect of χ-phase formation from that of σ-phase and Cr_2N. In contrast, because T_3 was above the expected stability range of χ-phase, the influence of isothermal Cr_2N could be separated from that of σ-phase. Table 3 shows the test matrix of the isothermal heat treatments.

Table 3: Isothermal heat treatment temperature-time (T_xt_y) combinations.

Temperature, °C	time, seconds
T_1 = 846	t_1 = 60
	t_2 = 90
	t_3 = 120
	t_4 = 240
	t_5 = 600
T_2 = 790	t_1 = 60
	t_2 = 120
	t_3 = 240
	t_4 = 600
	t_5 = 1200
T_3 = 920	t_1 = 60
	t_2 = 120
	t_3 = 240
	t_4 = 600
	t_5 = 1200

Characterization

Surface preparation for the characterization of the samples was carried out by grinding and polishing the samples down to 1 micrometer diamond particles. Afterwards, the samples were rinsed with acetone, followed by rinsing with distilled water and cleaned with ethanol in ultrasonic bath for 5 minutes. Then, characterization of the samples after the isothermal heat treatments consisted of different techniques:

LOM: Samples isothermally aged at 846ºC were electro-etched in 15 wt. %. KOH with an applied potential of 3 V for 12 seconds. Isothermal heat treated samples at 790ºC and 920ºC were electro-etched following the Statoil technical note MAT-2010080[20] which consisted of two different electro-etching steps: i) 10% oxalic acid with an applied potential of 5 V for 3 seconds and ii) 20% NaOH with an applied potential of 1.5 V for 10 seconds. Afterwards, the samples were taken to an infinite focus microscope (IFM) where optical images were acquired at a magnification between 10x and 50x.

SEM/BSE: The samples were taken to a SEM and analyzed by means of a back scattered electron (BSE) beam with an accelerated voltage of 20 kV to observe if precipitation of secondary phases had occurred.

EDS: This technique was used to examine the difference in composition of the secondary phases precipitating in the samples and to correlate the chemical composition measured to a type of intermetallic phase. In addition, measurements were carried out in the SA samples in order to obtain the chemical composition of ferrite grains (α), austenite grains (Ɣ) and bulk material with the aim to detect in which elements the intermetallic phases are enriched.

EBSD: The samples analyzed by means of EBSD had to go through extra surface preparation steps. After being polished down to 1 micrometer diamond particles, the samples were electro-polished in a mixture 5.3% H_2SO_4 - 94.7% Methanol at 18V for 30 seconds, followed by oxide polishing suspension (OPS) polishing that consists of a 0.02 µm colloidal silica suspension on a chemical cloth, which combined mechanical and chemical polishing. Quantitative analyses of volume fraction of the different phases were performed from the data acquired.

ASTM G48 modified

Corrosion resistance properties of the samples were tested as well for each isothermal heat treatment exposure. The test carried out consisted of a critical pitting temperature test in 6 wt. % $FeCl_3$, prepared by dissolving 100 g $FeCl_3 \cdot 6H_2O$ in 900 mL of distilled water. In this test, the samples were freely exposed to the electrolyte and the open circuit potential (OCP) was constantly monitored. The temperature was controlled to ± 1°C using a heating plate. The temperature was increased 5ºC every 24 hours until the potential dropped below +500 mV vs. SCE (Standard Calomel Electrode). Once the potential dropped below this value, it was considered that pitting had initiated in the sample. After the test, samples were taken to an infinite focus microscope (IFM) that acts as LOM and to SEM to document the localized attack.

RESULTS

Materials characterization

LOM: The microstructure of each sample was successfully revealed using the electro-etching method described above. Austenite (Ɣ) and ferrite (α) grains were easily discernible in all samples. In addition, Figure 1 includes pictures where precipitates can be observed in the samples with the longest isothermal heat treatments. It can already be seen that the secondary phases were smaller and fewer in the sample isothermally aged at 790ºC for 600 seconds (Figure 1 (b)) than for the other temperatures. On the other hand, samples isothermally aged at 920ºC for more than 600 seconds (Figure 1 (c) and (d)) showed the highest density of intermetallic phases.

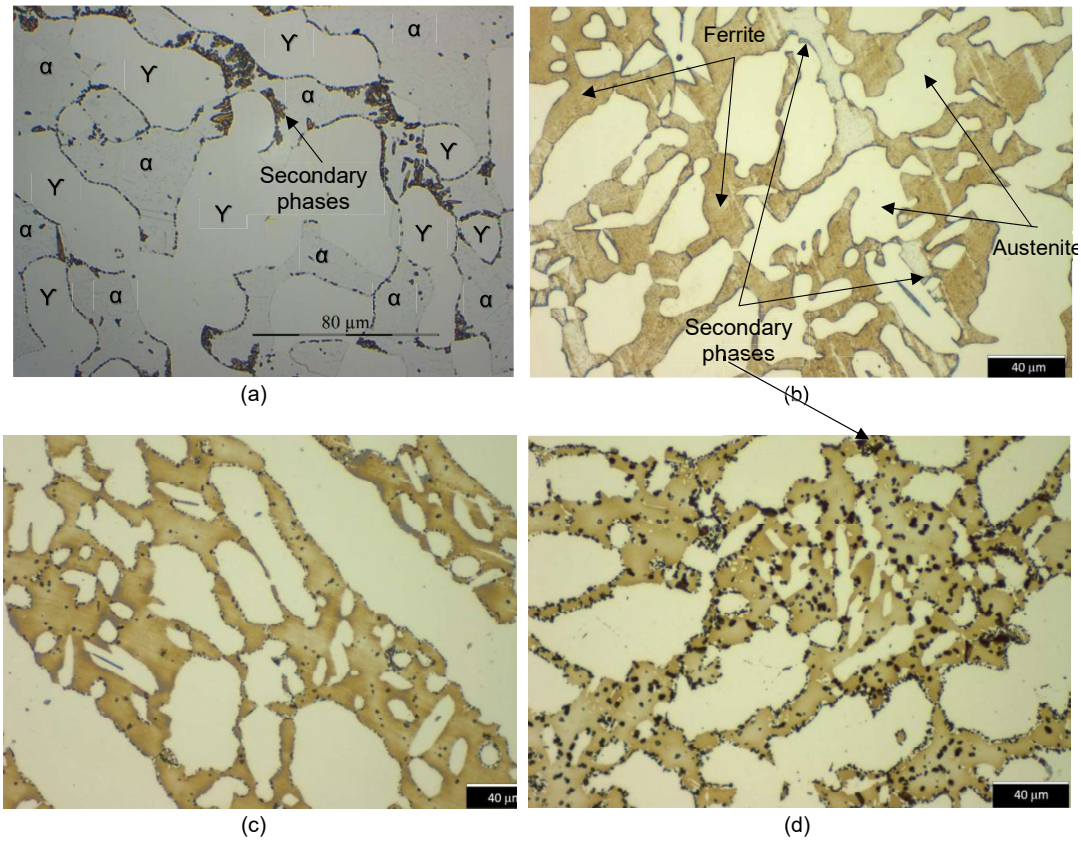

Figure 1: Light optical microscopy after isothermal aging at (a) 846ºC for 600 s, (b) 790ºC for 600 s, (c) 920ºC for 600 s and (d) 920ºC for 1200 s.

SEM/BSE: Precipitates are visible in the SEM by means of the BSE. As delivered (AD) and SA samples showed no precipitates. Isothermal heat treated samples showed precipitates at different times depending on the temperature of the treatment. At all three temperatures, secondary phases started precipitating at grain boundaries after 240 seconds. Nevertheless, the intermetallic phases were very small at 790ºC and 846ºC; especially when the isothermal heat treatment was performed for only 240

seconds. As the isothermal heat treatment time increased, the precipitates grew in size and started surrounding all the grain boundaries and, in some cases, started appearing in the ferrite grains as seen in Figure 2.

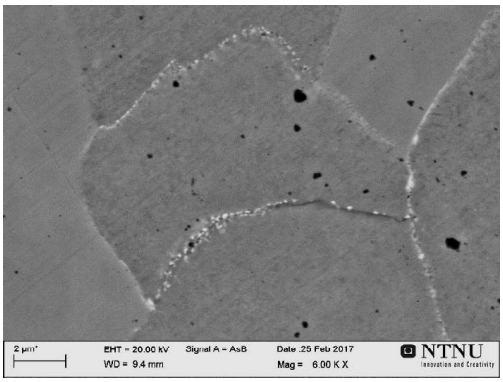

(a)

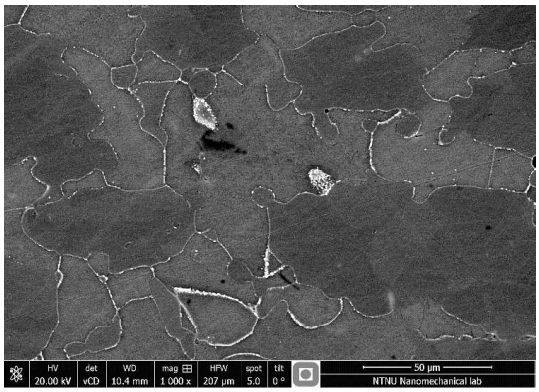

(b)

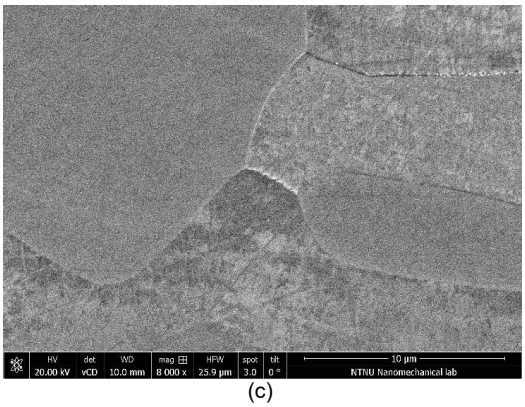

(c)

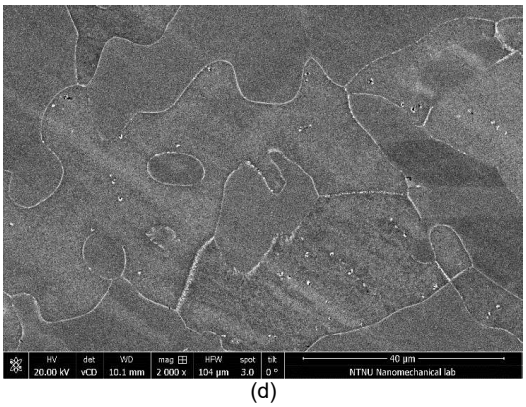

(d)

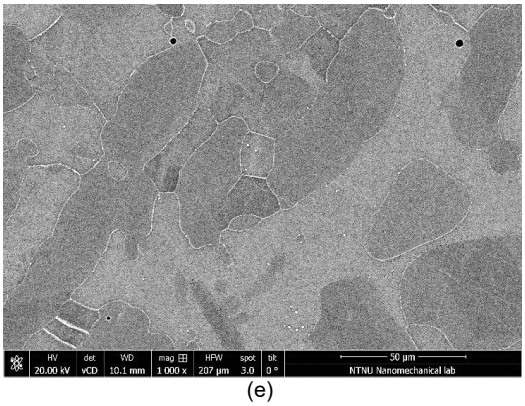

(e)

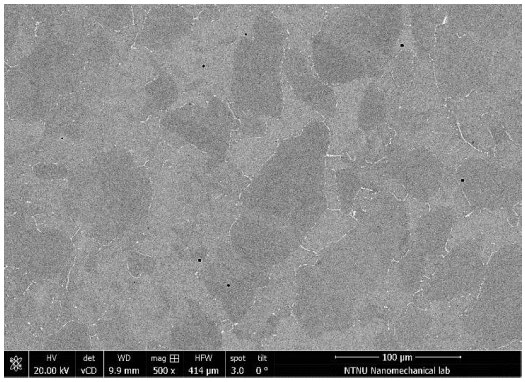

(f)

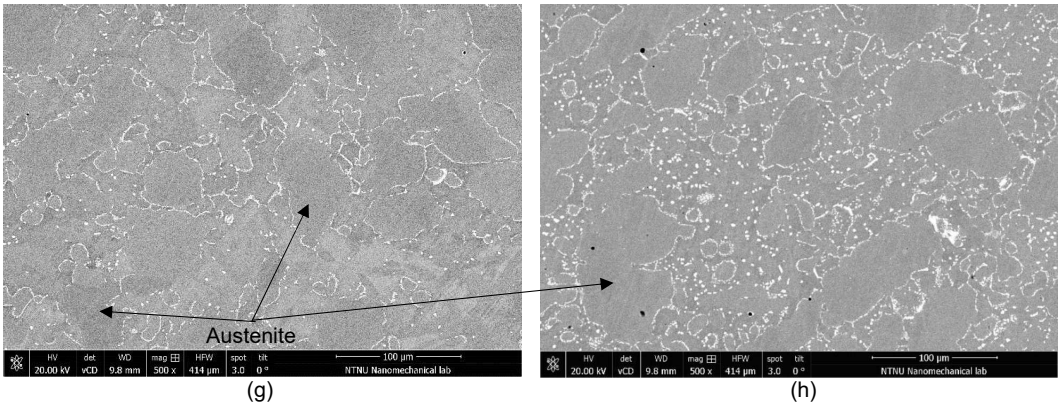

(g) (h)

Figure 2: Scanning electron microscopy after isothermal aging at (a) 846°C for 240 s, (b) 846°C for 600 s, (c) 790ºC for 240 s, (d) 790°C for 600 s, (e) 790ºC for 1200 s, (f) 920ºC for 240 s, (g) 920ºC for 600 s and (h) 920°C for 1200 s.

Another noteworthy result is that a different type of phase was observed precipitating on the grain boundaries at 920ºC starting after 600 seconds as illustrated in Figure 3. It is distinguishable from the previous intermetallic phase by its duller appearance with the BSE, meaning that it consists of lighter elements. This statement was confirmed afterwards by means of EDS and EBSD.

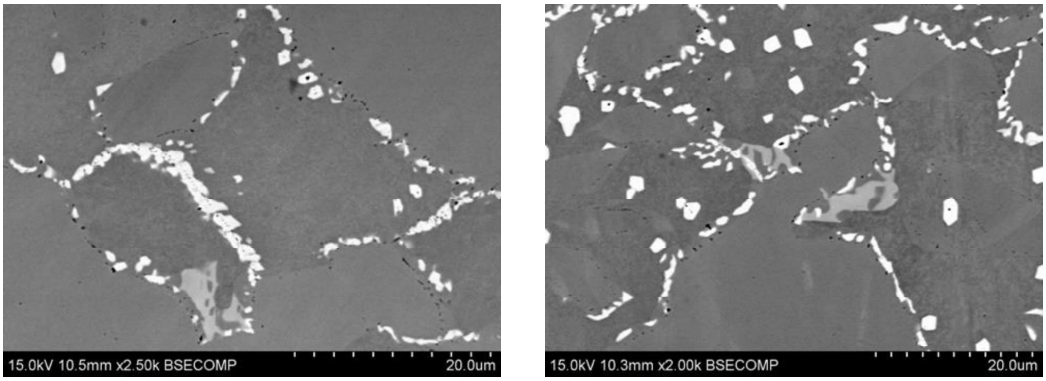

(a) (b)

Figure 3: Scanning electron microscopy after isothermal aging at (a) 920°C for 600 s and (b) 920°C for 1200 s

EDS: First, the brighter particles were analyzed and the results are summarized in Table 4 and Figure 4. It was not possible to perform analyses of the sample isothermally aged at 846ºC for 240 seconds because the precipitates were too small. Furthermore, the results obtained for isothermally aged samples at 790ºC are very scattered as seen in Figure 4 due to the same reason. It can be seen that this first secondary phase to precipitate is richer in Mo and W while it is depleted of Fe and Ni in comparison with the bulk composition of the material.

Table 4: Chemical composition of χ-phase in each sample compare to the bulk material in wt. %.

Elements	T1t5	T2t4	T2t5	T3t3	T3t4	T3t5	Bulk
Cr	27.04	25.32	24.80	25.20	25.72	25.04	24.9
Fe	49.85	57.10	52.02	51.60	50.34	49.16	61.8
Ni	3.31	4.54	4.46	3.39	3.03	2.87	6.3
Mo	9.47	7.25	9.76	10.25	11.01	12.14	3.1
W	7.33	5.96	8.07	9.20	9.83	10.76	2.1

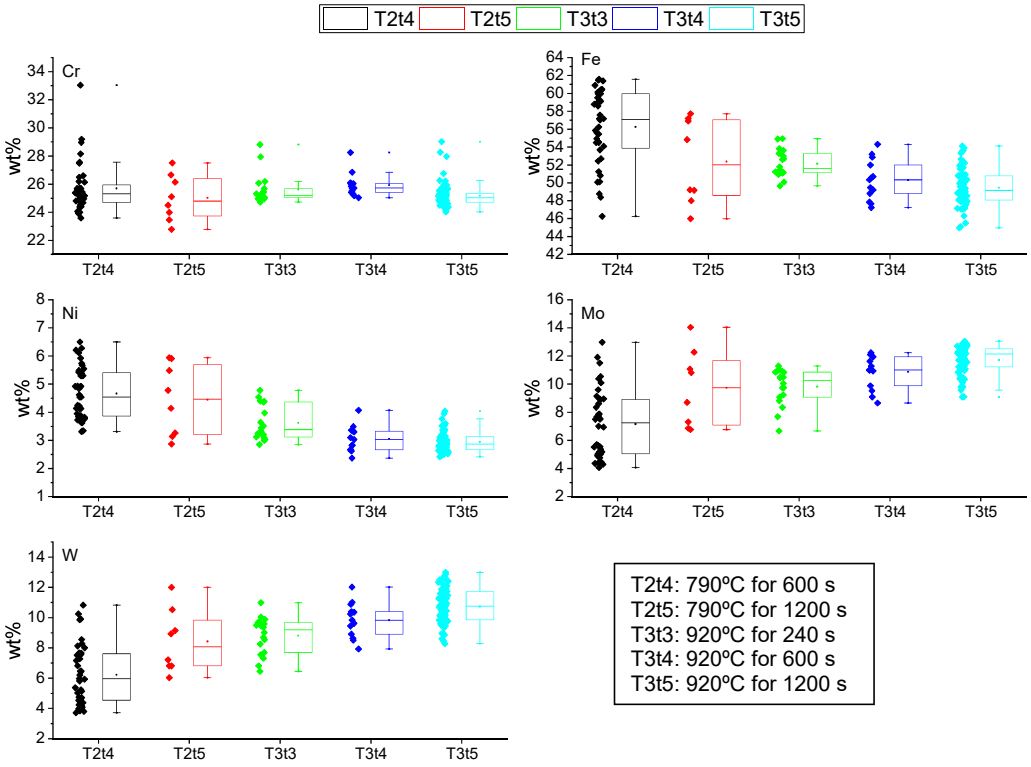

Figure 4: Box & whiskers plot of EDS analyses performed on bright precipitates.

The second intermetallic phase to precipitate at 920ºC after 600 seconds, i.e. the duller particles in Figure 3, was analyzed afterwards and the results are illustrated in Figure 5. It is enriched in Mo and W in comparison with the bulk material. However, in this case, the enrichment is not as large as in the previous precipitate. This is the reason why it appears duller with the BSE. In addition, it is found that it is enriched as well in Cr, and as before, it is depleted in Fe and Ni. Table 5 summarizes the chemical composition of each phase found in this SDSS.

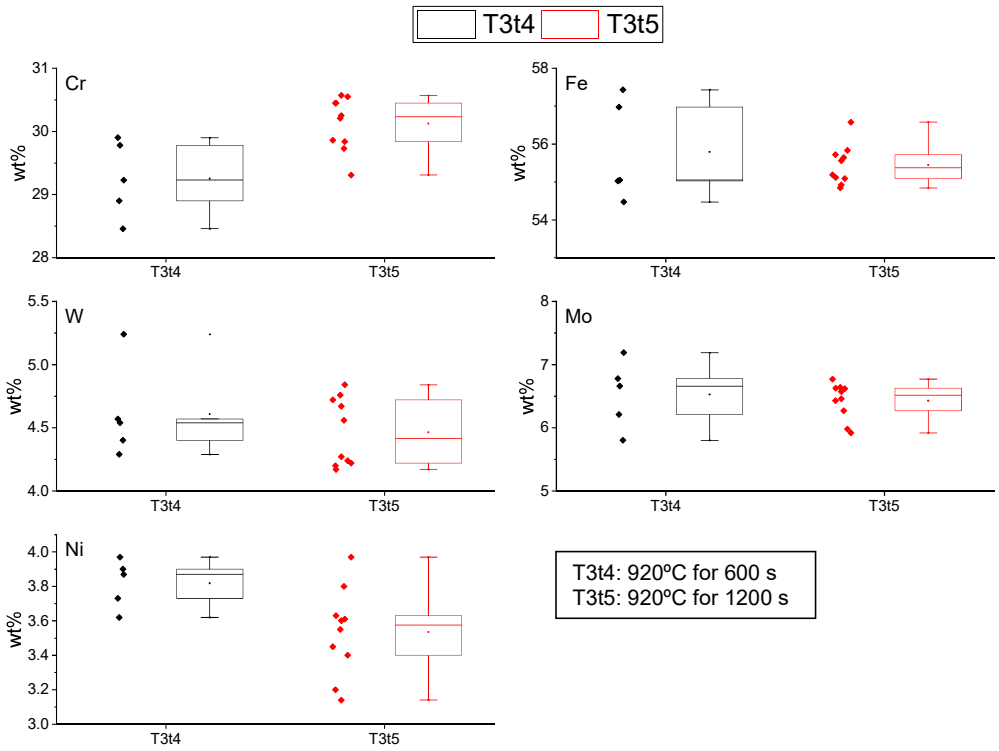

Figure 5: Box & whiskers plot of EDS analyses performed on dull particles.

Table 5: Average chemical composition of each phase found in wt. %.

Secondary phase	Fe	Cr	Ni	Mo	W
Ferrite, α	63.5	26.4	4.7	2.9	2.5
Austenite, γ	64.7	24.1	7.3	1.9	1.9
σ-phase	55.2	29.7	3.7	6.6	4.5
χ-phase	52.0	25.2	3.7	10.8	9.5

EBSD: All phases present are successfully detected as seen in the example in Figure 6. In this way, together with the EDS results, it is verified that the bright particles precipitating first are χ-phase, whereas the second phase with a duller appearance is σ-phase. From these analyses, volume fraction values were obtained for each phase.

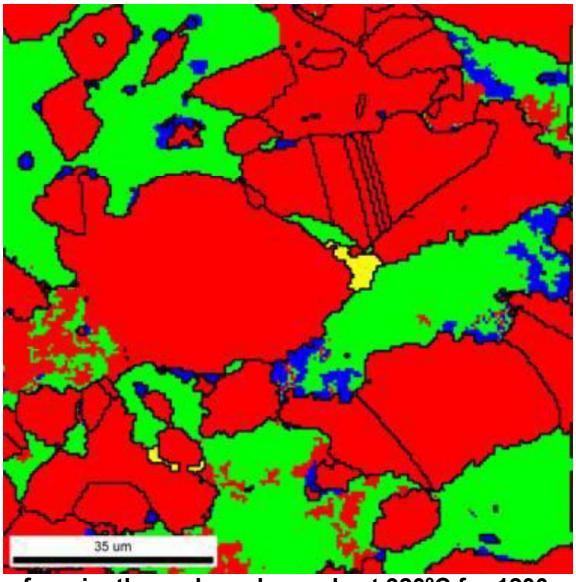

Figure 6: EBSD map from isothermal aged sample at 920ºC for 1200 s where the different phases can be seen (red = austenite, green = ferrite, yellow = sigma, blue = chi).

Correlation between microstructure and corrosion resistance

Thus far, corrosion tests have only been performed on samples isothermally aged at 846ºC. Figure 7 illustrates the results obtained for some of the samples. The results show that the CPT value decreases with increased isothermal heat treatment time. Furthermore, once the intermetallic phases are present in the microstructure, the decrease accelerates abruptly. This clear influence of the intermetallic phases on the corrosion resistance properties of the material is verified after analyzing the corroded samples in the SEM/BSE as illustrated in Figure 8. In these pictures, localized corrosion is seen where intermetallic phases were located.

Combining the results of the corrosion tests with the characterization of the intermetallic phases results in Figure 9. It consists of a TTT diagram with information of the precipitation kinetics of each secondary phase, as well as their effect on the corrosion resistance properties of the material shown by means of CPT values. When the difference in volume fraction of both deleterious phases (χ and σ) is less than one order of magnitude, it is represented in the TTT diagram as a circle half white and half black and the measured volume fraction for each phase is included under it (symbolized as “Sum” in the legend of Figure 9). Otherwise, the most abundant precipitate symbol is used as shown in the legend of Figure 9 with the volume fraction values measured for each type of secondary phase seen.

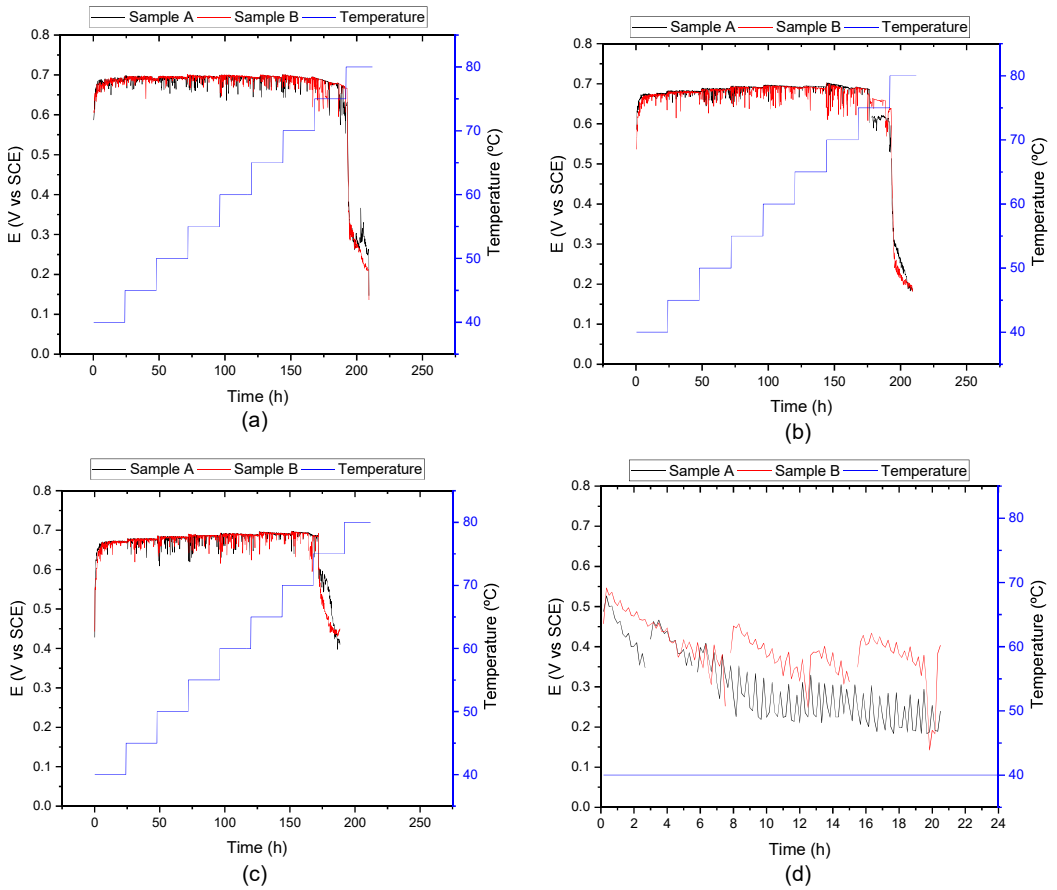

Figure 7: Open circuit potential in 6 wt. % $FeCl_3$ as a function of time and temperature after aging at 846°C for (a) 60 s, (b) 90 s, (c) 120 s and (d) 600 s.

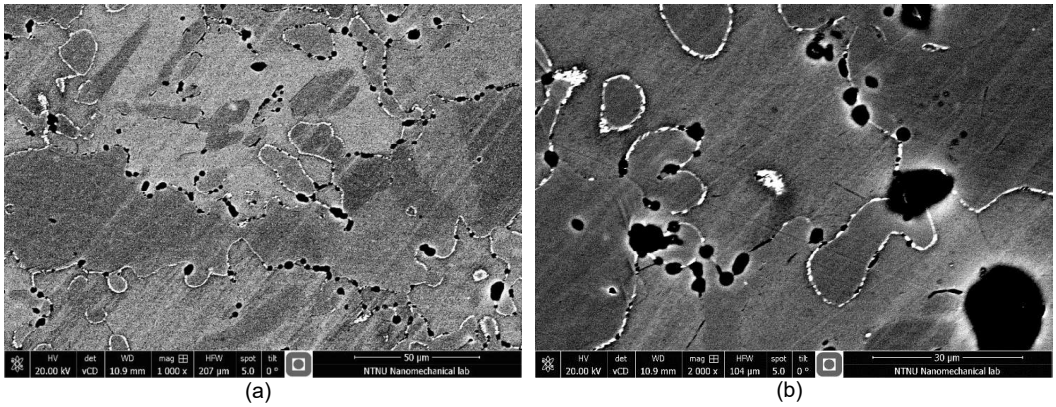

Figure 8: Scanning electron microscopy after CPT test of samples isothermally aged at 846°C for 600 s at (a) 1000x and (b) 2000x magnification. Black spots are corrosion attacks.

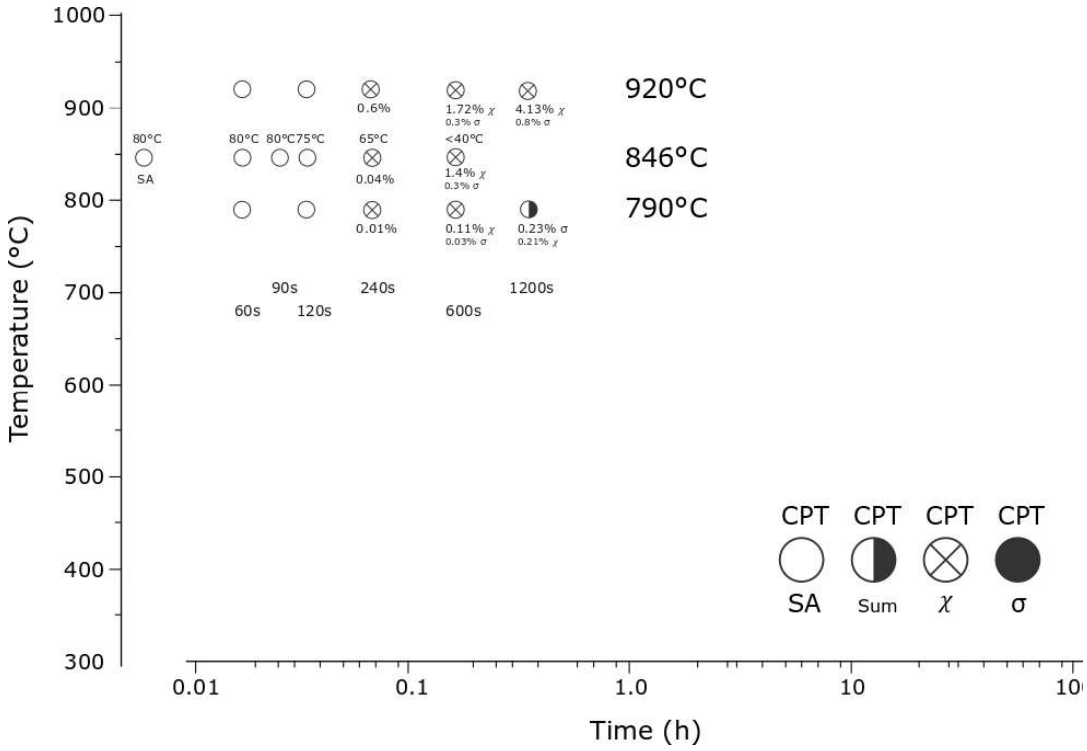

Figure 9: Summary of Time Temperature Transformation diagram overlapped with the corresponding minimum CPT.

DISCUSSION

The results obtained indicate that, even though intermetallic phases started precipitating at the same time at the three studied temperatures, the size of the intermetallic phases was not the same. The secondary phases were generally bigger at higher temperatures. In addition, the density of precipitates increased with increased exposure time. At the beginning, they precipitated at the grain boundaries. As the grain boundaries were filled, secondary phases started precipitating in the ferrite grains. In this study, the latter was only observed at 920ºC for isothermal heat treatment times longer than 600 seconds. It is explained in the literature[21] that intermetallic phases precipitate first in ferrite grains rather than in austenite because Cr and Mo have higher diffusion rate in ferrite. This faster diffusivity is due to the bcc structure of ferrite that is less compact than the fcc structure of austenite.

Two different secondary phases were identified precipitating in this SDSS. First, a small bright particle that was enriched in Mo and W, whereas it was depleted in Fe and Ni, was found at all temperatures for times longer than 240 seconds. The amount of these particles increased as the time of the isothermal heat treatment increased. This intermetallic phase was identified as χ-phase due to its high Mo content.[21-23] An attempt to analyze if there was any difference in chemical composition between the χ-phases precipitated at different temperatures and different times was carried out. Nevertheless, in some cases,

the precipitates were too small to be analyzed by means of EDS. Furthermore, EDS is not a technique that gives the exact chemical composition of a small particle since it analyzes as well the surroundings and the bulk material beneath. Therefore, no formal statistical analyses could be performed to see if significant differences existed; even though Figure 4 indicates that χ-phase incorporates more Mo and W as time and temperature increase, while it gets depleted of Fe and Ni.

On the other hand, a second intermetallic phase was found for isothermally aged times longer than 600 seconds. Besides being enriched in Cr in comparison to the bulk material, this phase was enriched as well in Mo and W, although not as much as χ-phase. Alike χ-phase, it was depleted in Fe and Ni. This secondary phase was present only at grain boundaries and it was incrementing in quantity as isothermal heat treatment time increased. This second intermetallic phase was identified as σ-phase due to its Mo content.[21-23] Figure 5 shows that there is no difference in chemical composition of σ-phase between isothermal aging times, even though a formal statistical analysis should be performed in order to be able to confirm that there is no significant difference.

Similar results were obtained in other studies published in the literature. For example, Calliari et al.[22] observed that below 900ºC, the only intermetallic phase precipitating in their SDSS was χ-phase. Above this temperature, σ-phase precipitated but only after χ-phase. Villanueva et al.[24] observed that, even though σ-phase precipitation kinetics were faster at about 850ºC for the duplex stainless steel they studied, a higher Mo content in the alloy shifted the precipitation temperature to higher values. Llorca et al.[23] observed that χ-phase was present in bigger quantities than σ-phase for short isothermal aging times in UNS S32750.

UNS S32750 (W-free) was also studied by Bernås et al.[13] together with a UNS S32760 with 0.62 wt. %. W isothermally aged at the same temperatures and times as in the present study. Their aim was to examine the effect of W on precipitation kinetics of secondary phases. Since they observed σ-phase after only 60 seconds at 920ºC for UNS S32760, whereas it precipitated after 240 seconds for UNS S32750; W seemed to promote σ-phase precipitation, i.e. W deteriorated corrosion resistance properties of the SDSS. However, in the present study, σ-phase was only seen after 600 seconds. Consequently, this result demonstrates that W retards precipitation of σ-phase when the SDSS has a content of 2.1 wt. % W in solid solution. Other authors[14, 17, 25] proved as well that W in SDSS retards σ-phase precipitation.

Finally, the results show clearly that the presence of intermetallic phases become detrimental for the corrosion resistance properties of the material since the CPT values obtained decreased when χ-phase was present. The drop in CPT is more abruptly seen for samples isothermally aged at 846ºC for 600 seconds. However, it is not clear whether the responsible is the precipitation of σ-phase or the bigger amount of χ-phase in the microstructure. The reason is that, since the secondary phases are enriched in Cr, Mo and W as seen in Table 5, there is a depleted area of these elements surrounding it. Consequently, this depleted area has a lower PRE number, making it more susceptible to localized corrosion. There are many studies[11, 13, 21] that show data in accordance to this conclusion. However, this study could not prove that σ-phase has a higher detrimental effect on the corrosion resistance properties of UNS S39274 than χ-phase as some literature suggests.[14, 17, 25]

Figure 9 summarizes all the data from both intermetallic phase characterization and corrosion testing in a complete and simple manner, making analyses and comparison of the results fast and easy. A similar diagram was prepared by Bernås et al.[13] for UNS S32750 (W-free) and UNS S32760 (0.61 wt. % W).

CONCLUSIONS

The following conclusions were drawn for UNS S39274 based on the outcome of the investigation described herein:

- The main secondary phase found at the studied isothermally aged temperatures and times was χ-phase. The size and quantity precipitated depended on time and temperature of the isothermal heat treatment. Size enlarged as temperature and time increased.
- W retarded σ–phase precipitation as it was only seen for isothermal aging longer than 600 seconds.
- The corrosion resistance deteriorated abruptly when secondary phases were present in the microstructure.
- A modified "TTT diagram" including CPT and the type of phase that precipitated has been established.

ACKNOWLEDGEMENTS

We thank Di Wan (NTNU) and Thibaud Choquet (INSA Lyon) for their help and technical support in the lab. This work was sponsored by General Electric, Co. (Oil and Gas, Norway) and conducted at NTNU's Department of Mechanical and Industrial Engineering (MTP).

REFERENCES

1. J.O. Nilsson, *Materials Science and Technology* 8, 8 (1992): p. 685-700.
2. J. Charles, "Super duplex stainless steels: structure and properties," Duplex Stainless Steels '91, (Beaune, Bourgogne, France: Proceedings. Les Éditions de Physique Les Ulis, 1991), p. 151-168.
3. L.F. Garfias-Mesias, J.M. Sykes, C.D.S. Tuck, *Corrosion Science* 38, 8 (1996): p. 1319-1330.
4. G. Byrne, R. Francis, G. Warburton, M. Maligas, "The Selection Of Superduplex Stainless Steel For Oilfield Applications," CORROSION 2004, paper no. 04123 (New Orleans, LA: NACE International, 2004).
5. R. Sriram, D. Tromans, *Corrosion* 45, 10 (1989): p. 804-810.
6. L.F. Garfias-Mesias, J.M. Sykes, *Corrosion* 54, 1 (1998): p. 40-47.
7. E.B. Haugan, M. Næss, C. Torres Rodriguez, R. Johnsen, M. Iannuzzi, *Corrosion* 73, 1 (2017): p. 53-67.
8. K.M. Lee, H.S. Cho, D.C. Choi, *Journal of Alloys and Compounds* 285, 1-2 (1999): p. 156-161.
9. R. Francis, G. Byrne, G. Warburton, "The Corrosion Of Superduplex Stainless Steel In Different Types Of Seawater," CORROSION 2011, paper no. 11351 (Houston, TX: NACE International, 2011).
10. J.O. Nilsson, P. Kangas, A. Wilson, T. Karlsson, *Metallurgical and Materials Transactions A: Physical Metallurgy and Materials Science* 31, 1 (2000): p. 35-45.
11. P. Paulraj, R. Garg, *Advances in Science and Technology Research Journal* 9 (2015): p. 87-105.
12. J.O. Nilsson, T. Huhtala, P. Jonsson, L. Karlsson, A. Wilson, *Metallurgical and Materials Transactions A* 27, 8 (1996): p. 2196-2208.
13. M. Bernås, I. Westermann, A. Jernberg, A.H. Qvale, R. Johnsen, C. Torres, M. Iannuzzi, "Effect of Tungsten on the Precipitation Kinetics and Localized Corrosion Resistance of Super Duplex Stainless Steels," CORROSION 2018, (Phoenix, Arizona, USA: NACE International, 2018), p. 15.
14. K.Y. Kim, P.Q. Zhang, T.H. Ha, Y.H. Lee, *Corrosion* 54, 11 (1998): p. 910-921.
15. S.-H. Jeon, S.-T. Kim, I.-S. Lee, J.-S. Kim, K.-T. Kim, Y.-S. Park, *Journal of Alloys and Compounds* 544 (2012): p. 166-172.
16. K. Ogawa, H. Okamoto, M. Ueda, M. Igarashi, T. Mori, T. Kobayashi, *Welding International* 10, 6 (1996): p. 466-472.
17. H.J. Park, H.W. Lee, *Int J Electrochem Sc* 9, 12 (2014): p. 6687-6698.
18. S. Wessman, R. Pettersson, *steel research international* 86, 11 (2015): p. 1339-1349.
19. J.O. Nilsson, *Materials Science and Technology* 8, 8 (1992): p. 685-700.

20. MAT–2010080, "Technical note – Metallographic etching of duplex stainless steels" (Oslo, Norway: Statoil ASA, 2010).
21. K.W. Chan, S.C. Tjong, *Materials (Basel)* 7, 7 (2014): p. 5268-5304.
22. I. Calliari, M. Pellizzari, E. Ramous, *Materials Science and Technology* 27, 5 (2011): p. 928-932.
23. N. Llorca-Isern, H. López-Luque, I. López-Jiménez, M.V. Biezma, *Materials Characterization* 112 (2016): p. 20-29.
24. D.M.E. Villanueva, F.C.P. Junior, R.L. Plaut, A.F. Padilha, *Materials Science and Technology* 22, 9 (2006): p. 1098-1104.
25. J.S. Kim, H.S. Kwon, *Corrosion* 55, 5 (1999): p. 512-521.